

In-situ investigations of adsorbed hydrocarbons – model systems of heterogeneous catalysis

Den Naturwissenschaftlichen Fakultäten
der Friedrich-Alexander-Universität Erlangen-Nürnberg
zur
Erlangung des Doktorgrades

vorgelegt von
Christian Papp
aus Erlangen

Als Dissertation genehmigt von den Naturwissenschaftlichen Fakultäten der
Universität Erlangen-Nürnberg

Tag der mündlichen Prüfung: 12.07.2007

Vorsitzender der Promotionskommission: Prof. Dr. Bänsch

Erstberichterstatte: Prof. Dr. Steinrück

Zweitberichterstatte: Prof. Dr. Libuda

Table of contents

1 Introduction.....	1
2 Fundamentals and techniques	5
2.1 X-ray photoelectron spectroscopy (XPS)	5
2.1.1 General remarks.....	5
2.1.2 Chemical shift.....	9
2.1.3 Vibrational excitations in XPS.....	10
2.1.4 Line profiles	15
2.1.5 Quantification of XPS data and photoelectron diffraction	16
2.1.6 X-rays from a synchrotron radiation source	17
2.2 TPXPS and TPD	19
2.2.1 Basic principles.....	19
2.2.2 Primary kinetic isotope effect in TPXPS and in TPD experiments.....	21
2.3 Low energy electron diffraction	22
2.4 Molecular beams	23
2.5 Basic considerations for the vibrational properties of molecules	24
3 Experimental section	29
3.1 “The Synchrotron machine”.....	29
3.2 Surface endstation of beamline I 5-11 at MAX Lab.....	31
4 Adsorption and reaction of benzene.....	33
4.1 Adsorption of pure benzene layers	34
4.1.1 Introduction.....	34
4.1.2 Adsorption of benzene (C ₆ H ₆ and C ₆ D ₆) at 200 K	36
4.1.3 Adsorption at 125 K and thermal evolution up to 220 K.....	48
4.2 Coadsorption experiments with benzene	54
4.2.1 Benzene coadsorbed with CO: (2√3x2√3) R30° benzene + 2 CO.....	55
4.2.2 Benzene coadsorbed with NO: (3 x 3) benzene +2 NO.....	59
4.3 Binding energy shifts in the XP spectra	64
4.4 Summary	65
5 Adsorption and reaction of cyclohexene	69
5.1 Introduction.....	70
5.2 Adsorption	73

5.2.1 Adsorption experiments at 125 K.....	73
5.2.2 Adsorption at elevated temperatures.....	77
5.3 Thermal evolution.....	82
5.3.1 TPXPS experiment of the layer adsorbed at 210 K.....	82
5.3.2 Temperature programmed desorption data.....	84
5.3.3 TPXPS experiment of cyclohexene adsorbed at 125 K.....	85
5.4 Summary and conclusions.....	88
6 Adsorption and reaction of heterocycles.....	91
6.1 Introduction.....	92
6.2 Adsorption of furan and pyrrole.....	95
6.3 Reaction of furan and pyrrole.....	101
6.4 Summary.....	112
7 Methane adsorption on stepped platinum surfaces.....	115
7.1 Introduction.....	116
7.2 Results and discussion.....	118
7.2.1 Adsorption experiments on Pt(355) and Pt(322).....	118
7.2.2 Thermal evolution of the adsorbed species.....	127
7.2.3 Radiation induced chemistry.....	131
7.2.4 Summary and conclusions.....	134
7.3 Methane adsorption on silver modified stepped Pt surfaces.....	135
7.3.1 Preparation of the silver layers.....	135
7.3.2 Adsorption of methane on the two silver modified stepped platinum surfaces.....	136
7.3.3 Thermal evolution of methyl layers on silver precovered platinum surfaces.....	140
7.3.4 Conclusions and summary.....	142
7.4 Kinetic isotope effects in the adsorption and decomposition of methane on stepped platinum surfaces.....	143
7.4.1 Kinetic isotope effects in the adsorption of methane.....	144
7.4.2 Kinetic isotope effect in the thermal evolution of methane.....	149
7.4.3 Summary.....	158
7.5 Summary.....	158
8 Summary.....	163

9 Appendixes.....	167
9.1 Appendix to chapter 2	167
9.1.1 Changes in the bond length and the vibrational excitations upon core excitation	167
9.2 Appendix to chapter 4	169
9.2.1 Modeling of XP spectra of benzene with different functions	169
9.2.2 Changes in desorption temperatures upon heat rate variation	171
9.2.3 Calculation of the minority population for the adsorption of benzene at 200 K.....	172
9.2.4 Low temperature adsorption of deuterated benzene	173
9.3 Appendix to chapter 6	174
9.3.1 Fits of furan C 1s spectra obtained during a TPXPS experiment	174
9.3.2 Fits of pyrrole C 1s spectra obtained during a TPXPS experiment.....	175
9.4 Appendix to chapter 7	177
9.4.1 Supporting information to chapter 7.2.....	177
9.4.2 Transition and characteristic temperatures together with the respective activation energies of methyl on Pt(111)	179
9.4.3 Kinetic energies of the methane	182
Literature	183

1 Introduction

In the past decades surface science has become a strongly evolving and still growing field of science. It is not only a large part of condensed matter physics but also an interdisciplinary field with great relevance for other research areas. The scientific disciplines involved in surface science range from physics to chemistry, biology and materials science. The main driving forces of surface science are not only the ever increasing demands of the semiconductor industry and their need for nanoscaled products but also the necessity for new materials and improved catalysts. One of the great motivations to study chemical reactions on surfaces is certainly the field of heterogeneous catalysis. This field is represented by prominent examples: the Haber-Bosch process, the production of ammonia from nitrogen and hydrogen and the Fischer-Tropsch chemistry. In the latter from CO and hydrogen all kinds of hydrocarbons are produced; last but not least the catalytic converters in automobiles have to be mentioned, which are the most widely spread application, responsible for the CO, NO and hydrocarbon conversion to CO₂ and N₂ in exhaust gases. These are some of the most prominent examples and the list of heterogeneously catalyzed reactions is certainly much longer, which represents itself in the billion dollar market for products from heterogeneous catalysis [1]. To talk about catalysis without mentioning examples from the biological world would only give an incomplete picture. Especially there one finds highly selective and highly active catalysis that make the world surrounding us, manhood itself would not exist without them. Catalysts in biology, e.g., enzymes, in their effectiveness are yet to be made by man and there is still a long way to go to reach this aim.

One way to understand heterogeneous catalysis is to systematically study the elementary processes happening on the catalyst surface at the atomic level: at first the adsorption of the chemical species onto the substrate has to be considered (in the case of chemisorption, the formation of a chemical bond has to be regarded or in the case of physisorption a weaker interaction, i.e., van-der-Waals interactions occurs): this might happen in a site specific way or (for chemisorption) it might even be accompanied by the dissociation of the adsorbate. After adsorption, diffusion of the molecules or atoms might play a role. The next step in the catalytic process is the reaction of the molecules on the surface, which might be dissociation or an associative reaction and which might be also site specific; it is then followed by the

desorption of the product. From the understanding of each of these steps one might get a detailed insight into heterogeneous catalysis and develop ideas for this research field.

One way to do this is to investigate model systems in a controlled (ultra high vacuum) environment with almost ideal single crystal surfaces, allowing an analysis of the chosen system in a step by step manner. This is nowadays possible as the advances in experimental techniques and theoretical methods in the field of surface science are enormous. Examples for this are the standard use of scanning probe microscopes for the imaging of surfaces at the atomic level and the use of X-rays from third generation synchrotron sources; the latter is discussed here.

A big achievement in surface science was the development of X-ray photoelectron spectroscopy in the 1960s [2]. Due to its high surface sensitivity this spectroscopy allows to obtain the crucial information on surface composition, the adsorption sites, chemical state of the adsorbed species as well as the reactivity of model systems. With the advent of the third generation synchrotron facilities, X-ray photoelectron spectroscopy advanced to an even more powerful tool to analyze surfaces and surface processes. This progress is not only leading to an ever increasing resolution, which allows to monitor the above mentioned properties for small molecules in unprecedented details, but also to determine such properties of larger, more complex molecules. Even information on the vibrational properties of such molecules in the gas phase as well as in the adsorbed state can nowadays be obtained [3, 4]. Another aspect is the rather long data acquisition time when using conventional lab sources, which is normally in the range of several minutes up to some hours, allowing only the study of static systems. The increasing flux from the synchrotron light sources additionally decreased the time scale for data acquisition tremendously. The time for a full spectrum can be as low as 50 ms, which allows following adsorption and reaction processes “in-situ”, giving access to the kinetics of elementary steps [5-9]. Although other techniques can also be trimmed to work in that time scale, e.g. time resolved electron energy loss spectroscopy [10], which is subject to the restriction that no larger molecules are accessible and that quantification is very difficult, or time resolved infrared absorption spectroscopy [11, 12], which has problems in detecting atomic species, make time dependent X-ray photoelectron spectroscopy one of the most promising tools.

In this work we use in-situ high resolution X-ray photoelectron spectroscopy to study two specific adsorption systems on metallic substrates: (1) ring systems as examples of relatively complex adsorbates and (2) methane as stable entity dissociatively adsorbing on a complex stepped surface. In chapter 4, data of the highly symmetric ring system benzene on a single crystalline nickel surface (Ni(111)) are presented. This prototype of an aromatic molecule can be described rather easily because benzene consists only of chemically equivalent sp^2 hybridized carbon atoms. The behavior upon adsorption at different temperatures as well upon annealing the surface layer was studied yielding the coverage and temperature dependent atomic arrangement with respect to the surface. The use of deuterated benzene allowed additional insights in the properties of the adsorbed molecule. Aside from the kinetic and the vibrational isotope effect, an additional structural isotope effect in the low temperature regime was discovered. The coadsorption of other species, in this case CO and NO, was also part of the study allowing to examine the influence of possible reaction partners on the benzene ring. The coadsorption phases were leading to different structural arrangements and adsorption sites of the benzene ring relative to the substrate. The model character of this system also allowed drawing general conclusions from the behavior of XP spectra towards interactions of different adsorbates on the surface and vice versa from the XP spectra to the interactions of the adsorbates among each other.

The basic knowledge of the benzene adsorption, its vibrational properties and its reaction behavior was used in chapter 5 to study the more complex adsorption and dehydrogenation of cyclohexene on Ni(111). At low temperatures differently hybridized carbon atoms were distinguished and their vibrational properties were examined. The partial decomposition of cyclohexene to benzene revealed interesting details on coadsorption phases and inhibiting processes on surfaces. The reaction of cyclohexene was also monitored in isothermal experiments yielding directly benzene, which in the strong coadsorption situation with hydrogen, displays similar properties as the pure benzene phase.

The reaction and adsorption of the five membered heterocycles pyrrole and furan is discussed in chapter 6. Both exhibit an easily interpretable molecular spectrum with vibrational fine structure, but display a difficult reaction behavior. Their thermal evolutions involve parallel reactions that allow no separation of all the respective reaction intermediates. Nevertheless, a great step towards the

understanding of this complex system was done. The concept of introducing a heteroatom into a molecular system that chemically shift certain parts of the XP spectrum and, thereby, allowing interpretation, was successfully used. The analysis of the reaction behavior was performed partly by using the known temperature and C 1s binding energy fingerprint of previously studied species such as CH and C₂H₂.

A different way to introduce complexity is not by the chemical system itself, but by the underlying substrate. In chapter 7 a study concerned with the adsorption of the simplest hydrocarbon, methane, on stepped surfaces will be presented. This system displays, as the aforementioned examples, a pronounced vibrational signature in the core hole state, which is analyzed in detail. The used platinum surfaces have regularly spaced (111) terraces and differently oriented monoatomic steps. This allows to study the influence of well defined “defects” that are also found on real catalysts. The adsorption of methane and the reaction of the formed intermediates was investigated: While the dissociative adsorption was not affected by the presence of steps, the thermal evolution was strongly influenced by them. To differentiate between chemical and geometric effects, the steps were additionally decorated with silver. The surface still showed the same geometry, but a different chemical surrounding was modeled. From these experiments it was concluded that the chemical surrounding is very important leading to a “poisoning” of the surface in the adsorption process. From a precise analysis of the observed effects in the experiments with methane and deuterated methane, information on the reaction mechanism of methyl on the platinum surfaces by regarding the primary kinetic isotope effect in this reaction were extracted.

In the two chapters following this introduction a short description of the methods, their theoretical background as well as of the experimental setups is given, to help the reader to get a better understanding of the following parts of the thesis. In chapter 8 the thesis is summarized.

2 Fundamentals and techniques

All studies were conducted in an UHV (ultra high vacuum) environment. This corresponds to a pressure regime of $1 \cdot 10^{-9}$ to $1 \cdot 10^{-11}$ mbar. This condition is chosen to get the possibility to examine model systems at clean and defined conditions. The contamination of a clean surface under UHV conditions takes approximately 10^3 to 10^5 s, respectively, allowing an investigation of this model system in a reasonable time scale, compared to only microseconds under ambient conditions.

Another important question in investigating surfaces is the question of surface sensitivity. The concentration of surface atoms relative to bulk atoms is rather low (1 in 10^8 atoms for a cube with 1 cm length), which is well below the detection limit of many common spectroscopies. The use of electrons as a probe solves this problem, as they are surface sensitive up to energies of ~ 2 keV, therefore probing only the uppermost layers of a sample [13].

At elevated pressures the use of electrons is limited due to the inelastic mean free path, which is low at high pressures, but at low pressures the mean free path is large enough to allow detection of these probes. A way to overcome this inherent “problem” of photoelectron spectroscopy is described in Refs. [14, 15]. This new experimental setup consists of several pumping stages that generate a high pressure gradient, which allows detecting photoelectrons up to pressures of 1 mbar.

2.1 X-ray photoelectron spectroscopy (XPS)

2.1.1 General remarks

Photoelectron spectroscopy depends on the interaction of photons with a certain energy, given by $E = h\nu$, with matter, in our case a metal or an adsorbate. This interaction results in an electron leaving the probed atom with a certain kinetic energy. In an ideal process, without additional interactions, this kinetic energy ($E_{kin,eff}$ in Fig. 2.1) and the binding energy (E_B) are linked by:

$$E_B = h\nu - E_{kin,eff}$$

The kinetic energy is determined by an electron energy analyzer. The setup used here works via a hemispherical capacitor, which deflects the electrons with the correct kinetic energy to the detector [13, 16].

For measurements in gas phase and for calculations, the vacuum level (E_{vac} in Fig. 2.1) is used as reference level, as it corresponds to the state with no interaction of the electron with the core hole state. This reference level is not used for our experiments. Due to the fact that both the sample and the analyzer are grounded, a common Fermi level is obtained that is used as reference. This method allows us to calculate the binding energy (E_B in Fig. 2.1) of the core levels without explicit knowledge of the work functions of the sample (Φ_S) and, thus, the kinetic energy (E_{kin}). Only the effective kinetic energy ($E_{\text{kin, eff}}$), measured relative to the Fermi level, is taken into account. For further details see Fig. 2.1.

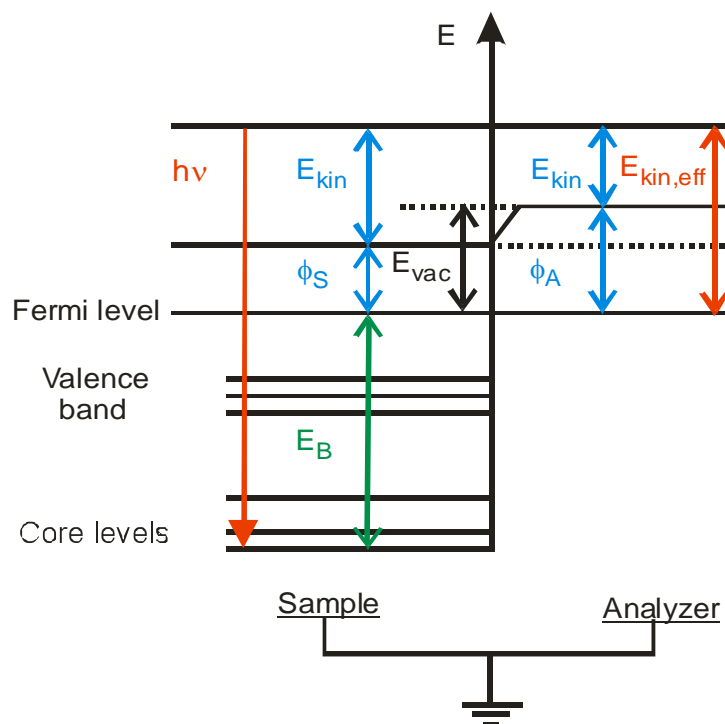


Fig. 2.1: Schematic energy diagram of the photoelectron spectroscopy [13, 16, 17].

To determine the position and the width of the Fermi edge a Gaussian error function ($\text{erf}(x)$) is fitted to the measured data. The Gaussian error function is the integral of the Gaussian normal distribution [18]. A typical result is shown in Fig 2.2:

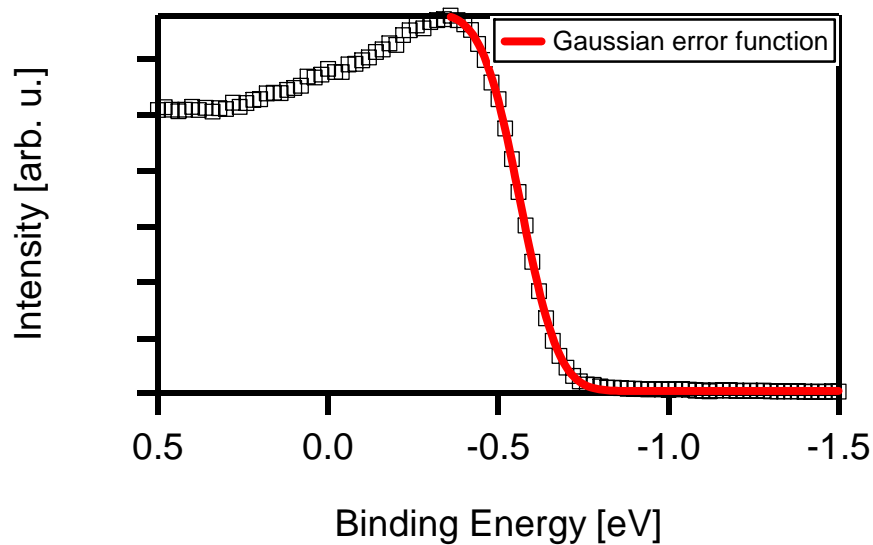


Fig. 2.2: Example for the determination of the energetic position of the Fermi edge of a Ni (111) crystal by fitting with a Gaussian error function. Here, the resulting width is 208 meV and a relative position of -0.564 eV is found. ($h\nu=380$ eV; normal emission).

The position of the inflection point of the Gaussian error function is the position of the Fermi edge. This position defined the zero point of the binding energy scale. The energy scale, thus, has to be shifted by that value to align it correctly, i.e., such that $E_F=0$.

The resulting width of the Gaussian error function is interpreted as the experimental broadening, as the Fermi edge is, at least at low temperatures ($T=0$), a step function. This experimental broadening can in fact be described by a Gaussian, see also chapter 2.1.3, in our fitting routines. Unfortunately, the resulting values for the relative energy position and the width determined in Fig. 2.2 can be modified by electron density near the Fermi level, e.g., of the 3d-band in the case of Ni.

In the XP spectrum the determination of the energetic position of the Fermi edge also depends on the occupation, i.e., the intensity of such bands. It can vary with, e.g., the coverage of adsorbates, and may therefore lead to variations in the assignment of the binding energy position of the Fermi edge. Upon choosing a standard condition, as in our case the clean surface, the deviations are expected to be small and systematic.

During the photoemission process, interactions of the outgoing electron with the surrounding matter can take place. Typical interactions are inelastic scattering such as excitations of electron-hole pairs at the Fermi level of metals, vibrational or other electronic excitations. A photoelectron may undergo multiple “energy loss events” leading to even lower kinetic energies of the primary electron. These multiple events may also cause a higher number of “secondary” electrons. The steep increase of the background at low kinetic energies is attributed to these effects. A typical example for this behavior of the background is shown in Fig 2.3 for a clean Ni(111) surface, showing an steep increase especially at binding energies above 550 eV, corresponding to kinetic energies of 100 eV or lower.

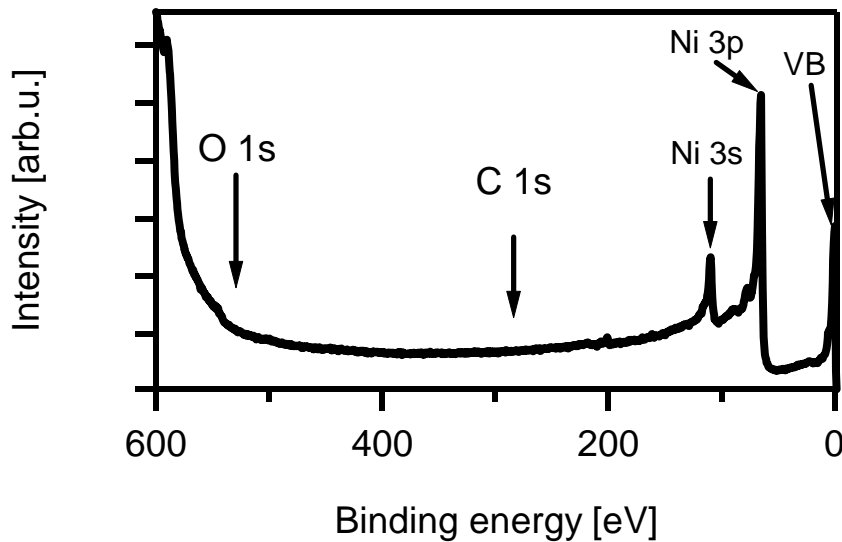


Fig. 2.3: XPS spectrum of a clean Ni(111) surface. Typical peak positions of Ni (3s, 3p and the valence band (VB)) carbon and oxygen are indicated. ($h\nu=650$ eV, normal emission).

Different elements, i.e., their core levels, are well separated in binding energy, as indicated in Fig. 2.3, for different carbon, oxygen and nickel signals. The chemical species can therefore be measured and analyzed separately in a quantitative fashion. This led to the term “electron spectroscopy for chemical analysis” (ESCA) [2]. Information on the quantification of adsorbate coverages will be given in chapter 2.1.5. The additional information that can be gained from XP spectra is described in the following chapter.

2.1.2 Chemical shift

Although the core electrons of a molecule are not directly involved in a bond, still they are influenced by their chemical surrounding. As a consequence they are shifted relative to one another. Typically, this effect can be divided so-called initial state and final state effects. The terms initial and final state effects refer to the respective energies in the photoemission process, whose difference result in the measured binding energy [13]:

$$E_B = E_f^{N-1} - E_i^N$$

with:

E_i^N : Energy of the initial state with N electrons

E_f^{N-1} : Energy of the final state with N-1 electrons

A typical initial state effect is a partial charge at the emitting atom. When this atom is probed the kinetic energy of the emitted photoelectron is higher for a negative and lower for a positive partial charge, due to higher/lower Coulomb interactions. A typical final state effect is a more efficient screening of the core hole or more efficient relaxation by surrounding electrons. This more effective screening leads to a higher energy of the photoelectron as the positive core hole is not interacting with the emitted photoelectron. On the other hand an inefficient screening leads to a strong interaction between the two charges, resulting in a lower kinetic energy of the emitted photoelectron. This shows that a negative partial charge or a bonding situation with a high electron density at the emitting atom is not necessarily leading to a higher binding energy. Nowadays, a precise description can be given by density functional theory calculations (see, e.g., [19]), which were not part of this work.

Another feature of XP spectra is the appearance of “shake off” and “shake up” satellites. They can also be assigned to the subgroup of final state effects. They appear when a second electron is excited into, typically, the valence band (“shake off”) or is totally removed from the atom (“shake up”) and show an additional discrete line near the main peak is observed. A typical example of a satellite is the so-called 6 eV satellite of nickel (for the Ni 3p peak an additional satellite at 12 eV can also be detected). It is detected due to different screening of the core hole from different bands [20].

If the excitations are small in energy as for example electron hole pair excitations in the valence band of a metal, an asymmetric lineshape with a tail to high binding energies is observed. This asymmetric peak shape can be described by a Doniach-Sunjic function described in chapter 2.1.4. A more detailed description of these phenomena can be found in Refs. [13, 16, 20, 21].

2.1.3 Vibrational excitations in XPS

A phenomenon also leading to discrete “satellites” in XP spectra is the vibrational excitation of molecules during electronic excitation with photons. The final, core hole state, can be additionally vibrationally excited, leading to a lower kinetic energy of the emitted electron. This effect is only measurable by high-resolution XPS experiments, as the difference between vibrational states is in the range of some 100 meV. Typical values for a C-H stretching frequency are 400 meV (see chapter 4 and 7) and for other vibrational excitations, like C-C stretching modes, values of 100 meV or less are found [21-23].

A model to describe vibrations in molecules is the harmonic oscillator. A model description of such a system are two vibrating masses that are coupled via a spring. In this ideal case the potential is given by a parabola (see Fig. 2.5). The frequency ν of this system is given by:

$$\nu = \frac{1}{2\pi} \sqrt{\frac{D}{\mu}}$$

with

D: spring constant

$$\mu = \frac{m_1 \cdot m_2}{m_1 + m_2} : \text{reduced mass}$$

The spring constant is related to the bond strength. From this equation, experiments with different isotopes can be interpreted by the change in the reduced mass and therefore in the frequency of, e.g., the C-H stretching frequency. This latter frequency is lowered approximately by the factor of $\sqrt{2}$ when hydrogen is exchanged by deuterium.

In a quantum mechanical approach, the energies of the vibrational levels are given by:

$$E_n = \left(n + \frac{1}{2} \right) h\nu$$

with

n: vibrational quantum number

h: Planck's constant

This equation, although a description of a strongly simplified model, shows the existence of the so-called zero point motion. However, it cannot account for the dissociation of a bond and the declining energy difference of neighboring vibrational levels at higher quantum numbers. For a more precise description, the Morse potential is a useful model [24].

After this general description of the vibrational excitations in molecules, we have to regard the electronic excitation. As depicted in Fig. 2.4, a vertical excitation between the ground state and the core hole final state occurs, the so-called Franck Condon transition.

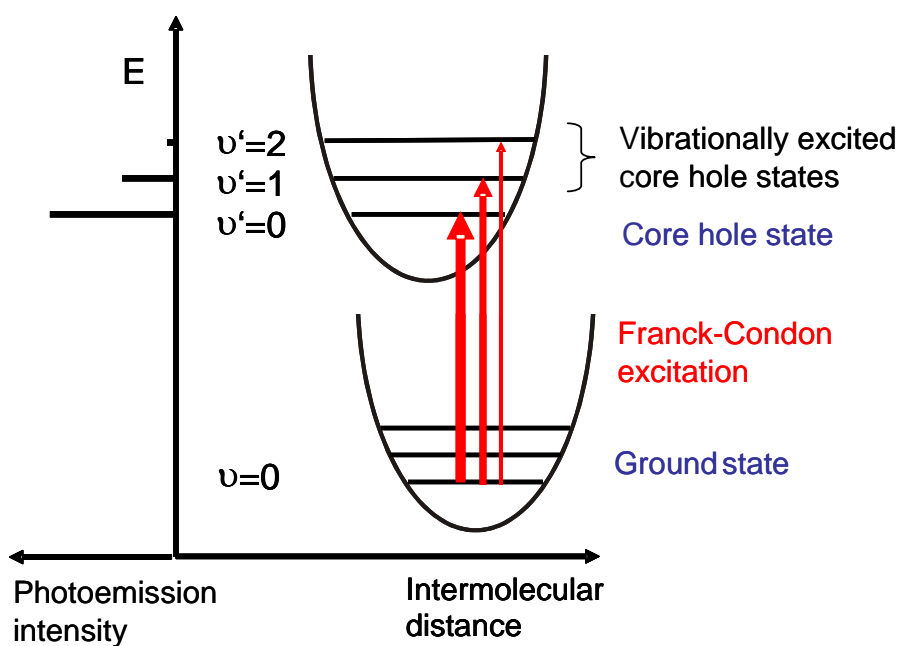


Fig. 2.4: Energy diagram of the electronic excitation and the vibrational excitation in XP spectroscopy. The red arrows indicate the different energies needed for excitation.

Thereby, it is assumed that the electronic excitation is much faster than the motion of the nuclei. This leads to the distribution of the intensities of the vibrational excitations according to the Franck Condon factor, i.e., the overlap integral between the vibrational wave functions of the respective potentials. In the case of a vibrational excitation of the core hole state, the XP spectra exhibit an intensity pattern as the one shown in Fig. 2.4.

A mathematical description of this excitation is given by Cederbaum and Domcke [25], see also [26], with the linear coupling model. It assumes that the ground state and the electronically excited state (core hole state) can both be described by the same harmonic potential, only differing in equilibrium position and energy. In the electronic ground state, only the vibrational ground state is populated ($v=0$), while in the core hole state vibrational excitation is possible ($v'=n$ and $n \geq 0$). The intensities of the vibrational excitations $I(0 \rightarrow n)$ in this model are then given by a Poisson distribution, which can be written as:

$$I(0 \rightarrow n) = e^{-S} \frac{S^n}{n!}$$

with

S: S factor

n: quantum number of the vibrational excitation

The S factor is an easily accessible value, as it is simply the ratio of the intensity of the first vibrationally excited state and the adiabatic excitation in a photoelectron spectrum. In the linear coupling model, the value for the S factor can be calculated by:

$$S = \frac{\delta^2 \mu \pi \nu}{\hbar}$$

$$\delta = \sqrt{m} \cdot \Delta r$$

$$S = \frac{m(\Delta r)^2 \mu \pi \nu}{\hbar}$$

with

m: number of equal bonds

μ : reduced mass

ν : vibrational frequency

Δr : change in the bond lengths upon excitation

It is possible to calculate the change in bond length upon excitation when the other values are known [4]. Additionally in the equation for δ we find that in the case of no bond length change, the intensity of the vibrationally excited states also becomes zero.

From these equations one can also predict the change in the S factor for an isotope exchange experiment, for the two isotopes 1 and 2.

$$\frac{S_1}{S_2} = \sqrt{\frac{\mu_1}{\mu_2}}$$

Explicitly for an exchange of hydrogen for deuterium: $S_D \approx \sqrt{2} \cdot S_H$. The C 1s spectra of Methyl (CH_3 and CD_3), showing a pronounced vibrational signature in the core hole state, will be discussed here exemplarily.

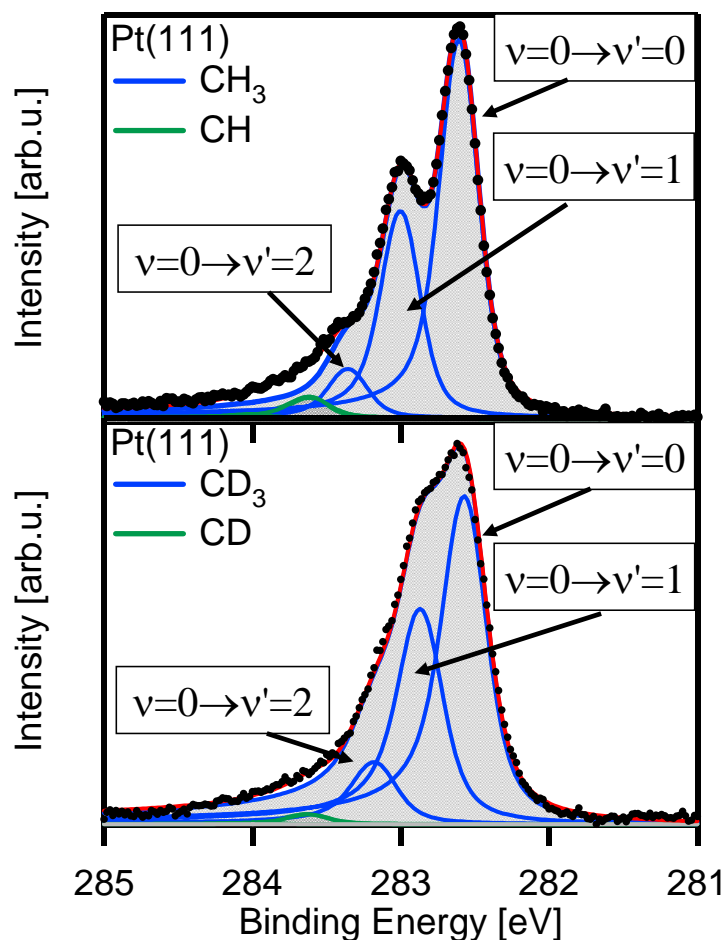


Fig. 2.5: C 1s spectra of a) methyl (CH_3) and b) deuterated methyl (CD_3) on Pt(111), with their corresponding fits. The photon energy was 380 eV and the electron emission angle was 45° off normal.

The separation of the adiabatic and the first vibrationally excited state for methyl is 400 meV, while the separation for the deuterated methyl is 295 meV. This difference corresponds well to the expected change in vibrational frequency of $\sqrt{2}$, due to the change in reduced mass. The exact change nevertheless is slightly lower (1.34) for C-H vibrations as was shown by [4]. The S factor in the case of methyl (CH_3) is 0.5, corresponding to 0.17 per C-H bonding, while the S factor for deuterated shows the expected $\sqrt{2}$ higher value of 0.7. Further examples for such analysis of the vibrational fine structure of deuterated and non-deuterated molecules are given in the chapters 4 and 7.

2.1.4 Line profiles

To quantitatively access the above described features in XP spectra, they are fitted by mathematical functions. These functions can model the different physical properties occurring in an XP spectrum. A peak has different contributions: (i) the line width due to the lifetime of the core hole state and (ii) an experimental broadening of the spectrum, due to a certain line width of the photons and the resolution of the electron energy analyzer. These two contributions can be modeled by (i) a Lorentzian convoluted with (ii) a Gaussian function. This results in a symmetric line shape known as Voigt function, which is found in many branches of spectroscopy. But, as can be seen in chapter 2.1.2, this description is insufficient as it is not describing the asymmetry of the recorded core levels; therefore asymmetric line shapes are used in this work. A simple form of this function is the asymmetric Pseudo-Voigt function consisting of the sum of a Lorentzian ($L(E, \omega, A)$) and a Gaussian ($G(E, \omega, A)$), with an asymmetry factor included in the width of the peak [27]:

$$V_{PS} = m \cdot L(E, \omega', A) + (1 - m)G(E, \omega', A)$$

with

E: energy position

m: mixing factor

ω, ω' : full width at half maximum including the asymmetry

A: amplitude / height

The asymmetry factor is given as α in the following equation

$$\omega'(E, \omega, \alpha) = \omega + 2\alpha(E - E_C)$$

with

ω : full width at half maximum

α : asymmetry factor

The use of the Pseudo-Voigt function yields a similar result as the use of a convolution of a Gaussian with a Doniach-Sunjic function [28], which is, however, more time consuming to compute. Nevertheless, it is often used, as more subtle information about the system, like the lifetime of the core hole, are accessible. In the

convolution of the two functions the Gaussian and the Lorentzian line width, are used. As the Gaussian width is known often, this leads to the possibility of determining the Lorentzian width that is correlated to the lifetime of the core hole. In more complicated cases as, e.g., the deconvolution of spectra of larger organic molecules, a direct determination of the lifetime is not possible, as vibrations, like C-C stretching modes, are not resolved and, thus, also contribute to the width of the fitted line profiles, leading to erroneous values for the Lorentzian width and, thus, the lifetime of the core hole.

The Doniach-Sunjic function can be written as:

$$D(E, \omega, \alpha) \propto \frac{(1-\alpha)}{[(E-E_C) + \omega^2]^{\frac{1}{2}(1-\alpha)}} \cdot \cos\left[\frac{\pi\alpha}{2} + (1-\alpha)\arctan\left(\frac{E-E_C}{\omega}\right)\right]$$

with

E: energy position

α : asymmetry factor

ω : width (Lorentzian width)

Note that other functions, like the Mahan function [29] also yield comparable results.

2.1.5 Quantification of XPS data and photoelectron diffraction

In the earlier parts of this chapter we learned about the origin of the energy position and the peak shape of an XP spectrum. This part is now dedicated to the possibility of quantification in photoelectron spectroscopy. In principle, XPS data are quantitative, as the cross section for the photoemission process is independent of the local surroundings of the emitting atom. Or in other words, the signal intensity is directly proportional to the amount of adsorbed molecules. This holds true for many cases, especially for electrons with high kinetic energies that are usually found in experiments with Mg or Al $K\alpha$ sources.

If the kinetic energy of the electrons is lower, approximately in the order of atomic distances (~ 100 eV), a high probability for non-forward scattering is given. This may even lead to multiple scattering and also to varying intensities for different scattering pathways. Thus, we find an angle dependent distribution of

photoelectrons, which is also depending on the kinetic energy. An example for the angle dependence in XP spectroscopy can be found in chapter 4.

This effect can be used to determine the structure of, e.g., adsorbates with a technique named after the effect: photoelectron diffraction (PED or PhD) [30-32]. If no photoelectrons are used, but backscattered electrons emitted from an electron gun, this leads also to a structure determination technique, called low energy electron diffraction (LEED), which will be discussed in chapter 2.2.

Another rather obvious effect, which can modify the results is damping. As the mean free path of the electrons is short, additional layers damp the signal of the underlying layers. However, the effect of damping is well understood and can even be used in the determination of the growth mode, or vice versa if the growth mode is known, the thickness of a layer can be determined, at least up to the length of the mean free path of the photoelectrons, which is depending on the kinetic energy.

2.1.6 X-rays from a synchrotron radiation source

All XPS experiments shown in this work were carried out at the third generation synchrotron sources BESSY II in Berlin, Germany and MAX II in Lund, Sweden. Synchrotrons provide a broad spectrum of intense light, from IR to hard X-rays. This shows the two major advantages of synchrotron light we used: (i) tunable energy and (ii) high intensity. Other advantages, we did not use, are, e.g., the high brilliance that can be used for microscopy, well defined polarization such as circular polarized X-rays that can be used for magnetic dichroism experiments, etc.

Synchrotron light is emitted from highly relativistic electrons (1.7 GeV at BESSY II, 1.5 GeV at MAX II), that are deflected (= accelerated) by a magnetic field and are, therefore, emitting radiation. Typical magnetic devices are “normal” dipole magnets or the more sophisticated undulators, consisting of an array of magnets with alternating polarity. This arrangement of magnets leads to a steep increase in the light intensity compared to a dipole. The electron in the magnetic field emits its light as described by an Hertz dipole antenna, but as it is relativistic a forward focusing of the emitted light, an increase in intensity and brilliance results [13].

To be more precise, BESSY II and MAX II, as we use them, are not operated as synchrotrons, but as storage rings; a synchrotron is a particle accelerator, whereas the electrons in the storage rings are kept at a constant energy. The

electrons in the storage ring have energies above 1 GeV, and are accelerated prior to injection to the synchrotron: First they are accelerated in a microtrone or a linear accelerator and subsequently in a “real” synchrotron. At BESSY II, when the energy of 1.7 GeV is reached, the electrons are injected into the storage ring and are kept there, as already mentioned, at a constant energy, to be used by experimentalists. In the case of MAX II the final energy of 1.5 GeV is not reached until they are accelerated in the “storage ring”, which makes MAX II a mixture of a synchrotron and a storage ring.

A wide spectrum of light is emitted from a dipole magnet; even an undulator is emitting only a broad line spectrum, roughly with a line width of $1/n$, with n corresponding to the number of alternating magnets. Thus a monochromator is needed between the insertion device and the end station, to achieve a low line width of the X-rays used in the experiments.

In our experiments, the tunable energy allowed us to use an photon energy at which the cross section for the photoemission is large compared to laboratory X-ray sources, as for example Al and Mg $K\alpha$. A direct comparison shows a 30 times higher cross section for the carbon 1s core level at 380 eV photon energy compared to an energy of 1486.6 eV of an Al $K\alpha$ source [33]. Additionally, the surface sensitivity is enhanced, as the mean free path of the electrons with 100 eV is low, but as we normally probe adsorbate levels, this enhanced surface sensitivity plays only a minor role, only leading to a lower background from substrate signals, thus, yielding a lower background in the adsorbate levels. Only when probing substrate core levels, in this work in the case of the silver adsorption on Pt(355) and (322), see chapter 7.3, the small escape depth [34] is of relevance, allowing to observe interface and surface contributions.

Due to the high flux of photons from the synchrotron radiation sources and the high cross section achieved we were able to perform in-situ experiments in a time dependent way. We are able to obtain XP spectra, while we adsorb gases, leading to so called “uptake” experiments or while we anneal the sample leading to so called TPXPS experiments which are discussed in the next section.

2.2 TPXPS and TPD

TPXPS is the abbreviation for temperature programmed X-ray photoelectron spectroscopy and its name is derived from the technique of temperature programmed desorption spectroscopy (TPD) [35]. The rather simple set up of a TPD experiment is replaced for a fast and in-situ measurement of XP spectra during annealing. The main difference towards TPD measurements is that not the gas phase is analyzed by a quadrupole mass spectrometer, but the reaction and its products on the surface are monitored directly. This technique thus delivers complementary information to TPD measurements. The theoretical treatment is, as the same processes are monitored, rather similar. As the theoretical description for TPD is more advanced than for TPXPS, at first basic considerations of TPD spectroscopy will be described and afterwards the relations to TPXPS will be shown.

2.2.1 Basic principles

TPD spectroscopy is a well known technique that allows insight into simple kinetics of desorption and surface reactions. Experimentally, we adsorb molecules and subsequently desorb them by annealing the surface with a constant temperature ramp (β). The desorbing particles are detected by a quadrupole mass spectrometer. A phenomenological description is given by the Polanyi-Wigner equation [36]:

$$\frac{d\Theta}{dT} = \nu \cdot \Theta^n \cdot \exp\left(-\frac{E_D}{k_B T}\right)$$

with

Θ : coverage

T: temperature

ν : preexponential factor

E_D : desorption energy

k_B : Boltzmann constant

n: desorption (reaction) order

This equation is valid in the case of a very high pumping speed compared to the flux of desorbing particles, which is given in our and most other UHV chambers. Typical scenarios are (i) 0th order desorption: a desorption that is independent of the

coverage, which typically is found for the desorption of multilayers. (ii) 1st order desorption: The desorption rate is proportional to the coverage, this desorption behavior can be found in the case of a desorption in the monolayer range with no lateral interactions. (iii) 2nd order desorption can be found, e.g., in the case of recombinative desorption.

In the case of first order desorption a simple way of estimating the desorption energy is proposed by Redhead [37]:

$$E_D = k_B T_m \left(\ln \left(\frac{\nu T_m}{\beta} \right) - 3.51 \right)$$

with

E_D : desorption energy

T_m : temperature maximum of the desorption

ν : frequency factor, usually estimated as 10^{13} s^{-1}

k_B : Boltzmann constant

β : heating rate

The Redhead equation is especially helpful, because it allows to estimate the change in the temperature of the desorption maximum, when different heating rates are used. This is especially important, as TPXPS experiments usually have noticeable lower heating rates than corresponding TPD experiments. The other link of TPD experiments and TPXPS experiments is certainly the coverage. The negative integral of the TPD signal leads to the coverage of, in the case of the TPD experiment, the desorbing particles:

$$\Theta_0 - \int \frac{d\Theta}{dT} d\Theta \propto \Theta_{XPS}$$

This is only true for the case of particles that desorb. Effects like the diffusion of carbon into the bulk of the sample are not considered. It should be mentioned, that certainly only the region monitored by XPS, e.g., the C 1s region, contributes to the above equation. In other words, if the total coverage of the C 1s region is regarded, one has to compare this to the desorption of all particles containing carbon. The big advantage of TPXPS measurements is after all the possibility to study surface

reactions, which are not accompanied by any desorption as side-effect. As example for such a behavior the reaction of cyclohexene discussed in chapter 5 and 7 shall be given. Additionally the existence of surface intermediates, occurring in a reaction, not associated with a desorption, are not accessible by TPD, but by (TP)-XPS [38].

2.2.2 Primary kinetic isotope effect in TPXPS and in TPD experiments

Experiments with different isotopes are usually performed to assure the assignment of vibrational modes, e.g., in HREELS experiments or in our case for the assignment of vibrational modes in XP spectra. Usually, it is assumed, that the replacement is not changing the chemical situation in the molecule. This is true in most of the cases, but a difference in reactivity, the so-called primary isotope effect [39], can be found.

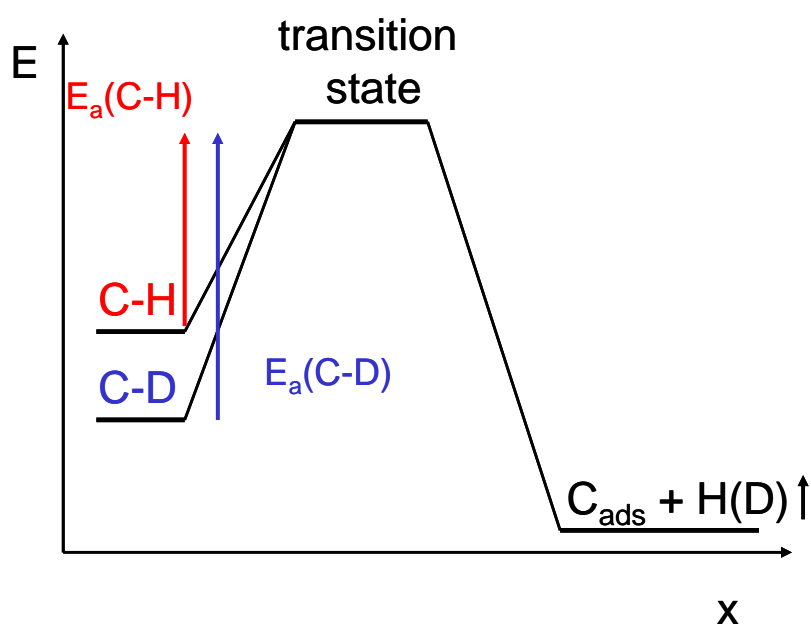


Fig. 2.6: Energy diagram of the kinetic isotope effect. Here for the scission of a C-H (D) bond.

The difference is due to the different energy of the vibrational ground state of the bond that is broken during the reaction. If for example a hydrogen atom is replaced by a deuterium atom in a C-H bond, the zero point energy is lowered. This energy difference, resulting from this effect, has also to be overcome to dissociate the bond. The possible energy difference in the transition state is expected to be rather low and not taken into account in the energy diagram in Fig. 2.5 [39].

Examples for this effect can be found in literature [40-42] and in the chapters 4 und 7. For a description of the secondary kinetic isotope effect, concerned with changes in the kinetic of reactions taking place not at the isotopic labeled bond but at an other bond of the molecule, we would like to refer to textbooks [43, 44], as it was not taken into account in this work.

2.3 Low energy electron diffraction

Low energy electron diffraction (LEED) is an important and well-established surface science tool for structure determination of the surface and for ordered adsorbate phases on the surface [45]. As the name already tells, low energy electrons are used. These electrons are emitted from a filament of an electron gun and are accelerated towards the surface with a kinetic energy of 20-500 eV. Electrons in this low energy regime have a de-Broglie wave length of 0.3 up to 0.05 nm, respectively, which is in the range of interatomic distances. They are, therefore, diffracted by the atoms of the surface and the adsorbate. Due to the perpendicular incidence of the electron beam and the shape of the fluorescence screen the backscattered electrons form a direct projection of the reciprocal space on the fluorescence screen. This allows us to draw conclusions on the periodicity and lattice constants of surfaces and adsorbate structures. To draw conclusions on the exact atomic arrangement of an adsorbate (adsorption sites and bond distances) or of the crystal structure, a LEED I-V analysis has to be performed, see e.g. [46], which is a measurement of the intensity of the diffraction spots, while changing the incidence energy of the electrons.

Low energy electrons strongly interact with the surface atoms and therefore only give information on the uppermost layers, which are interesting for surface science studies, see also chapter 2, in contrast to X-ray diffraction, which is used for bulk structure analysis. Also of importance is the possibility to identify ordered superstructures of adsorbates on the surface, which yield additional reflexes to the substrate reflexes. These adsorbate structures are often typical for a certain coverage of a molecule and can therefore be used for coverage calibration [38, 47-49] (see also chapter 4 and 7).

2.4 Molecular beams

Mainly two different types of molecular beams have been used in this work: effusive beams from multicapillary array dosers and a supersonic molecular beam. For completeness, also the adsorption from the background should be addressed here. For this last case, the chamber is backfilled with the gas, which is then adsorbed on the surface.

Effusive molecular beam sources have a Maxwell energy distribution. The advantage compared to backfilling the chamber is the fact that a capillary array doser focuses (if the diameter of an individual capillary is much smaller than the mean free path of the molecules) [50] the molecules onto the surface. This leads to a lower background pressure, compared to the background adsorption, which is desirable as higher pressures can be applied to the sample and the time for high exposures is lowered. This is also important with respect to the fact that adsorption / desorption equilibria on the chamber walls with unwanted gases may pose a problem.

The supersonic molecular beam, in this work mainly used for the activated adsorption of methane, has the most defined properties and has even more possible applications than effusive beams. The molecules in this molecular beam theoretically have a narrow energy distribution (in contrast to the Maxwell distribution of effusive sources). In practice the width of the energy distribution at a certain temperature is finite but much smaller than that of the Maxwell distribution of a comparable temperature [50]. Especially interesting for the adsorption of methane is the possibility to change the kinetic energy of the molecules by either heating the nozzle of the beam, by mixing another lighter gas ("seeding") or by combining these two effects. This allowed us to reach kinetic energies of the molecules of up to 0.83 eV (in a Maxwell distributed gas this would correspond to a temperature of ~6500 K). The kinetic energy of the molecular beam has been quantified by time of flight measurements in a similar set up [38]. Besides the defined kinetic energy, the supersonic molecular beam is spatially confined. This is again helpful to keep the background pressure low and may be used for sticking coefficient measurements by the method of King and Wells [51]. In this work, only the tunable energy of the supersonic molecular beam has been used, as the combination of molecular beam and XPS allows a direct observation of the activated adsorption of methane. This allows to determine, e.g., the relative initial sticking coefficient. The direct determination of the initial sticking coefficient is not possible, as the exact flux of

molecules impinging on the surface is not known, but the value can be compared to similar measurements, see chapter 7.

2.5 Basic considerations for the vibrational properties of molecules

A harmonic oscillator can be used to describe the vibrations of molecules, see chapter 2.1.3. The quantum mechanical treatment, solving the Schrödinger equation, leads to the following wave functions:

$$\frac{d^2\Psi}{dx^2} + \frac{2\mu}{\hbar^2} \left(E - \frac{1}{2} D x^2 \right) \Psi = 0$$

This leads to the eigenfunctions:

$$\Psi_\nu = N_\nu H_\nu(x) \exp\left(-\frac{1}{2}\beta x^2\right)$$

for $\nu = 0$

$$\Psi_0 = N_0 \exp\left(\frac{1}{2}\beta x^2\right)$$

for $\nu = 1$

$$\Psi_1 = N_1 2\beta^{\frac{1}{2}} x \exp\left(-\frac{1}{2}\beta x^2\right)$$

with $\beta = \sqrt{\frac{1}{\hbar^2}} \sqrt{\mu D} = \frac{2\pi}{h} \sqrt{\mu D}$

with $D = (2\pi\nu)^2 \mu$

$$\beta = \frac{2\pi}{h} \sqrt{\mu(2\pi\nu)^2 \mu} = \frac{(2\pi)^2}{h} \mu\nu = \frac{(2\pi)^2}{h^2} \mu\Delta E$$

with $\Delta E = h\nu$ from $E_n = \left(n + \frac{1}{2}\right)h\nu$

$$\Rightarrow \beta = \frac{(2\pi)^2}{h^2} \mu\Delta E$$

introducing

$$\sigma^2 \equiv \frac{1}{\beta}$$

leads to

$$f(x) = \frac{1}{\sqrt{2\pi}\sigma} \exp\left(-\frac{1}{2} \frac{x^2}{\sigma^2}\right)$$

The classical description of the turning point is:

$$\sigma = \sqrt{\frac{h^2}{(2\pi)^2 \mu \Delta E}} = \frac{h}{2\pi} \frac{1}{\sqrt{\mu \Delta E}}$$

This shows that in the classical description the turning point is found at 2σ of the Gaussian distribution (quantum mechanical treatment), as shown in Fig. 2.6.

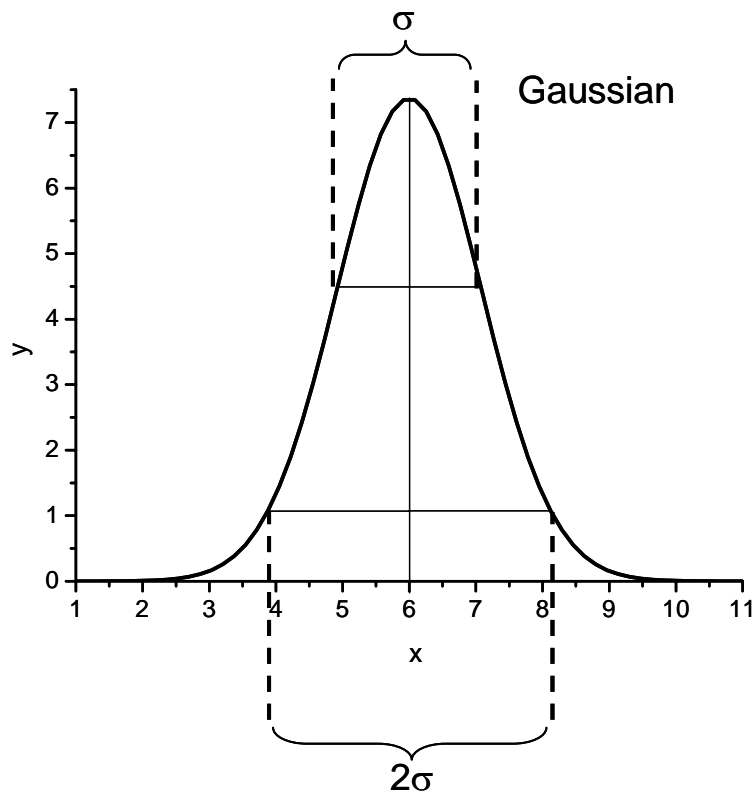


Fig. 2.7: Gaussian distribution, horizontal lines indicate the width σ and the turning point α at 2σ . The vertical line indicates the height of the Gaussian distribution.

The area enclosed in the classical description corresponds to 95 % of the area beneath the Gaussian function.

From these considerations we can quantify the relative vibrational amplitude of a C-H and a C-D bond by using the following equations:

$$E_n = h\nu \left(n + \frac{1}{2} \right)$$

$$E = \frac{1}{2} D x^2$$

$$\nu_0 = \frac{1}{2\pi} \sqrt{\frac{D}{\mu}}$$

$$\Rightarrow D = (2\pi\nu)^2 \mu$$

$$x_{\max} = \sqrt{\frac{2E}{D}} = \sqrt{\frac{2h\nu \left(n + \frac{1}{2} \right)}{D}} = \sqrt{\frac{2h\nu \left(n + \frac{1}{2} \right)}{(2\pi\nu)^2 \mu}}$$

$$x_{\max} = \sqrt{\frac{2h \left(n + \frac{1}{2} \right)}{(2\pi)^2 \nu \mu}}$$

for $n=0$

$$x_{\max} = \sqrt{\frac{h}{(2\pi)^2 \nu \mu}}$$

x_{\max} corresponds to the maximal amplitude of a C-H bond in the vibrational ground state. To calculate this value we have to know values for the vibrational frequency and the reduced mass. The vibrational frequency can be taken from vibrational spectroscopy, e.g., electron energy loss spectroscopy (EELS). The reduced mass can be either calculated by equation (1) with the knowledge of the ratio in the vibrational frequencies of the C-H and C-D vibrations, or calculated with the assumption, that only one carbon atom is involved in the vibration.

Calculated reduced mass of a C-H bond, yielding the “theoretical” value (calculation with $m_1=1u$ and $m_2=12u$):

$$\mu_{C-H} = 0.92307u = 1.54396 \cdot 10^{-27} \text{ kg}$$

Calculated reduced mass of a C-D bond, yielding the “theoretical” value (calculation with $m_1=2$ u and $m_2=12$ u):

$$\mu_{C-D} = 1.71429u = 2.86735 \cdot 10^{-27} \text{ kg}$$

Used constants:

$$h = 6.63 \cdot 10^{-34} \frac{\text{kgm}^2}{\text{s}^2} = 4.1357 \cdot 10^{-15} \text{ eVs}$$

$$c = 299792000 \frac{\text{m}}{\text{s}}$$

$$m(\text{proton}) = 1.67262 \cdot 10^{-27} \text{ kg}$$

The calculations were performed for the C-H (D) stretching mode and the C-H (D) out of plane bending mode of benzene. The results of these basic calculations will be used in chapter 4, when discussing the structural isotope effect. In Table 2.1 we show the results for the reduced masses, calculated from the vibrational frequencies, which were then used to calculate the amplitude of the C-H and C-D bonds in the ground state and the respective difference in extension of the molecules.

Table 2.1: Calculation of the reduced masses and the difference in extension from the vibrational frequencies of Ref. [52].

	E_{vib} [eV]	$\nu_{\text{H}}/\nu_{\text{D}}$	μ [u]	μ [kg]	x [Å]	Δx [Å]
CH, stretch	0.375		0.973	$1.628 \cdot 10^{-27}$	0.107	
CD, stretch	0.268	1.396	1.895	$3.170 \cdot 10^{-27}$	0.089	0.018
CH, o.o.p.	0.012		0.962	$1.609 \cdot 10^{-27}$	0.215	
CD, o.o.p.	0.008	1.388	1.853	$3.100 \cdot 10^{-27}$	0.183	0.033

The values for the amplitudes can also be calculated using the “theoretical” reduced masses, assuming the reduced mass of the second partner to be 12u, as shown in table 2.2:

Table 2.2: for the difference in the extension for C_6H_6 and C_6D_6 , using the “theoretical” value.

	x [m]	x [Å]	Δx [Å]
x_H , stretch	$1.095 \cdot 10^{-11}$	0.109	
x_D , stretch	$9.315 \cdot 10^{-12}$	0.093	0.016
x_H , o.o.p.	$2.199 \cdot 10^{-11}$	0.220	
x_D , o.o.p.	$1.901 \cdot 10^{-11}$	0.190	0.030

The differences between results for the calculated and the “theoretical” reduced mass ($m_2=12$ u) are not significant, as they are lower than 10%. But nevertheless we use the values resulting from the vibrational frequencies, as the partner in a C-H (D) vibration are expected to have a higher mass than just the bare carbon atom. This shows that organic molecules in the vibrational ground state show a different size if the hydrogen atoms are replaced by deuterium atoms.

3 Experimental section

The aforementioned methods are all ultra high vacuum techniques (UHV). This corresponds to a pressure lower than 10^{-8} mbar. These low pressures, in our case even down to 10^{-11} mbar, are nowadays achieved in bakeable stainless-steel chambers. The XPS measurements have been recorded in two different chambers, one located at the synchrotron radiation facility MAX Lab; for the measurements at BESSY II a transportable machine of our group was used, which will be shortly described in the following chapters.

3.1 “The Synchrotron machine”

The synchrotron machine was designed in our group [48]. It consists mainly of four separated parts: (i) a preparation chamber, (ii) the supersonic molecular beam (iii) the analysis chamber and (iv) a dosing system.

The preparation chamber is equipped with standard UHV tools such as LEED optics, a background gas dosing facility, space for evaporators, a quartz micro balance to calibrate the thickness of evaporated layers of, e.g., silver, and a sputter gun as cleaning facility for samples.

In Fig. 3.1 a sketch of the setup is shown, also showing the molecular beam with its three differentially pumped stages. In the first pumping stage the nozzle with a diameter of 100 μm is located; it can be heated up to 2000 K. The molecules leaving the nozzle are first collimated by a skimmer, which is ~ 2 cm away from the nozzle. In the 2nd pumping stage the molecular beam is spatially confined by different apertures; in our experiments the largest aperture with 3.7 mm was used, which results in a 14 mm spot in the chamber at the optimal sample position. Also in the 2nd pumping stage a fast switching pneumatic valve is installed for a fast switching (“temporal confinement”) of the molecular beam. The sample flag enables measurements of the initial sticking coefficient according to the King Wells method [51]. The supersonic beam can also be used for background measurements with a defined pressure.

The analysis chamber is equipped with an additional dosing facility with a capillary array doser, an electron energy analyzer and a quadrupole mass spectrometer for residual gas analysis and TPD measurements.

Gases dosed, either by background adsorption in the preparation chamber or by the capillary array doser in the analysis chamber, are coming from a separately pumped gas dosing system, which is connected via fast opening and closing pneumatic valves.

The alignment of the different parts is described in Ref. [48]. The angles of the sample relative to the analyzer, the incoming light and the molecular beam can be calculated using the equations from Ref. [48].

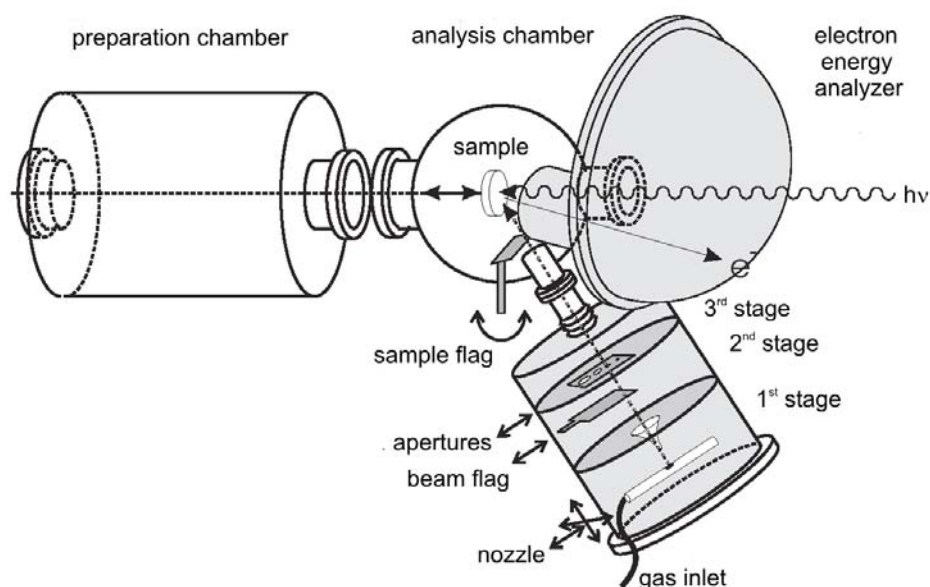


Fig. 3.1: Schematic sketch of the synchrotron machine [48].

By cooling the sample with liquid nitrogen sample temperatures of 115 K were achieved. A filament at the back of the sample was used for heating the sample during TPXPS experiments up to temperatures of 500 K. For cleaning reasons and to gain access to information of reactions taking place at even higher temperatures, the sample could be heated directly up to 1500 K. In contrast to the indirect heating with the filament, no XPS measurements are possible during the direct heating procedure, due to disturbances from the magnetic fields which result from the high, necessary heating currents.

3.2 Surface endstation of beamline I 5-11 at MAX Lab

This chamber is permanently installed at the beamline I 5-11 at the light source MAX II in Lund, Sweden. It mainly consists of three parts: (i) a preparation chamber, (ii) an analysis chamber and (iii) a gas dosing system.

The preparation chamber is equipped with standard surface science tools like a sputtering facility, LEED optics, a quadrupole mass spectrometer and a gas doser. The gas doser can be used either directly, with the sample in front of the doser or the chamber is backfilled to allow adsorbing gases on samples situated in the analysis chamber.

The analysis chamber is equipped with an electron energy analyzer (Scienta SES 2000). Since no gas dosing facility is installed, the above mentioned procedure has to be used to adsorb gases while measuring. The gas dosing system is separately pumped and is connected from the preparation chamber by a leak valve.

A more precise description of the beamline and the surface endstation can be found in Refs. [53, 54].

4 Adsorption and reaction of benzene

Benzene is the prototype of an organic molecule with an aromatic system. It consists of a flat ring system consisting of six sp^2 hybridized carbon atoms with always the same C-C bond length. To identify aromatic systems the Hückel rule can be applied, saying, that every ring system with $4n+2$ electrons ($n=0; 1; 2; \dots$) in the π -system is aromatic. Aromaticity can also be found in heterocycles, like pyridine or furan, which also obey the $4n+2$ rule of Hückel. Regarding molecules studied traditionally in surface science, benzene is a rather large molecule with 12 individual atoms, but despite its size, benzene has a high symmetry (D_{6h}) and, thus, an easy description is possible [55].

Aside from the fundamental aspects of the interaction of aromatic systems with surfaces, which has been studied on various single metal crystals [56-60], aromatic molecules are of great relevance in the petroleum reforming process and as reactant of many different large scale products. Benzene itself earlier was widely used as organic solvent, but it was replaced after its toxicity became obvious. Another important use is as additive to fuel as it increases the octane rating.

In this study nickel was used as substrate. It has been chosen as it is used as catalyst for, e.g., the heterogeneously catalyzed dehydrogenation of hydrocarbons [61]. The question of coverage and temperature dependent site selectivity is of great importance to heterogeneous catalysis as reactivity is different for different adsorption sites. The aim of this chapter is to show that from quasi-continuous coverage-dependent high-resolution XPS data, combined with the available information on molecular orientation, detailed conclusions on the adsorption site for the comparably large molecule benzene can be drawn. This information can be obtained over the whole coverage range by in-situ measurements during the adsorption process, which is studied at two different temperatures (125 and 200 K). Additionally, the thermal evolution of the adsorbed layers up to 320 K is examined in a similar way. In our work, we present a quantitative analysis of the measured C 1s XP spectra and a simple model to explain the observed effects on the surface. Both deuterated and non-deuterated benzene were studied to facilitate the spectral analysis and to reveal possible isotope effects. Additionally, we examined the behavior of coadsorption layers with NO and CO.

4.1 Adsorption of pure benzene layers

The adsorption of pure benzene layers, especially the adsorption at 200 K, are discussed in this first part as it shows the potential of in-situ XPS experiments and reveals, what information can be drawn from it, like a coverage dependent picture of the population of adsorption sites. Deuterated benzene was studied to correctly assign the vibrational modes in the XP spectra. The adsorption of pure benzene layers at 125 K shows an interesting effect, i.e., a structural isotope effect that can only be explained in the context of the adsorption and thermal desorption experiments at 200 K. This information is only accessible by very few methods, showing the value of fast high-resolution XPS measurements.

4.1.1 Introduction

The adsorption and reaction of benzene on Ni(111) has been the subject of many different studies with many different surface science tools. Temperature programmed desorption experiments of deuterated benzene displayed a sharp desorption peak at 290 K with a desorption shoulder up to 460-470 K. This study also showed, that 0.087 ± 0.005 ML of the saturated, chemisorbed layer (0.143 ML) are desorbing intact, while 0.056 ML decompose on the surface [62].

Non continuous measurements with LEED [62, 63], LEED I-V [40, 64], ARUPS [62, 65] and PhD [58] studied only few selected coverages, namely the saturation coverage at 200 K (0.143 ML) and in the case of ARUPS additional measurements at 0.1 ML and at 0.05 ML and in the case of PhD measurements at 0.1 ML were performed. The azimuthal orientation of benzene relative to the substrate has been studied by angle resolved ultraviolet photoelectron spectroscopy (ARUPS). These measurements showed that the benzene molecule lies flat on the surface with its C-C axis parallel to the $[\bar{2}11]$ direction of the substrate in the case of the 0.1 and the 0.05 ML. For the saturated layer, that exhibits a $(\sqrt{7} \times \sqrt{7})R19.1^\circ$ LEED pattern a different orientation was found, with one C-C axis of the molecule oriented along the $[\bar{1}10]$ direction of the substrate, but still flat lying. The conclusions were drawn using selection rules valid for UPS measurements that yield only the relative orientation but not the adsorption site. The azimuthal orientation of the benzene molecule was correlated to the sharp desorption peak found in the TPD spectra, that was correlated

with a phase transition [62]. For a saturation coverage of deuterated benzene the LEED I-V [40, 58] and PhD [58] measurements both yield the geometry of the molecule relative to the underlying nickel surface. Both studies find the adsorption on the hcp hollow site with one C-C axis pointing along the $[\bar{1}10]$ direction, see Fig. 4.1 (b).

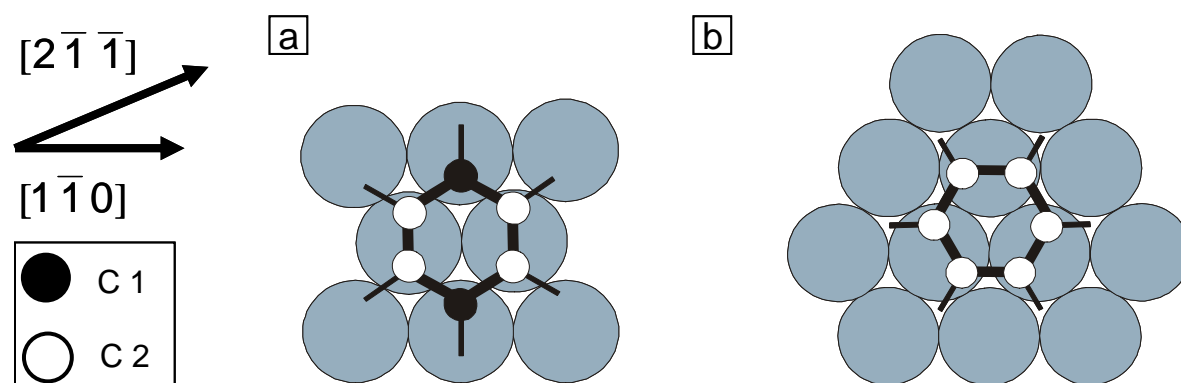


Fig. 4.1: Schematic drawings of a) benzene adsorbed on a bridge site and b) benzene adsorbed on a hollow site. C1 and C2 are indicating carbon atoms in different local environments. C1 carbon atoms are attached to one Ni atom and C2 carbon atoms are attached pair wise to one Ni atom.

For the dilute layer with 0.1 ML of benzene no long range order is found; thus, only PhD studies were performed on these layers. The measurements show the geometry found in Fig. 4.1 (a). Here the benzene molecule (C_6D_6) is adsorbed on a bridge site with one of its axis oriented along the $[\bar{2}1\bar{1}]$ direction of the substrate [58]. Therefore, all studies, known from literature, show similar results regarding the orientation relative to the substrate and the adsorption site.

The vibrational properties of the benzene molecule adsorbed on a Ni(111) surface were probed by high resolution electron energy loss spectroscopy (HREELS) [52]. The HREELS measurements showed values of 3025 cm^{-1} (375 meV) for the C-H stretching frequency of a non-deuterated benzene molecule and for the C-D stretching frequency of deuterated benzene 2250 cm^{-1} (279 meV) were found, as expected from the change in the reduced mass.

In two independent density functional theory calculations [66, 67] the authors discussed the adsorption properties and the electronic interactions of the benzene molecule with the surface. Both find the bridge adsorption site to be most stable up to

saturation coverage. Yamagishi et al. [67] partly consider adsorbate-adsorbate interactions but lack to include van der Waals interactions and entropic effects. Mittendorfer and Hafner [66] also did not fully model the lateral interactions and therefore did not obtain the experimentally determined hcp hollow sites.

4.1.2 Adsorption of benzene (C_6H_6 and C_6D_6) at 200 K

The adsorption of benzene (C_6H_6 and C_6D_6) at 200 K leads to a $(\sqrt{7} \times \sqrt{7})R19.1^\circ$ LEED pattern [40, 62, 64], which was used to determine the saturation coverage of 0.143 ML. In order to study the formation of this layer in detail, the adsorption behavior was studied by XPS in an uptake experiment, as shown in Fig. 4.2 (a).

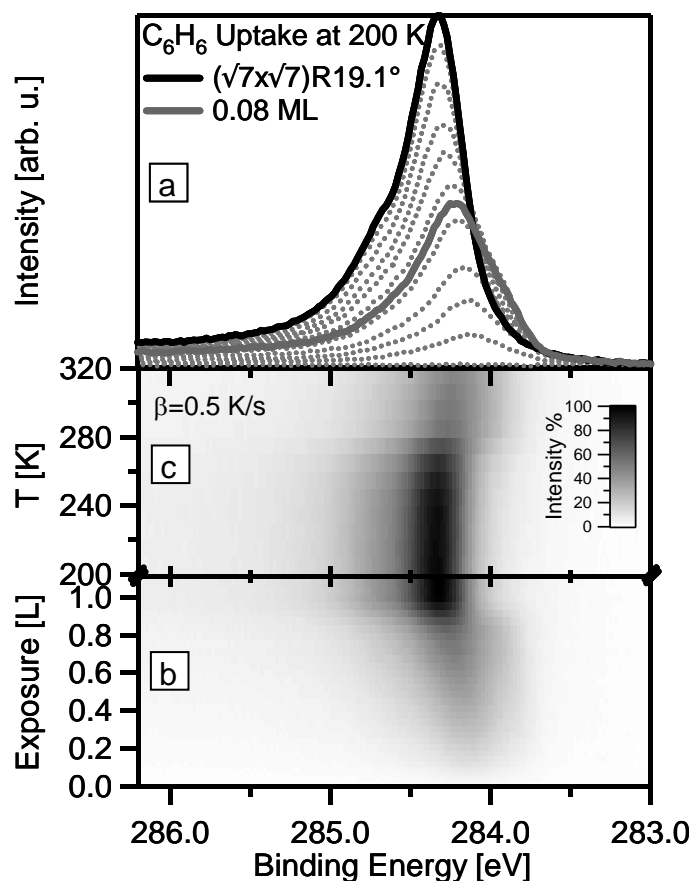


Fig. 4.2: a) Selected C 1s spectra of the adsorption of benzene (C_6H_6) at 200 K recorded at an emission angle of 45° , b) color coded density plot of the adsorption experiment and c) TPXPS experiment from 200- 320 K of this layer. The heating rate β was 0.5 K/s (spectra are recorded roughly every 10 K). Inset: relative intensity scale.

This uptake experiment and the subsequent TPXPS experiment are shown in Figs. 4.2 (b) and (c). At saturation coverage, solid black line in Fig. 4.2 (a), the C 1s spectrum exhibits two major features: a main peak at 284.3 eV and a shoulder at 284.7 eV. At lower coverages, e.g., 0.08 ML, an additional shoulder is observed at 283.9 eV, see Fig. 4.2 (a) solid grey line. The binding energy of the C 1s spectra is shifting to higher energies when the coverage is rising, see Fig. 4.2 (b), or, vice versa, is shifting to lower energies, when the coverage is lowered by heating, as can be seen in Fig. 4.2 (c). The overall peak shift of the main signal found, occurring during adsorption at 200 K, is approximately 200 meV for both deuterated and non deuterated benzene. A discussion of the peak shift is given in chapter 4.3.

In order to perform a quantitative analysis of the data, the spectra have been modelled with asymmetric Pseudo-Voigt line profiles for the different components observed. The resulting peak profiles agree, within the accuracy of our analysis, with the correct line shape resulting from a convolution of a Doniach-Sunjić and a Gaussian profile. A description of these line shapes is given in chapter 2.1.3. The results of the quantitative analysis do not depend on the line shape chosen, but the calculation time for the sum function is much shorter when the Pseudo-Voigt function is used. Nevertheless, a comparison of the analysis with the different line shapes is given in the appendix. In Fig. 4.3 we present typical examples of measured data and the line profiles used for the fit of C₆H₆ and C₆D₆ layers.

For the saturated layer a fit with two peaks, as shown in Fig. 4.3 (a) and (b), was used to describe the measured curves. We assign the peak at 284.32 eV (284.33 eV for C₆D₆), dotted lines in Fig. 4.3, to the adiabatic component and the smaller one at 284.73 eV (284.61 eV for C₆D₆) to the component arising from the vibrationally excited state of the C-H (C-D) stretching mode in the photoemission final state, dashed lines in Fig. 4.3. Similar vibrational splittings have been observed in XPS gas phase measurements (Ref. [22]) and adsorption studies of hydrocarbons [23, 68, 69]; further examples can be found in this work in the chapters 5, 6 and 7.

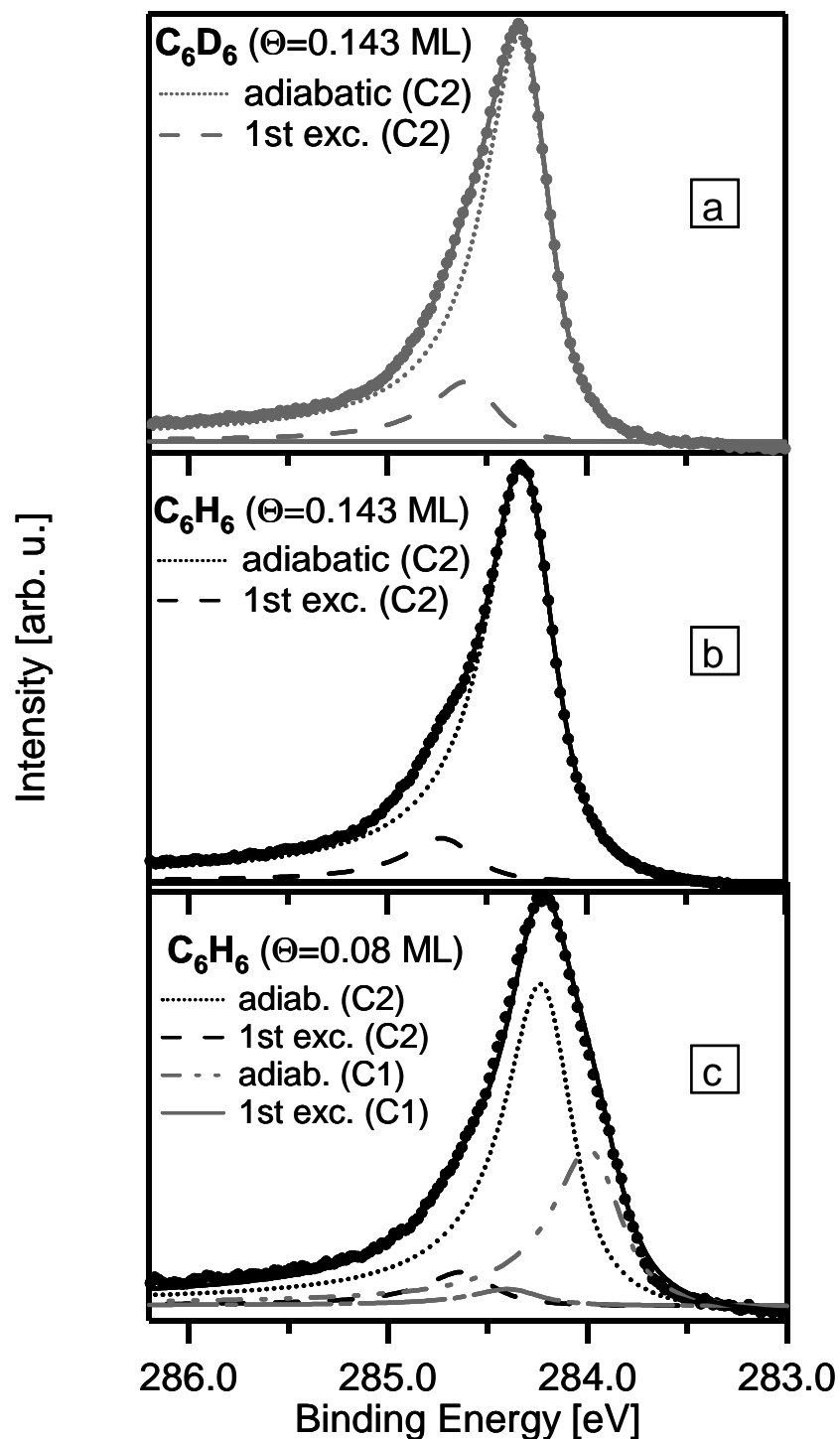


Fig. 4.3: C 1s spectrum of a) a saturated layer of C_6D_6 , b) a saturated layer of C_6H_6 and c) 0.08 ML of C_6H_6 . All spectra are recorded at an emission angle of 45° . The photon energy was 380 eV. All spectra are recorded at a sample temperature of 200 K. For further details see text.

To prove our assignment, the two major differences in the spectra for C_6H_6 and C_6D_6 are discussed. The binding energy difference between the adiabatic peak and the

peak of the first vibrationally excited state is 410 meV in the case of C_6H_6 and 280 meV in the case of C_6D_6 . This corresponds to the expected change in vibrational energy by a factor of $\sim 1/\sqrt{2}$ due to the change in the reduced mass [26] (see also chapter 2). DFT calculations to model gas phase XPS measurements [22] show a close agreement to our values, with 417 meV for C_6H_6 , and 310 meV for C_6D_6 . Comparable excitation energies are observed in HREELS studies of benzene on Ni(111) [52], which yield for the C-H stretching mode values of 375 meV for C_6H_6 and 279 meV for C_6D_6 . However, in HREELS the vibrational levels of the neutral state are probed, in contrast to XPS where the vibrational excitation occurs in the core hole final state, resulting in the observed deviations. Note that the C-C stretching vibration should also cause a shifted component in the XP spectra. In gas phase XPS, this is proposed to yield a binding energy difference of 132 meV [22]. This is, however, not resolved in our spectra for adsorbed benzene and, thus, is not included in the analysis as a separate peak, but contributes to the width and asymmetry of the C1 and C2 peaks.

Another difference between the C 1s spectra of deuterated and non-deuterated benzene is found in the relative intensities (peak areas) of the vibrationally split peaks. For C_6H_6 , the so-called S factor [26], which is the ratio of the intensities of the first excited state and the adiabatic peak, has a value of 0.10, and it increases for C_6D_6 to a value of 0.14. This again corresponds well to the expected increase by a factor of $\sim \sqrt{2}$. In the gas phase study of Myrseth et al. [22], a value of 0.103 for C_6H_6 was derived, in good agreement to our result.

The studies of Fuhrmann [38] showed a clear dependence of the S factor on the number of equal bonds, in this case of C-H bonds, leading to a significantly higher S factor of 0.17 ± 0.01 per C-H bond in the smaller adsorbates methyl (CH_3), ethylene (C_2H_4), acetylene (C_2H_2) and methylidyne (CH), see also [26, 70] and chapter 7. This difference can be explained by the different line shapes used in the analysis and in the more complex molecule studied here. Benzene shows a number of different not resolved vibrations, as the, already mentioned, C-C stretching mode and other low energy vibrations. But these vibrations are only partly modelled by the asymmetry of the Pseudo-Voigt function, leading to the observed deviations.

The unsaturated layer with a coverage of 0.08 ML of C_6H_6 , see Fig. 4.3 (c), exhibits an additional shoulder at the low binding energy side of the C 1s signal, compared to the saturated layer. As no dissociation of benzene occurs at 200 K, we

assign this contribution also to carbon atoms belonging to an intact benzene molecule. Thus this shoulder must, as the saturated layer, also consist of two peaks, again an adiabatic component and corresponding matching vibrational excited state (grey traces in Fig. 4.3 (c)). The S factor, binding energy difference, the line width and the line shape for this second component are set to be identical to the first carbon component, as they also originate from an intact benzene molecule, and were fixed during the final analysis.

We can summarize at this point that at benzene saturation coverage of 0.143 ML we observe one C 1s component (denoted as C2 in the following) for C_6H_6 and C_6D_6 , which is composed of two vibrationally split signals, one for the adiabatic excitation and one for a vibrationally excited state; at low coverages a second C 1s component (denoted as C1) arises that can also be described by two vibrationally split peaks. In this detailed analysis a binding energy shift of about 200 meV of both main signals is observed with coverage, which results from lateral interactions occurring in the benzene layer. This continuous shift is discussed in more detail in chapter 4.3. The possible origin of the two C 1s components is discussed in the following.

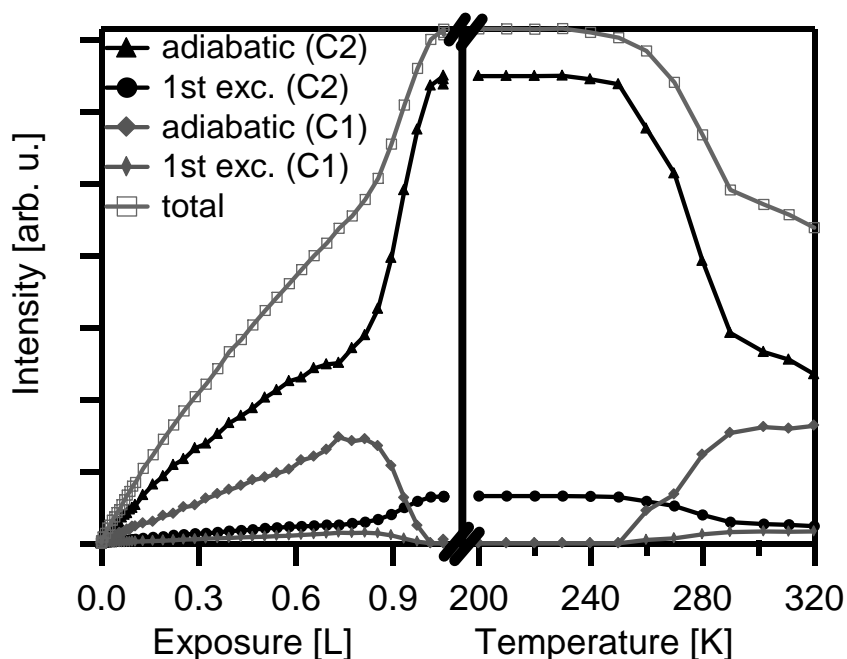


Fig. 4.4: Quantitative analysis of the adsorption and thermal desorption experiment of C_6H_6 shown in Fig. 4.2.

Using the described fitting procedure for a quantitative analysis of our uptake and TPXPS experiments for C_6H_6 , we obtain the exposure-dependent intensities shown in Fig. 4.4. Two major results are observed: (i) The adiabatic and vibrationally excited states of the C1 and C2-components change their intensities, while keeping a constant intensity ratio. (ii) Initially, both C 1s components (labelled as C1 and C2) increase together during the uptake experiment (left side), while for exposures above ~ 0.8 L the C1-component loses intensity to the C2-component, which is the only signal at benzene saturation coverage. The reversal of these findings is observed upon heating the saturated layer (right part); here, the C1-component appears again above 250 K, when the total coverage is reduced due to desorption. The exposure dependence of the corresponding total coverage will be discussed below.

The graph in Fig. 4.4 can also be plotted in terms of coverage, leading to a coverage scale for the uptake experiment, which is calibrated by the saturation coverage of 0.143 ML; for the TPXPS experiment this results in curves that point into the opposite direction as in Fig. 4.4, as the coverage is decreased by desorption during annealing the sample. This rescaling procedure leads to Fig. 4.5 (a). The total coverage is, due to the rescaling, a diagonal line, as the addition of the partial coverages is the total coverage leading to a total coverage vs. total coverage plot. The line is shown here to introduce the reader to this kind of plots and will not be considered anymore.

For a better comparison of the adsorption and thermal desorption of C_6H_6 and C_6D_6 , the areas of the peaks of the first vibrationally excited and the adiabatic state have been added for both components, resulting in the coverage-dependent contributions of the C1- and C2-components, as shown in Fig. 4.5 (b).

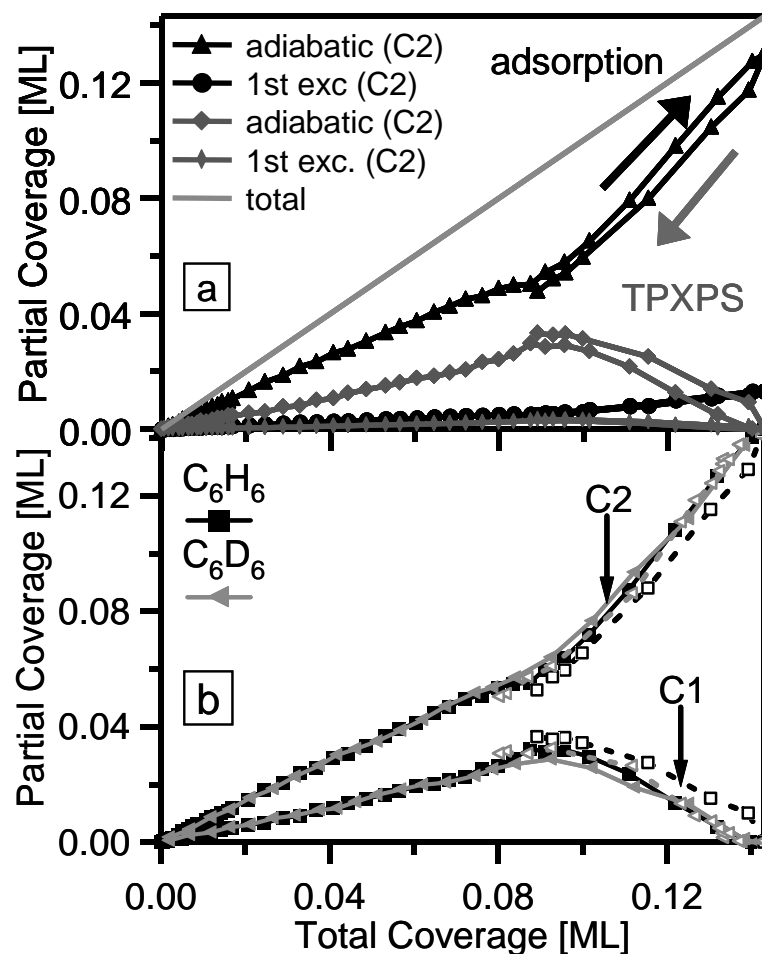


Fig. 4.5: a) Rescaled quantitative analysis of the adsorption and thermal desorption experiment of C_6H_6 shown in Fig. 4.2. The arrows are indicating the “direction” of the experiments. b) Comparison of the two components C1 and C2 of C_6H_6 and C_6D_6 for the adsorption experiments (solid lines, full symbols) and the thermal desorption (dotted lines, open symbols).

The known saturation coverage of 0.143 ML at 200 K (Ref. [62]) is used for a coverage calibration of the data resulting in this partial coverage vs. total coverage plot. Note that for simplicity the partial coverages assigned to the C1- and C2-components are also given in ML, i.e., benzene C_6 units per substrate atom (in order to obtain the coverage in terms of carbon atoms per substrate atom the axis has to be multiplied by a factor of 6).

The data in Fig. 4.5 (b) clearly shows the reversibility of adsorption (solid symbols) and thermal desorption up to a temperature of 320 K (open symbols). Interestingly, there is no significant difference in adsorption and thermal evolution

between non-deuterated and deuterated benzene, if prepared at 200 K. The small deviations observed are not discussed as they are within the experimental error.

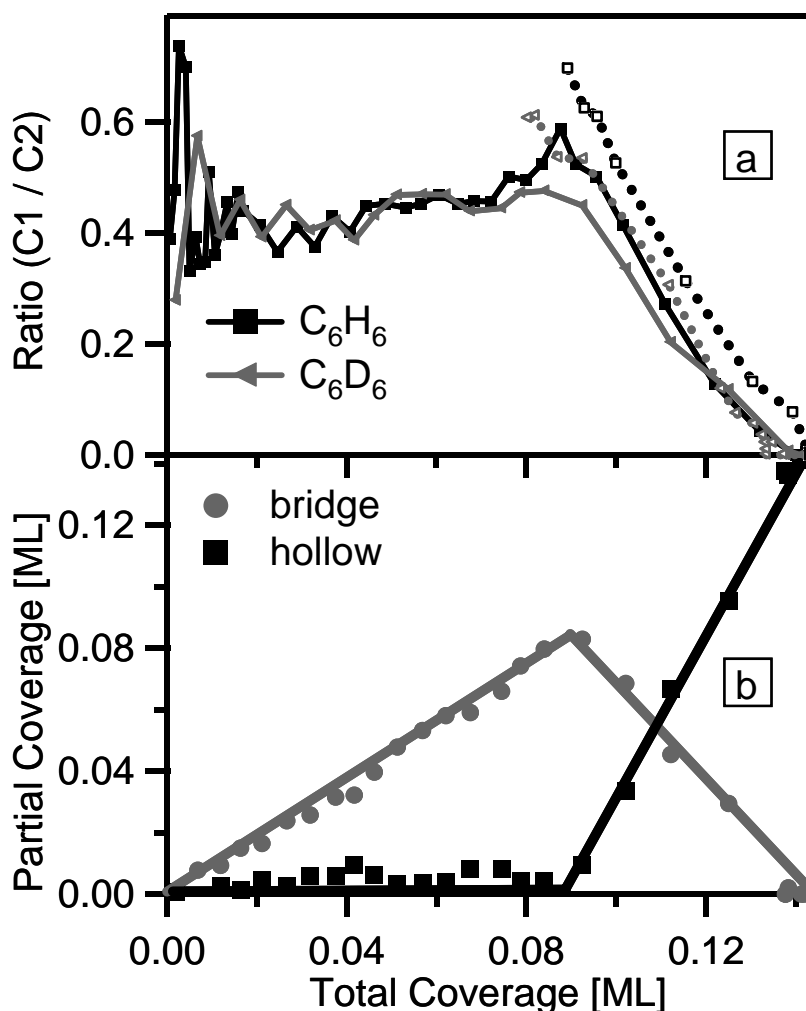


Fig. 4.6: a) Ratio of the two components of C_6H_6 and C_6D_6 for adsorption (solid lines, full symbols) and thermal desorption (dotted lines, open symbols). b) Occupation of adsorption sites during adsorption at 200 K.

As already observed in Fig. 4.4, a simultaneous increase of both components, C1 and C2, up to a total coverage of 0.09 ML is followed by a decrease of the C1-component and a further increase of the C2-component for higher benzene coverages. At saturation only the C2-component is present. These observations can be explained on the background of published results. By considering ARUPS data for intermediate coverages (0.05 and 0.1 ML) [65], we know that two C-C bonds of the

benzene molecule point along the $[2\bar{1}\bar{1}]$ direction (see Fig. 4.1 (a)). Since benzene is adsorbed on bridge sites, there are carbon atoms in two different positions relative to the underlying Ni atoms. Two of the carbon atoms (full circles) are attached to one Ni atom each and are denoted as C1-atoms, whereas four are attached pair wise on one Ni atom (open circles) and are denoted as C2-atoms. The ratio of the number of C1- to C2-atoms for the bridge site thus is 0.5. In Fig. 4.6 (a) the intensity ratio C1/C2 found in our analysis is shown. For coverages between 0.01 and ~ 0.09 ML, the ratio has an average value of $\sim 0.45 \pm 0.02$. This constant ratio supports the assignment of both carbon components (i.e., type of carbon atoms) arising from one molecule, since for different adsorption sites varying occupation ratios are expected [71]. The experimental ratio corresponds well to the expected value of 0.5 for benzene predominantly adsorbed at bridge sites, with deviations being due to photoelectron diffraction effects and some population of hollow sites (see below). It also shows that the different local environment of the carbon atoms C1 and C2 is reflected in the local electronic structure and, thus, in the C 1s binding energy. This is indeed found in theoretical calculations, resulting in different valence electron density for the singly-coordinated (C1) and the pair wise-coordinated (C2) carbon atoms [66, 67].

In Fig. 4.1 (b) a benzene molecule adsorbed on the hollow site, with C-C bonds along the $[1\bar{1}0]$ direction of the substrate, is depicted. In this geometry, which is reported for saturation coverage [40, 58, 63, 65], all six C atoms are equivalent and they are pair wise attached to one Ni atom. By comparison to the bridge adsorption site in Fig. 4.1 (a), one finds that these have the same local environment with respect to the Ni substrate as the C2-atoms (open circles) in the bridge site and they are thus also denoted as C2. The similarity of the C2-atoms in the two adsorption geometries can also be seen in the calculations by Yamagishi et al. [67] and Mittendorfer and Hafner [66], who depict a rather similar valence electron distribution for the corresponding carbon atoms in both sites. Therefore, for the hollow adsorption site, only one type of C atoms, namely C2, is present, and we expect a C1/C2 ratio of zero. This is indeed found for the saturation coverage of 0.143 ML, when only the C2-component is left (Fig. 4.5 (a)) and the ratio thus turns to zero (Fig. 4.6 (b)).

By increasing the temperature, the coverage is reduced by desorption, which results in an increase of the C1/C2 ratio, as seen by the open symbols in Fig. 4.6 (a). This is interpreted again as a coverage-dependent site change, now from hollow to bridge sites. In the region between ~ 0.10 and 0.143 ML, again a mixture of hollow

and bridge adsorbed benzene is present. At 320 K a situation is found which is similar to the one found during adsorption at a coverage of 0.09 ML. This change of the adsorption site happens at a similar temperature (about 270 K in Fig. 4.4, right part) as the sharp desorption peak at 290 K in the TPD spectra of the benzene layers [62] and thus should be correlated to it. The difference in transition temperature could be due to a different heating ramp (0.5 K/s for the TPXPS and 5 K/s for the TPD spectra). This assumption can be confirmed by using the “Redhead” equation [37] from chapter 2.2.1, which is valid for first order desorption behaviour. By assuming this first order desorption we can calculate the difference in the maximum of the desorption temperature, due to the different heating rates, leading to approximately 270 K, that were actually measured. For the tables and graphs created for this calculation see appendix. The value of the desorption energies (E_D) is not discussed, only the difference in the desorption temperature is taken into account.

By using the above information we propose, as schematically depicted in Fig. 4.6 (b), a predominant occupation of bridge sites at low coverage and a change to hollow sites, which goes along with an azimuthal reorientation of the molecules by 30° , for higher coverages. Thus, this site change seems to be induced by the increasing coverage and the accompanying adsorbate-adsorbate interactions.

At this point we want to address photoelectron diffraction effects, which depend on the local geometry around the emitting atom [30-32] and can lead to changes of the intensity ratio of different components, if the detection angle is changed with respect to the surface normal (see also chapter 2.1.4). Such effects have recently been reported, e.g., for CO on Pt(111) [71, 72]. They are also observed in our study, as can be seen in Fig. 4.7, where the intensities of the C1- and C2-components with increasing coverages are plotted, as obtained using different electron emission angles of 0° , 22° , 45° and 65° ; the intensity of the C2-signal decreases at the expense of the C1-signal, when increasing the emission angle. The resulting average C1/C2 ratios for coverages from 0.01 to 0.09 ML are 0.35, 0.42, 0.45 and 0.46 (all values are given with an error bar of ± 0.02), respectively.

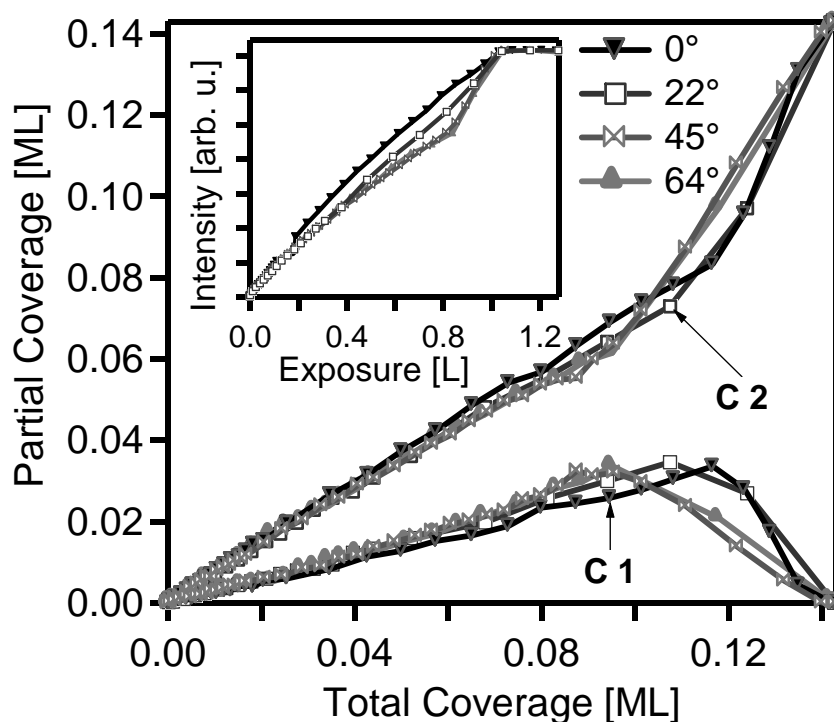


Fig. 4.7: Intensities of the components C1 and C2 during C_6H_6 adsorption at 200 K, taken at different emission angles with respect to the surface normal. Inset: corresponding total C_6H_6 intensity as a function of exposure of the adsorption experiments taken at different angles.

Due to the photoelectron diffraction effects, an unexpected change of the slope of the total coverage was observed at an exposure of 0.8 L in Fig. 4.4 for an emission angle of 45° . The inset of Fig. 4.7 shows these data again, together with data obtained at the other electron emission angles, namely 0° , 22° and 65° . While the data for 45° and 65° show a quite similar behaviour, we observe an approximately linear behaviour at 22° ; at 0° the curve even shows a convexity towards higher intensities. Since a linear coverage-exposure-relationship (i.e., a coverage independent sticking coefficient) was observed by Steinrück et al. in TPD experiments on Ni(111) [62], and also in the similar system C_6H_6 on Pt(111) [73], this suggests that the angle-dependent sensitivity factors for the intensities of the C1- and C2- components are approximately the same at 22° and that different scaling factors, to correct for PhD effects, would have to be applied to the C1- and C2-components, when calculating coverages from data at other emission angles. However, without independent reference coverages for both components, a rescaling has to remain somewhat

ambiguous and is, thus, not applied to the data shown in this publication. One should point out that, with few (mentioned) exceptions, this does not effect the conclusions derived from the data.

One value that is influenced by PhD effects is the coverage value, at which the change from bridge to hollow adsorbed benzene starts; this is evident in Fig. 4.7, where this onset (maximum of lower curve) shifts with emission angle. The value observed at 22°, where a linear coverage-exposure-relationship is observed, is understood as the true value and is determined to 0.10 ± 0.01 ML. From the deviation of the observed C1/C2-ratio of 0.42 for coverages up to ~0.09 ML from the expected value of 0.50, one can also roughly estimate the minority population of benzene molecules in hollow sites by using the following equations:

$$a(4x + 2y) + b(6x) = z$$

and $R = \frac{2a}{4a + 6b}$

with

R: ratio of the two components C1 and C2

a: percentage of bridge adsorbed molecules

b: percentage of hollow adsorbed molecules

x: pair wise adsorbed carbon atoms

y: carbon atoms adsorbed on one Ni atom

z: total number of carbon atoms (all x and y atoms)

With the above mentioned ratio of 0.42 we can thus estimate the minority population to be 10-15% of benzene molecules adsorbed in hollow sites instead of in bridge sites. Results for different percentages of the minority population and the resulting ratios are given in the appendix.

4.1.3 Adsorption at 125 K and thermal evolution up to 220 K

Another way to prepare the $(\sqrt{7} \times \sqrt{7})R19.1^\circ$ superstructure is to adsorb multilayers of benzene at ~ 125 K and subsequently desorb the excessive molecules by raising the temperature to 220 K [40, 64]. In order to study a possible influence of the preparation procedure on the site population, we show in Fig. 4.8 (a) the C 1s spectra of such a C_6D_6 adsorption experiment, and in Fig. 4.9 (a) the quantitative analysis of this experiment is displayed.

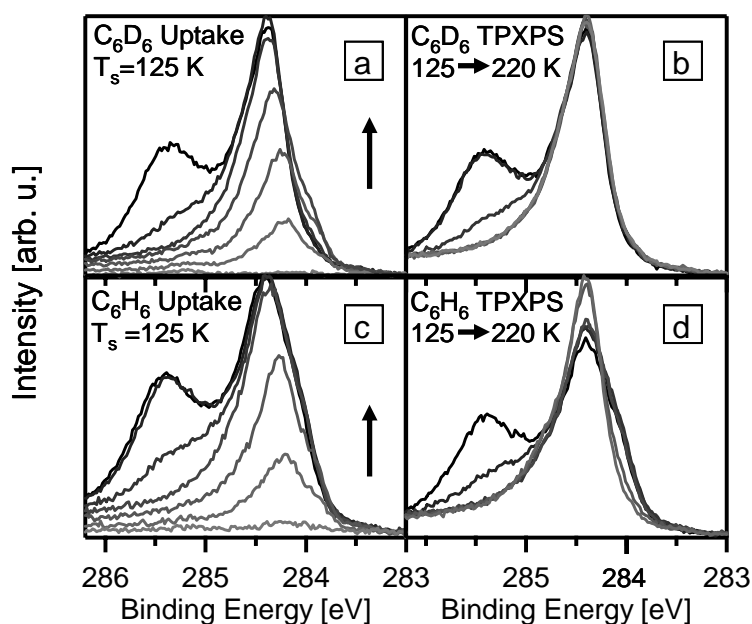


Fig. 4.8: Selected C 1s spectra of a) a C_6D_6 uptake experiment at 125 K (the arrow and the grey scale indicate the increasing exposure); b) a TPXPS experiment from 125 to 220 K of the C_6D_6 layer of a) (darker lines stand for lower temperatures); c) a C_6H_6 uptake experiment at 125 K (the arrow and the grey scale indicate the increasing exposure); d) a TPXPS experiment from 125 to 220 K of the C_6H_6 layer of c) (darker lines stand for lower temperatures). All spectra are collected with a photon energy of 380 eV at normal emission. For further details see Fig. 4.9 and text.

The spectra show the already discussed features and an additional broad peak at 285.4 eV, which is assigned to the adsorption of benzene in multilayers. The quantitative analysis is performed with the same parameters for the first benzene layer as before (the multilayer contribution is also modelled by an asymmetric Pseudo-Voigt function), resulting again in two carbon components, C1 and C2, increasing at low coverages (Fig. 4.9 (a)). This time the intensity ratio between the

two carbon components C1/C2 is smaller than for adsorption at 200 K (~ 0.28 vs. ~ 0.35), both measured at an emission angle of 0° . A possible explanation could be that for adsorption at 125 K the layer contains a larger number of hollow-adsorbed benzene in addition to the majority of molecules adsorbed on bridge sites, due to low mobility at this temperature. This would lead to an increased C2 contribution. At coverages above ~ 0.11 ML, the C1-component decreases while the C2-component increases. This is again attributed to the change of the adsorption site from bridge to hollow, as observed at 200 K (chapter 4.1.2). At total coverages above ~ 0.14 ML, we observe only the C2-component, i.e., C_6D_6 at hollow sites. The only difference is the growth of physisorbed multilayers after completion of the chemisorbed layer. This contribution reduces the intensity of the C2-component slightly, due to damping effects.

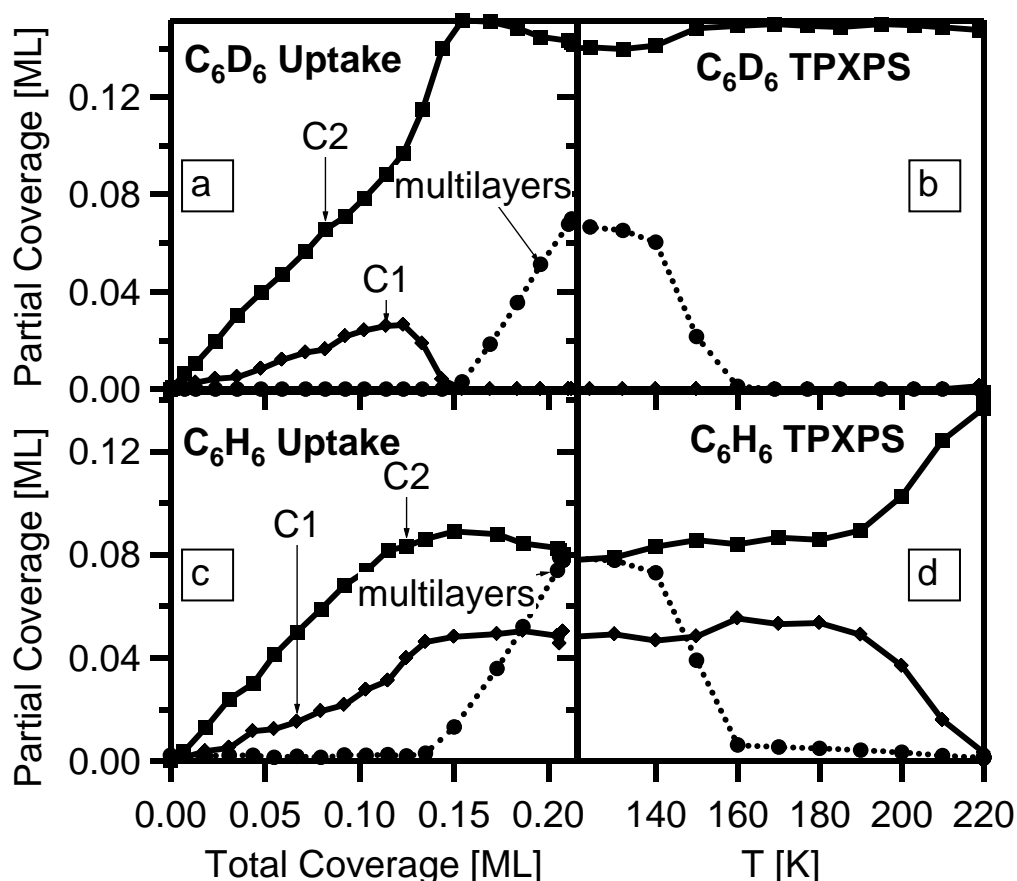


Fig. 4.9: Quantitative analysis of a) the C_6D_6 uptake experiment at 125 K; b) the TPXPS experiment from 125 to 220 K with the C_6D_6 layer of a); c) the C_6H_6 uptake experiment at 125 K; d) the TPXPS experiment from 125 to 220 K with the C_6H_6 layer of c).

In Fig. 4.8 (b) the C 1s spectra of the TPXPS experiment of this layer and in Fig. 4.9 (b) the quantitative analysis are shown. At 140 K the multilayers start to desorb, in agreement with TPD results [62]. In Fig 4.8 (b) this can be observed as the spectra at higher temperatures do not exhibit the broad peak at 285.4 eV. This leads to a decrease of the attenuation of the monolayer signal, i.e., an increase of the C2-component. From the fact that the C1-component is not populated up to 220 K, we conclude that no change in adsorption site (i.e. reorientation) of the molecules occurs up to that temperature. The resulting layer exhibits the $(\sqrt{7} \times \sqrt{7})R19.1^\circ$ superstructure (used again for coverage calibration) and upon further annealing behaves like the layers adsorbed at 200 K.

In Fig. 4.8 (c) the C 1s spectra and in Fig. 4.9 (c) the quantitative analysis of the adsorption experiment of non-deuterated benzene (C_6H_6) at 125 K are shown. At low coverages, the spectra are similar to the ones observed at 200 K: The main peak at ~ 284.2 eV and its shoulder at lower binding energies are the only signals. The additional peak at 285.4 eV for high coverages is again attributed to the adsorption of multilayers. At low coverages, the two carbon components, C1 and C2, are increasing again simultaneously, but for C_6H_6 the intensity ratio C1/C2 of 0.35 is similar, within the margins of error, to the value observed for the adsorption experiment at 200 K, performed at the same electron emission angle of 0° . From these results we conclude the predominant occupation of bridge sites both at 125 and at 200 K up to coverages of ~ 0.10 ML. Interestingly, in contrast to all other measurements, for total coverages above 0.10 ML, the C1-components does not decrease and even in the multilayer regime, i.e. at coverages above 0.143 ML, no change in adsorption site (i.e. reorientation) of the benzene molecules in the chemisorbed layer takes place. Note that a temperature of 120 K is sufficient to “freeze” also the site change of deuterated benzene, data shown in the appendix. Therefore the temperature difference of 55 K between the freezing of the deuterated benzene and the non-deuterated benzene is a rather exact value.

In Fig. 4.8 (d), the C 1s spectra of the thermal evolution of C_6H_6 up to a temperature of 220 K are shown, with the quantitative analysis displayed in Fig. 4.9 (d). We first observe the desorption of the multilayers between 140 K and 160 K, again accompanied by the removal of the attenuation of the monolayer signal, this can be noticed in the spectra in the loss of the broad peak at 285.4 eV in Fig 4.8 (d). At temperatures higher than 180 K, the signal of the C1-component starts to

decrease, reaching zero at 220 K. Simultaneously, the signal related to the C2-component reaches 0.143 ML, the value for the ordered saturation layer, indicating a site change from bridge to hollow, but now only after heating to 220 K. The resulting layer exhibits the $(\sqrt{7} \times \sqrt{7})R19.1^\circ$ LEED pattern used for coverage calibration. A schematic drawing of the situation of the layers beneath the multilayers is given in Fig. 4.10 (a) for C_6H_6 and (b) for C_6D_6 , showing the adsorption sites for the adsorption at 125 K and indicate possible lateral repulsive interactions in the case of C_6H_6 , due to steric considerations.

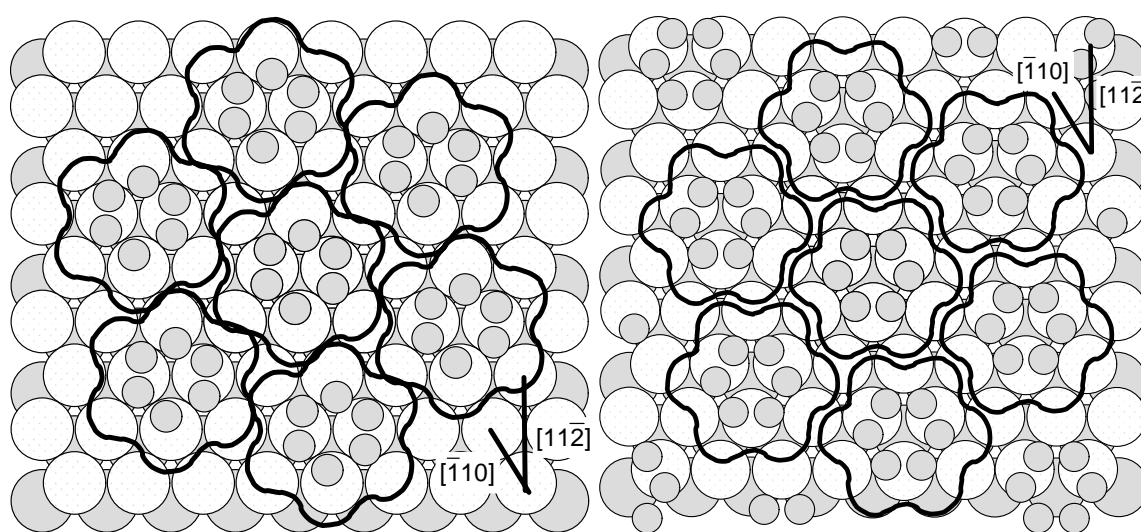


Fig. 4.10: Adsorption sites for a) C_6H_6 adsorption at 125 K and b) for C_6D_6 adsorption at 125 K. For both structures multilayers are physisorbed on top. The structure shown in b) is also valid for both C_6H_6 and C_6D_6 adsorbed at 200 K.

The continuing TPXPS experiments of these layers are shown in Fig. 4.11 (a) and (b). We again see the similar behaviour for deuterated and non-deuterated benzene, both changing their adsorption site from hollow to bridge at a temperature of approximately 270 K; showing us, that the difference for the two types of benzene only occurs at temperatures lower than 190 K. Differences in Fig. 4.11 are due to different temperature intervals during the measurement.

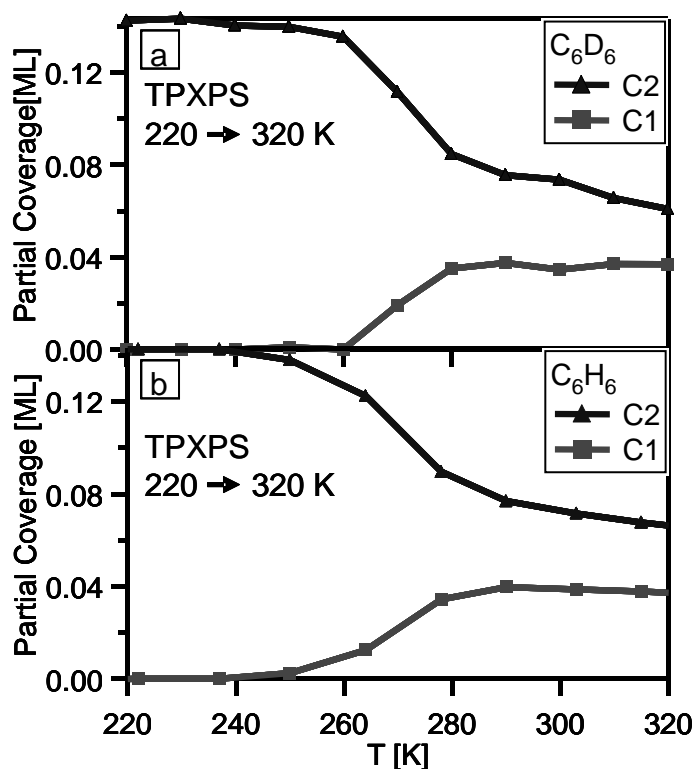


Fig. 4.11: TPXPS experiments from 220 to 320 K of the experiments from Fig. 4.9. a) TPXPS of a C_6D_6 layer, b) TPXPS of a C_6H_6 layer.

In the following we want to discuss possible reasons for this new isotope effect for the adsorption of benzene on Ni(111) at 125 K. To start out we consider different vibrational properties of the molecule: In the DFT study of Yamagishi et al. [67], the excitation energy of the frustrated translation for C_6H_6 from fcc hollow to bridge to hcp hollow sites was determined to be 11.4 meV. A similar value of 13.1 meV was experimentally found for C_6H_6 adsorbed on Rh(111) by Witte et al. [74] using inelastic helium atom scattering. By comparison to a thermal energy, kT , of 10 meV at 120 K (15 meV at 180 K) some excitation of this frustrated translation is to be expected. However, due to the small difference in the reduced masses of C_6H_6 and C_6D_6 (84 vs. 78 u) the expected differences in the degree of excitation are negligible and most likely not relevant.

When comparing C_6H_6 and C_6D_6 , the biggest difference is found for the C-H (C-D) vibrations, with values of 375 (279) meV for stretching mode and 93 (67) meV for the out of plane bending mode [52]. Because these vibrations are not populated at 125 K, the differences of the positional uncertainty ($\pm\sigma$ of the Gaussian) can be estimated from the corresponding zero-point energies ($1/2 h\nu$) using a harmonic

approximation, yielding differences of $\Delta\sigma = 0.018 \text{ \AA}$ for the C-H stretch and $\Delta\sigma = 0.033 \text{ \AA}$ for the C-H bending mode, with the larger values obtained for C_6H_6 ; these values correspond to the differences of the turning points of the classical harmonic oscillator. The difference in lateral extension due to the C-H zero point motion ($2 \times 0.018 \text{ \AA}$ due to two opposing C-H bonds) is rather small compared to the size of the molecule and thus is not expected to play a dominant role in the observed azimuthal reorientation. (The explicit calculations leading to these values are shown in chapter 2.6.) In contrast to that, the difference for the C-H bending mode of 0.033 \AA might lead to a significant difference in the adsorption enthalpy due to a different equilibrium distance to the surface for C_6H_6 and C_6D_6 : The adsorbate-substrate bond length results from a delicate balance between attractive interactions (back bonding) and repulsive interactions due to overlap of the hydrogen wave functions with the substrate – this effect has been described for different hydrocarbons on Cu(111) by Bagus et al. [75]. Due to the larger positional uncertainty perpendicular to the surface of the H atoms as compared to the D atoms, one would expect a larger bonding distance between substrate and C_6H_6 . This effect should vary when changing the adsorption site, in particular since the positions of the H (D) atoms with respect to the underlying substrate are different for the bridge and hollow site (see Fig. 4.1 (a) and (b)). Furthermore, one also expects differences for the activation energies for a change of the adsorption sites, e.g. from bridge to hollow site.

From these considerations, we propose that there is a small difference in the adsorption energy and the activation energy for a site change of C_6D_6 and C_6H_6 . For both molecules the bridge site is energetically favored at low coverage. As the coverage is increased towards $\sim 0.10 \text{ ML}$, the intermolecular distance decreases leading to repulsive interactions. Starting at this coverage it becomes energetically favorable for both molecules to change their azimuthal orientation by 30° and simultaneously the adsorption site to the hcp site, as has been proposed in Ref. [65]. This site change is an activated process. For adsorption at 200 K, the thermal energy is sufficient for both C_6D_6 and C_6H_6 , and reorientation occurs. At 125 K, reorientation only occurs for C_6D_6 , but not for C_6H_6 . Obviously, the thermal energy is not sufficient to overcome the energy barrier for the site change. We believe that this is most likely not a property of the individual molecule, but is a simultaneous rotation and site change of several molecules: At 0.10 ML the adsorbate layer is already relatively crowded and a site change can only be achieved by a concurrent motion of several

molecules. In order to induce the azimuthal reorientation in the saturated C_6H_6 layer adsorbed at 125 K, we have to heat this layer to comparably high temperatures. This could also be understood along the lines discussed above. In the saturated C_6H_6 layer (~ 0.14 ML) the molecules are very densely packed, which significantly increases the activation barrier for the site change, since now even larger fractions of the layer have to change simultaneously. Thus the onset for reorientation of C_6H_6 at ~ 180 K is 55 K higher than the temperature of 125 K for C_6D_6 , where reorientation is observed during adsorption at ~ 0.1 ML. We have to mention that these explanations of the observed isotope effect are speculative and need to be verified by detailed calculations.

It is interesting to note that Braun et al. [40, 64] observed by LEED an additional isotope effect concerning the adsorption geometry of the saturated layer: this study reveals that despite the fact that both C_6D_6 and C_6H_6 display a $(\sqrt{7} \times \sqrt{7})R19.1^\circ$ LEED pattern, the local adsorption geometries of the two molecules are different. While the first adsorbs on hcp hollow sites (as in Fig. 4.1 (b)), the latter adsorbs on bridge sites (similar to Fig. 4.1 (a)). The major difference to the present study is that the benzene layer was prepared by dosing benzene multilayers at 85 K followed by annealing to 220 K, and that the LEED measurements were performed at 85 K. Further measurements are planned to find out whether the observed difference in the orientation of C_6H_6 found in the present study is due to the differences in the layer preparation or in the temperature during the measurements.

4.2 Coadsorption experiments with benzene

In the previous part of this chapter the adsorption of benzene has been studied in great detail. We identified the different coverage dependent adsorption sites by in-situ XPS. This insight can be used to understand possible reaction pathways in the decomposition of cyclohexene, discussed in chapter 5. Another key step for surface reactions and to understand surface reactions is the coadsorption of possible reaction partners. In particular, the arrangement of the molecules is of interest, as it is important for possible reactions or transition states. The adsorption site might, thus, change the reactivity of a molecule on a surface due to different local environment. The determination of such rather complicated structures is certainly a typical task for

diffraction methods, but as shown before, in-situ XPS can also help to understand the site preference of benzene, and as the chemical shift of the investigated coadsorbates (NO, CO) is large, the benzene signal can be analyzed separately, to gain access to the adsorption geometry. The advantage of our analysis is that we use a straight forward model and no time consuming calculations have to be performed, which are necessary for diffraction methods, furthermore, no long range order of the adsorbates is necessary for our experiments.

4.2.1 Benzene coadsorbed with CO: $(2\sqrt{3} \times 2\sqrt{3})R30^\circ$ benzene + 2 CO

The coadsorption of benzene with CO has already been the subject of some surface science studies. The first studies with TPD and LEED were performed by Huber [76] showing a well ordered $(2\sqrt{3} \times 2\sqrt{3})R30^\circ$ superstructure. The TPD spectra showed, that the sharp desorption peak of benzene at 290 K vanishes and only parts of the high temperature desorption shoulder can still be observed [40]. Also ARUPS measurements were performed, and by applying symmetry selection rules the orientation of the benzene relative to the substrate was determined, yielding the orientation of the C-C axis parallel to the $[\bar{2}11]$ direction of the Ni(111) crystal [65]. A XPS study was performed by Held et al. [77], that was mainly concerned with the adsorption sites of the coadsorbed CO and it was argued on the ground of steric reasons for the adsorption sites of benzene. Their interpretation of the data lead to a threefold hollow site for CO and for benzene, but they could not exclude a bridge site for CO resulting also in a bridge site for benzene. In a LEED I-V study Braun [40] investigated the adsorption geometry. He found a slightly “distorted” hcp hollow adsorption site for benzene with the C-C axis oriented along the $[\bar{2}11]$ direction of the substrate, see Fig. 4.12. The benzene molecule is not adsorbed as ideal as in the $(\sqrt{7} \times \sqrt{7})R19.1^\circ$ structure of the pure benzene layer, discussed in chapter 4.1.

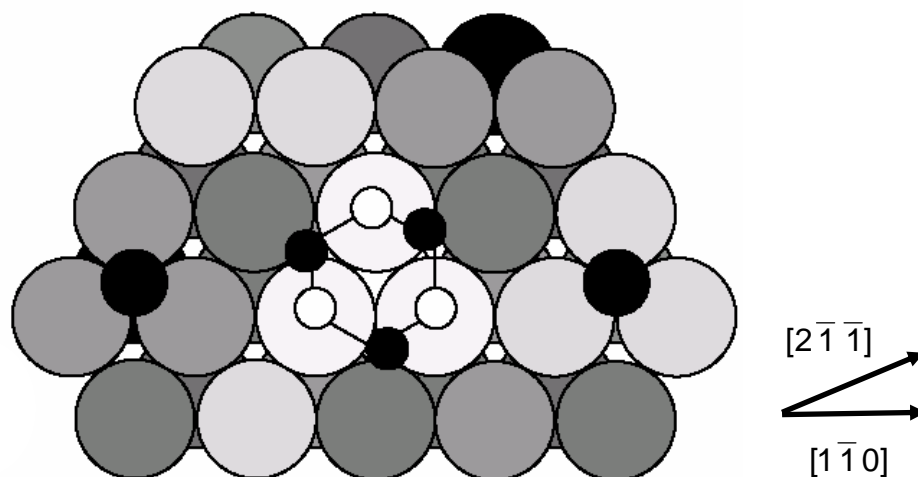


Fig. 4.12: Adsorption geometry of the coadsorption of benzene with CO, exhibiting a $(2\sqrt{3} \times 2\sqrt{3})R30^\circ$ LEED pattern [40].

The vibrational properties were determined by EELS measurements [78]. The authors accidentally prepared the coadsorption layer which exhibits the $(2\sqrt{3} \times 2\sqrt{3})R30^\circ$ LEED pattern. The differences in the vibrational properties compared to pure benzene layers are nevertheless not significant, and can therefore be neglected. These facts showed us, that the same analysis, again the two species C1 and C2 each consisting of an adiabatic and a vibrational contribution. As the vibrational properties of the molecule are not changing the same parameters as in the case of the pure benzene layers are appropriate.

For preparing a coadsorption layer initially benzene and subsequently CO are dosed at 310 K. Benzene is dosed until it saturates and afterwards the surface is exposed to CO, in this case 2.1 L. XP spectra recorded during this procedure are shown in Fig. 4.13. The resulting layer exhibits the $(2\sqrt{3} \times 2\sqrt{3})R30^\circ$ LEED pattern.

In the lower part of Fig. 4.13, for benzene adsorption, we observe one peak at 284.1 eV rising, which shifts to higher binding energies with increasing coverage. This phenomenon was also observed for the pure layers adsorbed at 200 and at 125 K. The XP spectrum of the resulting dilute benzene (C_6D_6) layer is marked as dash dotted line in Fig. 4.13. When coadsorbing CO an additional peak at 284.95 eV evolves. A small shift of this peak to higher binding energies by 50 meV with increasing coverage is observed. A more drastic shift in the binding energy can be observed for the benzene signal, which is shifting by 150 meV to lower values upon

CO exposure. The XP spectrum of the ordered coadsorption layer is the uppermost spectrum, marked as a dotted line, now exhibiting two distinct peaks due to benzene at 284.05 eV and CO at 285.0 eV. The binding energies of [79] are in good agreement with the results achieved here.

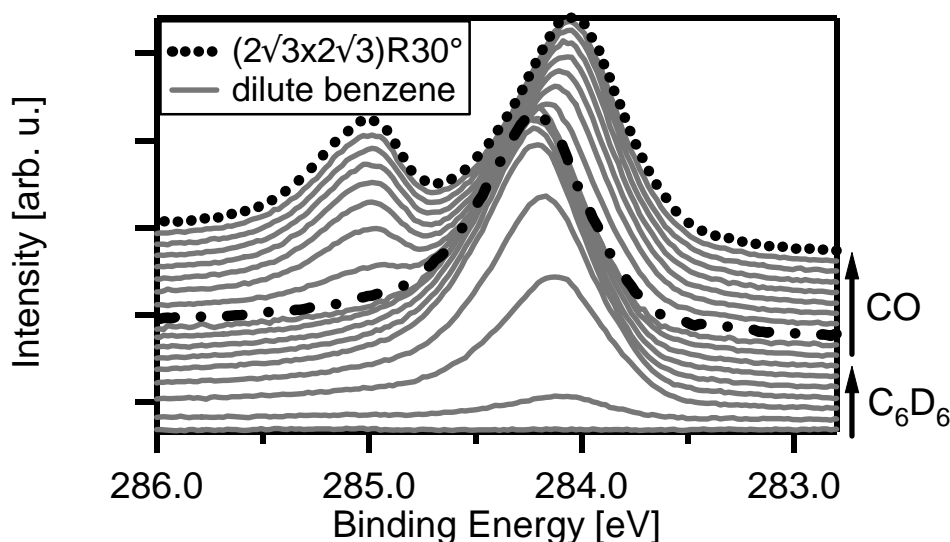


Fig. 4.13: Selected XP spectra of an adsorption experiment at 310 K. At first benzene and subsequently CO was adsorbed. The spectra are recorded at normal emission with a photon energy of 380 eV.

A quantitative analysis of the XP spectra was carried out. The dilute benzene layer shows the typical pattern of the bridge adsorbed benzene. It can also be observed in the TPXPS experiments of the pure benzene layers at 310 K, shown in chapter 4.1.

The quantitative analysis, shown in Fig. 4.14 (a), shows two carbon components and an additional coverage due to the adsorption of CO. The nominal benzene coverage of this coadsorption phase is 0.083 ML and the nominal CO coverage is 0.167 ML [62]. In our analysis we find quite similar values of 0.082 ± 0.002 ML of benzene and 0.167 ± 0.002 ML of CO. The coverage given for CO given in Fig. 4.14 has to be multiplied by 6, as we refer in this graph to monolayers of benzene, which consists of 6 carbon atoms.

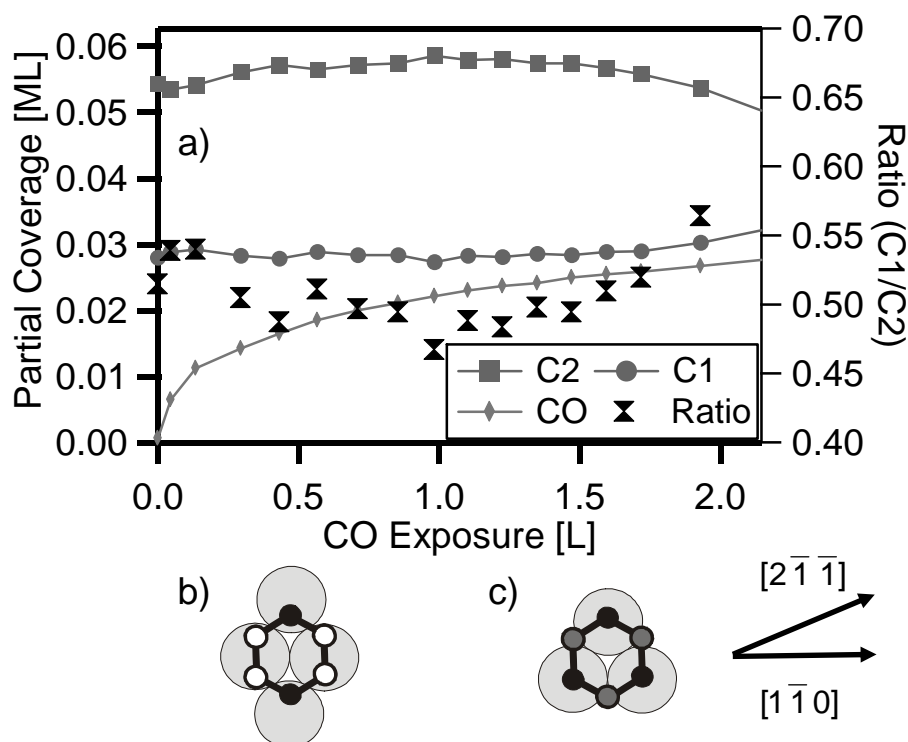


Fig. 4.14: a) Quantitative analysis of the coadsorption experiment of Fig. 4.13, leading to a $(2\sqrt{3}\times 2\sqrt{3})R30^\circ$ LEED pattern. The scale for the partial coverages of the different carbon components is at the left hand side, the scale for the ratio is located at the right hand side. Note that the coverage scale for CO has to be multiplied by 6. b) Schematic picture of benzene adsorbed on a bridge site with its C-C axis along the direction $[2\bar{1}\bar{1}]$ of the surface. c) Schematic picture of benzene adsorbed on a hollow site with its C-C axis along the direction $[2\bar{1}\bar{1}]$ of the surface.

The ratio of the two carbon components C1 and C2 reaches values of up to 0.67 at the highest CO exposure. At this exposure, the layer exhibits the $(2\sqrt{3}\times 2\sqrt{3})R30^\circ$ LEED pattern. If the spectrum is taken from a new spot on the sample, not affected by prior exposition to the intense x-rays from the synchrotron, even a ratio of 0.8 is reached. This is interpreted as an adsorption site for benzene between the bridge site with the C-C axis along the $[2\bar{1}\bar{1}]$ direction and the hollow adsorption site with the C-C axis along the $[2\bar{1}\bar{1}]$ direction, see inset of Fig. 4.14 (c). A pure form of the benzene adsorbed on the hollow site adsorbed with the C-C axis along the $[2\bar{1}\bar{1}]$ direction of the substrate would yield a ratio of 1. As the authors of [79, 80] pointed

out, the adsorption site of benzene is also determining the adsorption site of CO, due to steric reasons. We, therefore, can assign the adsorption site of CO to be hcp hollow.

The exact interpretation of this scenario is certainly rather difficult, as a new local environment is present for the carbon atoms adsorbed at the hollow sites in this new species. This new local environment might lead to a new behaviour regarding photoelectron diffraction. Thus our analysis may yield a higher error as for the aforementioned examples. But nevertheless the interpretation leads us to a result which is similar to the result of the LEED I-V analysis of Braun [40], showing a distorted hcp hollow site. Another interpretation of these results would be that a combination of both benzene adsorbed on bridge sites with C-C axis aligned along the $[\bar{2}\bar{1}\bar{1}]$ direction of the Ni(111) substrate and on hollow sites with the C-C axis pointing along the $[2\bar{1}\bar{1}]$ direction are present on the surface at the same time, resulting in a mixture of the two ratios, showing some disorder in the layer examined. Both interpretations are in line with the ARUPS results of Huber, showing an alignment of the C-C axis along the $[\bar{2}\bar{1}\bar{1}]$ direction of the substrate for the coadsorption phase, and in the dilute layer consisting of bridge adsorbed molecules [80], see Fig. 4.14 (b).

4.2.2 Benzene coadsorbed with NO: (3 x 3) benzene +2 NO

The coadsorption of NO with benzene leads, like the coadsorption of CO with benzene, to ordered structures. In the case of NO coadsorbed with benzene more than one ordered structure is known. In a publication of Zebisch et al. [81] five different structures are reported, exhibiting a $c(2\sqrt{3}\times 4)rect$, a (3×3) , a $(2\sqrt{3}\times 2\sqrt{3})R30^\circ$, a $(2\sqrt{3}\times 4\sqrt{3})R30^\circ$ and a blurred $c(4\times 2)$ LEED pattern. In this study TPD spectroscopy was also used to examine this system. A detailed angle resolved ultraviolet photoelectron spectroscopy study on these structures was performed and by means of symmetry selection rules the orientation of the benzene molecules relative to the substrate was determined, but not the adsorption sites. A PhD study [82] has been performed on the coadsorption phase of benzene and NO leading to the $(2\sqrt{3}\times 2\sqrt{3})R30^\circ$ structure. The authors concluded from a comparison of the PhD data of Schaff et al. [58] that the benzene molecules occupy the same adsorption

sites as in the case of pure benzene at intermediate coverages, which is the bridge site with the C-C axis of the benzene molecule aligned along the $[\bar{2}\bar{1}\bar{1}]$ direction. The alignment of the C-C axis is in agreement with ARUPS results [80]. Their main concern, nevertheless, was to determine the adsorption site of the coadsorbed NO.

In this chapter, we are mainly concerned with the coadsorption layer of benzene with NO exhibiting the (3×3) LEED pattern, which was prepared by first dosing benzene at 200 K. This leads to the spectrum of the saturated chemisorbed layer known from the chapter 4.1, corresponding to the dotted black spectrum in Fig. 4.15. Thereafter, the benzene layer was flashed to 320 K to reduce the benzene coverage, allowing NO adsorption. The dash-dotted line in Fig. 4.15 corresponds to this dilute benzene layer, which consists of bridge adsorbed benzene molecules. It can be seen clearly, that the binding energy of the main benzene signal shifts to lower energies by 150 meV due to the desorption of benzene. Starting from this point, with ~ 0.10 ML of bridge adsorbed benzene, 1.3 L of NO were adsorbed. The change in the C 1s signal was monitored, showing a binding energy shift to lower binding energies of ~ 180 meV (a comparable effect is observed for CO coadsorption, see chapter 4.2.1).

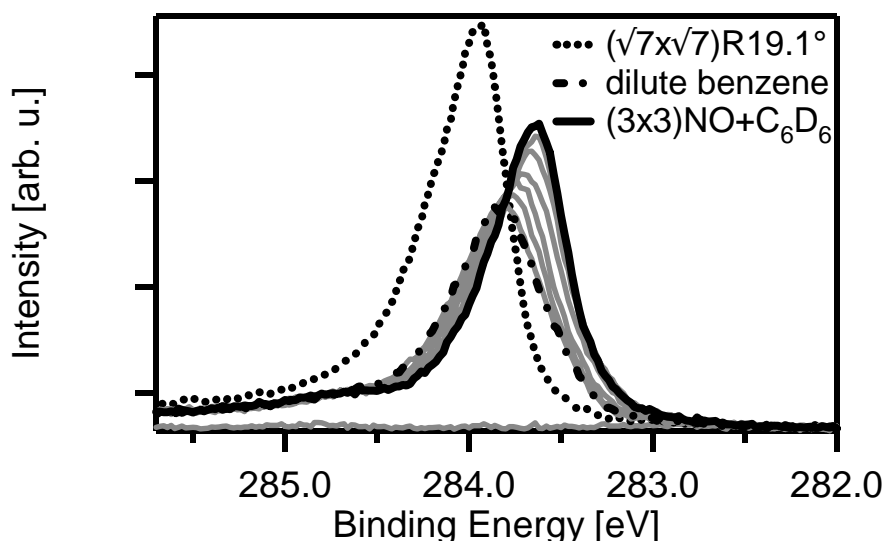


Fig. 4.15: Selected C1s XP spectra of the preparation of a (3×3) benzene + 2 NO layer. The photon energy was 380 eV and the experiment was measured in normal emission geometry.

A subsequent LEED experiment confirmed the expected (3x3) pattern. In our quantitative analysis of this experiment we found a total benzene coverage of ~ 0.095 ML. Although from the LEED pattern nominal coverages of 0.111 ML of benzene and 0.222 ML of NO were expected, we found the ordered layer. Some disordered surface regions might explain this difference.

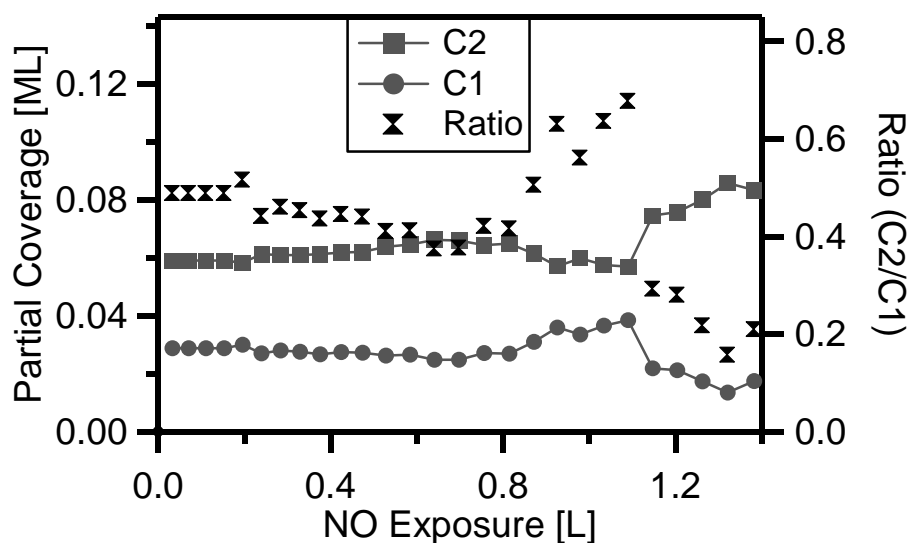


Fig. 4.16: Quantitative analysis of the experiment of Fig. 4.15. Note that the partial coverage scale for the carbon components is on the left side and the scale for the ratio is on the right side.

The quantitative analysis of the different carbon components and their respective ratio is shown in Fig. 4.16. This rather unusual run of the curves can be understood by regarding the previously published results by Zebisch et al. [81], shown in Fig. 4.17.

The adsorption of benzene and the subsequent annealing procedure lead to a coverage of ~ 0.095 ML of benzene, corresponding to the greyish area in Fig. 4.17. According to this graph, adsorption of NO in this coverage range of benzene can lead to 3 different ordered structures: at first, at low NO coverages the $c(2\sqrt{3}\times 4)rect$ structure is found. At slightly higher coverages of ~ 0.1 ML of NO a change to the $(2\sqrt{3}\times 2\sqrt{3})R30^\circ$ structure was observed by LEED. Then again, rising the NO coverage the (3x3) structure is the stable super structure.

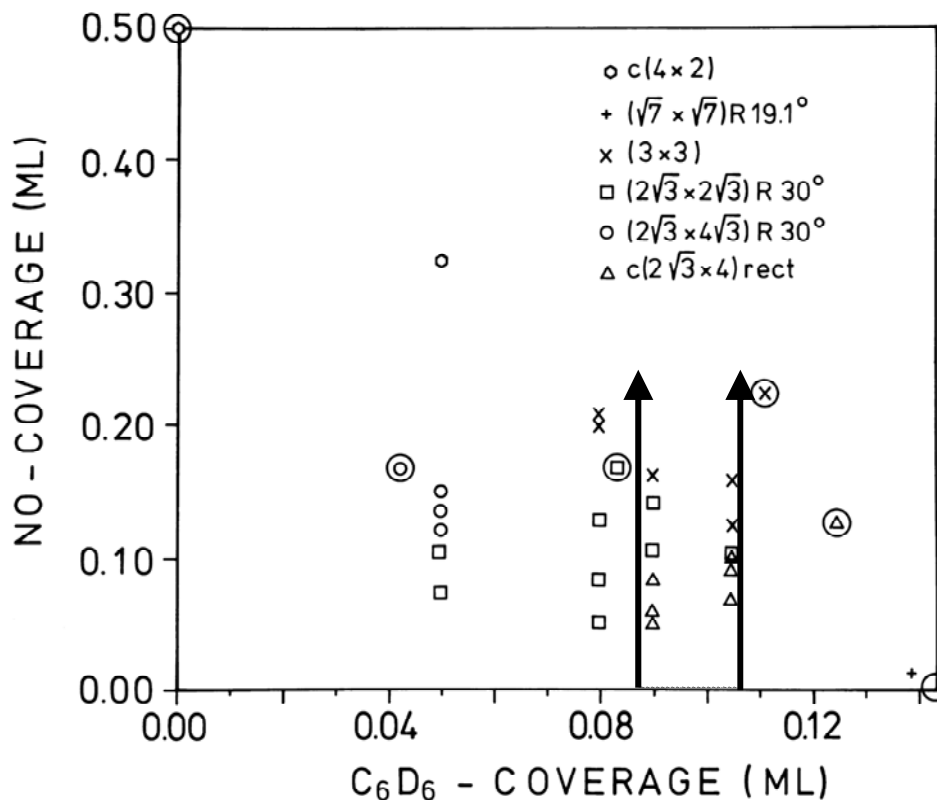


Fig. 4.17: Overview of the benzene and NO coverages where the various ordered structures were observed. The encircled symbols indicate the ideal benzene and NO coverages of the homogeneous mixed layers (taken from [81]). The additionally added grayish area and the arrows indicate the region where our experiments took place.

A close look at the quantitative analysis of the XPS data, especially at the ratio of the two carbon components C1 and C2 of the benzene molecules, used in chapter 4.1 for structure determination, indeed shows a behaviour which can be explained with the data in Fig. 4.17. In the adsorption experiment at first a ratio of 0.5, corresponding to bridge adsorbed benzene, is found, see chapter 4.1. Upon adsorption the ratio is not changing, which shows, that this bridge adsorbed benzene seems to correspond to the $(2\sqrt{3} \times 4)$ rect superstructure observed in LEED experiments, at low NO coverages.

At a NO exposures of 0.8 up to 1 L the ratio is rising and a site change of benzene to a hcp hollow sites takes place. Here benzene is oriented with its C-C axis parallel to the $[\bar{2}11]$ direction of the substrate. This effect of the rising ratio happens in an intermediate NO range, which should exhibit, according to Fig. 4.17, a

$(2\sqrt{3}\times 2\sqrt{3})R30^\circ$ superstructure. The situation is similar to the case of benzene coadsorbed with CO in the $(2\sqrt{3}\times 2\sqrt{3})R30^\circ$ layer and the interpretation is in agreement with the ARUPS results of [80]. The finding of a benzene adsorbed on the hcp hollow site is in contradiction to the results of the PhD study of Bao et al. [82] who found benzene molecules adsorbed on bridge sites. This difference might be due to a poorly ordered layer, as the preparation of these mixed phases is known to be rather tricky.

When the coverage of NO is further raised a steep change in the ratio to small values can be observed. This small value can be understood in the terms of a hcp hollow adsorbed benzene with its C-C axis aligned along the $[\bar{1}10]$ direction of the substrate as in the $(\sqrt{7}\times\sqrt{7})R19.1^\circ$ layer of pure benzene, see chapter 4.1. This layer, at high NO coverages, showed the (3×3) superstructure. The steep change might also be explained using Fig. 4.17: the rising NO coverages at a benzene coverage of 0.105 ML shows, that the transition from one ordered structure to the another is very sharp and the values for the coverages can be quite far from the nominal value still exhibiting the desired LEED pattern.

This leads to the conclusion, that XPS can observe conformational changes, also in this mixed layer system, but as we are far from the ideal coverages, we might find minority species, which are not ordered or are still ordered in a different manner, like e.g. islands of a $(2\sqrt{3}\times 2\sqrt{3})R30^\circ$ ordered structure in a (3×3) layer. These non-ideal coverages are not observed in LEED, as in contrast to XPS, only the ordered parts contribute to the spectra.

In summary, the benzene coverage of the coadsorption layer is very critical. A higher benzene coverage would not allow the formation of the $(2\sqrt{3}\times 2\sqrt{3})R30^\circ$ ordered structure leading to only two, potentially, ordered structures during adsorption, see Fig. 4.17. This can be seen in a quantitative analysis of a coadsorption experiment with a higher benzene coverage that does not exhibit the maximum in the C1/C2 ratio at 1 L of NO, but only leads to the low ratio at high NO coverages. More experiments are necessary to obtain all possible coverage dependent reorientations of benzene on the surface, but for our cases a good agreement with already published data was achieved and the structural changes were extractable.

4.3 Binding energy shifts in the XP spectra

Finally, we want to discuss the observed continuous coverage-dependent shifts in the C 1s binding energies during our adsorption and TPXPS experiments. For both C_6H_6 (Fig. 4.2) and C_6D_6 we observe a total shift of all C 1s components of 200 meV to higher binding energies during an uptake experiment from 0 to 0.143 ML. When annealing the benzene layers to 320 K, this shift is reversed according to the reduced coverage. The shift is continuous with coverage and does not reflect the site change taking place. It is, therefore, no indicator of the adsorption geometry, but rather for the lateral interactions between the molecules.

Further insight into this problem is given by the coadsorption experiments with CO and NO (chapter 4.2) where strong binding energy shifts to lower values are observed. These shifts are also continuous with rising coverage of the coadsorbate. Since different benzene adsorption sites have been proposed for both coadsorbate systems, again no clear correlation to the benzene adsorption geometry and the binding energy position is found. However, one nicely observes that adsorption of benzene with molecules inducing a positive surface dipole, as benzene itself, causes a shift to higher binding energies, while adsorption with molecules inducing a negative surface dipole, as CO and NO, leads to a shift to lower energies.

In the mentioned cases on Ni(111), the binding energy shift seems to be predictable. The adsorption of only negative surface dipoles (e.g., CO on Ni(111) data not shown) leads to a binding energy shift to higher binding energies, the same happens, when only positive surface dipoles (e.g., benzene on Ni(111) are adsorbed. On the other hand if we coadsorb benzene, a positive surface dipole, and CO or NO, negative surface dipoles, the benzene signal shifts to lower binding energies. If we turn around the adsorption sequence and start with CO we also find a decreasing binding energy, this time for the CO C 1s signal. This is summarized in Table 1.

Table 4.1: Binding energy shifts in C 1s XP spectra on Ni(111).

	pos. surf. Dipole	neg. surf. Dipole
pos. surf. dipole	pos. BE shift	neg. BE shift
neg. surf. dipole	neg. BE shift	pos. BE shift

On the Ni(111) surface, interestingly, this binding energy shift also goes along with the predicted lateral interactions of the “coadsorbed” molecules. Upon adsorption of

benzene, the “coadsorption” of benzene with benzene, a positive binding energy shift is observed in the C 1s spectra. Note that benzene is known to show repulsive interactions with itself, therefore not leading to island formation [62]. The same is true for the adsorption of CO [77], which also shows this binding energy shift to higher values. On the other hand the coadsorption of molecules that show an attractive interaction, like the electronegative molecules NO and CO respectively, with the preadsorbed benzene molecules, or vice versa if CO is preadsorbed and benzene is adsorbed as second component, the binding energy shifts to lower values. A similar behavior was also found by Fuhrmann [38] for the adsorption of different other hydrocarbons as, e.g., methane and acetylene on the Ni(111) surface.

Unfortunately this is not true on all surfaces. The adsorption of methane on platinum surfaces also leads to a binding energy shift to higher values, see chapter 7 and [68], but in the adsorption of CO [71] no significant shift of the binding energy was observed. Therefore the above shown table seems to be true for the adsorption of hydrocarbons and small molecules on the Ni(111) surface and is not transferable to adsorption scenarios on other single crystal surfaces.

4.4 Summary

The adsorption behavior of pure and mixed deuterated benzene and non-deuterated benzene layers on Ni(111) was studied in-situ with continuous and highly-resolved XPS. In particular, the adsorption of benzene layers at 200 and 125 K as well as their thermal evolution were investigated. Additionally the coadsorption layers of benzene with CO and NO were studied. In the case of the pure layers we were able, by considering vibrational splitting in the C 1s spectra of C_6D_6 and C_6H_6 , to identify the adsorption sites in the disordered and ordered layers, as a function of coverage by means of a quantitative analysis. This is possible, because the carbon atoms within the benzene molecules have a C 1s binding energy, which depends on the local neighborhood of the atom: Two components, C1 and C2, with a difference of about 250 meV are assigned to carbon atoms (C1) that are attached to one Ni atom each or to carbon atoms (C2) that are attached pair wise to one Ni atom. From the ratio of the number of C1- to C2-atoms the adsorption site can be determined based on

previous structural studies with a value of 0.5 for the bridge adsorption site and 0 for the hollow adsorption site.

For benzene adsorption at 200 K an identical behavior is found for both C_6H_6 and C_6D_6 , with adsorption at bridge sites up to a coverage of 0.10 ML, followed by a site change to hcp hollow sites for higher coverages. For the saturated layers that show a $(\sqrt{7} \times \sqrt{7})R19.1^\circ$ LEED pattern, exclusively hcp hollow sites are populated. The adsorption process is fully reversible up to temperatures of 320 K, the onset of benzene dissociation.

When benzene is adsorbed at 125 K, an interesting isotope effect is found. It manifests itself in the lack of the site change for C_6H_6 , which remains adsorbed on bridge site even at monolayer saturation coverage. Only upon heating to temperatures above 180 K the adsorption site for C_6H_6 also changes to hollow, resulting again in the $(\sqrt{7} \times \sqrt{7})R19.1^\circ$ superstructure at 220 K. In contrast, C_6D_6 behaves very similar to the adsorption at 200 K, performing the site change during uptake at a total coverage of around 0.1 ML. We have proposed a simple explanation for the origin of the observed isotope effect, assuming different activation energies for the adsorption site change due to different positional uncertainties of the H and D atoms perpendicular to the surface. A detailed understanding of the observed effect requires, however, a theoretical description including the proper adsorbate interactions and zero-point energy arguments.

In the case of the coadsorption experiments we were able to extract the adsorption sites for the coadsorption experiments. The results were obtained by using the considerations of the adsorption of pure benzene layers.

For the coadsorption with CO we find a hollow adsorbed benzene with its C-C axis oriented along the $[\bar{2}11]$ direction, which agrees nicely with measurements known from literature, showing the applicability of HRXPS also in coadsorption systems. For the coadsorption of NO with benzene, we were able to correlate the adsorption site changes with the known LEED patterns and the corresponding ARUPS measurements reported by Zebisch et al. [81].

All measurements are summarized in Fig. 4.18: It shows the ratio of the two carbon components in dependence on the relative saturation coverage.

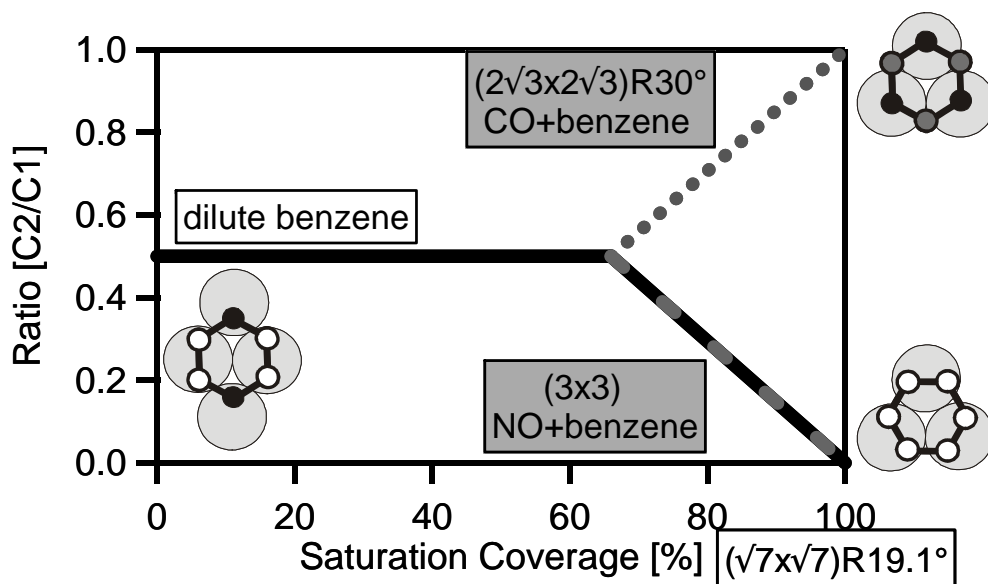


Fig. 4.18: Adsorption sites for the different adsorption scenarios examined in this work.

Certainly the results can also be used as a fingerprint for further investigations. An example is the reaction of cyclohexene on a Ni(111) surface, which will be the subject of the following chapter.

5 Adsorption and reaction of cyclohexene

In the previous chapters the coverage dependent site selectivity of benzene adsorbed on a nickel single crystal was discussed. Now we want to discuss the dehydrogenation of cyclohexene, a partly saturated cyclic hydrocarbon, to its unsaturated analogue benzene. This allows us to learn about the heterogeneous catalyzed (de-)hydrogenation of cyclic compounds on nickel surfaces and compare our data with theoretical and experimental work published lately. Important questions of catalysis, like the reactivity and selectivity of different adsorption sites and possible poisoning effects in this reaction will be discussed. Additionally, we are able to learn about comparability of gas phase data to data of adsorbed hydrocarbons.

Unfortunately, the reaction of the completely saturated molecule cyclohexane is not possible under UHV conditions, as only molecular adsorption and desorption is occurring upon annealing [83]. The group of Zaera [84] tried to avoid this by using halogenated hydrocarbons, especially iodo compounds, which readily dissociate on the surface at low temperatures. This leads to a chemisorbed species which further dehydrogenates on the surface, but the additionally adsorbed halogens may lead to differences in the reaction mechanism and in the reactivity. Certainly also coverage dependent effects, like, e.g., “poisoning” with hydrogen, can not be taken into account as the surface is already blocked with the large iodine atoms.

A better way to study this dehydrogenation reaction is to use cyclohexene that is chemisorbed on the surface. This ignores the first step in the catalytic dehydrogenation reaction, see Fig. 5.1, but allows a contamination free examination of this system. Additionally, cyclohexene is an interesting system, as it allows us to study a hydrocarbon ring system with differently hybridized carbon atoms. Cyclohexene has 4 sp^3 hybridized carbon atoms and two which are sp^2 hybridized, thus, allowing us to simultaneously study both types.

In this chapter we want to present the reaction and adsorption behavior of cyclohexene on a Ni(111) surface. Our examination covers the influence of coverage and temperature on the reaction and on the adsorption of cyclohexene. The experiments cover the adsorption of cyclohexene at 125 and at 200 K as well as the thermal evolution of these layers.

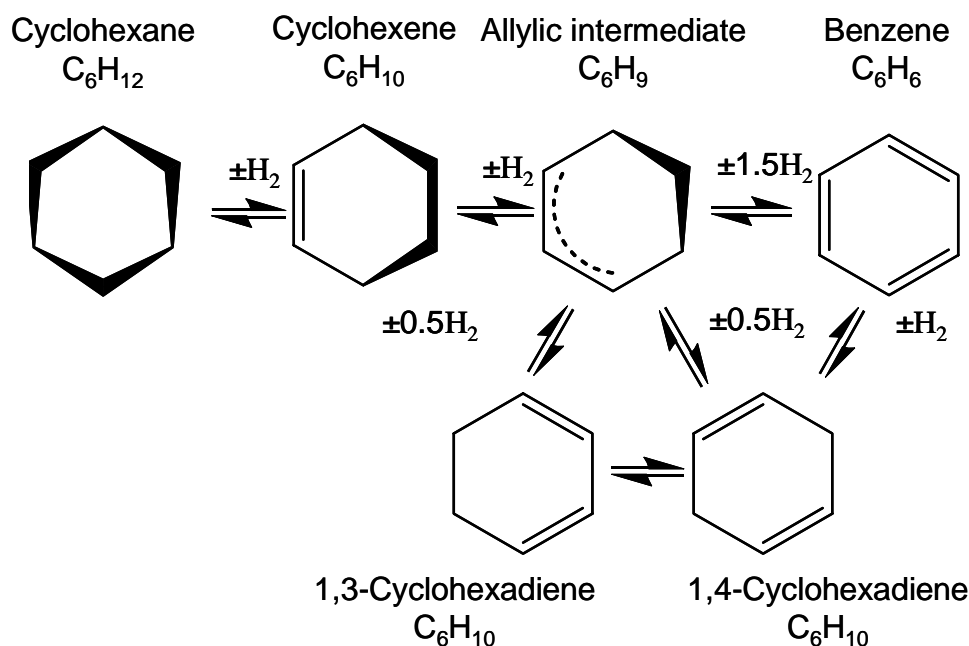


Fig. 5.1: Schematic drawing of the (de-)hydrogenation of cyclohexane to benzene. Depicted are possible reaction intermediates. The paper plane corresponds to the nickel surface.

5.1 Introduction

The adsorption of cyclic hydrocarbons and their reaction on transition metal surfaces is an intensively studied field, see e.g. Refs. [47, 85-91]. The importance of these systems results from the application of the heterogeneously catalyzed dehydrogenation of hydrocarbons over, e.g., platinum and nickel. These dehydrogenation reactions are studied in the laboratory and are used in high-throughput industrial applications, like the nickel based petroleum reforming process [61].

On the Ni(111) surface, the reaction of cyclohexane (C_6H_{12}), which would be the mostly favored reactant for this catalytic dehydrogenation, to benzene (C_6H_6) does not occur under ultra high vacuum (UHV) conditions. This was shown by Huber et al. [83], who studied the adsorption and desorption kinetics as well as the ordering of cyclohexane. Below 200 K, this saturated hydrocarbon displays long range order and from temperature-programmed desorption (TPD) experiments it was concluded that cyclohexane is desorbing molecularly without dehydrogenation.

To investigate the group of six membered cyclic hydrocarbons, we therefore focus on direct adsorption of cyclohexene (C_6H_{10}), the partly unsaturated analogue, which is proposed as a reaction intermediate in the dehydrogenation of cyclohexane in Ref. [84]. Their approach to access this important system is the use of iodo- and bromo- substituted cyclic hydrocarbons [84], which readily dissociate on the Ni(100) surface, leading to other possible reaction intermediates, like a cyclohexyl (C_6H_{11}) species. However, in this approach undesired coadsorption effects with the adsorbed halides can play a major role; it is, therefore, not chosen here.

The adsorption and/or reaction of cyclohexene on transition metal surfaces was already studied by different surface science approaches including a theoretical treatment. By density functional theory (DFT) calculations the hydrogenation reaction of benzene to cyclohexene on Pt(111) and Pd(111) was studied by Morin et al. [92]. For Pd(111) they propose that the first step in the hydrogenation is rate limiting and thus no reaction intermediates are expected to be accessible by experiments on that surface. On Pt(111), the rate limiting step is found in later in the reaction leading to stable intermediates, like the allylic C_6H_9 . Indeed, this species was found by vibrational spectroscopy on Pt(111) [86, 93-95]. Mittendorfer et al. [96], who studied the hydrogenation of benzene on Ni(111), identify the first step (to the intermediate 1,3-cyclohexadiene (C_6H_8)) as the rate limiting step, as found on Pd(111). Consequently, no other product than benzene should be stable on the surface and no other reaction intermediate should be observed on both surfaces, as was pointed out by Morin et al. [92]. Lately, the adsorption and reaction of cyclohexene on Ni(111) was subject of a combined high resolution electron energy loss spectroscopy (HREELS) and TPD study [97], mainly concerned with bimetallic surfaces of Pt on Ni(111) and vice versa [87]. The authors describe the selectivity and the activity of the reaction of cyclohexene to benzene by using the vibrational properties of the relevant species, benzene and cyclohexene. For Ni(111), without an additional layer of platinum, they claim to have found a direct conversion of cyclohexene to benzene at 100 K by HREELS.

Oltedal et al. [3] performed an extensive gas phase high-resolution XPS study on the cyclic six-membered hydrocarbons benzene, 1,3-cyclohexadiene, 1,4-cyclohexadiene, cyclohexene and cyclohexane. Their analysis of the spectra is supported by DFT calculations yielding the assignment of the C 1s peaks. For cyclohexene they find a main peak at a binding energy of 290.3 eV that is assigned

to the saturated (sp^3 hybridized) carbon atoms in cyclohexene and a second peak shifted by 400 meV to lower binding energy, related to the unsaturated (sp^2 hybridized) carbon atoms. In order to illustrate this assignment, a schematic sketch of the molecule on a surface is shown in Fig. 5.2 (a). Interestingly, for benzene with only unsaturated carbon atoms a similar binding energy value is found as for the sp^3 hybridized carbon atoms of cyclohexene. We propose that final state effects, as discussed in chapter 2.1.2, explain this behavior.

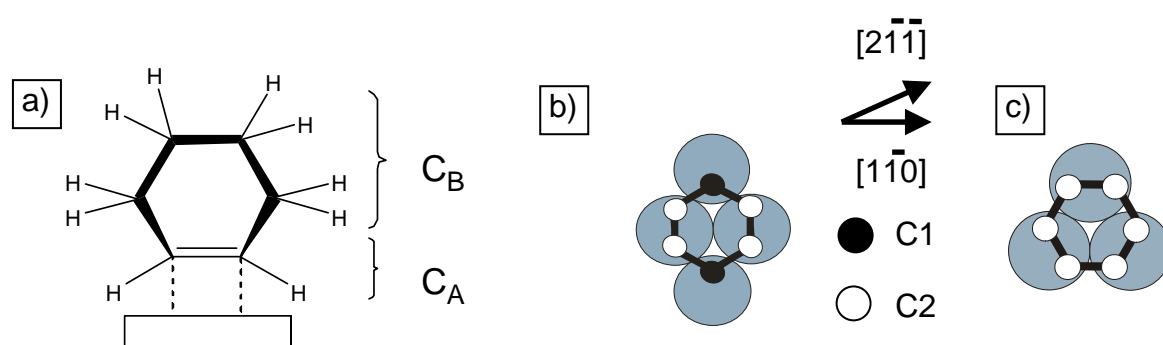


Fig. 5.2: a) Schematic drawing of cyclohexene on a Ni(111) surface. C_A (C_2H_2 -part) and C_B (C_4H_8 -part) indicate non-equivalent carbon atoms, due to different hybridization already in the free molecule. b) Benzene adsorbed at a bridge site, with the C-C axis along the $[2\bar{1}\bar{1}]$ direction. c) Benzene adsorbed at hollow site with the C-C axis along the $[1\bar{1}0]$ direction. C1 and C2 indicate carbon atoms with different local geometry.

In this chapter adsorption experiments of cyclohexene on Ni(111) at different surface temperatures, monitored by in-situ high-resolution XPS, are presented. Additionally, we will present temperature programmed XPS data: In these experiments a linear heating ramp is applied to the adsorbate system while XP spectra are recorded continuously, leading to a detailed picture of the surface species during reaction. TPD measurements, which show the desorbing reaction products, will also be discussed. (For a discussion of these techniques, see chapter 2.)

5.2 Adsorption

5.2.1 Adsorption experiments at 125 K

At first we want to discuss the molecular adsorption of cyclohexene at 125 K, which allows a comparison to the gas phase XPS measurements. Selected C 1s spectra of an adsorption experiment are shown in Fig. 5.3 (a).

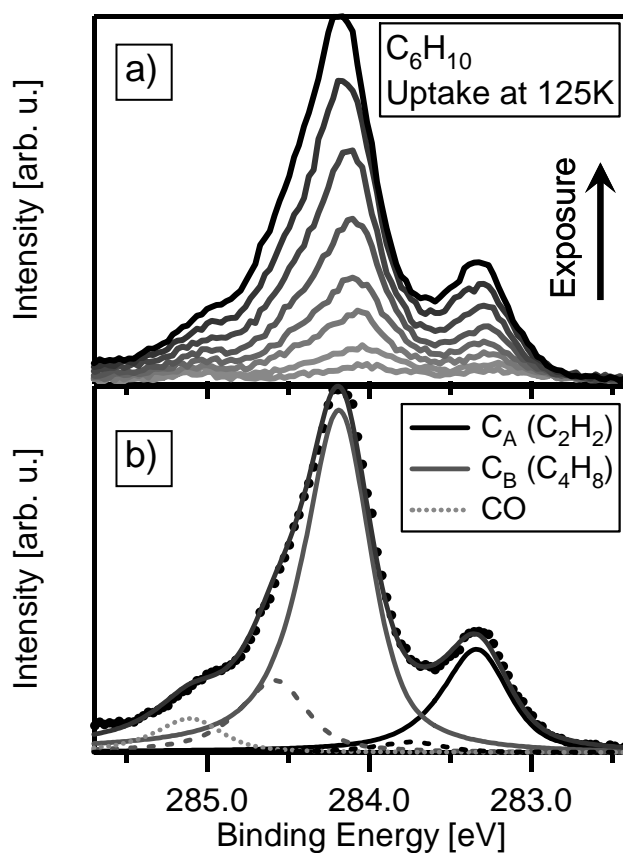


Fig. 5.3: a) Selected C 1s spectra collected during exposure of cyclohexene onto Ni(111) at 125 K. The grey scale (from light to dark) indicates the rise in coverage. The spectra were recorded at 5° off normal emission, at a photon energy of 380 eV. The maximum exposure was ~ 2.4 L at a pressure of $\sim 2 \times 10^{-9}$ mbar. b) Decomposition of the uppermost C 1s spectrum of the adsorption experiment of a); the solid lines indicate two nonequivalent carbon atoms (C_A and C_B) in cyclohexene; the dashed lines, which are shifted to higher binding energies by 400 meV, indicate the corresponding peaks due to vibrational excitation of the final state.

In the uppermost spectrum three clearly distinguishable peaks at 283.3, 284.2 and 285.2 eV are found. With increasing exposure a shift to higher binding energies is observed for the peaks at 283.3 and 284.2 eV, which are assigned to molecular cyclohexene. The third peak at 285.2 eV is attributed to the unintended coadsorption of CO in small quantities; this assignment is based on the binding energy and the desorption temperature [79], obtained from TPXPS experiments.

In order to perform a quantitative analysis, additional information was used. From our recent study of benzene on Ni(111) [47] we know that the adiabatic transition for a particular carbon atom is accompanied by a second peak at higher binding energy, separated by ~ 400 meV, due to an excitation of the C-H vibration in the photoemission process; the intensity ratio of the vibrationally excited and the adiabatic peak is called S factor [25, 26] and amounts to 0.1 for benzene, with one H atom per C atom. This value is somewhat smaller than the value of 0.17 observed for smaller hydrocarbons [21], most likely due to unresolved other vibrational excitations in the adiabatic peak of benzene.

In analogy to the case of benzene [47], the two main peaks in the spectra for cyclohexene are fitted by two adiabatic peaks and their two corresponding vibrationally excited peaks, after also testing different other scenarios. We are using an asymmetric Pseudo-Voigt function (see chapter 2.1.4) for each component. The asymmetry in the line profiles is due to unresolved vibrational excitations, e.g., C-C or ring deformation vibrations with a low energy, and electron hole pair formation at the Fermi level. Throughout this chapter, parameters like peak width and asymmetry are determined from prototypical spectra and are kept constant throughout the data sets. A small CO contamination is included at 285.2 eV. The resulting fit of the uppermost C 1s spectrum is shown in Fig. 5.3 (b). For the larger peak at 284.2 eV we found an S factor of 0.2 with a binding energy difference of 400 meV, which were then fixed in the final analysis of the spectra. The value for the S factor corresponds to a carbon atom with two attached H atoms (sp^3 hybridized), as the S factor scales with the number of H atoms [26, 47] (Note that we are comparing our results to benzene discussed in chapter 4). In Fig. 5.2 (a), which shows a schematic drawing of the molecular geometry, these carbon atoms are denoted C_B . Accordingly, the S factor of the second species was set to be 0.1, as in the case of benzene, i.e., carbon atoms with only one H atom attached (sp^2 hybridized), denoted as C_A in Fig. 5.2 (a). In addition, the binding energy difference is fixed at 400 meV. This procedure results in

a satisfying fit of the C 1s spectrum shown in Fig. 5.3 (b) and also for the spectra at lower coverages.

Interestingly, the binding energy difference of ~ 0.9 eV for the two C 1s peaks is significantly larger than the value of ~ 0.35 eV found in gas phase [3]. This reflects the strong influence of the molecule-surface bond on the binding energy. For the observed binding energies we find the same correlation between the hybridization of the carbon atoms and their appearance in the XP spectra as for the gas phase: For cyclohexene on Ni(111), the sp^2 hybridized carbon atoms (C_A) have a binding energy of 283.3 eV and the sp^3 hybridized carbon atoms (C_B) of 284.2 eV. The latter value is very similar to the C 1s binding energy of benzene at 284.1 eV [47], which, however, consists only of sp^2 hybridized carbon atoms in a ring system. Again, final state effects are proposed to be responsible.

The binding energy difference between the two chemically shifted adiabatic peaks of cyclohexene changes with increasing exposure, from 0.78 to 0.86 eV. This indicates that the adsorbate-adsorbate interactions change differently for the sp^2 hybridized carbon atoms that are considered to be responsible for the bonding to the surface and for C_B carbon atoms in the C_4H_8 part of the molecule that is not directly involved in the surface-molecule bonding, see Fig. 5.2 (a). With increasing exposure this might lead to a change in the bending or orientation of the molecule, which in turn could also lead to a change in the local diffraction environment. DFT calculations for Pt(111) and Pd(111) show cyclohexene bound to the surface via the two C_A carbon atoms [92]. This geometry is also consistent with the observation that the C 1s peak assigned to the C_4H_8 (C_B) part of cyclohexene shows no broadening, which would be indicative of an interaction of this part of the molecule, thus, leading to inequivalent C_B atoms, with the surface.

Performing the above described fitting procedure for the whole series of C 1s spectra of this adsorption experiment leads to the graph in Fig. 5.4, displaying the coverage vs. exposure curves. The coverage scale in Fig. 5.4 is obtained by the comparison with benzene adsorption experiments, and refers to C_6 units. Benzene saturates at 200 K on Ni(111) exhibiting a $(\sqrt{7} \times \sqrt{7})R19.1^\circ$ superstructure with a coverage of 0.143 ML, as determined by LEED and TPD experiments [98]. A coverage of 0.1 ML of C_6 molecules would correspond therefore to 0.6 carbon atoms per Ni atom. The assignment as C_B (C_4H_8) and C_A (C_2H_2), corresponding to the sp^3 and sp^2 hybridized parts of C_6H_{10} , respectively (see Fig. 5.2 (a)), should not be

misinterpreted as molecules, but only as partial coverages corresponding to C atoms in different hybridization states. Possible errors in the total and in the partial coverages can be as high as 20%, as different diffraction conditions due to the different local environments are present [72].

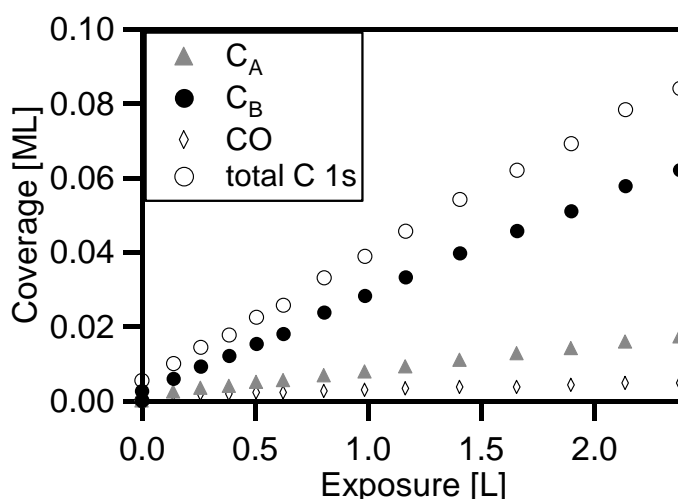


Fig. 5.4: Quantitative analysis of the uptake experiment shown in Fig. 5.2 a). The different carbon species C_A and C_B include their corresponding vibrationally split signals. A contaminant CO contribution is also displayed. The coverages are shown in C_6 units (see text).

The intensity ratio of 0.3 – 0.4 (slightly changing with coverage, see below) of C_A to C_B is lower than the expected value of 0.5 (see Fig. 5.2 (a)). This can be explained by different local environments and the related different diffraction conditions for the respective photoelectrons; furthermore, damping effects for the C_A atoms in direct contact with the substrate may also play a role. The ratio decreases in the low coverage regime (from ~ 0.4 to ~ 0.3 at 0.6 L) and thereafter remains constant. This moderate decrease is consistent with the existence of only one type of adsorbed molecules, if we attribute the change in the low coverage regime to changing adsorbate-adsorbate interactions on the surface, inducing a different local environment (bonding geometry) that influences the photoelectron diffraction. Another aspect, which can not be totally ruled out, is the partial decomposition of cyclohexene to benzene. This would also result in a changed intensity ratio of the peaks assigned to the two carbon species, but as benzene is expected to contribute only to the peak

at 284.2 eV the ratio should rise with coverage and it could not explain the constant ratio above 0.6 L.

5.2.2 Adsorption at elevated temperatures

To investigate the temperature dependency of the adsorption of cyclohexene we performed adsorption experiments at 185 and 210 K. Adsorption at 185 K yields the same results as adsorption at 210 K and will, therefore, not be discussed separately. We wanted to address possible intermediates and the evolution of the system under isothermal conditions (in contrast to the situation in TPXPS experiments, see chapter 5.3.2).

Selected C 1s spectra measured during exposing the Ni(111) crystal to cyclohexene at 210 K are shown in Fig. 5.5 (a). At saturation a main peak at 284.1 eV is observed, which exhibits a shoulder at 284.5 eV; also some CO is found, contributing to the C 1s signal at a binding energy of ~ 285.1 eV. No obvious shift of the main peak occurs during the adsorption experiment, but at lower coverage a shoulder on the low binding energy side is present at 283.7 eV. The fit of this data is shown in Fig. 5.5 (b) and (c) for two selected coverages (for coverage calibration see previous chapter). Again, two adiabatic peaks with their corresponding vibrational fine structure have been used. When fitting the spectrum of the saturated layer, we find parameters comparable to those observed for the saturated benzene layer on Ni(111) [47] (see chapter 4), differing only slightly due to a different background and a different resolution. The observed binding energy difference of 400 meV and the S factor of 0.1 are typical for benzene. This leads us to the conclusion that the observed peak and shoulder represent one carbon component (in benzene), denoted C2 in Fig. 5.2 (b), consisting of a contribution from the adiabatic transition and the transition to the first vibrationally excited final state. The only difference to the saturated layer of pure benzene is that the absolute binding energies are 200 meV lower in Fig. 5.5.

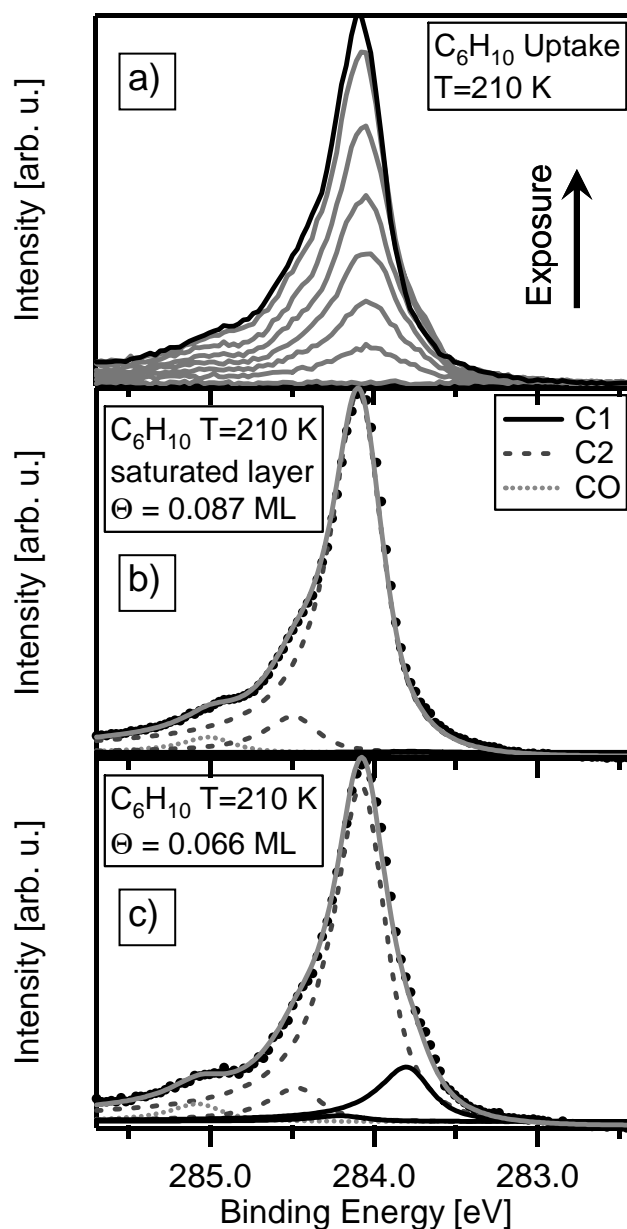


Fig. 5.5: a) Selected C 1s spectra collected during exposure of cyclohexene onto Ni(111) at 210 K and $\sim 2 \cdot 10^{-9}$ mbar; the layer saturated after an exposure of ~ 3.6 L. The spectra were recorded 5° off normal emission at a photon energy of 380 eV. b) Fit of the uppermost C 1s spectrum at saturation, shown in a). c) Fit of the C 1s spectrum of an intermediate coverage, also shown in a). The dashed and the solid lines indicate contributions from two nonequivalent carbon atoms (C1 and C2) in benzene and the corresponding peaks due to vibrational excitation of the final state, which are shifted to higher binding energies by 400 meV.

From the adsorption of pure benzene layers at 200 K we know, that at lower coverages an additional second carbon component (C1, see Fig. 5.2 (b)) is observed [47]. A similar shoulder at 283.7 eV is also found upon exposure of cyclohexene at 210 K, see Fig. 5.5 (a) and (c). In analogy to the analysis of the pure benzene layers, we fitted this component C1 by an adiabatic peak plus a vibrational peak, using the parameters of the carbon component C2.

The quantitative analyses of cyclohexene adsorbed at 210 K and also benzene adsorbed at 200 K are shown in Fig. 5.6, with the C 1s spectra fitted according to the procedure described above. The binding energy of the C2 component at 284.10 eV varies by ± 20 meV for different coverages, with the difference to the C1 component always being 260 ± 25 meV. In Fig. 5.6 (a), the coverages derived for the two carbon components C2 and C1, which result from cyclohexene exposure, are again given in C_6 units. The error bars for the partial coverages, obtained from the fitting procedure, are estimated to 0.002 ML. In Fig. 5.6 (b) the partial coverages assigned to the C1 and C2 components are displayed vs. total coverage and are compared to results for direct benzene adsorption for similar electron emission angles. The data for benzene have been rescaled by ~ 0.6 to fit the lower saturation coverage (~ 0.09 ML) achieved in the cyclohexene experiment. Overall, the resulting curves for both adsorption systems are similar, with some deviations at intermediate coverages.

For benzene, the ratio of the two carbon components C1 and C2 was used to determine the adsorption site of the molecule on the surface [47] (see chapter 4): At low coverage, benzene is adsorbed at bridge sites with its C-C axis oriented along the $[\bar{2}11]$ direction of the substrate (Fig. 5.2 (b)), whereas at saturation benzene is adsorbed on a hollow site with its C-C axis oriented along the $[\bar{1}10]$ direction (Fig. 5.2 (c)). This is correlated with a change in C1/C2 ratio from nominally 0.5 for bridge sites to 0 (i.e. only C2) for hollow sites.

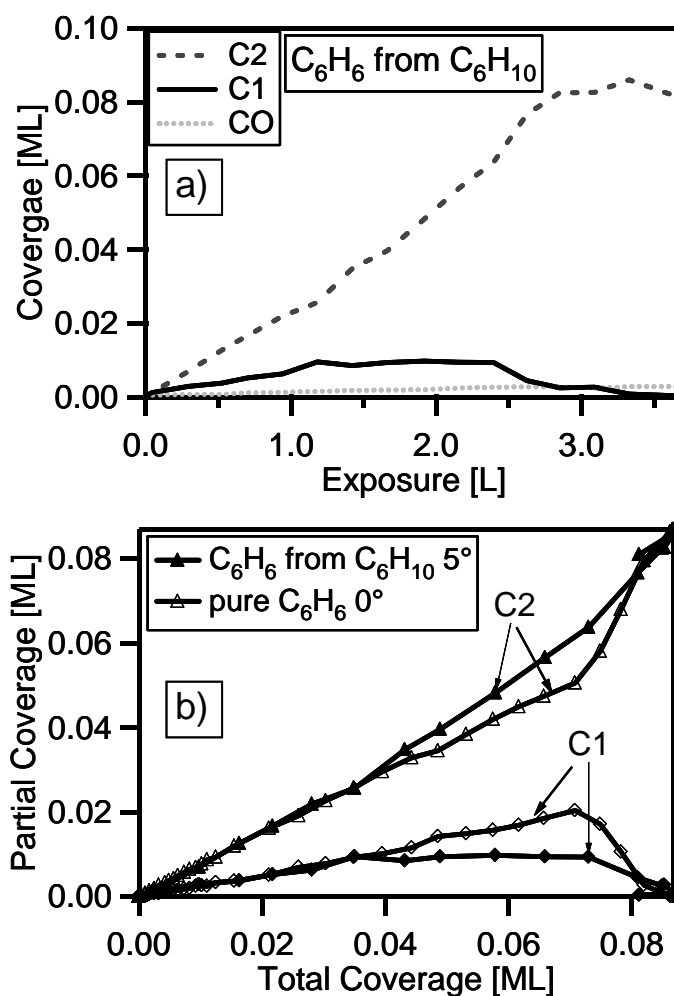


Fig. 5.6: a) Quantitative analysis of the experiment shown in Fig. 5.5; the different carbon species C1 and C2 include the corresponding vibrationally split signals. b) Partial coverages of components C1 and C2 from a) as a function of total coverage. For comparison, the data for pure benzene taken at a comparable emission angle are also shown; note that these data are normalized to their respective saturation coverage.

For pure benzene, at low coverages a value of 0.35 is found for the ratio C1/C2, if the experiments are performed at normal emission, i.e., at measuring geometries close to those of cyclohexene. The curves in Fig. 5.6 (b) and the corresponding C1/C2 ratio of ~ 0.35 resulting from cyclohexene exposure are similar up to a coverage of ~ 0.04 ML, and at saturation. At intermediate coverages some deviations are observed, which are most likely induced by coadsorbed hydrogen. Nevertheless, the overall

similarity is a strong indication that upon cyclohexene exposure at 210 K direct dehydrogenation takes place yielding benzene and hydrogen.

A difference between pure benzene layers and for cyclohexene adsorption at 210 K is the coverage-dependent binding energy shift of the C 1s signal. For pure benzene we find a binding energy shift of ~ 120 meV to higher binding energies when adsorbing 0.09 ML of benzene (200 meV for the saturation coverage of 0.143 ML), while in the case of cyclohexene we find only a shift of ~ 20 meV. The C 1s binding energy found for benzene, originating from the dehydrogenation of cyclohexene, shows the same value as for pure benzene adsorption at very low coverages [47]. The most likely explanation for the smaller binding energy shift is the coadsorption of H and possibly also CO. Principally, CO could induce a shift to lower binding energies, but its coverage is rather small (~ 0.02 ML).

There is a large amount of hydrogen produced from cyclohexene dehydrogenation (four hydrogen atoms per cyclohexene molecule). This hydrogen obviously limits the saturation coverage to 0.09 (0.087 ± 0.005) ML, as compared to 0.143 ML in case of pure benzene. The value of 0.09 ML corresponds to 63% of the value for pure benzene; on the other hand 0.09 ML cyclohexene yield 0.36 ML of atomic hydrogen, which represents 36% of a pure saturated hydrogen layer with a coverage of 1.0 ML [99]. Thus the fractions of benzene (63 %) and hydrogen (36 %) nicely make up ~ 100 % of a complete layer.

From these considerations we conclude that in the benzene + hydrogen layer we find bridge adsorbed benzene at low coverage and hollow adsorbed benzene at higher coverage, as for the pure benzene layer. The overall agreement after scaling to the saturation coverage of benzene suggests a phase separation between benzene and hydrogen, with the benzene islands behaving like a pure benzene layer. One possible explanation for the rather small binding energy shift in the XP spectra is that the extension of the islands is small as compared to pure benzene layers. This indicates an interaction of benzene from cyclohexene with the coadsorbates carbon monoxide and hydrogen.

5.3 Thermal evolution

5.3.1 TPXPS experiment of the layer adsorbed at 210 K

Cyclohexene adsorbed at 210 K yielded benzene and hydrogen as dehydrogenation products. The resulting saturated layer shows the typical characteristics of benzene adsorbed on a hollow site with the C-C axis oriented along the $[\bar{1}10]$ direction of the substrate, i.e., only C2 carbon atoms are present. According to the results known from the adsorption of pure benzene [47], a site change, back to the bridge site, should occur during thermal treatment of the layer as the adsorbate-adsorbate interactions should decrease upon partial benzene desorption. In Fig. 5.7 (a) selected spectra of such a TPXPS experiment for the benzene + hydrogen layer from cyclohexene exposure are shown.

We again find the peak position at 284.1 with its vibrational excited core hole state as a shoulder at 284.5 eV as well as the small contribution from CO at ~285.0 eV, i.e., the spectrum for 210 K in Fig. 5.7 (a) corresponds very well to the last spectrum of the series in Fig. 5.7 (a). Upon heating, benzene desorption occurs, as deduced from a decreasing intensity and the beginning formation of a weak shoulder on the low binding energy side.

The quantitative analysis of the above TPXPS experiment more clearly demonstrates these changes and is shown in Fig. 5.7 (b). It is performed in the same manner as the analysis for the adsorption experiment, including line shapes, intensity ratios and binding energy differences; the estimated fitting error is again ± 0.002 ML.

Initially, there is only one carbon component C2. At ~250 K the second carbon component C1 is evolving as shoulder at the low binding energy side of the main peak at 284.1 eV. The overall behavior is similar to the TPXPS experiment of a pure benzene layer adsorbed at 200 K, which is also shown in Fig. 5.7 (b), again normalized to the same saturation coverage. While for the pure benzene layer a sharper transition is observed taking place between 260-280 K, for the benzene + H layer changes already start at ~230 K. This difference is attributed to the coadsorption of hydrogen, which is still present on the surface, see below.

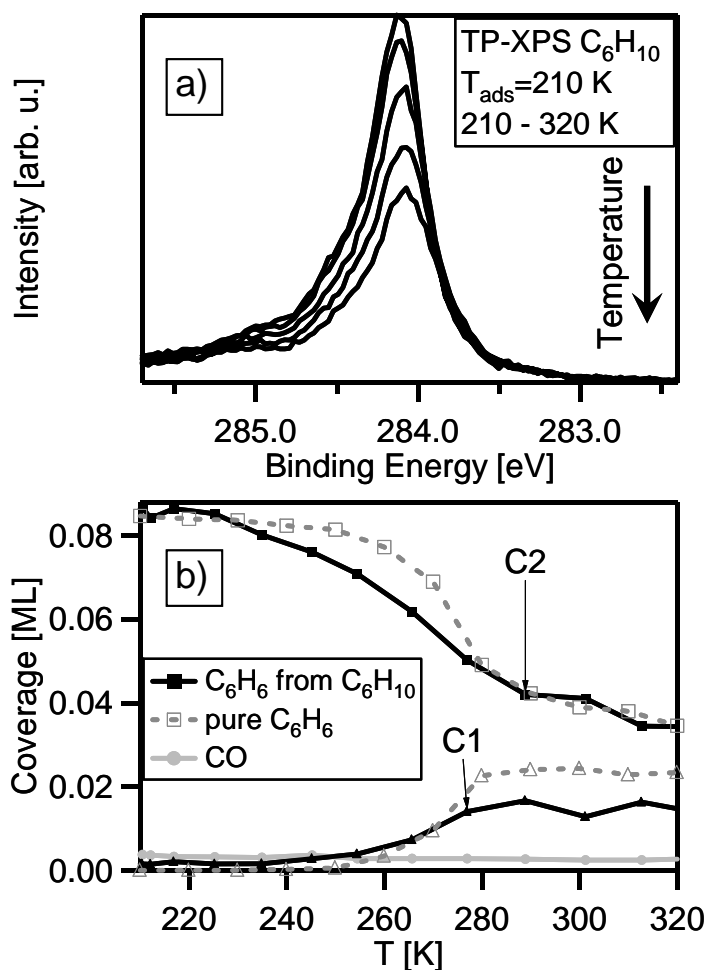


Fig. 5.7: a) Selected C 1s spectra of the TPXPS experiment of the benzene + H layer formed upon cyclohexene exposure at 210 K, collected at temperatures of 210, 235, 265, 290, 320 K, respectively (from top to bottom). The spectra were recorded 5° off normal emission at a photon energy of 380 eV, and at a heating rate, β of ~ 0.2 K/s. b) Partial coverages of components C1 and C2 from a) as a function of temperature. The light grey symbols and lines indicate the results from a similar experiment of a pure benzene layer. Coverages are again rescaled for easier comparison, as in Fig. 5.6.

One small difference between the TPXPS experiments for pure benzene and for the cyclohexene-derived layers adsorbed at 210 K is the heating rate, ~ 0.5 vs. 0.2 K/s, which induces a shift of the desorption temperatures to lower values by ~ 7 K for lower heating rates, as estimated using the Redhead equation [100]. This small shift cannot explain the observed differences, which are thus again attributed to the coadsorbed hydrogen. This result is also consistent with the TPD spectra in Fig. 5.8

(see below), which also show benzene desorption already at lower temperatures, with the rate maximum at 250 K as compared to 290 K for pure benzene [98].

Summarizing the results obtained for exposure of Ni(111) to cyclohexene at 210 K, we find that cyclohexene directly dehydrogenates to benzene and hydrogen. This benzene shows the typical coverage dependent reorientation from $[\bar{2}11]$ bridge sites to $[\bar{1}10]$ hollow sites during adsorption and vice versa for desorption, also known from the pure benzene layers, which confirms our assignment.

5.3.2 Temperature programmed desorption data

The TPD spectra in Fig. 5.8 have been measured after dosing cyclohexene at 85 K with a heating rate of 2 K/s. Note that the intensities of the different species are not comparable as no pressure calibration for the respective species was performed.

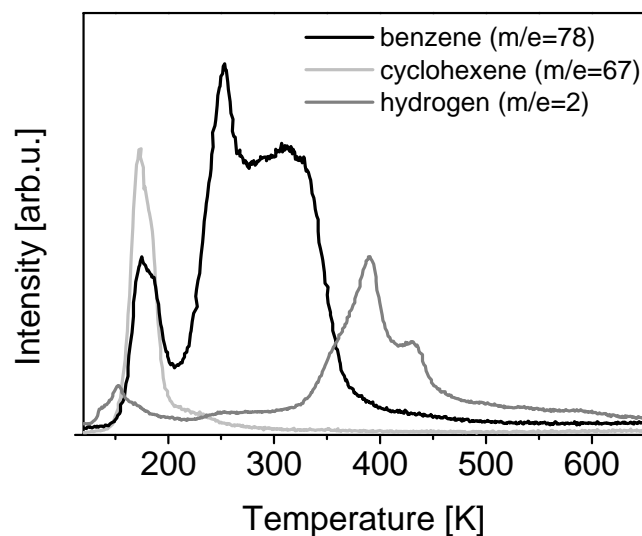


Fig. 5.8: TPD spectra for cyclohexene (main fragment), benzene and hydrogen collected after exposure of cyclohexene onto Ni(111) at 85 K ($\beta=2$ K/s).

The spectrum of cyclohexene (measured for the most intense fragment at $m/e=67$; light grey line) shows only one desorption peak at 170 K, which is attributed to desorption of adsorbed multilayers, with a small possible contribution from the monolayer (see discussion below). In the benzene signal ($m/e=78$), a corresponding

peak is observed at the same temperature, but it is due to the cracking pattern of cyclohexene. The peak at 250 K and its shoulder at 310 K are assigned to desorption of benzene formed by dehydrogenation of cyclohexene. The comparison to a TPD spectrum of a pure benzene layer [98] shows a strong shift of the whole spectrum to lower temperatures by 40-50 K. This indicates a lower binding energy of the adsorbed benzene when produced from cyclohexene, i.e., in the presence of significant amounts of coadsorbed hydrogen. The hydrogen desorption, shown in Fig. 5.8, starts at lower temperatures than for pure benzene [98]. The first maximum (not counting the small feature at 150 K, which is most likely due to desorption from the sample holder) at 390 K is in the range of the hydrogen desorption of the (2x2)-2H hydrogen superstructure on Ni(111) [99]. The second maximum at 430 K coincides with the hydrogen desorption maximum of a pure benzene layer, where it is correlated to the decomposition of benzene on the surface [98]. The maximum at 430 K, therefore, is due to the dehydrogenation of benzene, while the first desorption maximum at 390 K is most likely not related to a reaction on the surface.

5.3.3 TPXPS experiment of cyclohexene adsorbed at 125 K

Selected C 1s spectra of a TPXPS of a cyclohexene layer with a coverage of $\sim 0.082 \pm 0.005$ ML adsorbed at 125 K are shown in Fig. 5.9 (a). The top spectrum, recorded at 130 K, exhibits the spectral features already discussed in section 5.2.1: One main peak at 284.2 eV (C_B), a smaller one at 283.3 eV (C_A), and the small CO signal at ~ 285.0 eV. At ~ 180 K (fourth spectrum from top) the peak at 283.3 eV has decreased to a shoulder and is shifted by 250 meV to higher binding energies. This decrease is accompanied by the formation of a distinct shoulder on the high binding energy side of the main peak, at 284.5 eV. Between 180 and 270 K the intensity is almost constant and only a small shift of the peak at ~ 283.5 eV and the shoulder at 284.5 to lower binding energies by 100 meV is observed. Above 270 K, the main peak now at ~ 284.1 eV starts to decrease. This goes along with the decrease of the shoulder now at ~ 283.4 eV.

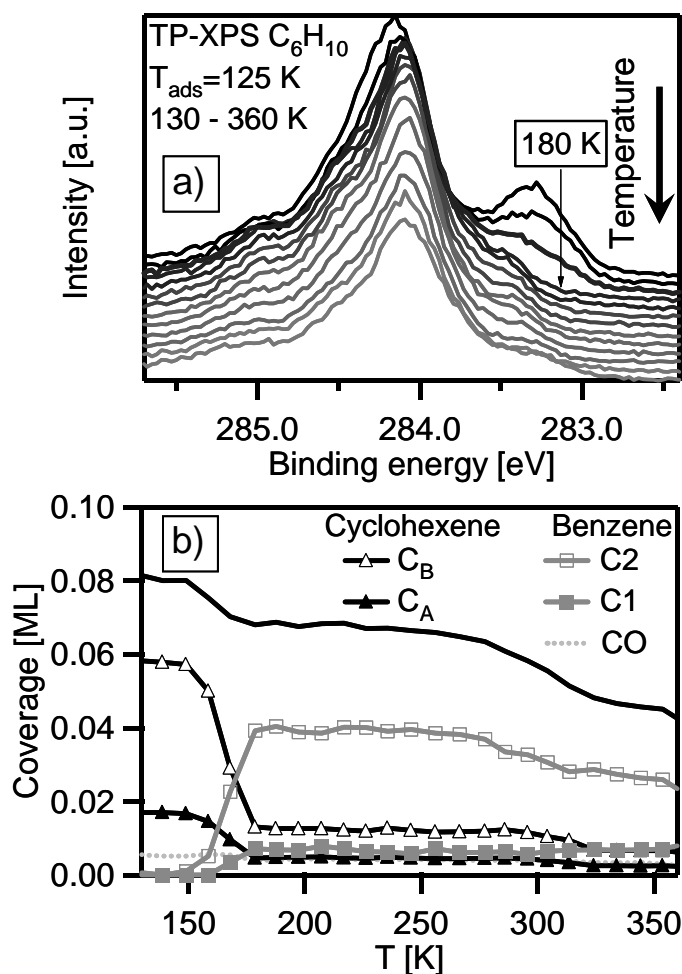


Fig. 5.9: a) Waterfall plot of selected C 1s spectra of a TPXPS experiment collected after cyclohexene exposure onto Ni(111) at 125 K. The spectra were measured 5° off normal emission, with a photon energy of 380 eV and a heating rate, β , of ~ 0.2 K/s. The uppermost spectrum was recorded at 130 K, while the lowest is recorded at 360 K. b) Quantitative analysis of the TPXPS experiment of a). The different carbon components of cyclohexene (C_A and C_B) and benzene ($C1$ and $C2$) are labeled with different symbols. The total coverage is given as solid black line, CO as dotted line.

A quantitative analysis of the surface species is given in Fig. 5.9 (b). As determined from the experiments described above, four contributions for carbon species C_A , C_B (for cyclohexene) and $C1$, $C2$ (for benzene resulting from dehydrogenation) have been included, all with their respective vibrational splitting and with their parameters fixed to the values determined in the previous chapters. At 130 K, we find the already described cyclohexene, consisting of the two different adiabatic contributions at 283.3 and 284.2 eV, due to C_A carbon atoms (C_2H_2 part) and C_B carbon atoms (C_4H_8

part), respectively. Upon annealing, above 160 K a strong decrease of the peaks assigned to both carbon atoms C_A and C_B is observed. Simultaneously, the C1 and C2 species of benzene at 283.85 and 284.10 eV are populated. Also, partial desorption of cyclohexene occurs, as deduced from the decrease in total peak area in Fig. 5.9 (b) and also from the TPD spectra in Fig. 5.8. Nevertheless, the decrease of the C_A and C_B signals at 160 K is predominantly due to the dehydrogenation of cyclohexene to benzene, with the dominating peak in the C 1s spectra at \sim 284.1 eV. These findings are consistent with the results of the DFT calculations, also showing that the product of cyclohexene dehydrogenation is benzene [92, 96].

The decrease of the signal of the C_A carbon atoms and its shift from 283.3 to 283.5 eV is accompanied by an intensity increase at 284.5 eV due to a shifted C_B component. We propose that both new features belong to one adsorbate with differently hybridized carbon atoms. This is supported by TPXPS experiments (data not shown) starting from different initial coverages: for higher initial coverage both features increase. Their binding energy difference has increased by 150 meV as compared to cyclohexene at 130 K. We propose to assign the two components again to cyclohexene, but now in a strong coadsorption situation with hydrogen and benzene, which changes continuously and leads to the observed shifts – therefore in Fig. 5.9 (b) one cyclohexene species (triangles) is shown over the whole temperature range. (Note that the observed shift could also be due to a decrease of the peak at 283.3 eV and an increase of a peak at 283.5 eV, which would, however, not alter our conclusions.)

In the fits we again find the two carbon components C1 and C2 of benzene. As seen from Fig. 5.9 (b) the major contribution at 284.1 eV (C2) takes over most of the intensity at this binding energy, which below 160 K was assigned to the C_B part of cyclohexene (at 284.2 eV). From the fits it is difficult to reliably determine the intensity ratio of the C1 and C2 components, due to the superimposed signals of the cyclohexene species between 160 and 310 K. Above 310 K, the cyclohexene signal vanishes and we only find bridge adsorbed benzene on the surface, with a similar C1/C2 ratio as in the case of a pure benzene layer.

Interestingly, the conversion of cyclohexene to benzene is not complete above 180 K, in contrast to the direct adsorption experiments at 185 and 210 K. Of the 0.082 ML of cyclohexene, only \sim 0.06 ML decompose upon heating to \sim 300 K. Obviously, when starting with a cyclohexene layer of \sim 0.08 ML adsorbed at 125 K,

after initial dehydrogenation of cyclohexene to benzene and hydrogen, the surface reaches a state where no further dissociation of cyclohexene can occur due to crowding and, therefore, part of the cyclohexene stays intact. For larger initial coverages (data not shown) the amount of intact cyclohexene increases. The hydrogen atoms remain on the surface, since we know from the TPD spectra in Fig. 5.8 that hydrogen only desorbs above 360 K. Obviously, this stabilized cyclohexene is only formed when heating a layer that was prepared at lower temperature. Most likely, cyclohexene, benzene and hydrogen are homogeneously distributed in this layer with a strongly reduced mobility of these adsorbed species. Otherwise one would expect that the phase separation into benzene and hydrogen islands should occur, which was proposed for direct adsorption at 185 and 210 K. Between 280 and 310 K partial desorption of benzene occurs, as is deduced from the decrease in the corresponding C 1s signal. Above 310 K, the cyclohexene coverage drops to the detection limit. This most likely indicates that as benzene desorption takes place the dehydrogenation reaction to benzene “restarts”, as there is space for the dehydrogenation products on the surface. An alternative route of a direct full dehydrogenation of cyclohexene to carbonaceous species can not be excluded, as the benzene coverage does not increase.

5.4 Summary and conclusions

We investigated the interaction of cyclohexene with a Ni(111) surface using *in-situ* high-resolution X-ray photoelectron spectroscopy at different temperatures and the thermal evolution of the corresponding layers by temperature-programmed X-ray photoelectron spectroscopy as well as temperature-programmed desorption.

For exposure at 125 K, cyclohexene is molecularly adsorbed and the C 1s spectra show two peaks, which both display vibrational fine structure, in good agreement with gas phase measurements. Distinct binding energy changes due to the interaction with the substrate are observed. For exposure at 185 and 210 K complete dehydrogenation to benzene is found. Interestingly, benzene, which is coadsorbed with hydrogen also formed in the dehydrogenation process, shows the same behavior as the pure layers of benzene adsorbed at 200 K: At low coverages, we find benzene adsorbed at bridge sites, and at higher coverages a change of the adsorption site from bridge to hollow occurs. The main difference to pure benzene

layers is that this transition is observed at a lower benzene coverage, which is attributed to the coadsorbed hydrogen: 0.09 ML benzene cover 63% of the surface and 0.36 ML H from the reaction cover 36%, summing up to ~100%, which is attributed to a phase separation into pure benzene and H islands upon exposure at 185 or 210 K. Upon heating, these layers show the coverage dependent site changes also found for pure benzene layers.

The cyclohexene layers adsorbed at 125 K show a more complex reaction behavior with only partial conversion of cyclohexene to benzene at 210 K. We propose that after initial dehydrogenation a stable coadsorption phase with a homogeneous distribution of benzene, hydrogen and cyclohexene is formed, covering the complete surface. In this layer the mobility of the adsorbed species is reduced such that no phase separation can occur, in contrast to direct exposure at 210 K. Above 300 K the dehydrogenation reaction is restarted consuming all cyclohexene yielding benzene and subsequently carbonaceous species on the surface.

From our in-situ study, significantly new insights in the temperature dependence of the dehydrogenation of cyclohexane on Ni(111) are obtained. They are in agreement with an earlier HREELS study [97] concerning the formation of benzene, and provide detailed information on the adsorption site of the formed benzene as well as differences in the thermal evolution after adsorption at different temperatures. The direct formation of benzene is also concluded for Ni(111) and Pd(111) from density functional theory calculation [92, 96], whereas for Pt(111) the formation of an allylic C₆H₉ species is proposed [86, 93-95].

The following chapter will again deal with cyclic hydrocarbons and their reactions, but this time heteroatoms incorporated in the ring will significantly change the adsorption and reaction properties.

6 Adsorption and reaction of heterocycles

This chapter covers the experiments of the interaction of the heterocycles furan and pyrrole with a Ni(111) surface. Our interest in heterocycles lies in the fact that they are basic building blocks found in, e.g., porphyrines, which again are part of bigger hydrocarbons like, e.g., hemoglobin or chlorophyll [101]. Additionally, they are of interest to petrochemistry [102] as our experiments give an insight to the process of the heteroatom removal from, e.g., petroleum. Five-membered heterocycles are also discussed as conducting polymers and have a number of possible applications in integrated circuits [103].

Furthermore, additional information on the behavior of aromatic molecules on surfaces can be obtained. In particular on the reactivity of the molecules and possible changes of their reaction behavior, due to the adsorption on a surface and due to the different heteroatoms can be studied.

Furan, depicted in Fig. 6.1 (a), is a five membered ring with four carbon atoms, which are sp^2 hybridized, and one oxygen atom. The π -system of the molecule has six electrons, thus, obeying Hückel's rule for aromatic molecules. From these six electrons in the π -system, four belong formally to the carbon atoms and the remaining two are contributed by one of the oxygen lone pairs.

The heterocycle pyrrole, see Fig. 6.1 (b), also is a five membered ring system, again with four sp^2 hybridized carbon atoms, but instead of the oxygen as heteroatom as in the case of furan, a protonated nitrogen atom is incorporated. Again, the π -system of the molecule has six electrons and is therefore aromatic, according to Hückel's rule. Four of the electrons formally belong to the carbon atoms and the remaining two are contributed by the nitrogen lone pair.

Due to the symmetry of the heterocycles, only two different types of carbon atoms have to be considered. The carbon atoms, which directly bond to the corresponding heteroatom, are labeled as C_α . The C_β carbon atoms have no heteroatom as neighbor.

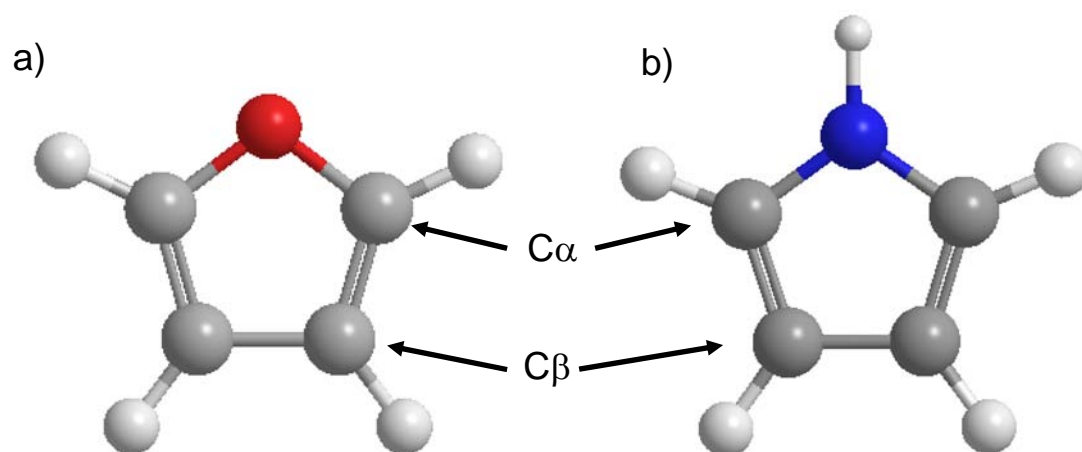


Fig. 6.1: Schematic representation of a) furan and b) pyrrole. The same nomenclature of $C\alpha$ and $C\beta$ is applied to both molecules.

In this chapter the influence of the different heteroatoms on the adsorption behavior and in this context the XP spectrum of pyrrole and furan is discussed. Additionally the reaction of furan and pyrrole upon annealing of the surface is investigated.

6.1 Introduction

Heteroatomic compounds, like furan, pyrrole and thiophene, are used as model systems for the heteroatom removal process, or, in other words, deoxygenation, denitrogenation or desulfurization, see e.g. [102, 104-106]. The harmful effects of these compounds, like, e.g., corrosion of engine parts, degradation of catalysts, contamination of the environment and so forth, make the heteroatom removal process an important issue. Interestingly, late transition metals like Ni and Co are known as promoters, which enhance the catalytic activity in the heteroatom removal process [107]. By studying different heteroatoms we can investigate the effect of the heteroatom on the surface chemistry and find trends in reactivity, allowing us to draw conclusions on questions concerned with catalysis and on other applications of these molecules. This holds true, especially, for the question of organic conducting films consisting of five-membered heterocycles that might be in contact with transition metal electrical contacts [108]. As already mentioned, pyrrole is also an important part of biologically relevant molecules, which allows to study the interactions

occurring between larger biomolecules and a transition metal surface, using a model system.

The adsorption and reaction of pyrrole was studied on Cu(100) [109], iron oxide [110], Pt(111) [111], Ni(100) [112], Rh(111) [113], Mo(110) [114], Si(100) 2x1 [115] and Pd(111) [106, 116]. Due to the wide variety of surface science tools used, different informations on the adsorption process were gained. The study on Pd(111) [116], the most comprehensive concerning the surface chemistry, used XPS, TPD, HREELS. A coverage dependent N-H cleavage at 200 K and a recombinative desorption of parts of the pyrrole monolayer upon heating was found. The remaining fragments partly recombine and desorb and partly decompose to form HCN, hydrogen and carbon fragments, according to the TPD results. The studies on the orientation of pyrrole on Cu(100) [109], Pt(111) [111] and Rh(111) [113] all yielded that the molecular plane is parallel to the surface. The work on Rh(111) [113] was, additionally, concerned with the chemistry of pyrrole on the surface, drawing conclusions from TPD data, which showed HCN desorption at 450 and 500 K and H₂ desorption at 375 K. The examination of pyrrole on Ni(100) [112] showed that it decomposed on the surface, but due to different heating rates (45 K/s and 8 K/s) different desorption products, molecular desorption of pyrrole and desorption of reaction products like HCN, respectively, were monitored and correlated to different surface reactions.

The adsorption of furan was investigated in various surface science studies on Pd(111) [106, 117-120], Cu(111) [109, 121], Ru(0001) [103, 122] and Si(111) 7x7 [123]. Photoelectron spectroscopy measurements of the gas phase [124] and condensed layers [125] can be found, allowing us to discuss differences occurring due to the interaction with the Ni(111) surface. Furthermore, information on the electronic structure can be found [125]. Studies on the orientation of furan on the surface by NEXAFS, EELS and XPS showed a tilted molecule on Pd(111) [120] and Pt(111) [111], while on Ru(001) [122] a mixture of tilted and flat lying molecules is postulated. The studies on the reactivity on some surfaces were conducted mainly with TPD, XPS, EELS and LITD measurements [106, 117, 118, 120, 122]. It was mainly found that CO elimination is the first step in the decomposition, yielding a C₃H₃ fragment, which is proposed to recombine to form benzene.

The adsorption and reaction of thiophene also has been studied on different surfaces and with a variety of surface science tools. As thiophene was not studied in

this work we will only comment in certain parts about conclusions drawn in earlier works.

In this chapter, the adsorption and reaction of furan and pyrrole are described in order to show differences in the interactions of the two heterocycles with the substrate. A description of the reaction pathways of pyrrole and furan on Ni(111) will be given, allowing to draw conclusions on the effect of the different heteroatoms. A comparison to condensed [124, 125] and gas phase [126] data will be made. For pyrrole, we also compare our data with the XPS experiments of adsorbed porphyrines [127].

6.2 Adsorption of furan and pyrrole

To obtain the XP spectra of the adsorbed, intact molecules, we monitored the adsorption of furan and pyrrole at low temperatures. This allows the comparison to the data from gas phase and condensed phase measurements, which gives insight in the interaction of the molecule and the surface. Selected C 1s spectra of the adsorption experiments of the two different heterocycles are shown in Fig. 6.2.

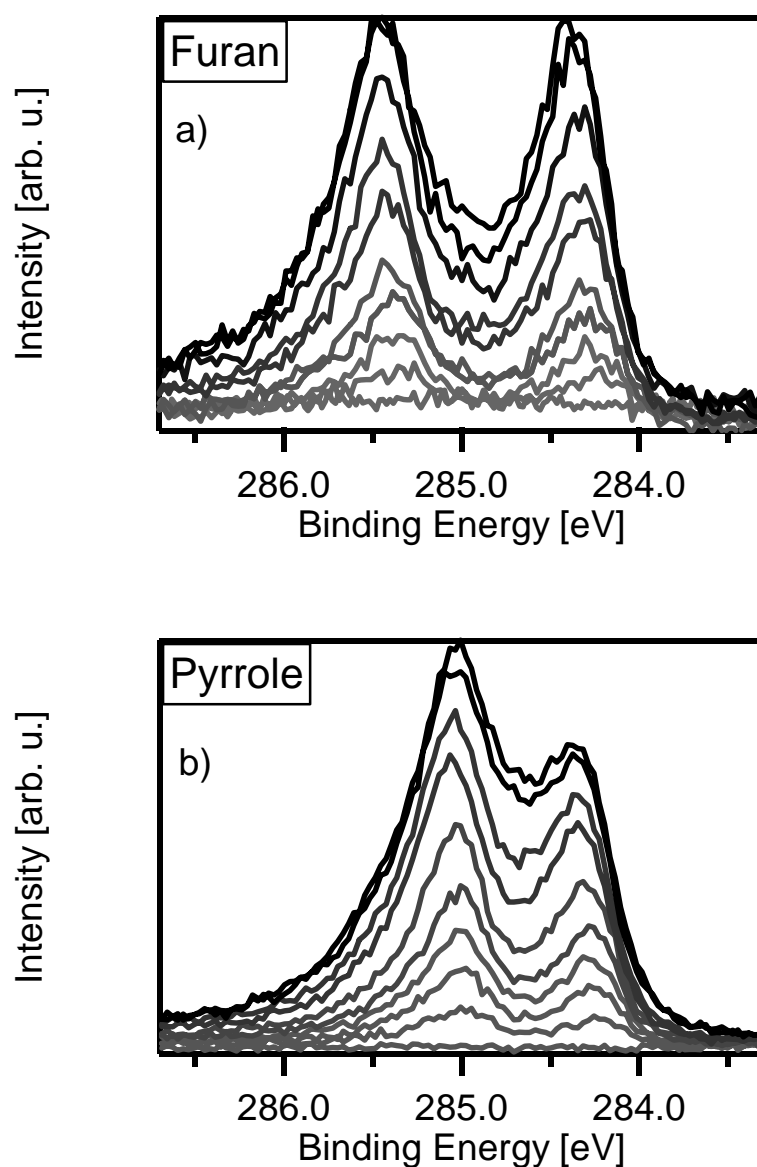


Fig. 6.2: Selected C 1s spectra of the adsorption experiments at 120 K of a) furan and b) pyrrole. (Darker lines stand for higher exposures.) The photon energy was set to 380 eV and the electron emission angle was 5° off normal emission.

For both adsorbates two clearly distinguishable peaks are found. In the case of furan, in Fig. 6.2 (a), two peaks at 284.2 and 285.3 eV appear at low coverages. Both are shifting to higher binding energies by approx. 200 meV, while the coverage is raised. In the spectra for pyrrole shown in Fig. 6.2 (b) two peaks are found at 284.3 and 285.0 eV, and again a shift to higher binding energies is observed, while raising the coverage, but only of 100 meV. The energy separation of the two peaks for furan is 1.1 eV and for pyrrole 0.7 eV. This difference can be explained by the different electronegativities of the heteroatoms. A high electronegativity of an atom in a molecule leads to a reduced electron density in adjacent atoms, thus, leading to a higher binding energy in the XP spectrum for this neighboring atoms. For oxygen the electronegativity is 3.5 and for nitrogen 3 [128]. The gas phase photoelectron spectrum of furan shows a similar separation of 1.2 eV [124]. The values for pyrrole are slightly lower, being 1.0 eV in the gas phase [126] and 0.7 eV in our case. The gas phase PES measurements of thiophene, the third comparable heterocycle, show a separation of 0.3 eV [129]. This would support the argument of the peak separation to be an initial state effect, as the peak separation for thiophene is also lower, as expected for an even lower electronegativity of 2.6 for sulfur [128]. Interestingly, for the two heterocycles the peak at lower binding energy is at a comparable binding energy position as the main peak of benzene (at saturation coverage of 0.143 ML, see chapter 4) and, thus, seems to be only slightly affected by the different heteroatoms.

A quantitative analysis was performed by decomposing the C 1s spectra of both heterocycles. All contributions in the analysis are described by Doniach-Sunjić profiles, which are described in chapter 2.1.4. Two typical examples of the applied fit procedure are shown in Fig. 6.3.

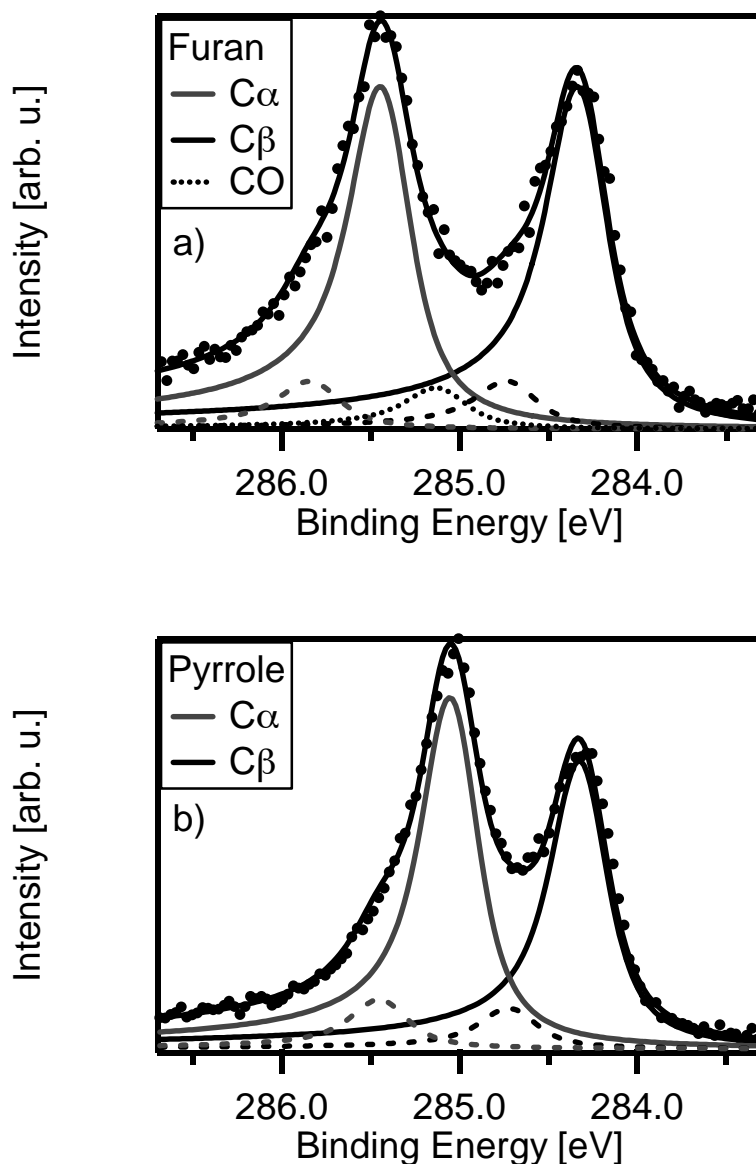


Fig. 6.3: Fit of the uppermost C 1s spectrum of a) furan and b) pyrrole taken from the experiments shown in Fig. 6.2. The dashed lines represent the first vibrationally excited state of the respective carbon atom.

The spectrum of furan shows two main peaks at 284.3 and at 285.0 eV. Both are accompanied by a second smaller peak, which is included to model vibrational splitting caused by excitations of C-H stretching modes (a more detailed description of vibrational excitations in the core hole state is given in chapter 2.1.3). For both peaks, the vibrational excited state was introduced using parameters of benzene, the model system of aromatic molecules, see chapter 4 and appendix to chapter 4. Benzene also consists of aromatic sp^2 hybridized carbon atoms with one hydrogen

atom attached to it, as in pyrrole and furan, see Fig. 6.1. The ratio of the vibrational excited peak to the adiabatic contribution was set to be 0.14, while the binding energy differences were each set to be 400 meV. For the C_{α} carbon atoms at higher binding energies these parameters were also achievable by a “free fit” of the data, but for the C_{β} , carbon atoms they are not obtained due to the overlap of the different C 1s contributions. For furan, at 284.8 eV, an additional peak is present, which belongs to a CO contamination coadsorbed from the residual gas; the assignment will be discussed in the following chapter, which deals with the thermal evolution of the heterocycles. Similar results were obtained for pyrrole: one peak at 284.3 eV with its vibrational satellite state and the second adiabatic peak at 285.0 eV again with a vibrational satellite on the high binding energy side. As mentioned above, the binding energies of ~ 284.3 eV of the C_{β} peaks is very similar to that found for benzene, with C 1s binding energies between at 284.1 – 284.3 eV for different coverages. This has already been pointed out by Rennie et al. [124]. Coadsorbed CO could not be detected in the C 1s spectra of the pyrrole adsorption experiment, as the binding energy of CO is similar to that of the C_{α} -atom of pyrrole. The relative intensities of the main contributions slightly differ (furan: $C_{\beta}/C_{\alpha} \approx 1.02$; pyrrole: $C_{\beta}/C_{\alpha} \approx 0.91$). This might be due to a different bonding to the surface and therefore a different local surrounding of C_{β} and C_{α} for the two different molecules, leading to different scattering scenarios. An additional reason for the difference might be a small amount of coadsorbed CO in the case of pyrrole, which is, due to the similar binding energy of ~ 285.1 eV (differing for different coverages and coadsorption situations), not distinguishable from the C_{α} peak at 285.0 eV, and therefore may lead to the apparent higher intensity of it. The results of the quantitative analyses of all spectra are shown in Fig. 6.4.

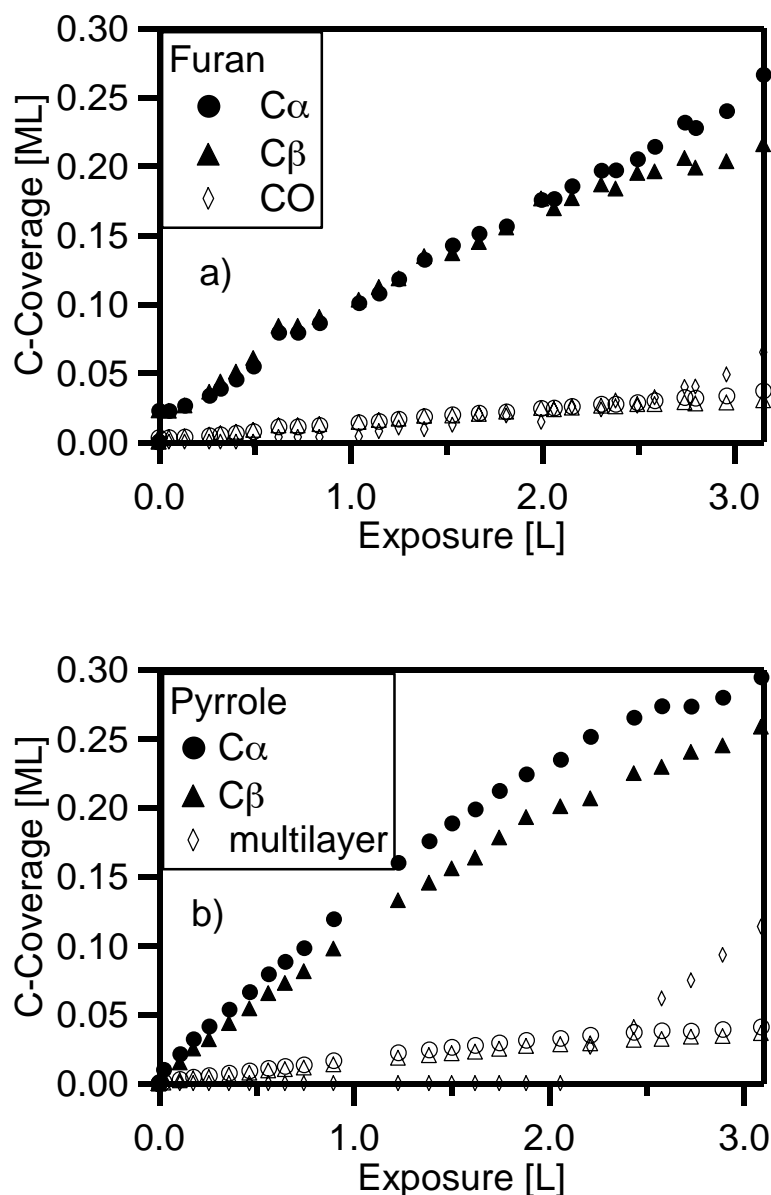


Fig. 6.4: Quantitative analysis of the adsorption experiments of a) furan and b) pyrrole in Fig. 6.2. Shown are the partial coverages of each peak; the filled symbols describe the adiabatic states and the blank symbols their corresponding 1st vibrationally excited state, if not denoted otherwise. Note that the coverage scale is given in carbon atoms per nickel atoms. For further details see text.

The coverage scales of Fig. 6.4 were obtained by comparing the data with benzene adsorption experiments (see chapter 4) measured in a comparable geometry. The two adiabatic and their respective vibrationally excited peaks rise with exposure for both adsorbates as expected. For furan, depicted in Fig. 6.4 (b), the additional peak of the (unintentionally) coadsorbed CO is found; in the case of pyrrole the probably

also existing CO-peak was not distinguishable from the other contributions. For pyrrole, an additional contribution attributed to multilayers, also consisting of two peaks, was found. This difference might be due to a different growth mode or growth kinetics compared to furan, or a different sensitivity of the ionization gauge towards the two adsorbates, leading to a different exposure scale. This was, however, not investigated further. The first layer of pyrrole starts to saturate at ~ 2.8 L, which can be seen in Fig. 6.4 (b), as the slope of the area of the two main peaks is decreasing, reaching almost zero. For furan, this behavior is only found for one of the main peaks; this may be attributed to the fitting procedure, not allowing us to distinguish between multilayers and the monolayer. This decrease of one main peak, nevertheless, is interpreted as saturation, leading to a saturation coverage of 0.14 ± 0.02 ML (molecules per surface atom). For pyrrole, it can be stated that a monolayer consists of 0.165 ± 0.02 ML (molecules per surface atoms), which is higher than the saturation coverage of benzene at 200 K (0.143 ML), leading to 0.858 adsorbate atoms (carbon and nitrogen) per Ni atom for benzene and 0.825 adsorbate atoms per Ni atom for pyrrole and 0.7 adsorbate atoms (carbon and oxygen) per nickel atom for furan.

A comparison with the relative and absolute binding energies found for condensed and gas phase measurements is discussed in the following. For furan on Ni(111) a binding energy difference of 1.1 eV with the C 1s signals at 284.3 and 285.4 eV was found; for pyrrole on Ni(111) adsorbed pyrrole the C 1s peaks are located at 284.3 and 285.0 eV, yielding a difference of 0.7 eV. In condensed phase measurements of furan, the binding energy difference was found to be 1.0 [125] and 1.3 eV [124], well comparing to the result of 1.1 eV obtained in this study. For pyrrole in the condensed phase a value of 0.8 eV [125] was found, which is again very similar to our value. The small differences in binding energy separation may be due to the bonding to the substrate. In gas phase XPS measurements [126] the peak separation of furan and pyrrole was determined to be 1.2 and 1.0 eV, respectively. Intermolecular interactions might be responsible for the difference in peak separation observed for pyrrole.

An interesting result from literature should be mentioned here: The similarity in the binding energy of the C β atoms seen on the Ni(111) surface seems to be a result of the bond to the surface, as in gas phase the C β atoms of furan and pyrrole have a difference in C 1s binding energy of 0.5 eV [126].

6.3 Reaction of furan and pyrrole

To learn more about the interaction with the Ni(111) surface we studied the evolution of the two adsorbed heterocycles during temperature programmed reaction. Typical spectra of furan are shown in Fig. 6.5 (a) as waterfall plot and (b) as density plot.

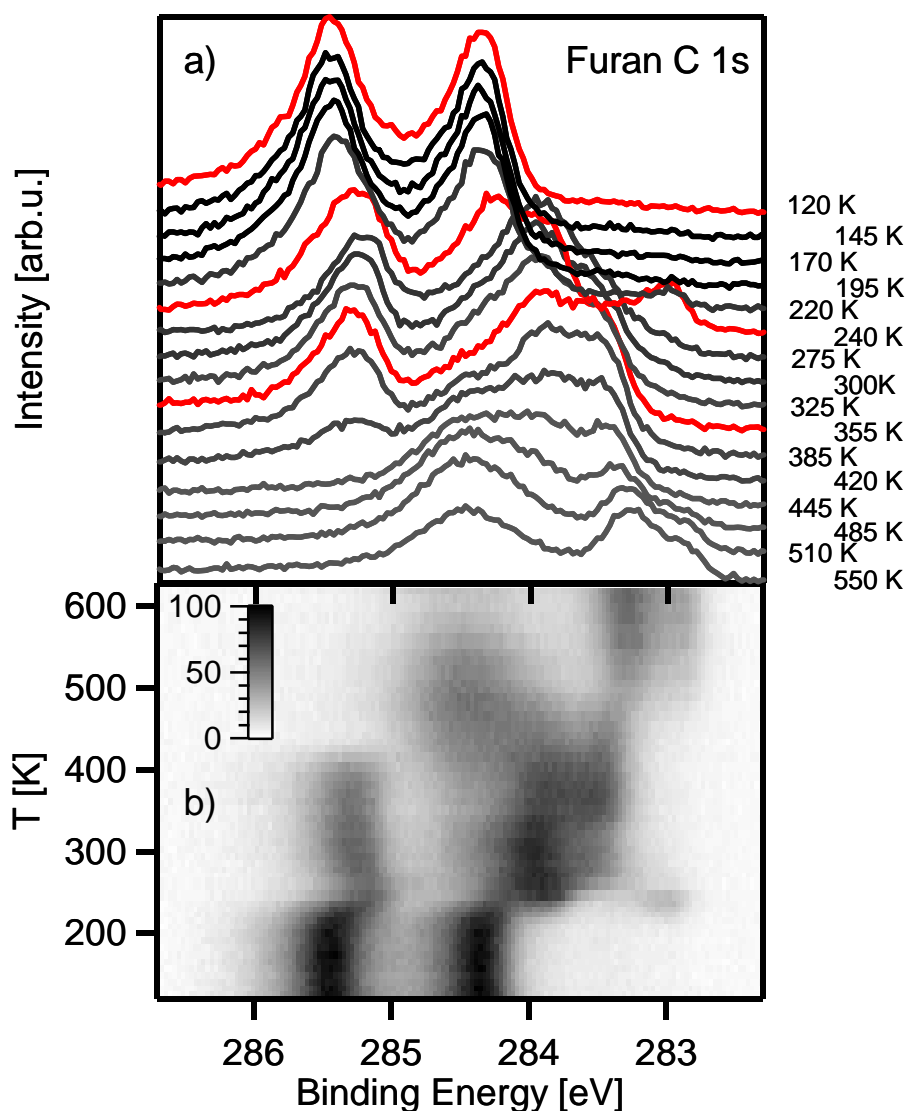


Fig. 6.5: a) Selected C 1s XP spectra of the thermal evolution of furan shown as waterfall plot; b) color coded density plot of the TPXPS experiment with furan. ($\beta \approx 0.1$ K/s) Note that the temperature scales are reversed in a) and b). Inset: relative intensity scale of the density plot.

The topmost spectra in Fig. 6.5 (a) show the already described features of furan adsorbed at 120 K, with two main features at 284.3 and 285.4 eV. Up to

temperatures of 230 K, no significant changes are observed. Then, starting at 250 K, a small feature at 282.9 eV, a larger one at 283.9 and a third one at 285.2 eV are evolving from the initial signal. The small feature at 283.1 eV is vanishing again already at 260 K. At 420 K, the peak at 285.2 eV is gone. 10 K later at 430 K the peak at 283.9 eV is splitting; this is the typical behavior of other hydrocarbons, such as benzene [130], acetylene [38], decomposing on the surface. The spectra show different unidentified C_xH_y components, which at temperatures above 500 K are finally all dehydrogenated, to yield pure carbon.

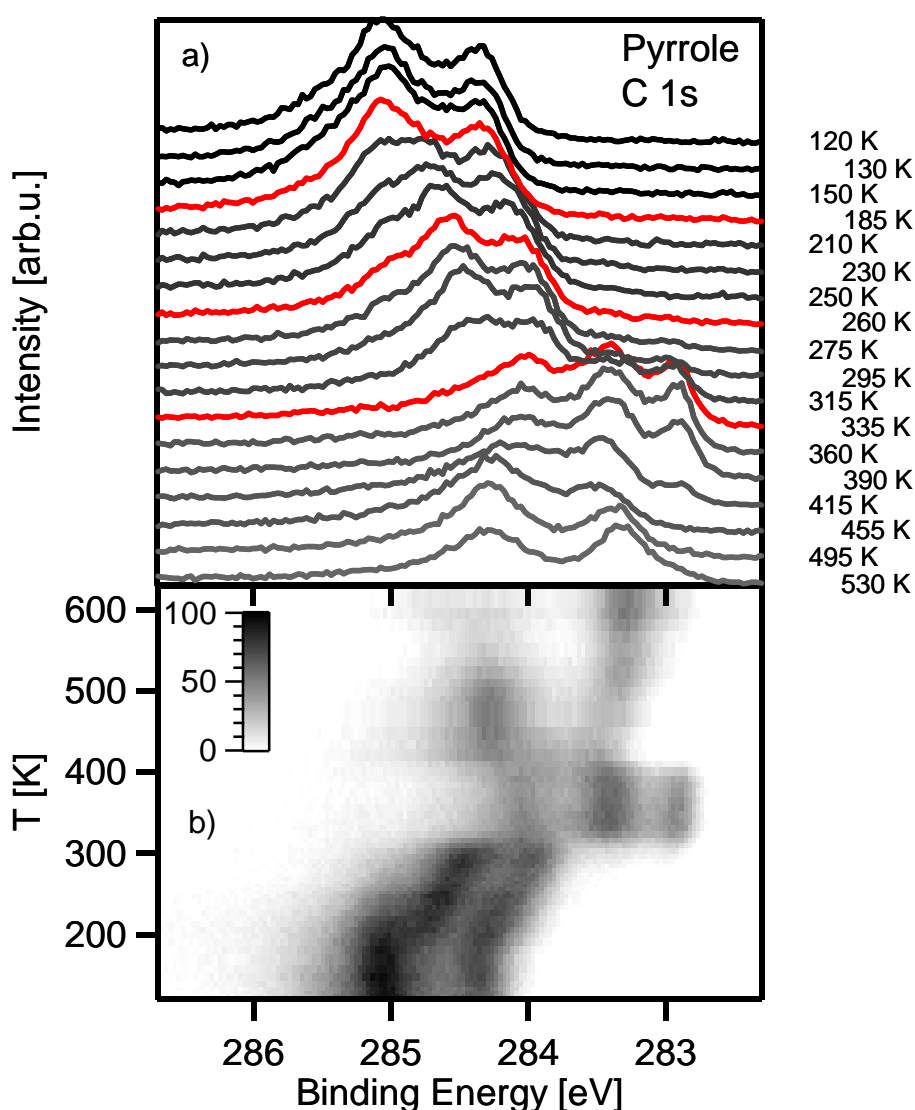


Fig. 6.6: a) Selected C 1s XP spectra of the thermal evolution of pyrrole shown as waterfall; b) color coded density plot of the TPXPS experiment with pyrrole. ($\beta \approx 0.1$ K/s) Note that the temperature scales are reversed in a) and b). Inset: relative intensity scale of the density plot.

For the thermal evolution of adsorbed pyrrole, shown in Fig. 6.6, we find the already known signature of the intact adsorbed molecules up to 200 K. Above this temperature the two main peaks are shifting to lower binding energies and at ~300 K the characteristic signature is vanishing, yielding three peaks at 282.9, 283.4 and 284.1 eV. These three peaks are again indicating the typical dehydrogenation process starting above 430 K, already described for the thermal evolution of furan.

Since heterocyclic compounds are investigated, core level spectra of the heteroatoms, in this case the O 1s and N 1s signals, can additionally be used for analysis. The corresponding spectra for furan and pyrrole are shown in Fig. 6.7 and in Fig. 6.8.

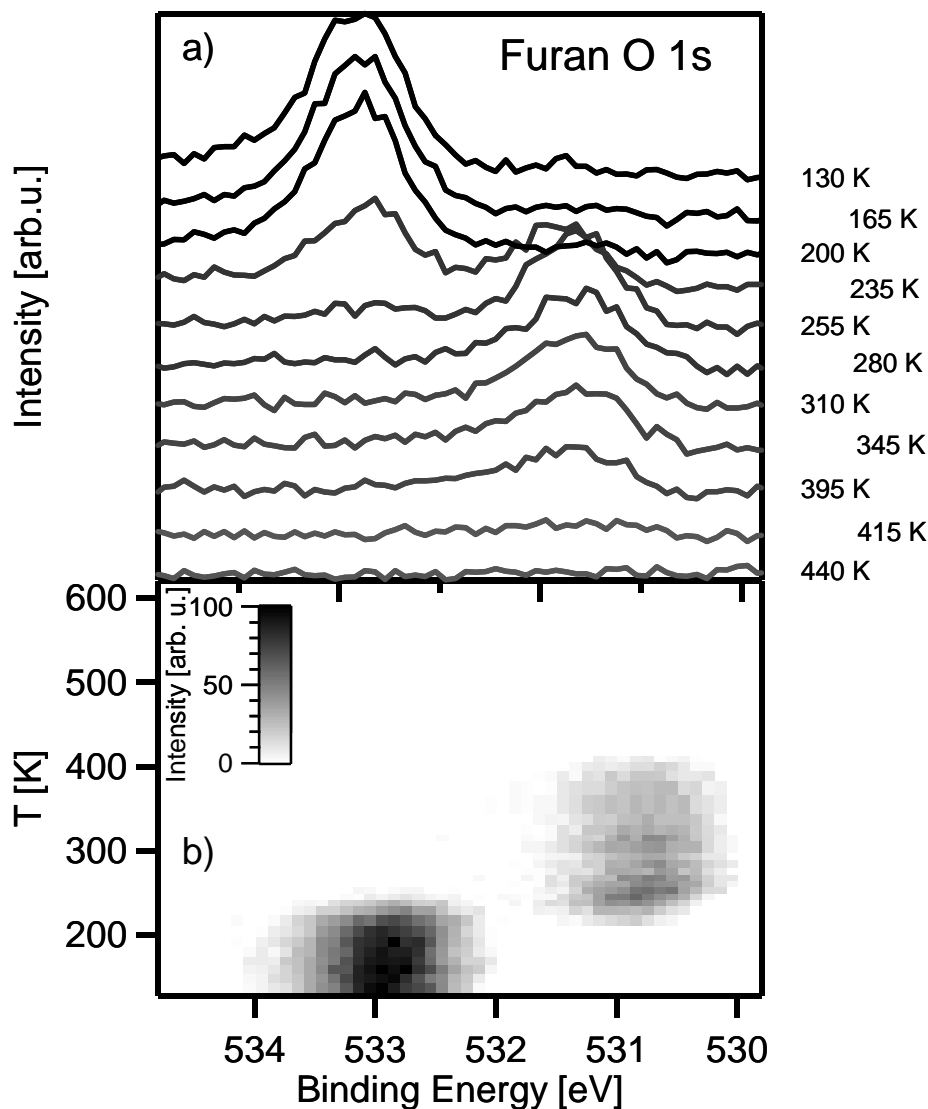


Fig. 6.7: a) Selected O 1s XP spectra of the thermal evolution of furan shown as waterfall plot; b) density plots of furan of the same experiment ($\beta \approx 0.1$ K/s). The measurements were performed at 5° off normal emission geometry. The photon energy was set to 650 eV. Note that the temperature scales are reversed in a) and b). Inset: relative intensity scale of the density plot.

The O 1s spectra of the decomposition of furan show only two features. At low temperatures a peak at 533.0 eV and at temperatures above 240 K a peak at 530.8 eV is present, which is vanished at 420 K.

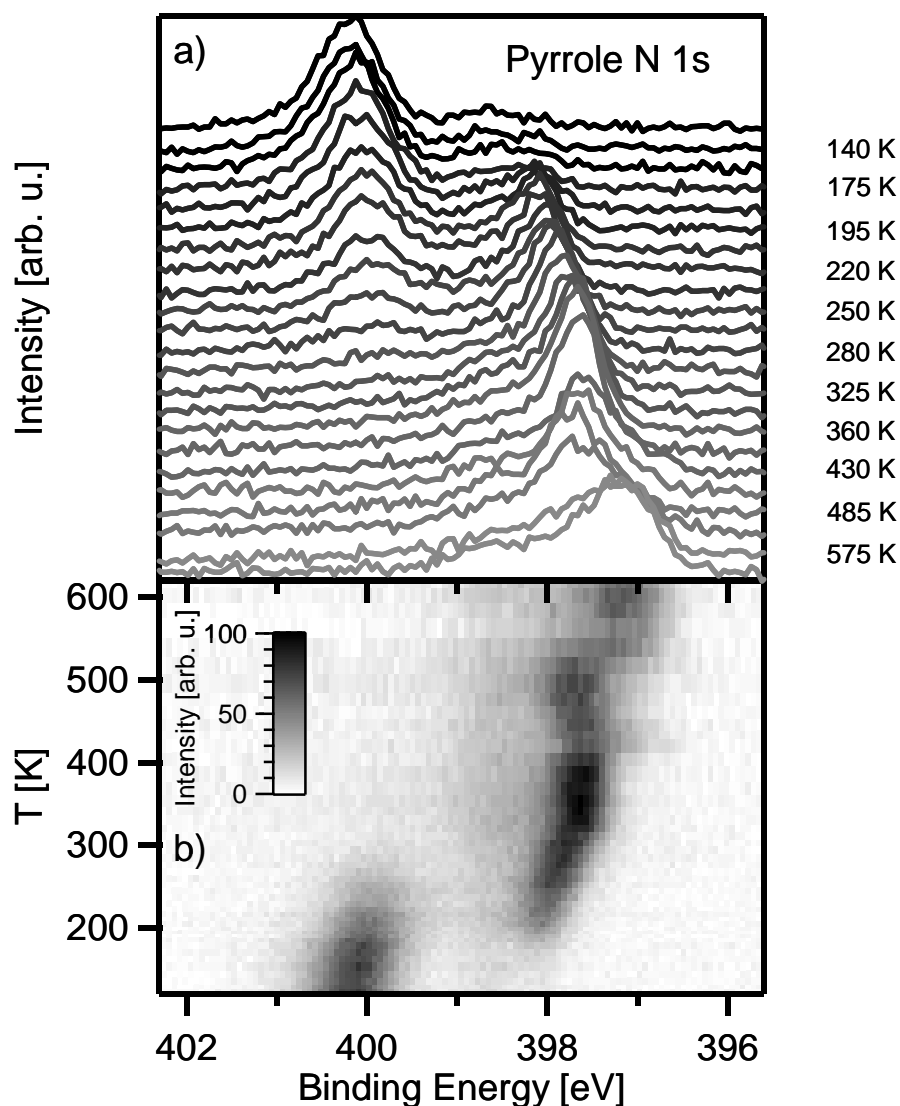


Fig. 6.8: a) Selected N 1s XP spectra of the thermal evolution of pyrrole shown as waterfall plot; b) density plots of pyrrole of the same experiment. ($\beta \approx 0.1$ K/s) The measurements were performed at 5° off normal emission geometry. The photon energy was set to 500 eV. Note that the temperature scales are reversed in a) and b). Inset: relative intensity scale of the density plot.

At low temperatures the N 1s spectra of adsorbed pyrrole show only one peak at 400.1 eV. At a temperature of approximately 200 K a second peak at 398.3 eV is evolving. This peak is shifting to higher binding energies by 600 meV between 200 to 300 K. From 300 to 400 K, only one peak at 397.7 eV is present. At 400 K, an intensity drop is observed; a discussion of this effect will be given later in this chapter.

At approximately 550 K a new peak at 397.3 eV is arising on the expense of the peak at 397.7 eV.

A quantitative analysis of the different TPXPS experiments allows a closer look on the different evolving species. For an easier view of the different reactions taking place on the surface we show the corresponding C 1s and O 1s or N 1s analysis together and will discuss the similarities and differences later in the chapter.

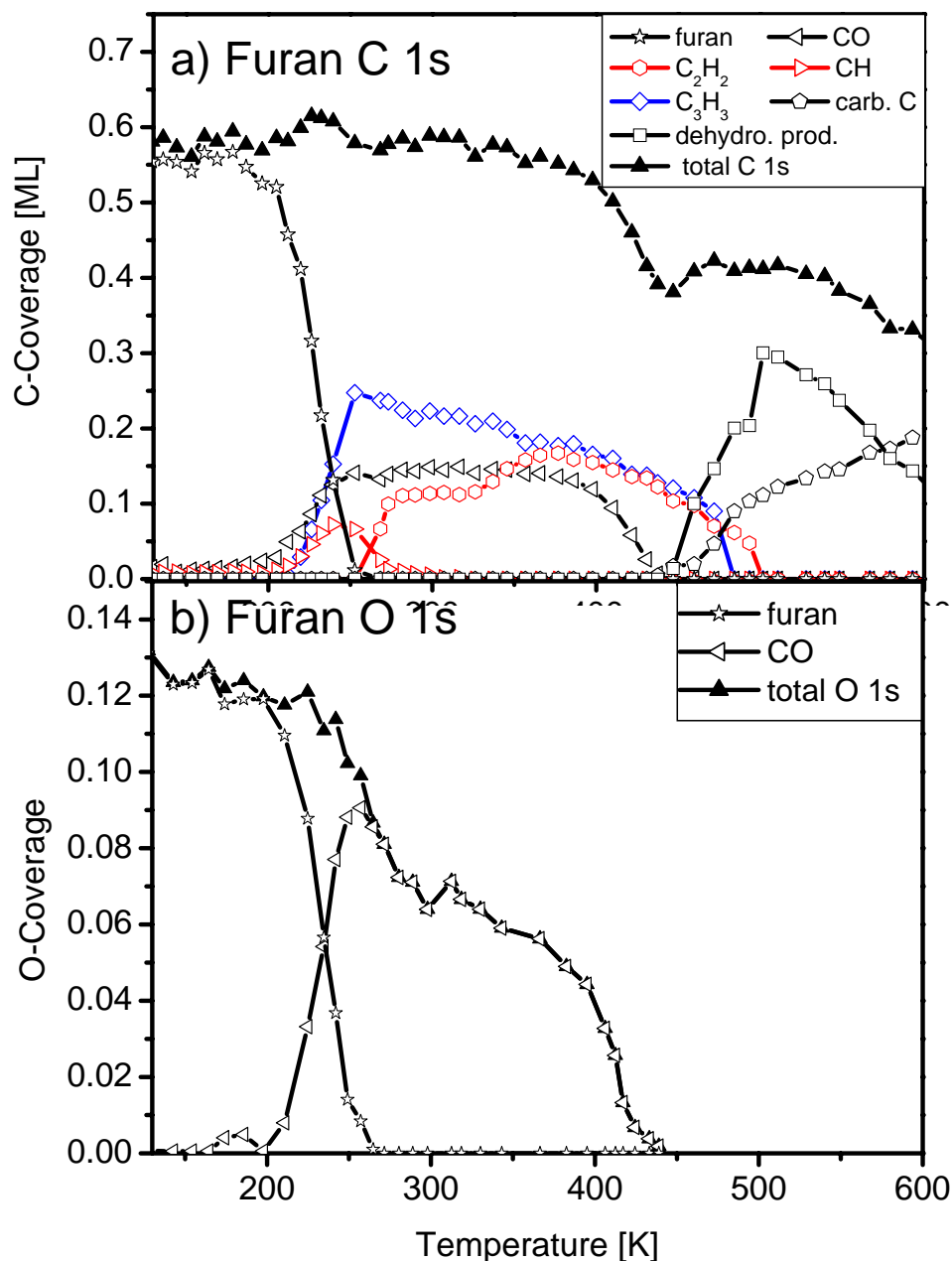


Fig. 6.9: Quantitative analysis of a) the C 1s and b) the O 1s TPXPS experiments of furan, shown in Fig. 6.5 and 6.6.

At low temperatures, the quantitative analysis of Fig. 6.9 (a) shows one contribution arising from furan, of which the spectral features were already discussed in chapter 6.2. Connected with these furan C 1s spectra one corresponding feature is observed in the O 1s region. Above 200 K, a new species evolves at 2.3 eV lower binding energies in the O 1s spectra (see Fig. 6.7 (b)). Simultaneously, a small shift of the C 1s peak at 285.4 eV by 200 meV to lower binding energies occurs. These peaks can be unequivocally assigned to CO, due to the binding energy position in the C 1s and O 1s region and the desorption temperature of 420 K [40]. The decrease in the O 1s signal, occurring at the transition from furan to CO, is most likely related to dramatically changing photoelectron diffraction conditions upon the change from the flat lying configuration in furan to the upright standing CO. It also has to be mentioned that a decrease of 30 % in the O 1s region is related only to a decrease of ~ 10 % in C 1s region, which cannot be ruled out with our data. This shows that the ring system broke into at least two pieces above ~250 K. CO is the only oxygen containing species found, showing that CO is the heteroatom containing reaction product. The reaction of furan to CO certainly shows that the heterocycle break up is completed at ~250 K.

The hydrocarbon parts of the furan ring, not containing CO, show a more complex reaction behavior with three different contributions: (i) at 283.0 eV, which is assigned to CH, (ii) at 283.4 eV that is correlated with acetylene and (iii) at 283.9 eV that is assigned to a C₃H₃ species. Typical fits of the C 1s spectra of the TPXPS experiments are shown in the appendix. In the following we will discuss these assignments.

Upon ring break up a species is observed at 283.0 eV, which is only stable in a small temperature range from 240 to 260 K. Comparable results regarding the C 1s binding energy and the reaction temperatures were reported by Fuhrmann upon decomposition of methyl to methylidyne on a Ni(111) surface [38]. The reaction temperature and the binding energy position indicate that CH is produced here, although in a strong coadsorption situation, as its binding energy position is shifted by 300 meV to higher values (note that in the case of Fuhrmann only a coverage of up to 0.1 ML was present). The existence of only a small amount of this C1 species already indicates the decomposition of furan occurs via parallel reactions. Fuhrmann [38] also showed, that the CH on the Ni(111) surface easily undergoes a C-C coupling reaction yielding acetylene, found at a binding energy of 283.3 eV. A

contribution at 283.4 eV is also found in our XP spectra, nevertheless, a clear identification is not possible, due to the overlapping C 1s signals of the different carbon fragments and the possible differences, due to the strong coadsorption situation present on the surface, allowing no clear assignment by comparison to “fingerprint” data.

Based on stoichiometric considerations we can state, that acetylene, also only stable up to 400 K, has to be found already in the primary reaction step as the C_3H_3 species remaining of the CO removal is fragmenting into one CH certainly also a C_2H_2 group has to be found on the surface. Another contribution found at a binding energy of 283.9 eV is most likely an intact C_3H_3 fragment of the ring breakup, but cannot be identified unequivocally. A similar fragment was identified on the Pd(111) surface [106, 117, 118], upon dissociation of furan [120]. At temperatures above 350 K parts of this C_3H_3 species are converted to most likely yield acetylene, probably from decomposition and from subsequent coupling of the C1 components.

At 420 K, the already mentioned desorption of CO is observed. Subsequently, the typical behavior of the decomposition of adsorbed hydrocarbons on the surface is observed. The rather broad peak at ~284.3 eV found at temperatures above 430 K is attributed to dehydrogenating carbon fragments, which cannot be specified further, while at the same temperature carbidic and graphitic carbon species are evolving, which are shown as one contribution in Fig. 6.9 (a). The proposed reaction path of the decomposition of furan on Ni(111) is schematically shown in Fig. 6.10.

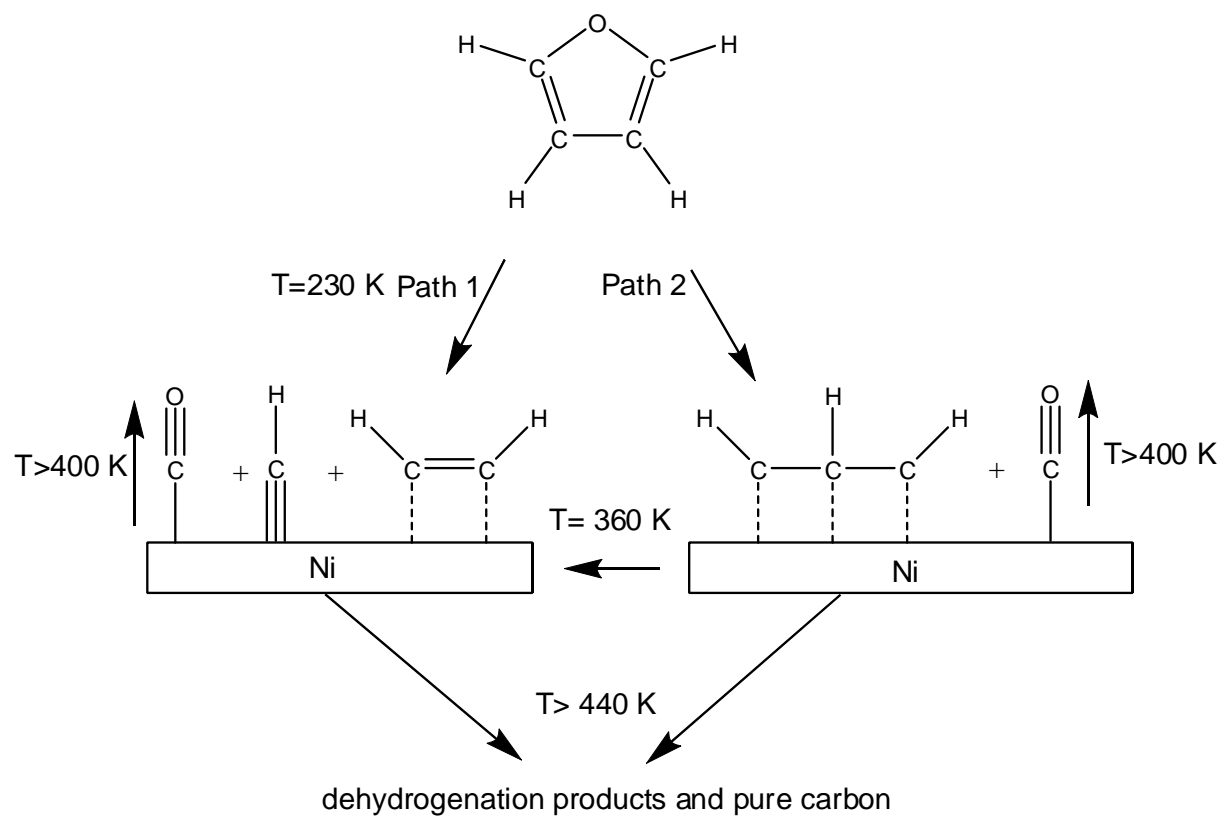


Fig. 6.10: Reaction pathway for the decomposition of furan on Ni(111).

The quantitative analysis of the C 1s spectra and the N 1s spectra of pyrrole are shown in Fig. 6.11.

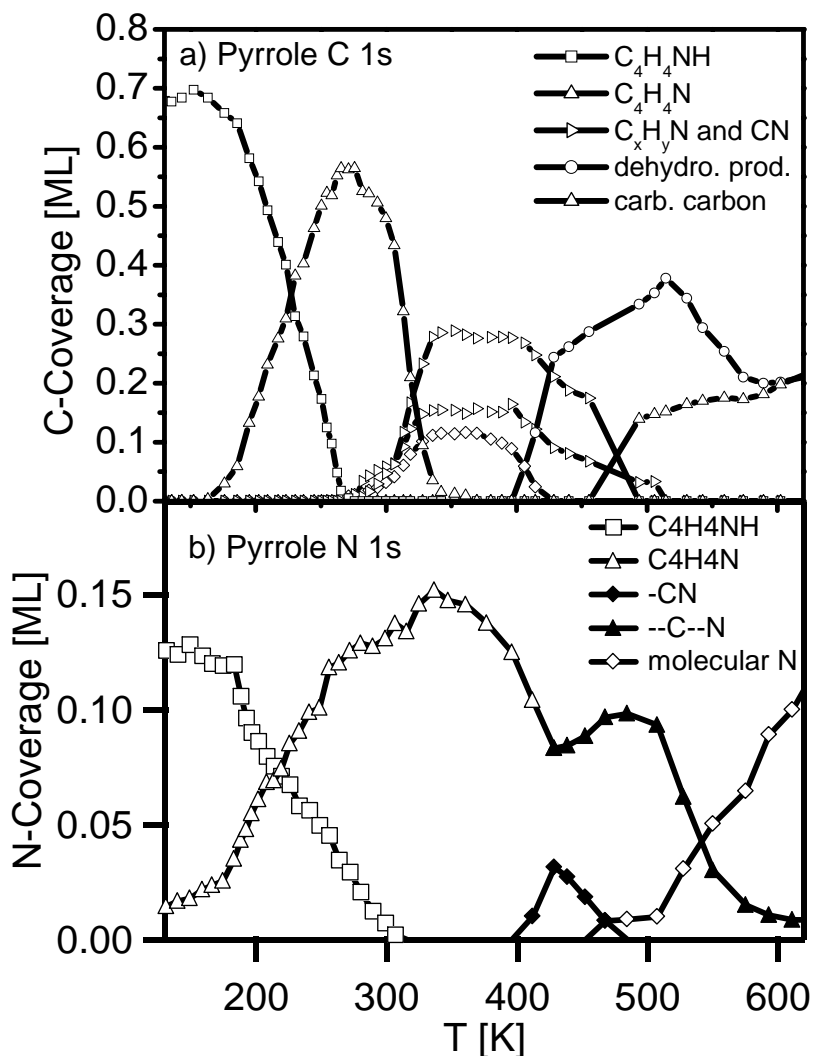


Fig. 6.11: Quantitative analysis of a) the C 1s and in b) the O 1s TPXPS experiment of pyrrole shown in Fig. 6.5 and 6.6 is shown.

In Fig. 6.11, the chemical species deduced from the XP spectra are plotted. Typical examples for the fit of the C 1s spectra of the TPXPS experiment are shown in the appendix. At low temperatures pyrrole is found; upon annealing, above 200 K, a strong shift in the C 1s spectra is observed. In the N 1s spectra a new feature is found, located at 398.3 eV. This is interpreted as the quantitative dehydrogenation of the nitrogen atom, yielding an analogue to the furan structure, but with nitrogen as heteroatom. This is also deduced from the still pronounced two peak structure in the

C1s spectra. Similar results, are found for the porphyrine macromolecule adsorbed on a Ag(111) surface [127]. In the porphyrine molecule two different types of nitrogen atoms are present, namely a pyrrolic and an iminic nitrogen with N 1s peaks at 400.1 and 398.1 eV, respectively. The nitrogen atom in pyrrole is at first protonated with a N 1s binding energy of 400.1 eV like in the porphyrine molecule, while the deprotonated form, corresponding to the iminic form, has a binding energy of ~ 398.1 eV, well comparing to the results of Gottfried et al. [127]. At 300 K, the further decomposition, most likely a ring breakup, of this species is taking place. This, however, can only be observed in the C 1s region, yielding again three different features, but in the N 1s region no change is observed. This fact indicates that the nitrogen atom is still in a similar chemical surrounding as in the initial C₄H₄N species. One should note, however that there are examples showing that, e.g., different adsorption geometries are not necessarily reflected in the N 1s binding energy [131], which might not allow to draw this conclusion.

Above 430 K, the species found in the C 1s region start to yield the already discussed typical dehydrogenation species and pure carbon, which is known for many different hydrocarbons. Interestingly, we can now identify different species in the N 1s region. A possible interpretation might be that a C-N like species is found between 400 and 480 K, that is more strongly bound to the Ni(111) surface than on other surfaces like, e.g., Pd(111) [120] or Pt(111) [122], to finally yield molecular nitrogen on the surface. The assignment of this species to atomic nitrogen is based on the binding energy [132] as well as the fact, that no change in the C 1s spectra was found, compared to pure carbon species. This indicates that the carbon and nitrogen species are adsorbed on the surface without forming a compound. Unfortunately, the exact stoichiometry of the surface species is hard to determine, as no additional information on the reaction behavior exists. In contrast to the reaction of furan, dominated by the ring break up yielding CO, the reaction of pyrrole yields different C_xN-species, which are hard to distinguish. Only at temperatures higher than 450 K an assignment is possible. As the overall N 1s intensity is not varying in the examined temperature range it can be excluded that HCN or other N-containing species desorb. The deduced reaction mechanism is schematically depicted in Fig. 6.12.

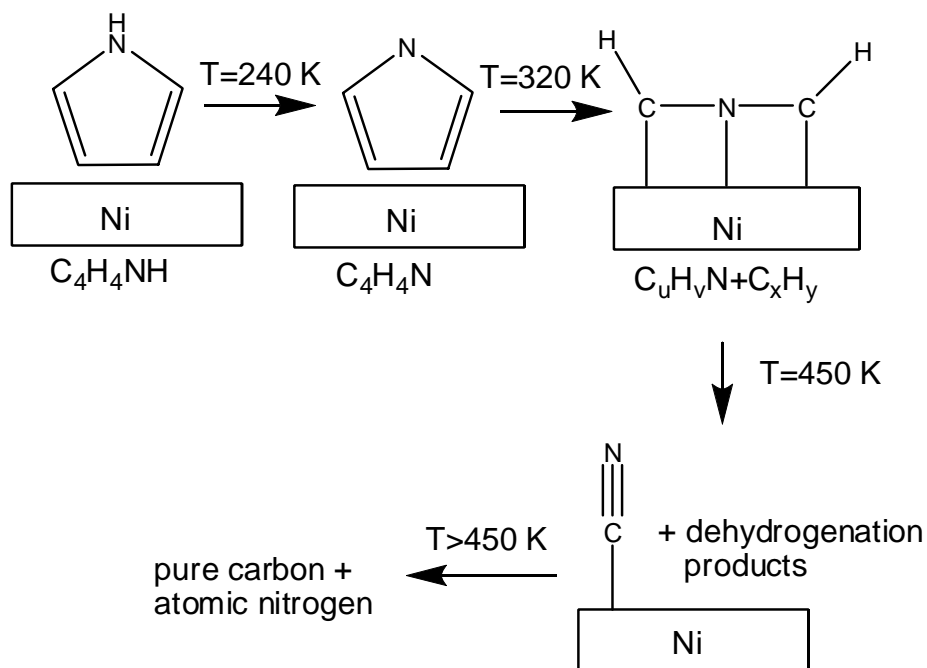


Fig. 6.12: Reaction pathway for the decomposition of pyrrole on Ni(111).

6.4 Summary

This chapter was concerned with the adsorption and reaction of the heterocycles pyrrole and furan, which was monitored by in-situ XPS measurements. Upon adsorption for each heterocycle a C 1s spectrum dominated by two peaks, which are separated by 0.7 eV in the case of pyrrole and 1.1 eV in the case of furan, were observed. This is interpreted as an initial state effect, which is related to the different electronegativities of the neighboring heteroatoms, N and O, respectively. Thus, the C 1s peaks at higher binding energies are assigned to the carbon atoms which are in direct neighborhood to the heteroatoms. For the case of the sulfur containing analogous a binding energy difference of the two adiabatic states of 0.3 eV was reported, which is in line with the given interpretation. For both heterocycles the two adiabatic peaks of C_α and C_β show a small contribution at 400 meV higher binding energies, which is due to a vibrational excitation in the core hole state. Interestingly, the C 1s peak at lower binding energies, $\sim 284.3\text{ eV}$, is not affected in its binding energy by the variation of the heteroatom and appears at a similar binding energy as in benzene.

The reaction of the adsorbed heterocycles was investigated by TPXPS for furan the C 1s and the O 1s region and for pyrrole the C 1s and the N 1s regions were monitored in-situ. From the data it was possible to deduce the reaction pathways of the two heterocycles. Furan shows as first step, at 230 K the formation of CO, which is desorbing at 420 K, and different hydrocarbon fragments, which are a mixture from C₁ (methylidyne) to C₃ moieties; they are further dehydrogenated on the surface to yield pure carbon at higher temperatures. The reaction of pyrrole starts at first with the N-H bond scission yielding a deprotonated form of pyrrole. The subsequent reaction yields also a mixture of different hydrocarbon species, but no methylidyne, as in the case of furan, was found. A clear distinction between possible reaction intermediates at this stage of the reaction was difficult as different C_x-N and C_yH_z moieties were present on the surface, allowing no clear distinction by XPS. This lead to the conclusion that CO as leaving group is favored over the nitrogen analogue CN. In the later reaction we find atomic nitrogen on the surface which is formed from the C_xN species and the same is found for carbon which originates from the dehydrogenation of the carbon containing chemical species. Another important finding is the release of toxic gases, while in the case of furan CO is desorbing, we do not find HCN desorbing from the surface for pyrrole. Most probably the desorption of hydrogen and nitrogen from pyrrole layers has to be considered.

Summing up, the adsorption of the two heterocycles, furan and pyrrole, shows a rather similar behavior, but the reaction behavior upon annealing of the adsorbed layers differs significantly.

7 Methane adsorption on stepped platinum surfaces

The previous chapters dealt with the reaction and adsorption properties of rather large organic molecules. They were adsorbed on flat model surfaces allowing us to study these systems and to accurately describe them. In this chapter we now want to move on to more complicated and, therefore, more realistic surfaces used as substrates. More realistic in the sense that heterogeneous catalysis is usually performed at highly disperse particles which certainly exhibit steps, kinks and other defects. Our approach now is to introduce well defined steps on the surface. The description as “well defined” extends to the “concentration”, the quantity of steps relative to the terraces, and to the orientation of the steps. A schematic drawing of the two stepped platinum surfaces used, Pt(355) and Pt(322), is shown in Fig. 7.1.

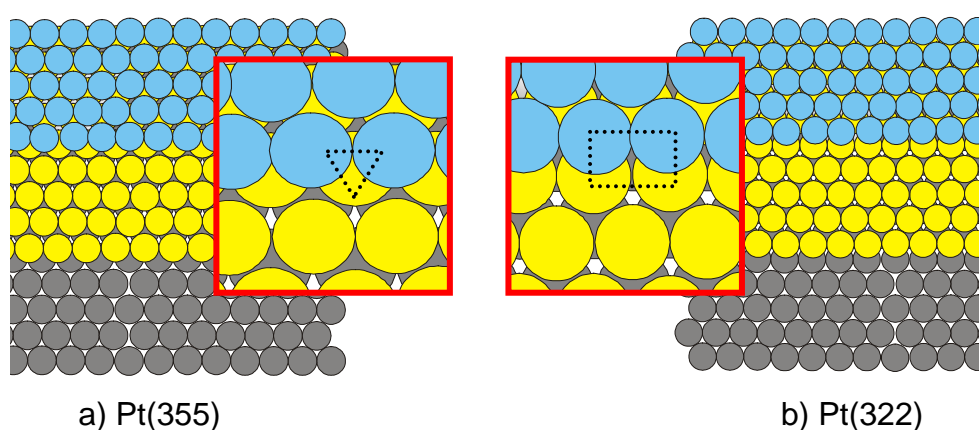


Fig. 7.1: Schematic drawing of the two stepped surfaces, a) Pt(355) and b) Pt(322). The upper part shows a top view, with a magnification of the a) (111) steps and b) (100) steps. The dotted lines indicate the fourfold and threefold sites of these steps. The lower part shows a side view of the surfaces.

Pt(355) and Pt(322) both have nominally five atom rows wide (111) terraces, but the steps are oriented along the (111) and (100) directions, respectively [133]. As both surfaces have “only” 20% of steps and 80% (111) terraces, the Pt(111) surface was

used as a reference. In contrast to the previous chapters the complexity of the system, now, is depending on the substrate and not on the adsorbate. Therefore, we used a well studied and simple molecule, namely methane, the simplest hydrocarbon. However, a closer look shows that the exact description of the XP spectra is not that easy, as we have to regard the internal vibrations in the core hole state of the molecule. The high stability of methane leads only to physisorption of the molecule on the surface. To overcome the activation barrier of the activated dissociative adsorption a supersonic molecular beam is used, which facilitates this reaction. To access the vibrational properties and the time dependent picture of adsorption and reactions certainly a high flux and high resolution X-ray source, i.e., a synchrotron, is needed.

As the effect of steps on the reaction and adsorption is part of this chapter, we also want to cover the passivation and or poisoning of these intentionally introduced defects. For this purpose the steps were decorated with silver, an almost inert metal. The resulting “loss” of steps is discussed in chapter 7.4. In chapter 7.5 a more fundamental aspect is discussed, namely the kinetic isotope effect of deuterated and non-deuterated methane upon adsorption and reaction.

7.1 Introduction

Methane is one of the most important natural resources, as it is used in many different technologically relevant processes, such as steam reforming [134]. Furthermore, due to its high hydrogen content it is relevant as H₂ source, e.g., for fuel cells [135-137]. As the simplest hydrocarbon, methane also serves as a model system for the understanding of the activated adsorption behavior of saturated hydrocarbons on surfaces.

The interaction of methane with the Pt(111) surface has been subject to a great number of studies with different surface science methods under various conditions; the goal was to obtain a detailed understanding of its adsorption, desorption and reaction behavior on this model surface. For temperatures below 73 K molecular adsorption has been reported [138-143]. Luntz and Bethune [144] were among the first to study the dissociative adsorption of methane with a supersonic molecular beam, which is needed to overcome the activation barrier for methane

dissociation under UHV conditions. Their study and also later investigations by other groups were performed at surface temperatures above 500 K to avoid contamination and to stay close to technically relevant conditions. In these studies the initial sticking coefficient [145-147], the scattering properties [148, 149] and surface reactions [150] were investigated. Lately, the activated, dissociative adsorption at low temperatures and the thermal evolution of the formed surface intermediates on Pt(111) were studied by a combination of high resolution XPS in combination with a supersonic molecular beam by Fuhrmann et al. [68, 151]. They reported C 1s spectra with a fine structure due to vibrational excitations in the core excited final state. This effect is well known from gas phase XP spectra of methane (Ref. [152] and references therein) and other adsorbate systems [23, 68, 69].

One step further towards real catalysis is the introduction of well-defined surface defects on single crystal surfaces. It has been shown that the reactivity of steps and other defects can be quite different from that of the flat crystals [153]. However, for hydrocarbons, little is known with respect to the influence of steps on the adsorption behavior [154, 155], reaction pathways or reactivity towards dehydrogenation. Only some studies concerned with precursor assisted adsorption can be found [154, 156]. The only study concerning the direct adsorption of methane addresses the dissociation on Pt(533) [157]. The corresponding molecular beam experiments were performed at 600 K and show a, by a factor of three, enhanced initial sticking coefficient for methane as compared to Pt(111).

To systematically elucidate the influence of steps, we investigated the dissociative adsorption of methane on two stepped surfaces with different step orientations, namely the Pt(355) and Pt(322), and compare the results to those obtained for Pt(111) [68]. The adsorption process on the different platinum surfaces is followed by in-situ time-dependent high resolution XPS in combination with a supersonic molecular beam, which allows to identify and quantify the reaction products on the surface. Furthermore, by so-called TPXPS experiments [35], the thermal evolution of the reaction intermediates is followed in-situ during annealing of the surface.

7.2 Results and discussion

7.2.1 Adsorption experiments on Pt(355) and Pt(322)

In Fig. 7.2 (a) C 1s spectra of the dissociative adsorption of methane on Pt(111) at ~ 120 K are shown.

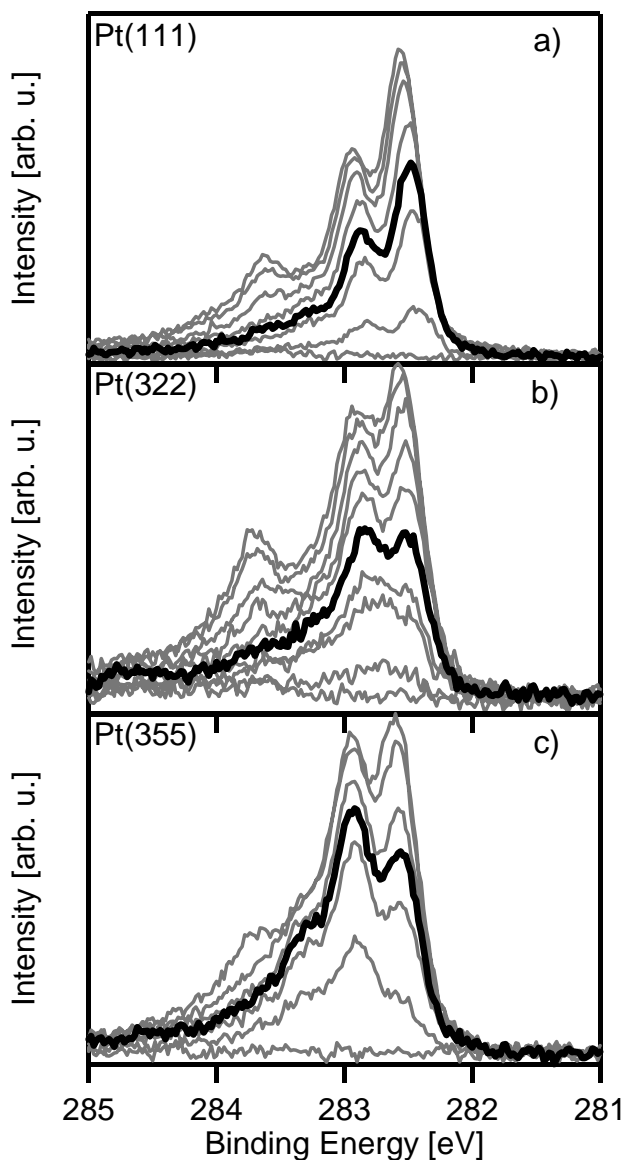


Fig. 7.2: Selected C 1s spectra collected during adsorption of methane on a) Pt(111) ($E_{kin}(\text{CH}_4)=0.71$ eV), b) Pt(322) ($E_{kin}(\text{CH}_4)=0.45$ eV) and c) Pt(355) ($E_{kin}(\text{CH}_4)=0.45$ eV). All spectra were recorded with a photon energy of 380 eV at an electron emission angle of 45° . The sample temperature was ~ 120 K.

The spectra are dominated by three different distinct peaks, at binding energies of 282.6, 283.0 and at 283.6 eV, while the last is only clearly visible at higher exposures (note, that all peaks display a shift of ~ 140 meV to higher binding energies with increasing coverage). The spectra for Pt(322) and Pt(355), shown in Figs. 7.2 (b) and (c), respectively, show a similar signature. However, we find different intensity ratios of the two peaks at ~ 282.6 and ~ 283 eV as compared to the (111) surface. This effect can be observed especially in the spectra at lower coverages (e.g., thick black spectra), where the ratio is sometimes even reversed in comparison to Pt(111), with the peak at 282.6 eV being higher than the one at 283 eV.

For further analysis, the spectra of Fig. 7.2 were fitted in a consistent way using several peaks, each consisting of an asymmetric Doniach-Sunjjic function convoluted with a Gaussian. The width of the Gaussian was determined by the width of the Fermi edge, in order to represent the experimental broadening. The resulting Lorentzian contribution due to the lifetime was approx. 90 meV, which corresponds well to gas phase values [152]. The asymmetric line shape is due to electron-hole-pair excitations near the Fermi edge.

Fig. 7.3 shows the peak analysis of the C 1s spectra on all three surfaces for an intermediate coverage.

For Pt(111), see Fig. 7.3 (a), the predominantly adsorbed species has been identified to be methyl (CH_3) [140, 142, 148], in agreement with vibrational spectroscopy [158]. The observed fine structure is attributed to vibrational excitations of C-H stretching modes of methyl in the photoemission process. The peaks at 282.6 and 283.0 eV are due to the adiabatic transition and to the transition to the first vibrationally excited state, respectively, upon core ionization of methyl. Independent of coverage, the two peaks display a constant intensity ratio, i.e., S factor (see [25, 26] or chapter 2.1.3), of 0.5 and a constant binding energy difference of 400 meV. A second vibrationally excited peak is also observed, shifted to higher binding energies by 386 meV, with respect to the first vibrationally excited state. It also has a constant intensity ratio of 0.09 with respect to the adiabatic methyl peak. This assignment was verified by similar experiments with deuterated methane (CD_4), which showed the expected rise of $\sim\sqrt{2}$ in intensity ratios (S factor) and drop by $\sim 1/\sqrt{2}$ binding energy differences, see Fig. 7.4 (a) [151]. The remaining peak at 283.6 eV is assigned to a second chemical species present on the surface, namely methylidyne (CH), caused by radiation damage induced by synchrotron radiation or by thermal treatment [151].

It is fitted by a fourth and fifth peak, to again describe the adiabatic transition and the transition to the first vibrationally excited state. The analysis of the vibrational fine structure of CH yields an S factor of 0.16 and an energetic separation of 420 meV, both again independent of coverage [68].

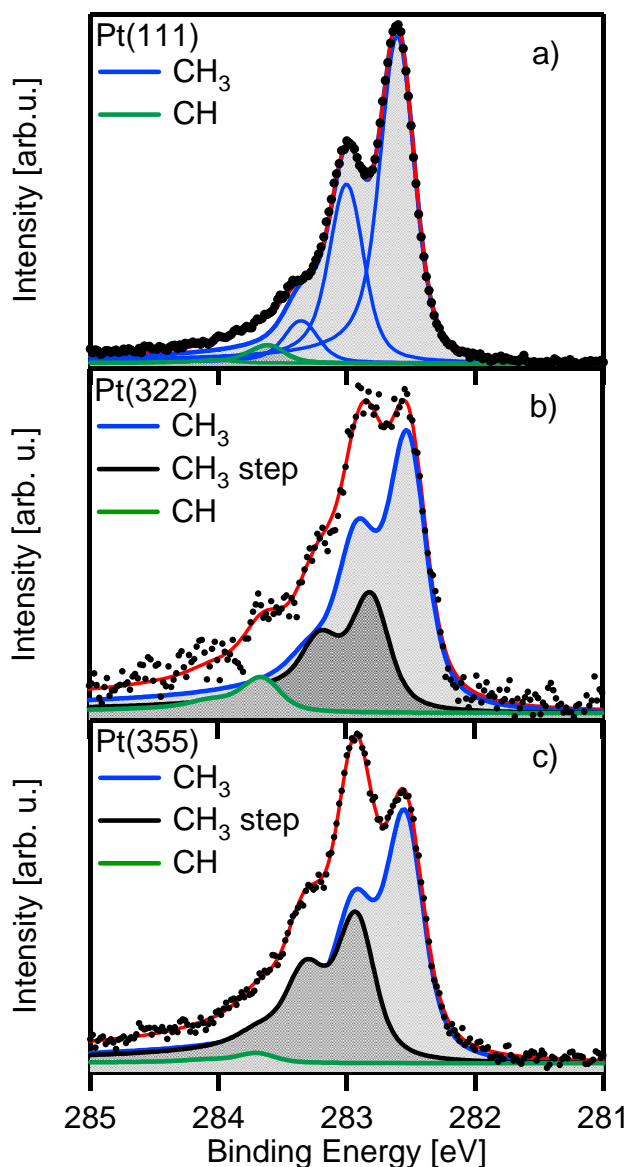


Fig. 7.3: C 1s line profiles of adsorbed methyl on a) Pt(111), b) Pt(322) and c) Pt(355). In a) the individual vibrational contributions of the methyl signal are shown as thin blue lines; in b) and c) the individual peaks are not shown, but their envelopes (thick lines), corresponding to methyl adsorbed at steps and terraces as well as methylidyne. For details see text.

The analysis of the spectra for methane dosed onto Pt(322) and Pt(355) in Figs. 7.3 (b) and (c), respectively, show similar energetic positions of the two dominating peaks at ~ 282.6 eV and ~ 283.0 eV than on Pt(111). However, the already mentioned change of their intensity ratio with exposure (coverage) is not compatible with an interpretation in terms of a simple vibrational fine structure, which immediately indicates a different situation on the two stepped surfaces as compared to the flat Pt(111) surface. To account for that we propose the existence of two distinguishable methyl species on both stepped surfaces, one adsorbed on the flat terraces (similar as on Pt(111)) and the other adsorbed at the steps, with the binding energy of the latter being significantly shifted to higher values. In order to obtain reliable fits of the spectra (i.e., fits with only few parameters), we assume that the vibrational fine structure of both species is identical to that on Pt(111), i.e., both have the same intensity ratios and energetic separations of the second and first excited peaks to the adiabatic peak. This means that there are only two free parameters for each species, namely the energetic position and intensity of the adiabatic peak. Furthermore, the CH species again present on both surfaces due to dehydrogenation induced by the high radiation intensity, is modeled by using the energetic separation and the S factor found for Pt(111). With these constraints, we are able to fit the data for both stepped surfaces satisfactorily.

For the Pt(322) surface (Fig. 7.3 (b)), we find a methyl species with the adiabatic peak at a binding energy of ~ 282.6 eV, which is very similar to the value observed for methyl on Pt(111). It is therefore attributed to CH_3 adsorbed on the terraces. The second methyl species has the adiabatic peak at ~ 282.9 eV, i.e., shifted to higher binding energies by 330 meV. This species is attributed to CH_3 adsorbed at the steps. As on Pt(111), we observe CH on the surface, with the adiabatic peak again at ~ 283.6 eV.

On Pt(355) we obtain similar results: One methyl species with the adiabatic peak at ~ 282.6 eV, which is attributed to terrace adsorption, and a second methyl species with the adiabatic peak at ~ 283.0 eV, attributed to step adsorption. The exact analysis shows that the binding energy difference to methyl on terraces is 370 meV as compared to 330 meV on Pt(322) (Fig. 7.3 (c)). Once more, a CH species was found at similar binding energies as on Pt(111). The difference in the binding energy shifts between the two methyl species adsorbed at step and terraces sites of the Pt(355) and Pt(322) crystals can be understood in terms of a different bonding

geometry occurring due to a different local surrounding at the step sites and the possibly different electronic density of states at the step sites.

To verify our assignment, we also performed experiments with deuterated methane. The corresponding spectra and their decomposition are shown in Fig. 7.4 (b) and (c).

On both stepped surfaces, we again identify two different adsorbed methyl species. The peak fitting has been performed in an analogous way as described above, using the peak shape observed for Pt(111), see Fig. 7.4 (a) (adapted for a slightly different resolution). As already mentioned above, the vibrational fine structure exhibits the expected decrease in the vibrational splitting by $\sim\sqrt{2}$ and the corresponding increase of the S factor by $\sim\sqrt{2}$. Again the adiabatic peaks of the two step-site methyl species, adsorbed at the differently oriented steps, exhibit different binding energy shifts as in the case of the non-deuterated methane, i. e., 330 meV for Pt(322) and 370 meV for Pt(355).

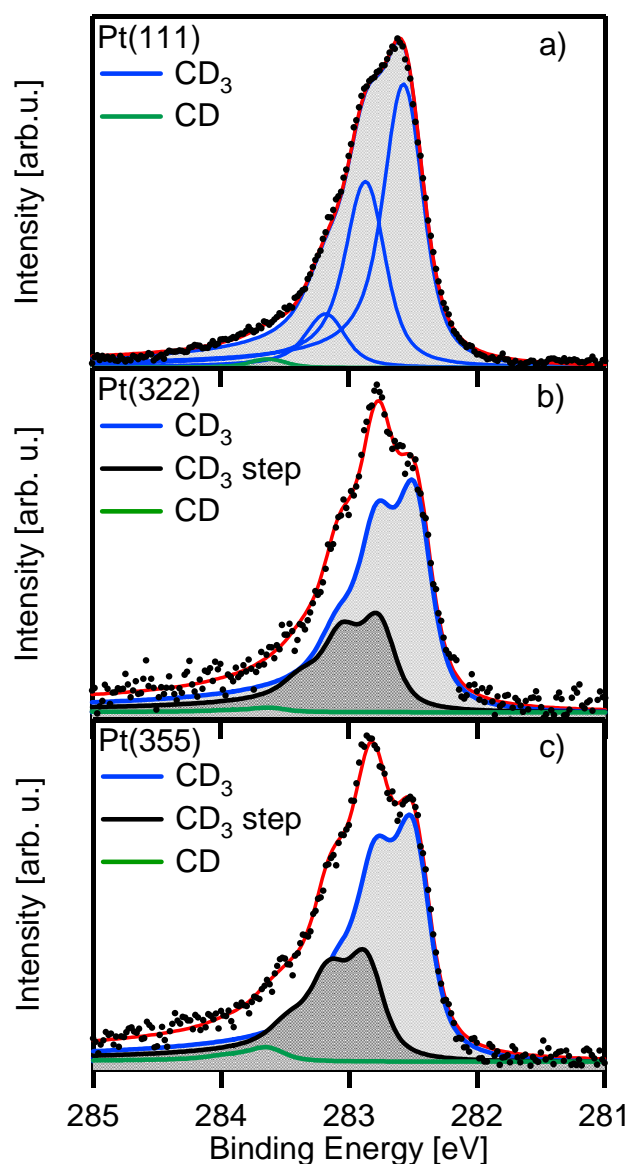


Fig. 7.4: C 1s line profiles of adsorbed deuterated methyl on a) Pt(111), b) Pt(322) and c) Pt(355). In a) the individual vibrational contributions of the methyl signal are shown as thin blue lines; in b) and c) the individual peaks are not shown, but their envelopes (thick lines), corresponding to methyl adsorbed at steps and terraces as well as methylidyne. For details see text.

At this point, we can summarize that we are able to clearly distinguish between three different chemical species on the stepped surfaces, namely methyl adsorbed at step sites, methyl adsorbed on the (111) terraces and a CH species. Interestingly, we observe only one CH species on the surfaces.

The quantitative peak analysis of all the C 1s spectra leads to a time dependent picture of the adsorption experiments. In Fig. 7.5 we present the total coverages ((a) and (b)) and the methyl coverages at steps ((c) and (d)) on Pt(322) and Pt(355), respectively, for kinetic energies of 0.54, 0.60 and 0.71 eV.

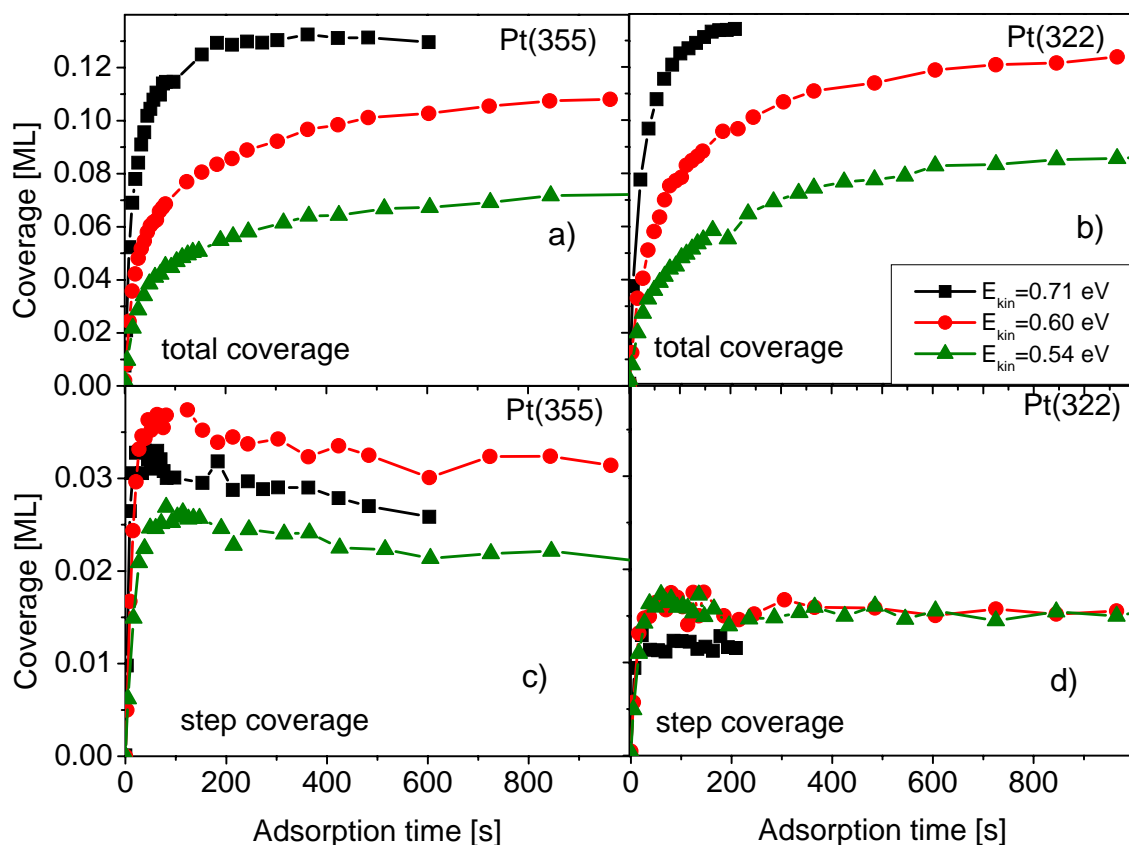


Fig. 7.5: Coverage during exposure to methane, with kinetic energies of 0.54, 0.60 and 0.71 eV of the impinging molecules: total coverage on a) Pt(355) and b) Pt(322), methyl coverage at steps on c) Pt(355) and d) Pt(322); the data were determined by fitting spectra as shown in Fig. 7.2 by the procedure described in the text.

The coverages were derived by comparison to C 1s spectra of ethene adsorbed on Pt(111) with a known coverage [68]. All kinetic energies of methane were achieved by seeding 5% CH₄ in He, but with different nozzle temperatures to vary the kinetic energies (and implicitly the vibrational excitation) of the impinging molecules (the relation between flux, nozzle temperature and kinetic energy of the methane molecules is given in the appendix). The behavior of the total coverages on the

stepped surfaces and on the Pt(111) surface (see Ref. [68]) shows a good resemblance despite the different surface orientations. For all surfaces, the methyl coverage at a given exposure increases with increasing beam energy. The saturation coverages obtained for the three surfaces with a kinetic energy of 0.71 eV are very similar, with values of 0.16 ± 0.02 , 0.14 ± 0.02 and 0.13 ± 0.02 ML for Pt(111), Pt(355) and Pt(322), respectively.

For methyl adsorbed at the steps, no clear dependence of the adsorption behavior on the kinetic energy of the impinging methane molecules is found. In all cases a fast saturation is observed. The data in Fig. 7.5 (d) show that the coverage of methyl adsorbed at step sites on Pt(322) saturates at an average value of 0.016 ± 0.005 ML for all beam energies studied. For Pt(355), a slightly higher average saturation coverage of 0.027 ± 0.007 ML for the methyl at step sites is found, as shown in Fig. 7.5 (c). For both surfaces the deviations for the different energies are within the experimental error (note the very small absolute coverage values). This different saturation coverage for methyl at step sites is a rather unexpected result, as the number of steps is approximately the same for both surfaces. However, similar results are observed for the adsorption of CO on these two surfaces, again with a higher CO step population on the Pt(355) surface. There, this behavior was attributed to a weaker bonding of CO on (100) steps than on the (111) steps and different influence of intermolecular interactions [49].

Summarizing this, the important results are: (i) the total amount of methyl adsorbed is similar for both stepped surfaces and (ii) also for the flat (111) surface; (iii) the steps saturate after a shorter adsorption time than the terraces; (iv) the amount of methyl adsorbed at steps is independent of the kinetic energy of the impinging molecules and (v) different for the two step orientations.

In Fig. 7.6, the relative initial sticking coefficients (rel. S_0) of methane on Pt(355), Pt(322) and Pt(111) are plotted versus the kinetic energy. They were determined from the initial slopes of the data in Figs. 7.5 (a) and (b) (and corresponding data for Pt(111) [68]). For that purpose the data were interpolated with a function, which was then differentiated to determine the relative initial sticking coefficient. Note that we can determine only relative sticking coefficients, since we cannot quantify the absolute flux of methane molecules with the required accuracy. The inset in Fig. 7.6 shows the magnification of the initial coverage increase of data shown in Fig. 7.5 and additionally of data obtained on the Pt(111) crystal for a kinetic

energy of 0.54 eV of the impinging methane molecules; for discussion of the curves, see below.

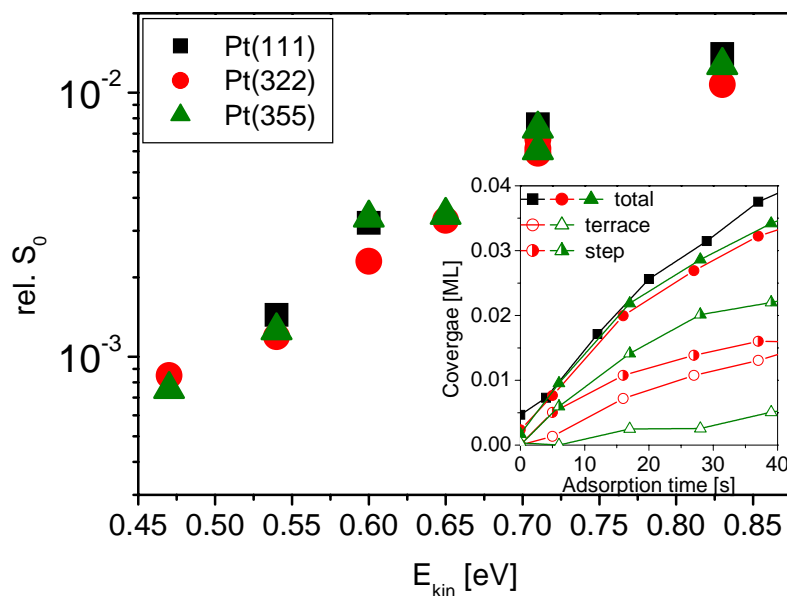


Fig. 7.6: Relative initial sticking coefficients ($rel. S_0$) plotted versus the kinetic energy of the impinging methane molecules for Pt(355), Pt(322) and Pt(111). All experiments were performed with a seeding ratio of 5% methane in helium. The change in kinetic energy was achieved by changing the nozzle temperature. Inset: Magnification of the initial coverage increase of the data shown in Fig. 7.5 and additionally of data for Pt(111). The kinetic energy of methane was 0.54 eV for all surfaces.

The relative initial sticking coefficients for Pt(111), Pt(355) and Pt(322) show a nearly identical behavior. For all three surfaces a more or less exponential increase (nearly linear on the logarithmic scale in Fig. 7.6) is observed with rising kinetic energy, as expected for activated adsorption [144]. The identical behavior for the three surfaces is in apparent contradiction to the work by Gee et al. [157], who find a higher sticking coefficient (by a factor of ~ 3 in the energy range discussed here) for Pt(533) than for Pt(111), but who measured at an elevated surface temperature (600 K), as compared to $T < 130$ K in the present study (this aspect will be further addressed below). On the other hand, there is a correspondence to the results of a theoretical study of methane adsorption on Pd(110) and the stepped Pd(320) [159]. Although the authors

expect steering effects on the stepped surface, no difference in the initial sticking coefficient is predicted.

One might be tempted to relate the initial slopes of the curves for the individual species, i.e., methyl adsorbed at step and terrace sites, to the relative initial sticking coefficient of these species. This analysis is, however, complicated, since methyl seems to have a very high mobility on the terraces at 125 K. This is concluded from the fact that on Pt(355) for very low coverage, i.e. ~ 0.01 ML, methyl is found to occupy predominantly the steps, with a terrace occupation being smaller at least by a factor of 5 – 10 (inset of Fig. 7.6), indicating that only 10-20 % of methyl is adsorbed on the terraces (the value could be even smaller, but is very difficult to determine more accurately due to the low signal). From the comparison to Pt(111), where one obtains the same total coverage under the same conditions (beam energy and exposure), one, however, would expect a terrace population on the stepped surfaces of 80 %, corresponding to the fraction of terraces on the surface. If one assumes a similar initial sticking coefficient on Pt(111) and on the terraces of the stepped surfaces, methyl initially adsorbing on the terraces, therefore, has to diffuse to the steps. The fact that the data in Fig. 7.5, and also in the inset of Fig. 7.6, show the same initial slope for Pt(111) and the two stepped surfaces (for all energies studied), indicates a very similar total relative initial sticking coefficient in all cases. As a consequence, the initial sticking coefficient at the steps must be similar to that on the terraces. This is true for both stepped surfaces, as they show the identical sticking coefficients at given conditions.

The lower increase in step coverage, or vice versa the steeper increase of the terrace coverage, found on Pt(322) compared to Pt(355) shows a lower trend of diffusion to the step sites, see inset of Fig. 7.6. This could result from a stronger bonding of the methyl at the (111) oriented steps of the (355) surface, as compared to the (100) steps of the Pt(322) surface. The bond strength will again be discussed in chapter 7.3 in context with the passivation of the surface with silver.

7.2.2 Thermal evolution of the adsorbed species

To study the thermal evolution of the adsorbed methyl layers, we heat the prepared layers to 500 K, while applying a linear heating rate of 0.5 K/s. In Fig. 7.7 (a), (b) and (c) typical temperature programmed (TP)-XPS experiments of methyl on Pt(111) [68], Pt(322) and Pt(355), respectively, are shown

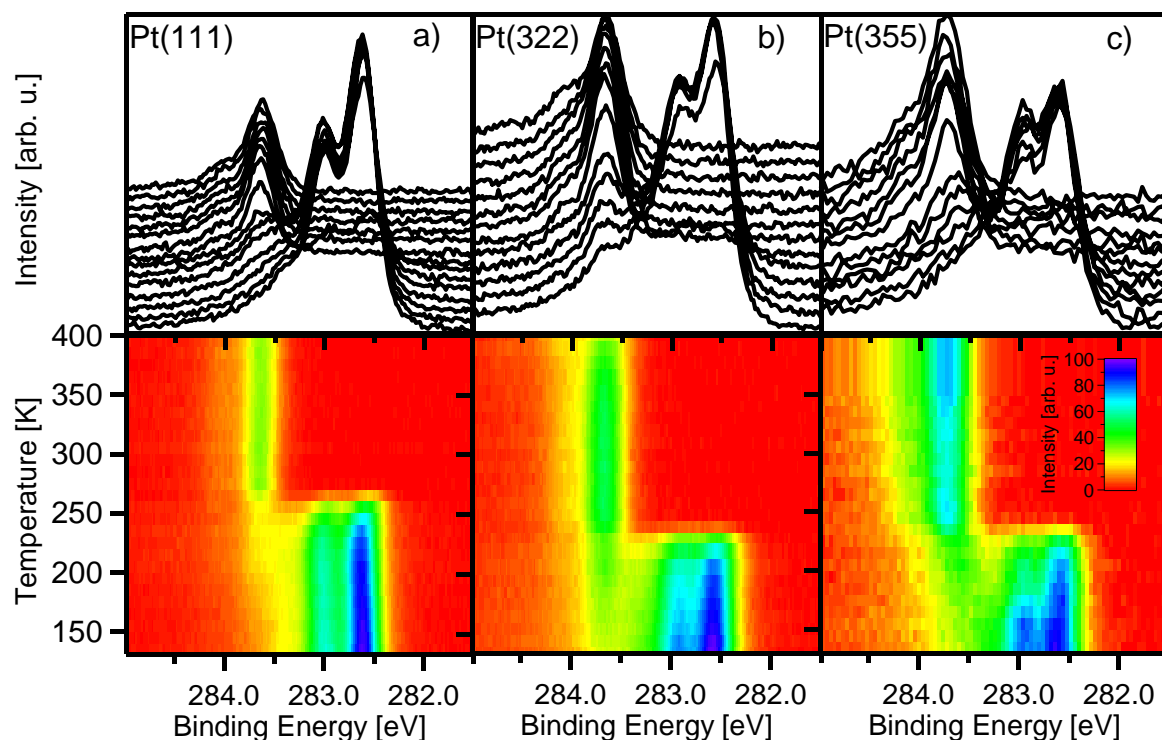


Fig. 7.7: Waterfall plots (top) and colour-coded density plots (bottom) of C 1s spectra obtained by TPXPS during heating of methyl layers on a) Pt(111), b) Pt(322) and c) Pt(355). The heating rate was in all cases 0.5 K/s; temperature increases from bottom to the top. The intensities in the density plots are represented by a colour scale, as indicated in c), ranging from low intensity (red) to high intensity (blue). All spectra were recorded with a photon energy of 380 eV at an electron emission angle of 45°. For further details see text.

In the upper parts we show waterfall plots of the C 1s spectra acquired during heating; the lower parts show color-coded density plots of the same experiments. The spectra for all surfaces clearly show the transition from methyl to methylidyne, with the adiabatic peaks at 282.6 and 283.6 eV, respectively. The quantitative analysis of the data in Fig. 7.7 is shown in Fig. 7.8. It is performed with the same parameter set as for the above mentioned adsorption experiments.

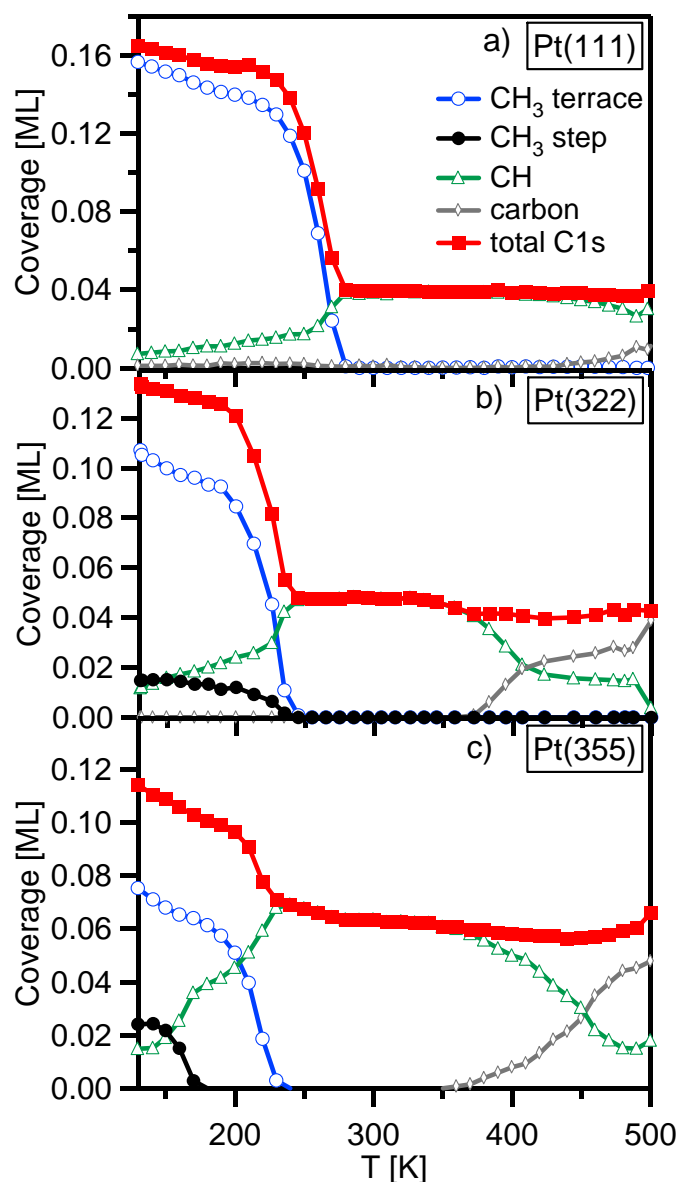


Fig. 7.8: Quantitative analysis of the TPXPS experiments shown in Fig. 7.7; a) Pt(111), b) Pt(322) and c) Pt(355).

The data for Pt(111) show CH₃ as the predominantly adsorbed species at low temperatures. The small amount of CH is due to the radiation-induced dehydrogenation of the surface methyl. Below 250 K only a small decrease of the CH₃ signal and a slight increase of the CH signal are observed, both effects being due to beam damage. Between 240 and 280 K, temperature induced dehydrogenation occurs; the CH₃ signal drops to zero ($T_{50\%}=260 \pm 5$ K; $T_{50\%}$ denotes the characteristic temperature, where the signal of a species has dropped to 50% of its intensity) and simultaneously the CH signal increases to 0.04 ± 0.005 ML. The fact

that the total C 1s signal is much smaller above 280 K than the initial CH₃ coverage, indicates that parallel to dehydrogenation also recombinative desorption of methane takes place [68, 158]. Upon further heating, starting at around 450 K ($T_{50\%}=500 \pm 10$ K) dehydrogenation of CH takes place, forming carbonaceous surface species.

For the two stepped surfaces, at low temperatures, we find methyl adsorbed on terraces and at steps. As on Pt(111), some CH is found due to the radiation-induced methyl dehydrogenation. For Pt(322), we find dehydrogenation to CH between 190 and 240 K ($T_{50\%}=220 \pm 5$ K), again accompanied by recombinative desorption of methane (as deduced from the drop in the total C 1s signal) - see Fig. 7.8 (b). This dehydrogenation happens for both, the methyl on steps and on the terrace sites, in the same temperature range. Above 250 K coverage of 0.050 ± 0.007 ML for CH is found, slightly higher than on Pt(111). The CH species starts to further dehydrogenate to carbon at temperatures of ~ 370 K ($T_{50\%}=415 \pm 20$ K). This process ends at higher temperatures generating pure carbon.

For Pt(355), upon heating we initially find dehydrogenation of methyl adsorbed at steps ($T_{50\%}=160 \pm 5$ K), leading to an increase in the amount of CH on the surface - see Fig. 7.8 (c). Simultaneously, the total coverage slightly decreases, again due to recombinative desorption of CH₄ and some contribution due to beam damage. This higher reactivity of the steps towards CH₃ dissociation is not found for Pt(322). Upon further heating, the terrace-adsorbed methyl is also dehydrogenating to CH at temperatures ($T_{50\%}=215 \pm 5$ K) ~ 40 K lower than on Pt(111). The resulting CH coverage of 0.065 ± 0.007 ML on Pt(355) is higher than on Pt(111) and Pt(322). Dehydrogenation of CH to adsorbed carbon starts at 370 K ($T_{50\%}=450 \pm 20$ K), i.e. significantly lower than on Pt(111). The results for the thermal evolution of methyl on Pt(322) and Pt(355) are summarized in Tab. 7.1.

Table 7.1: Temperatures of the chemical transitions and methyldiyne coverage found on the three different surfaces.

Surface	$T_{50\%}$ CH ₃ terrace dehydrogenation	$T_{50\%}$ CH ₃ step dehydrogenation	$T_{50\%}$ CH dehydrogenation	CH coverage at 300 K [ML]
Pt(111)	260 ± 5 K	-	500 ± 10 K	0.040 ± 0.005
Pt(322)	220 ± 5 K	220 ± 5 K	415 ± 20 K	0.050 ± 0.007
Pt(355)	215 ± 5 K	160 ± 5 K	450 ± 20 K	0.065 ± 0.007

While the initial sticking coefficient for dissociative adsorption of methane is similar for Pt(111), Pt(322) and Pt(355), the comparison of the thermal evolution on Pt(111) and the two stepped Pt surfaces shows significant differences, indicating an enhanced reactivity of the stepped surfaces towards CH₃ dehydrogenation as well as CH dehydrogenation: The characteristic temperature for CH₃ dehydrogenation is reduced from 260 K on Pt(111) to 220 and 215 K for CH₃ adsorbed on the terraces of the Pt(322) and (355) surfaces respectively. While this temperature is the same for CH₃ at steps and at terraces on Pt(322), we find a much lower value of 160 K for methyl at steps on Pt(355). A possible explanation could be a stronger bonding of methyl on the (111) steps of Pt(355), thus facilitating easier dehydrogenation. Stronger bonding on (111) steps has also been proposed for CO on Pt(355) [49]. This would be in line with the differences in diffusion mentioned above. A similar trend to enhanced reactivity of the stepped surfaces is seen for the dehydrogenation of CH with characteristic temperatures of 415 and 450 K for Pt(322) and Pt(355), respectively, as compared to 500 K for Pt(111).

The apparent contradiction to the work of Gee et al. [157], which shows an enhanced initial sticking probability for the stepped (533) surface, may result from the different reactivity of the stepped surfaces compared to the Pt(111) surface. As their work was performed at 600 K, the found higher sticking probability might be due to the higher reactivity towards methyl and methylidyne dehydrogenation of the stepped surface. This higher reactivity, however, has only indirect influence on the primary dissociation channel, i.e., methane dissociation to methyl.

7.2.3 Radiation induced chemistry

This chapter is concerned with the changes of the adsorbed methyl during exposure to the intense X-ray beam of a synchrotron facility. In the work of Fuhrmann [38] a similar experiment on the flat surface was shown. Upon exposure of the methyl layer to the radiation at 120 K, he found a reduction in the total coverage and a conversion of methyl to methylidyne. In our case, an additional component is involved, namely the methyl adsorbed on step sites. For both stepped surfaces quantitative analyses of such experiments are shown in Fig. 7.9 (a) and (b) for Pt(322) and Pt(355) respectively. Unfortunately, a direct, quantitative comparison between those three

experiments is not possible, as a precise knowledge of the radiation dose is needed, which, however, varies with many parameters, e.g., the current of the storage ring, the mirror alignment, the slit width, etc. Nevertheless, the data in Fig. 7.9 seems to show rather similar radiation doses, under the reasonable assumption of similar reactivity, which can be seen from the loss in total coverage (in both cases $\sim 18\%$), and the comparable amount of CH_3 and CH at the beginning and the end of the experiment.

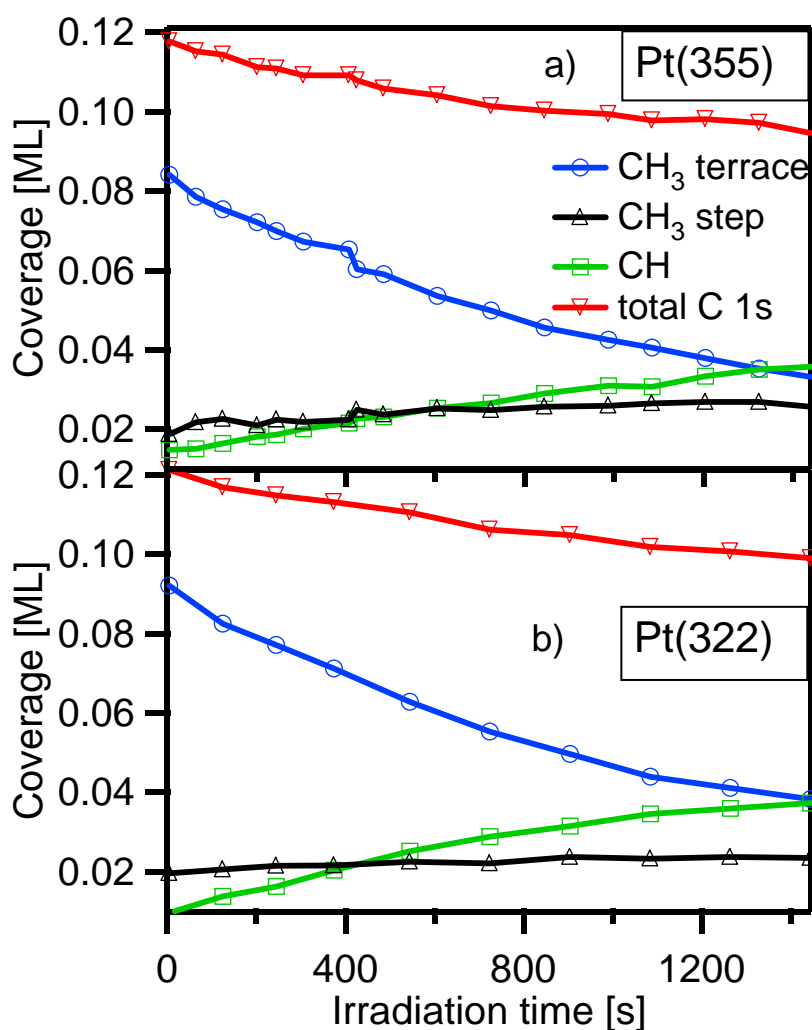


Fig. 7.9: Quantitative analysis of the decomposition of methyl layers adsorbed on a) Pt(355) and b) Pt(322) due to radiation induced dehydrogenation. ($T_S=120$ K) The photon energy was 380 eV and the electron emission angle was 45° .

The analyses for both surfaces show similar trends: The total coverage is reduced as well as the methyl coverage. The methyldyne coverage on the other hand is gaining

intensity throughout the exposure to the X-rays, while the coverage of methyl adsorbed at step sites stays almost constant. Although Fuhrmann [38] claims that the reduction in coverage might be due to photoelectron diffraction, we believe this to be a possible side effect, but overall the effect is too high to be explained exclusively by photoelectron diffraction. It seems more likely that the decomposition of methyl is going along with the desorption of methane [151], even at these low temperatures, due to the space needed for the hydrogen coming from this reaction. Alternatively, the well known effect of photon stimulated desorption PSD could play a role [160].

A quite astounding effect is the relatively inert methyl adsorbed at step sites. Although we have a 50 - 60 % reduction of the methyl adsorbed at terrace sites, we do not observe a decrease in the coverage of methyl adsorbed at step sites, neither from photon stimulated desorption nor from decomposition, compared to the thermal evolution, where the methyl adsorbed at step sites is as reactive as (Pt(322)) or even more reactive (Pt(355)) than the terrace adsorbed methyl. An explanation for this difference is given in the following:

The photon induced desorption might also happen to methyl adsorbed at step sites, but the already discussed diffusion of the methyl on the terraces is always refilling the empty adsorption sites, arising from the desorbing methyl particles. Therefore, the photon induced desorption of the step methyl is in some way contributing to the loss of terrace methyl and might only be found there. Additionally the decomposition of methyl adsorbed at step sites may play a minor role, but is not observed. This might be due to the effect of a different core hole screening. In a DFT study an adsorption site of methyl at the on top sites on a Pt(111) surface is predicted, which we also assume for the adsorption on the terrace sites of the stepped surface. This goes along with the finding of two methyl species, which are similar to the ones found on the (111) surface. A methyl adsorbed on a step site might show a higher degree of interaction with the surface. Upon ionization this higher interaction might facilitate an easier and more efficient movement of the core hole and therefore avoid a decomposition, due to the extra charge in the hydrocarbon system. This higher efficiency in charge transportation is certainly also found for excitations due to secondary electrons from the substrate. Similar results are obtained in the system cyclohexane on Ni(111). Cyclohexane is physisorbed on the surface and upon exposition to an intense X-ray beam desorption and rapid decomposition is observed [130]. The system of chemisorbed benzene, another six

membered cyclic hydrocarbon, on Ni(111) shows different results. No photon stimulated desorption and no significant decomposition are found, which might be due to the enhanced coupling to the substrate, therefore allowing a more efficient screening of the core hole and an improved transport of charge from the substrate to the adsorbate [47].

7.2.4 Summary and conclusions

A combined XPS and molecular beam study of the adsorption properties of methane on the (355) and (322) surfaces of platinum was carried out and the data were compared to results obtained for the Pt(111) surface. From the high resolution C 1s spectra, we were able to distinguish different adsorbed species. For the two stepped surfaces, we found a methyl species adsorbed at step sites and a methyl species adsorbed on the terraces. In our analysis we observe different binding energy differences between the step and terrace species for the two stepped surfaces, which we attribute to the different step orientations and, therefore, different local adsorption sites. From the quantitative analysis, the total coverages as well as (for the stepped surfaces) the partial step and terrace coverages were obtained. The total coverages of Pt(111), Pt(322) and Pt(355) were found to be similar; however, for Pt(355) we found a lower terrace coverage and a higher step coverage as compared to Pt(322). The total relative initial sticking coefficients (for steps + terraces) were found to be similar for all surfaces studied, i.e., for Pt(111), Pt(322) and Pt(355), independent of the steps and their orientation. The detailed analysis showed that on Pt(355) at very low coverages significant diffusion of methyl from the terraces to the steps occurs, which is less pronounced on Pt(322).

The thermal evolution of the adsorbed species was examined by temperature programmed XPS experiments. We found a higher reactivity towards the dehydrogenation of methyl to methylidyne and also of methylidyne to carbon for the stepped surfaces as compared to the flat surface. Additionally, we found differences in the reactivity of the step sites: Methyl adsorbed at the (111) steps of the Pt(355) surface is dehydrogenated at significantly lower temperatures than methyl on terraces and also than methyl adsorbed at the (100) steps of the Pt(322) surface. In contrast to the thermal evolution we found a high stability of the step adsorbed species towards any photon induced reaction, which is attributed to the enhanced

coupling of the step adsorbed methyl as compared to the terrace adsorbed methyl species.

In conclusion, it was shown, that steps have no influence on the direct dissociation channel, but do change the reactivity for following surface reactions. The consequence for realistic processes, taking place at higher temperatures, is a higher overall reactivity of stepped surfaces.

7.3 Methane adsorption on silver modified stepped Pt surfaces

In the previous chapter the adsorption and reaction of methane on stepped surfaces were discussed. It was shown, that the primary adsorption step was not influenced by the existence of steps. The reaction on the other hand showed a large effect with a shift of the dehydrogenation temperatures of the chemical species to lower temperatures. Now the question arises whether also chemically modified steps, in our case consisting of chemically inert silver, still facilitate a comparative sticking probability. Certainly also the total and partial coverages of the carbon species present are of interest and the question whether the blocking of step sites occurs.

The reaction is addressed again by TPXPS experiments, which shall show whether the “passivation” of the step sites with silver leads to a decreased reactivity, or whether the existence of steps, independent of their chemical reactivity allows for a reaction at lower temperatures.

At first the preparation of the silver layers is shortly discussed. In the second part the adsorption and in the third part the reaction of methyl on such silver precovered platinum surfaces is described.

7.3.1 Preparation of the silver layers

The silver was evaporated by an electron beam evaporator, from a molybdenum crucible with a growth rate of $\sim 0.5 \text{ \AA} / \text{min}$. The growth rate was determined by a quartz micro balance before every preparation. The sample temperature was 300 K during the evaporation as pseudomorphic growth and step decoration is predicted at this temperature [161-164]. The actual thickness was subsequently verified with XP spectra of the Ag 3d and the Pt 4f regions. The definition of coverage was adapted

from Davies [164] and is analogous to the work of Tränkenschuh [4], who showed that 0.2 ML of silver correspond to one row of silver atoms decorating the steps. For a more detailed description of the silver layers and their preparation see Refs. [4, 165].

7.3.2 Adsorption of methane on the two silver modified stepped platinum surfaces

In Fig. 7.10 selected C 1s spectra of the adsorption of methane on silver precovered Pt(355) and Pt(322) are shown.

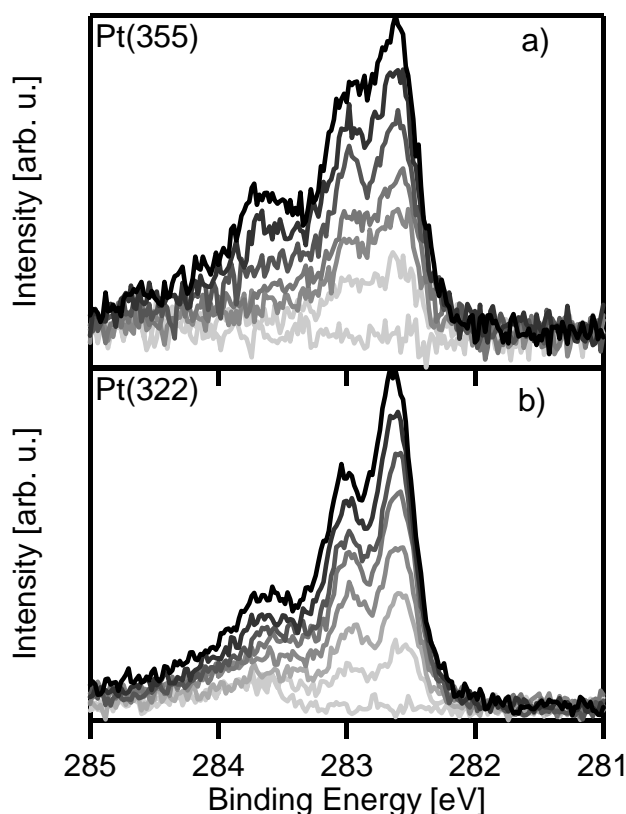


Fig. 7.10: Selected C 1s spectra of the adsorption of methane ($E_{kin} = 0.45$ eV) on a) a Pt(355) surface, precovered with 0.30 ML of silver and b) a Pt(322) precovered with 0.32 ML of silver. The spectra were recorded with a photon energy of 380 eV at an electron emission angle of 45° . The sample temperature was ~ 120 K. The grey scale indicates the rising coverage; darker lines stand for higher exposures.

The spectra display the features already discussed in chapter 7.2.1. We find three main peaks in the spectra at 282.6, 283.0 and 283.6 eV in the C 1s spectra of methyl on the silver precovered surface. The main difference to the spectra reported in chapter 7.2, is that the ratio of the second peak in respect to the first peak at 282.6 eV is significantly lowered, which leads to a high similarity to the spectra of methane on the flat Pt(111) surface. In chapter 7.2 it was shown, that this ratio is a measure of the (in-) existence of methyl adsorbed at step sites. Nevertheless, as we are studying a stepped surface, although silver modified, the modeling of the XP spectra will include a step methyl species, to achieve satisfying results and to judge the extent of the passivation by the additionally adsorbed silver.

A more accurate description is given by a quantitative analysis of the C 1s spectra, which is shown in Fig. 7.11 (b) and (c) for Pt(355) and Pt(322) respectively. Additionally we added for an easy comparison an analysis for data on the Pt(111) crystal in Fig. 7.11 (a). The quantitative analysis is performed as described in the previous chapters. We again used two independent methyl species each consisting of three dependent peaks and a single methylidyne species consisting of two dependent contributions. An exact description of the parameters and functions used is given in chapter 7.2.

A decrease of the total coverage is found for both silver precovered stepped surfaces, as compared to the Pt(111) surface. Note that the total coverage of the clean, stepped surfaces and the flat surface are similar. A clear difference between the two stepped surfaces is the existence of a small amount of methyl adsorbed at step sites on the (355) surface, while the (322) surface shows almost no population of these sites. The (322) surface precovered with 0.32 ML of silver shows a behavior that goes along with the description of a silver passivated platinum surface. The silver arranged at the step sites hinders the dissociative adsorption of methane at and the diffusion of methyl to these sites, as the sticking coefficient of methane on silver is negligible, as was shown by an adsorption experiment of methane on a Pt(111) surface precovered with 1 ML of silver. The lower total coverage is also supporting this argumentation, see below.

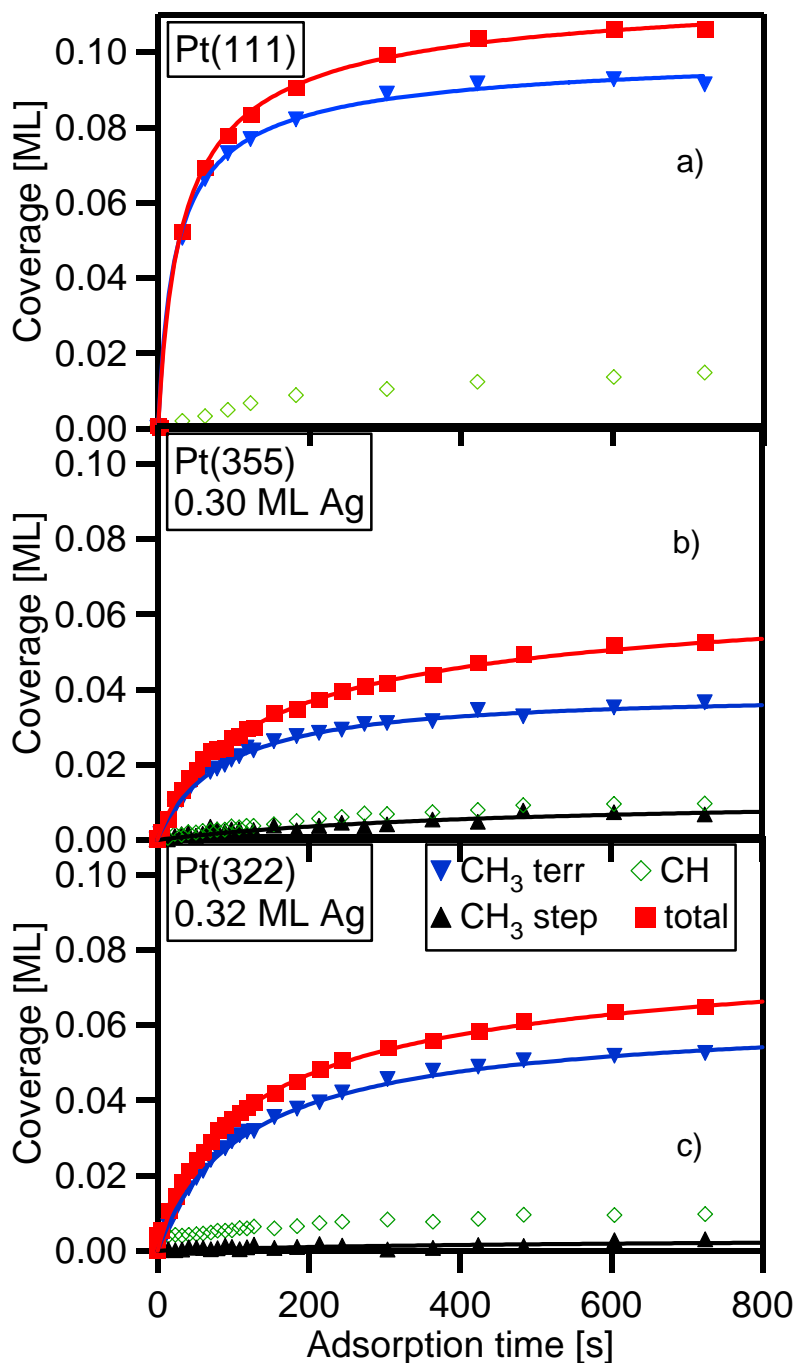


Fig. 7.11: Quantitative analysis of the experiments shown in Fig. 7.10. Coverage during exposure to methane with a kinetic energy of 0.45 eV. Shown are the total as well as the partial coverages of the involved chemical species on a) Pt(111), b) Pt(355) precovered with 0.30 ML of silver and c) Pt(322) precovered with 0.32 ML of silver. The legend in Fig. 7.11 (c) is valid for all experiments.

The behavior on the (355) surface nevertheless is rather different. Although we find again a reduced total coverage, as expected from the passivation with silver, a small, but significant step contribution is observed. A closer examination shows a slow increase of the step species, in contrast to the step increase of the step methyl on

the clean surface. This change in the population rate indicates a higher adsorption energy of the step sites for methyl compared to the previously adsorbed silver. Note that the passivation is, thus, not complete. The silver lowers the total coverage but cannot prevent the diffusion to step sites. This happens only for the stronger bond methyl at the (111) steps of the (355) surface, which also show a higher reactivity in the TPXPS experiment in chapter 7.2.2. The methyl bond at the (100) steps is not showing a higher binding energy than silver towards the step binding site and is therefore not displacing it there. A similar behavior was observed with CO on silver precovered stepped platinum surfaces [4]. Here CO displaces the silver on both surfaces: in the case of the (355) surface the silver is totally removed from the steps to form islands on the terraces, while in the case of the (322) surface only a partial removal of silver step atoms is observed. In the case of CH₃ adsorption reported here only a comparatively low methyl step coverage on the (355) crystal was found; this points to the fact, that only a partial removal of silver from the step sites by methyl took place, while on the (322) crystal the bond energy of the silver adsorbed on the step sites is higher compared to methyl and, therefore, no removal takes place. This again shows the high mobility of the methyl adsorbed on the platinum surfaces, already discussed in chapter 7.2.1. The reduction of the total coverage is in both cases ~40% compared to the clean crystals. Which is slightly higher than the expected value (0.3 ML correspond to ~ 30 % of the surface), and shows, that the silver is indeed passivating the platinum surfaces, allowing no adsorption on the silver precovered parts.

The coadsorption of NO or CO on an already methyl precovered stepped platinum surface, showed similar results: A depletion of the reactive step sites for the methyl was observed, leading to NO and CO adsorbed at the step sites and methyl adsorbed on the less reactive terraces. These conclusions might enable us to learn about relative binding energies by rather simple coadsorption experiments, which is a valuable tool to estimate possible poisoning processes in heterogeneous catalysis.

The relative initial sticking coefficient of methane with a kinetic energy of 0.73 eV was determined to be $5 \cdot 10^{-4}$ and $7 \cdot 10^{-4}$ for the silver precovered Pt(355) and Pt(322) surfaces, respectively. The rel. S_0 was determined as explained in chapter 7.2.1. The decrease by a factor of ~5 in the rel. S_0 , compare to Fig. 7.6, cannot only be explained by the passivation of 30 % of the platinum surface, leading to a decrease of 30% in the rel. S_0 . Also the passivation of the step sites should not

influence the sticking probability, as the step sites do not influence the sticking probability, as we know from chapter 7.2.1. Therefore we have to consider electronic effects to be responsible for this drastic effect. Nevertheless, we have to mention that a further investigation of these effects should be considered as only a small number of measurements were performed up to now.

7.3.3 Thermal evolution of methyl layers on silver precovered platinum surfaces

In the thermal evolution of adsorbed methyl on silver passivated platinum surfaces the question arose, whether the mere existence of steps is sufficient to change the transition temperatures or whether the chemical nature of the steps is of interest. Selected C 1s spectra of TPXPS experiments of methyl layers on the silver-precovered stepped platinum surface are shown in Fig. 7.12.

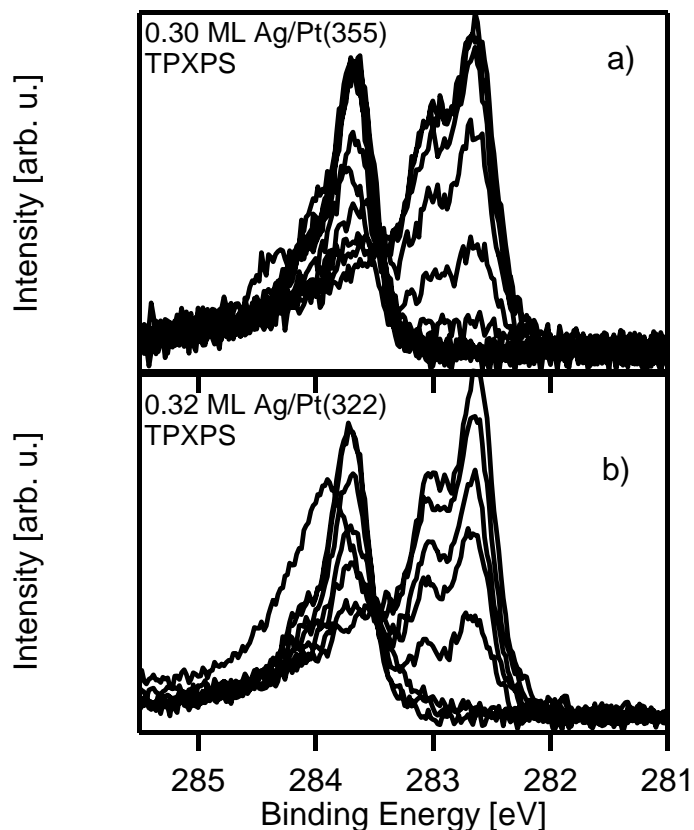


Fig. 7.12: Selected C 1s spectra of TPXPS experiments of the methyl layers on a) Pt(355) and b) Pt(322) shown in Fig. 7.10. The silver precoverage was 0.30 and 0.32 ML for the Pt(355) and the Pt(322) surface, respectively. ($\beta=0.5$ K/s)

A qualitative comparison of the two experiments shows a rather similar picture of which only a quantitative analysis, shown in Fig. 7.13, will give a deeper insight. The modeling of the spectra again was done according to the procedure discussed in chapter 7.2.1. It has to be mentioned, that the TPXPS experiments were conducted on the same layer as shown in the adsorption experiments in chapter 7.4.2, but on a different spot on the crystal, leading to the expected lower methylidyne coverage and to minor differences in the step coverages which are well within our error of $\sim 0.05\%$ of a monolayer. Nevertheless, the trend observed in the adsorption experiments is still clearly visible. The coverage of methyl adsorbed at step sites in the case of the (355) surface is still higher than in the case of the (322) surface.

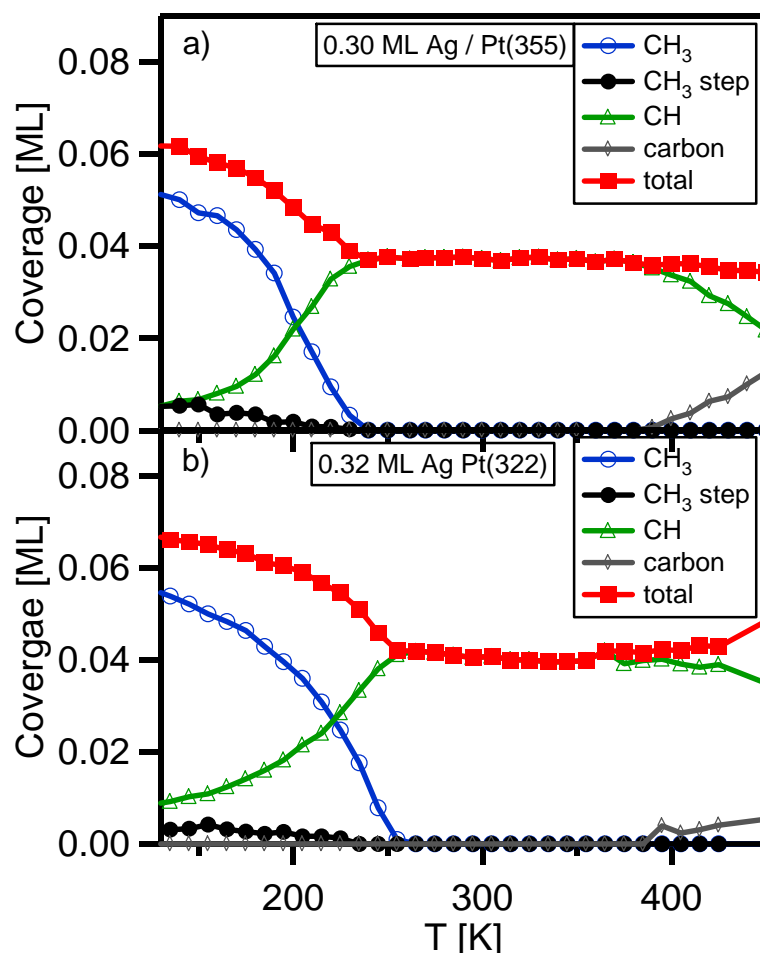


Fig. 7.13: Quantitative analysis of the TPXPS experiments on a) Pt(355) and b) Pt(322), shown in Fig. 7.12. The silver precoverage was 0.30 and 0.32 ML for the Pt(355) and the Pt(322) surface, respectively. The experiments were starting from the layers shown in Fig. 7.10.

In the quantitative analysis, shown in Fig. 7.13 (a) and (b), of the experiments on the silver precovered surfaces we find a similar result as for the clean stepped surfaces: The conversion temperature ($T_{50\%}$) of both crystals is reduced compared to the flat surface. For the silver covered Pt(355) surface we find a temperature of 205 ± 5 K for the conversion of methyl to methylidyne and for the (322) surface a conversion temperature of 220 ± 5 K again for the decomposition of methyl to methylidyne. A comparison to the clean stepped surfaces shows clearly that the surface reaction of the methyl adsorbed on terrace sites is not affected within the margins of error by the additional silver on the surface, predominantly adsorbed at steps. An exact value of the conversion temperatures for methyl adsorbed at the step sites is not given, as the amount is too low to give significant values. The transition temperatures of methyl to methylidyne shows that mainly the geometric alignment and the different electronic structure related to the reduced terrace width are responsible for the higher reactivity of the stepped surfaces. The steps, at least partially are passivated by the silver atoms.

The methylidyne coverage is 0.04 ± 0.01 ML on the (355) and 0.045 ± 0.01 ML on the (322) surface. This corresponds, within the margin of error, to a 30% reduced CH coverage as could be expected when regarding a 30% “smaller” surface due to silver adsorption. For the values of the clean stepped surfaces see chapter 7.2.2.

7.3.4 Conclusions and summary

In this chapter we discussed the effects of silver towards the adsorption of methane and the reactivity of methyl on stepped platinum surfaces. In-situ HRXPS results of the dissociative adsorption of methane showed a lower value for the total coverage, and additionally in the partial coverages on the silver precovered surface. The reduced methyl coverage can be explained by silver passivation of the surface not allowing adsorption on the silver covered parts. Interestingly on the (355) surface a significant amount of methyl adsorbed at step sites was found indicating that parts of the silver atoms are moved away from the step edges to the terraces, allowing methyl adsorption at the step edges. This only happens on the (355) surface but not on the (322) surface, which was proposed to have a weaker bonding between the methyl and the step sites, resulting in a different step coverage. The reaction during the temperature-programmed experiments showed no significant differences between

the clean and silver precovered surfaces. The conversion temperatures are similar to the ones observed for the reaction on the clean stepped surfaces. This shows that the electronic alignment due to the reduced dimensions of the terraces is more important than the chemical nature of the steps and their surrounding.

7.4 Kinetic isotope effects in the adsorption and decomposition of methane on stepped platinum surfaces

For the dissociative adsorption of methane a kinetic isotope effect was found. The initial sticking coefficient of deuterated methane was reported to be only one third compared to the one of non deuterated methane [144]. On Ru(001) an even larger kinetic effect was found [166]. The authors of Ref. [166] also point out, that the tunneling mechanism discussed in some publications is not necessary to explain the results, but it was used in early, three-dimensional calculations. In the deuterated state differences, in comparison to the non-deuterated case, as, e.g., energy of the transition state, internal vibrations, vibrational frequencies and their excitation etc. are observed, which might lead to this large isotope effect, have to be considered. Unfortunately almost all measurements, reported in literature, were performed at elevated surface temperature, which might lead to further differences between calculations and experiment, as theory only discusses the first step of the dehydrogenation of methane to methyl. The further dehydrogenation, from methyl to methylidyne and subsequently to carbon, also happening at higher temperatures, was not taken into account. The effects occurring at these higher temperatures are discussed in chapter 7.4.2.

At first we want to discuss the extent of the isotope effect in the adsorption at low temperatures by time dependent in-situ XPS which allows determining exact values for the relative sticking coefficient of deuterated methane. The adsorption at low temperatures might allow a better comparison to theoretical calculations, only concerned with the activated dissociative adsorption of methane, which are not including the subsequent surface reactions ($\text{CH}_3 \rightarrow \text{CH} \rightarrow \text{C}$). In the second part the decomposition of methyl on the surfaces of the three platinum crystals will be discussed, separately from the adsorption. The implication of steps in our analysis might lead to a further insight into the mechanism of the associative desorption and

the decomposition of methyl on the surface and certainly in the dissociative adsorption of methane.

7.4.1 Kinetic isotope effects in the adsorption of methane

In the chapter 7.2 the adsorption of methane was discussed and a comparison to adsorbed, deuterated methyl was shown. The whole adsorption experiments are shown in Fig. 7.14. The adsorption leads to the already in chapter 7.2 discussed spectral features: On the (111) surface of platinum three peaks can be observed, one at 282.6 eV which was assigned to the adiabatic transition, one at 282.9 eV which is attributed to the first vibrationally excited state of the core hole state. The third peak at 283.6 eV belongs to the second chemical species present on the surface, namely methylidyne. For the stepped surfaces the same peaks can be found, but in addition a second methyl species adsorbed at step sites can be found with the peak of the adiabatic transition at ~282.9 eV, leading to additional intensity at this position. This can easily be seen at low coverages, due to the fast population of the step sites compared to the terrace sites.

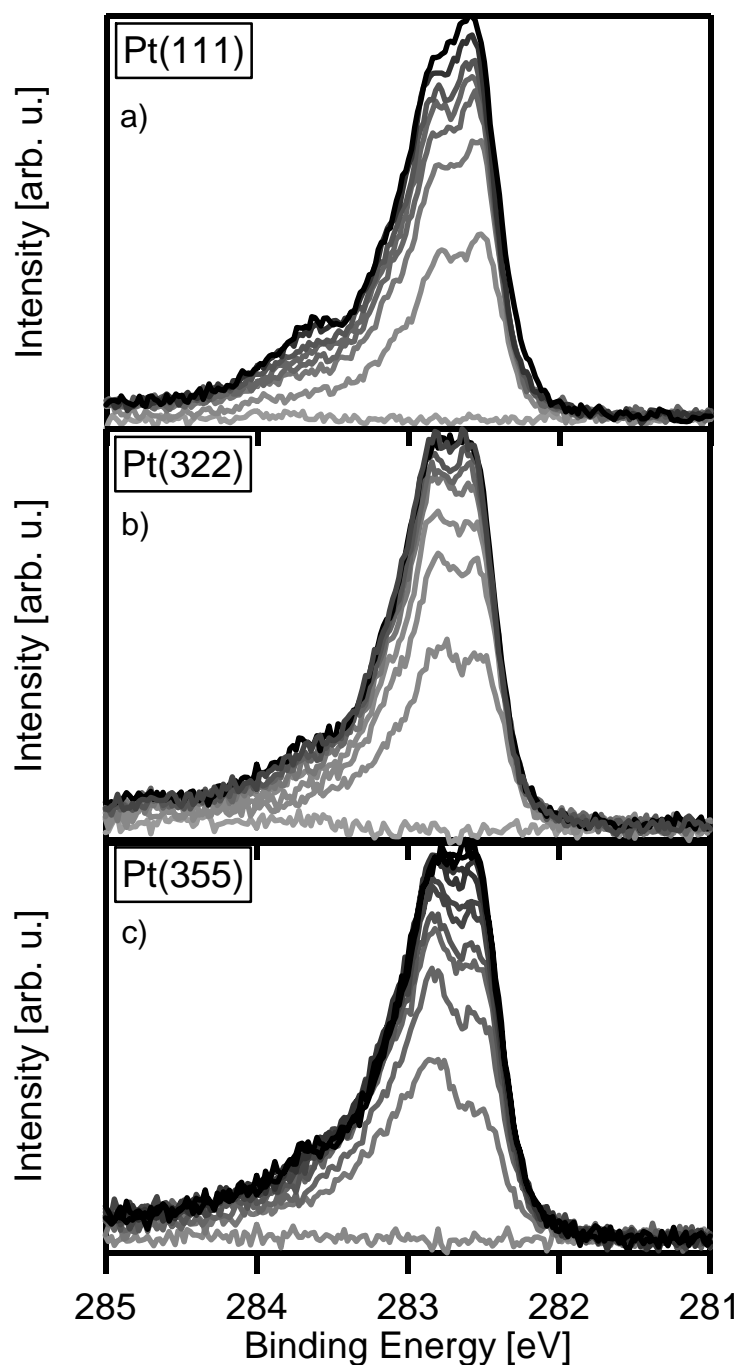


Fig. 7.14: Selected C1s spectra of the adsorption of deuterated methane on a) Pt(111), b) Pt(322) and c) Pt(355). The methane molecules were impinging at normal incidence. The value for the kinetic energy of the impinging CD_4 molecules is discussed in the text. The electron emission angle was 45° .

Although the experiments of deuterated methane were performed with the same parameters, as nozzle temperature, seeding ratio, the kinetic energy of the impinging

molecules is not the same as in the case of the non deuterated methane, due to their different molecular weight. The mean velocity of molecules from a supersonic molecular beam can be estimated by:

$$\langle v \rangle = \sqrt{\frac{(5 + A_{Me})kT_0}{A_{He}m_{He} + A_{Me}m_{Me}}}$$

with

A_{He} , A_{Me} : fraction of helium, methane

m_{He} , m_{Me} : mass of helium, methane

T_0 : nozzle temperature

k : Boltzmann constant

The estimation of the absolute velocity of, e.g., CO from this equation is known to yield errors of up to 30% [167]. This high error is occurring due to the velocity slip in the seeding procedure, which depends on the mass of the participating gases. We only calculate the relative velocity of methane and should therefore get a result with a lower absolute error. Starting from the measured values of the kinetic energy of methane, a ~3% higher terminal velocity for the deuterated methane can be calculated. This leads to a ~8% higher kinetic energy for the deuterated species, in this case 0.77 eV. Still some errors might be included, as we did not estimate the velocity and the temperature slip of the heavier (deuterated) molecules, which might lead to a slightly lower kinetic energy as the estimated value discussed above and also to a higher flux of deuterated methane molecules on the surface.

The quantitative analysis of the experiments of Fig. 7.14 are shown together with analysis of similar experiments on the stepped surfaces with non deuterated methane, as well as of experiments on the flat (111) surface.

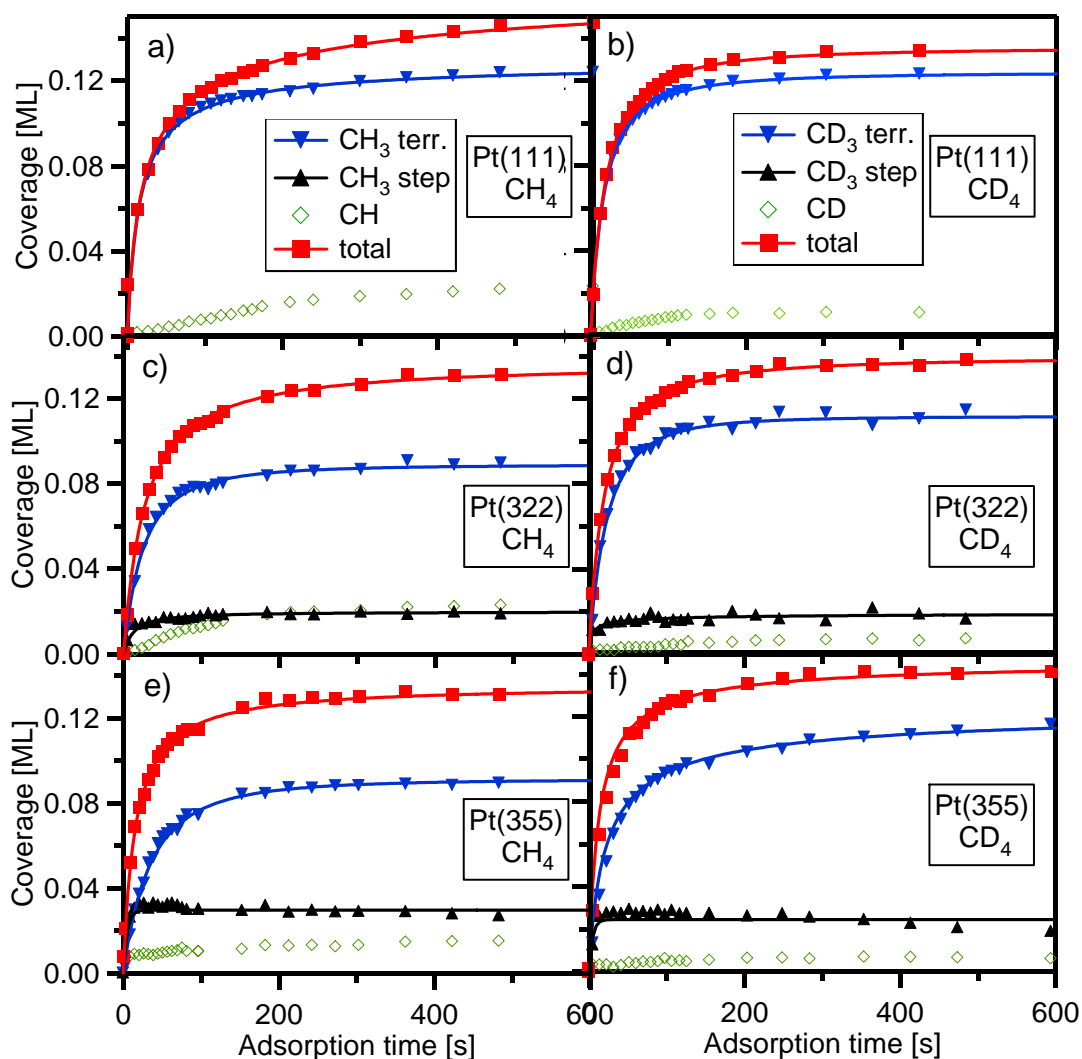


Fig. 7.15: Quantitative analysis of the experiments shown in Fig. 7.13 and of similar experiments with non-deuterated methane. In a), c) and d) the results from experiments of the adsorption of CH_4 ($E_{\text{kin}}=0.71$ eV) on Pt(111), Pt(322) and Pt(355), respectively, are shown. In b), d) and f) the respective experiments with CD_4 ($E_{\text{kin}}=0.77$ eV) on the Pt(111), Pt(322) and Pt(355), respectively, are shown.

The coverage vs. adsorption time plots for the respective surfaces show rather similar results as can be seen in Fig. 7.15 (a)-(f). The total coverages for the deuterated and the non deuterated molecules are similar, but the CD_3 coverage is in all cases larger than the corresponding CH_3 coverage on terraces, which is compensated for by the higher amount of CH formed by radiation. This already shows a trend of CD_3 to be slightly more stable due to the lower zero point energy of

the CH bond. The amount of methyl species adsorbed at step sites is unaffected by the different isotope used.

The mathematical modeling (solid lines) of the data shown in Fig. 7.15 is used to calculate the relative initial sticking coefficient, shown in Fig. 7.16.

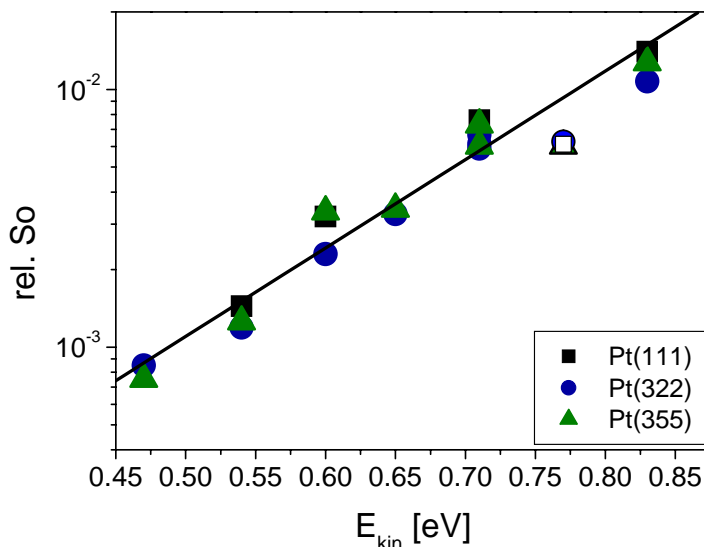


Fig. 7.16: relative initial sticking coefficient (rel. S_0) of CH_4 (filled symbols) and CD_4 (open symbols).

The relative initial sticking coefficient of the deuterated methane show a similar behavior for all surfaces, as expected from the experiments with non-deuterated methane. The relative initial sticking coefficient of deuterated methane would be similar to the rel. S_0 of non-deuterated methane, without the correction of the kinetic energy performed above. Nevertheless, only a factor of approx. two is found, compared to the predicted factor of three from literature [144]. This holds true for the adsorption on the stepped as well as the flat surface. A larger data set is not shown as no further conclusions are drawn and the literatures data was well reproduced. The expected error in the kinetic energy and the difference in flux may be responsible for this difference to the literature results. Certainly this also might be explained by the difference in surface temperature in this report (120 K) and in literature results (>500 K). The thermal evolution, i.e., the surface reactions are discussed in the following chapter.

7.4.2 Kinetic isotope effect in the thermal evolution of methane

The TPXPS experiments of deuterated methyl and non-deuterated methyl are shown in Fig. 7.17.

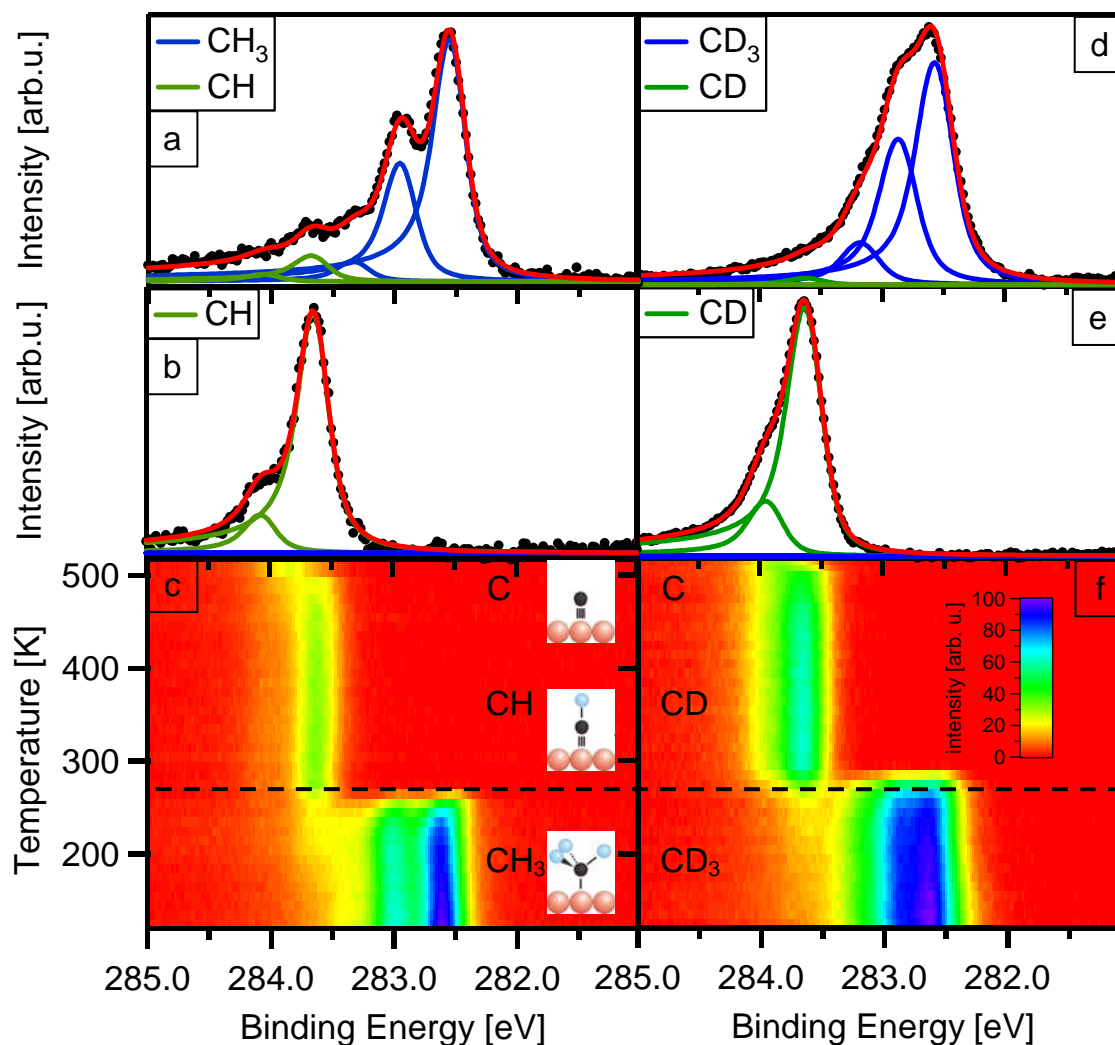


Fig. 7.17: C 1s spectra of the adsorbed non-deuterated (left) and deuterated (right) species on Pt(111). (a) and (c) show the spectra of CH_3 and CD_3 , formed after exposing the surface to CH_4 and CD_4 , respectively, including the corresponding fits. (b) and (d) show the spectra of CH and CD, respectively, formed after heating the adsorbed methyl layers to 350 K, with the corresponding fits. In (c) and (f) C 1s spectra recorded continuously during heating the adsorbed methyl layers to 350 K are shown as color-coded density plots; ($\beta=0.5$ K/s). All C 1s spectra were recorded at 45° off normal emission, with a photon energy of 380 eV. The insets show the intensity scale for the density plots and schematic pictures of the surface species.

The corresponding C1s spectra of CH₃ and CD₃ on Pt(111) are shown in Fig. 7.17 (a) and (d) (top). They display a main peak at 282.6 eV, accompanied by two equidistant satellite lines at higher binding energies, due to vibrational excitations upon photoionization. The energetic separations of 400 and 295 meV, in Fig. 7.17 (a) and (d), are typical of C-H and C-D vibrations, respectively, with a ratio of close to $\sqrt{2}$, as expected [26]. Upon heating to ~ 300 K, the spectral shape of the C 1s spectra changes dramatically, leading to the spectra shown in Fig. 7.17 (b) and (e), which are indicative of the formation of methylidyne, with the main peak at 283.61 eV [4, 68]. For both CH and CD again a satellite line is observed, now with energetic separations of 420 and 317 meV, respectively. In comparison to methyl the intensity ratio of the first satellite peak relative to the main peak is strongly reduced, from 0.50 (0.71) to 0.16 (0.22), when comparing CH₃ (CD₃) and CH (CD). This decrease by about a factor of 3 is attributed to the fact that the number of H (D) atoms per carbon atoms is reduced from 3 to 1 [4].

Similar experiments for the thermal evolution of deuterated methyl on the two stepped surfaces have been performed, and are shown in Fig. 7.18.

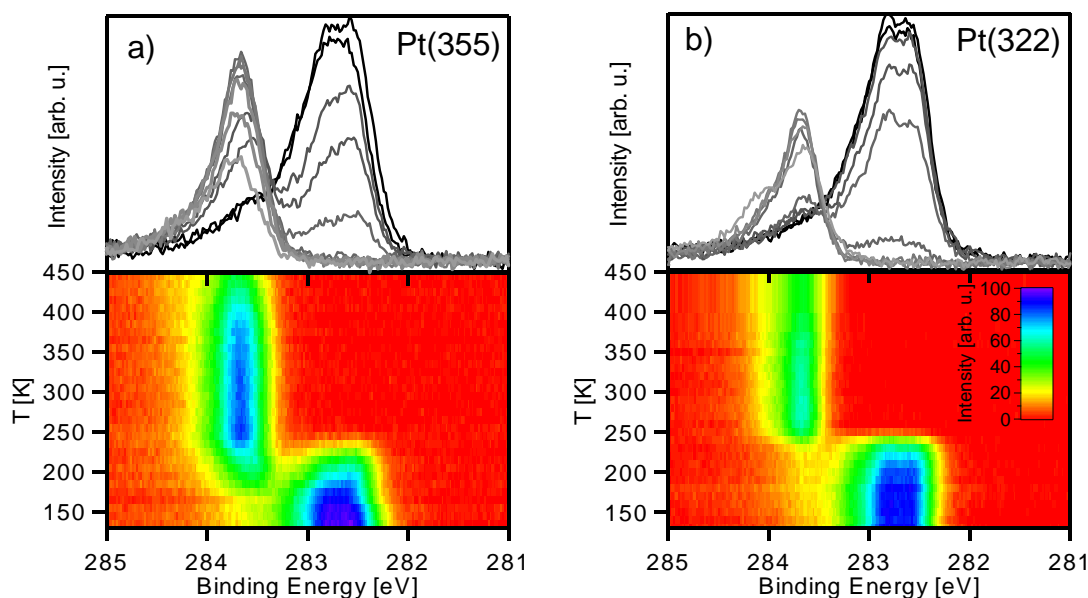


Fig. 7.18: Selected C 1s spectra of the thermal evolution of deuterated methane on a) Pt(355) and b) Pt(322). Color coded density plots of the same experiments are shown in the lower part. The heating rate was 0.5 K/s. Inset: intensity scale of the density plots.

In the upper parts waterfall plots of the C 1s spectra acquired during heating of a CD₃ layer on the Pt(355) (Fig. 7.18 (a)) and the Pt(322) (Fig. 7.18 (b)) surface are shown; the lower parts show color coded density plots of the same experiments. The spectra for the two surfaces clearly show the transition from deuterated methyl to deuterated methylidyne, with the adiabatic peaks at 282.6 and 283.6 eV, respectively.

For both stepped surfaces (see chapter 7.2.1), an additional methyl species can unequivocally be identified, which is attributed to adsorption at step sites; the corresponding XP spectra obtained after adsorption at <120 K and the peak fitting can be found in Ref. [168] / chapter 7.2.1. Interestingly, upon heating the stepped surfaces with methyl adsorbed at terrace sites and step sites, only one CH species was observed [168]; this is also found for the decomposition of deuterated methyl on the stepped surfaces in this chapter.

The transition from methyl to methylidyne for all substrates was followed in situ for comparable initial methyl coverages (0.11 – 0.13 ML), using a heating rate of 0.5 K/s; the corresponding spectra for Pt(111) are shown in a color-coded density plot in Fig. 7.17 (c) and (f) for CH₃ and CD₃, respectively and for CD₃ on the two stepped surfaces in Fig. 7.18. The quantitative analysis of the data obtained for the reaction on the (111) surface is shown in Fig. 7.19, where the coverage of methyl and methylidyne, as determined from the C1s peak areas, are plotted versus temperature. From the data in Figs. 7.17, 7.18 and 7.19, it is evident that no surface species other than methyl and methylidyne are present in the temperature range up to 400 K. In particular, there is no evidence for the formation of methylene (CH₂ or CD₂), which has been proposed in one previous study [169]. Furthermore, for both CH₃ and CD₃ a significant reduction of the total coverage occurs parallel to the transition from methyl to methylidyne, due to recombinative desorption of methane, formed from methyl and atomic hydrogen. To illustrate this behavior, the amount of desorbed methane (CH₄ and CD₄) is plotted in Fig. 7.19 for Pt(111); it is determined by subtracting the total coverage at a given temperature from the initial total coverage.

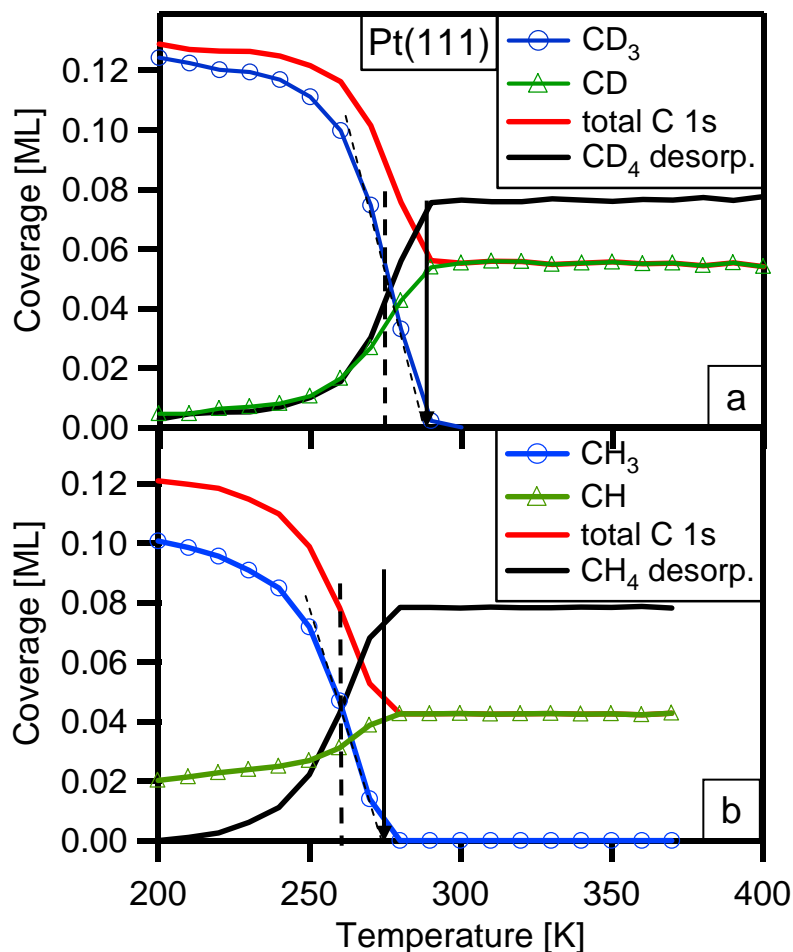


Fig. 7.19: Quantitative analysis of the TPXPS experiments of a) deuterated methyl (CD_3) and b) non-deuterated methyl (CH_3) adsorbed on Pt(111). The dotted line indicates the $T_{50\%}$ value, while the arrow indicates the characteristic temperature. For further information see text.

For both isotopes, a small initial methyldiene coverage is observed in our experiments, due to radiation damage by synchrotron radiation, which increases with temperature (i.e., measuring time) due to the accumulated exposure to photons. The magnitude of this effect is more pronounced for the non-deuterated species.

The comparison of the thermal evolution of CH_3 and CD_3 on all surfaces studied reveals a pronounced isotope effect in both the transition temperature from methyl to methyldiene and in the desorption temperature of methane. To analyze the decomposition process, we use the temperature, where the methyl coverage becomes zero (as determined by linear interpolation of the data) as characteristic temperature.

For Pt(111) (and also for the terrace methyl on the stepped surfaces, see below) this temperature coincides with the temperature, where the CH coverage reaches its saturation to within ± 2 K. Using this approach, the characteristic temperatures for CH₃ and CD₃ on Pt(111) are determined to 274 ± 2 K and 290 ± 2 K, respectively, yielding an isotope effect of 16 ± 2 K. Alternatively, we can also determine the temperature, where the methyl signal is decreased to 50% of its initial value (determined at 200 K); the corresponding values are 260 ± 3 K for CH₃ and 275 ± 3 K for CD₃, yielding an isotope effect of 15 ± 6 K. However, this approach has significantly larger error bars and, thus, is not used in the following.

For CH₃ on Pt(111), also measurements at other total initial coverages, ranging from 0.04 to 0.17 ML have been performed. They show a tendency to lower transition temperatures at lower coverages, with a value of 269 ± 2 K for 0.04 ML. This indicates that the characteristic temperature only weakly depends on the initial coverage. Furthermore, measurements with different fractions of CH formed by beam damage prior to heating yield identical characteristic temperatures, ensuring that this value is not significantly affected by the methylidyne already formed by radiation damage. The measurements with different initial coverages of 0.04, 0.11, 0.14 and 0.17 ML yield methylidyne coverages of 0.03, 0.04, 0.04 and 0.05 (± 0.01) ML, respectively, indicating that there is a saturation coverage of adsorbed CH and that the amount of desorbing methane strongly increases with initial methyl coverage. The latter observation is in line with investigations of Zaera, who only found methane desorption after dissociatively adsorbing methyl iodide (yielding surface methyl) when coadsorbing significant amounts of hydrogen [170].

The quantitative analysis of the thermal evolution of methyl on the two stepped surfaces is shown in Fig. 7.20.

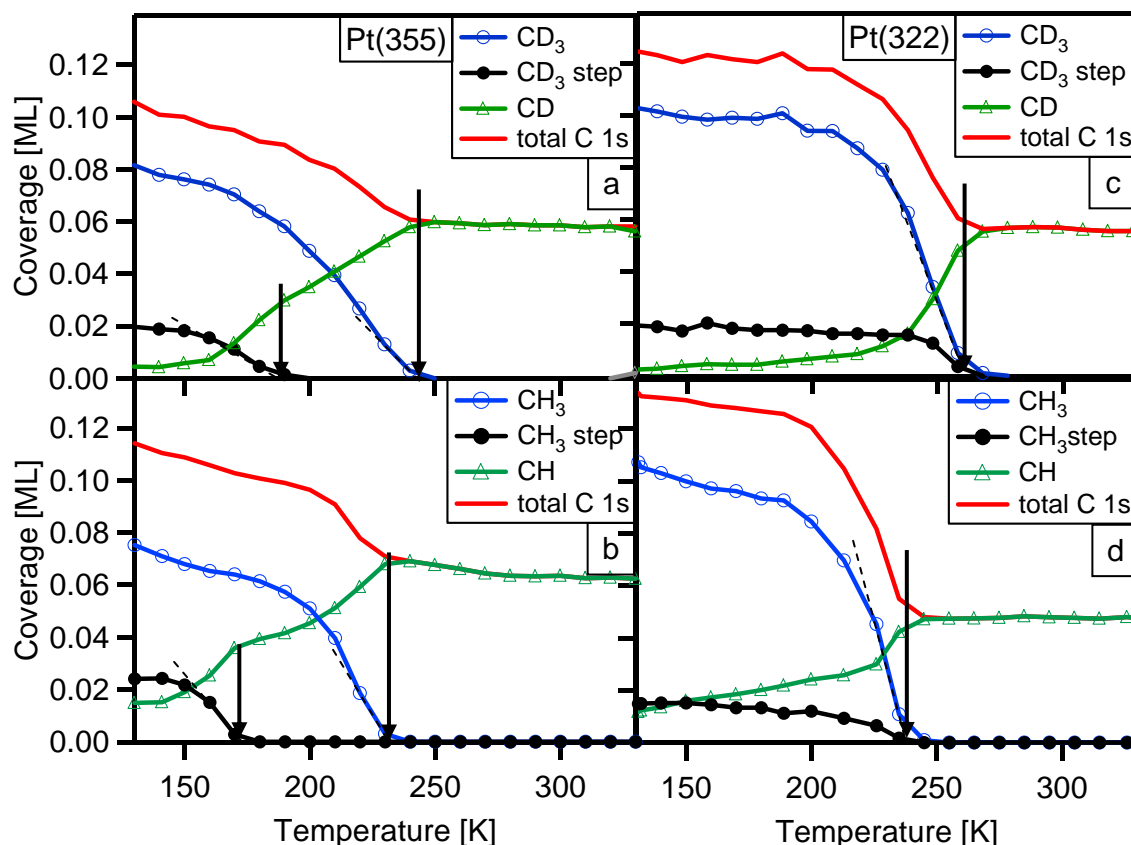


Fig. 7.20: Quantitative analysis of the TPXPS experiments of a) deuterated methyl (CD_3) on Pt(355), b) non-deuterated methyl (CH_3) on Pt(355) and c) deuterated methyl (CD_3) on Pt(322), d) non-deuterated methyl (CH_3) on Pt(322). The arrows indicate the characteristic temperatures.

For both surfaces dehydrogenation of both CH_3 and CD_3 occurs at lower temperatures than on Pt(111), indicating an enhanced reactivity of the steps towards dehydrogenation of methyl (note that no difference was observed in the dissociation probability of methane to methyl at 120 K [168]). For Pt(322), decomposition of terrace methyl and step methyl to methylidyne occurs at the same temperature, with characteristic temperatures of 238 ± 3 K for CH_3 and 260 ± 3 K for CD_3 yielding an isotope effect of 22 ± 6 K. As compared to Pt(111), the characteristic temperature for CH_3 and for CD_3 dehydrogenation are shifted to lower values by 36 and 30 K, respectively.

For Pt(355), different dehydrogenation temperatures are observed for terrace methyl and step methyl, yielding values of 232 and 243 K for CH₃ and CD₃ at terrace sites, i.e., shifted to lower temperatures as compared to Pt(111) by 42 and 47 K respectively; the characteristic temperatures for methyl at steps are 173 ± 3 K for CH₃ and 189 ± 3 K for CD₃. The corresponding isotope effects for terrace and step sites are 11 ± 6 K and 16 ± 6 K, respectively. Note that the error bars for the stepped surfaces are larger than for Pt(111), where a larger data set is available.

For all substrates the analysis shows that after the initial reaction (= activated dissociative adsorption)



at low temperature, yielding adsorbed methyl and atomic hydrogen, upon heating two reactions occur parallel on the surface, namely CH₃ dehydrogenation and recombinative methane desorption:



The analysis of the isotope effect is complicated by the facts that these two reactions occur in parallel and are coupled, i.e., H formed by reaction (2) will contribute to reaction (3). Furthermore, the observed saturation of the CH coverage at ~0.05 ML indicates that CH₃ decomposition is limited by the available adsorption sites for the products, i.e. CH and 2H; note that desorption of hydrogen only occurs above 320 K [68], at a temperature, where reactions (2) and (3) are already completed.

Despite this complexity, we will try to derive some conclusions. If we assume first order kinetics for the decomposition of methyl to methylidyne and a frequency factor of 10¹³ s⁻¹ for both isotopes, we can determine the activation energies for CH₃ and CD₃ decomposition on Pt(111) from the T_{50%} temperatures, which is a reasonable estimation for the rate maximum within the accuracy of our analysis. Using Redheads equation [37] values of 732 ± 9 and 776 ± 9 meV, respectively, are obtained yielding a difference of 44 ± 11 meV, due to a kinetic isotope effect (KIE) in

the rate determining step. The estimated activation energies are in good agreement with calculations by Michaelides and Hu [171], which yield a reaction barrier for CH₃ dehydrogenation to CH₂ of 820 meV. The assumption of first order kinetics is justified by the fact that the characteristic transition temperatures are only weakly dependent of coverage (see above); furthermore, we also note that a change in the frequency factor by 10 leads only to a change of 3 meV for the difference in activation energy. Interestingly, the observed difference in the activation energy agrees very well with the value of $\sim 48 \pm 4$ meV observed by Madix and Telford between breaking a C-H and a C-D bond in CH₃O and CD₃O adsorbed on Cu(110), respectively [172].

If we take the characteristic temperatures for the dehydrogenation of terrace methyl on the stepped surfaces, we find isotope effects of 22 ± 6 K for Pt(322) and 11 ± 3 K for Pt(355); for the step site on Pt(355) a value of 16 ± 3 K is found. Within the error bars, the observed values agree with the value of 16 ± 4 K observed for the Pt(111), based on larger number of experiments.

Since reactions (2) and (3) have comparable rates, the activation energies for both should also be comparable, if one assumes the same frequency factor for reaction (3). Indeed, the calculations by Michaelides and Hu [171] yield a value of 740 meV. This analysis is certainly a very crude approach, in particular as the dehydrogenation (reaction 2) should roughly follow first order kinetics, whereas the recombinative desorption (reaction 3) should follow second order kinetics.

The higher temperatures for dehydrogenation and desorption of the deuterated species than for the non-deuterated species can be attributed to a difference in zero point energies in the initial state. For the dehydrogenation process this primary kinetic isotope effect only depends on the vibrations relevant for the C-H (C-D) bond breaking. To calculate the difference in the zero point energies, $E = \frac{1}{2} h \cdot \nu$, for the C-H and C-D stretching modes, the corresponding vibrational frequencies are required. While the value for the C-H vibration for CH₃/Pt(111) is known to be 358 meV [158], the value for CD₃/Pt(111) is estimated to 267 ± 8 meV, using the ratio of 1.34 ± 0.02 typically observed for the frequencies of C-H and C-D vibrations [4]. With these numbers one obtains a value of 45 ± 4 meV for the difference in zero point energy. If one assumes that the difference in the zero point energies of the transition state is negligible small (this is a reasonable assumption, considering the fact that along the reaction coordinate the isotope effect is zero (the H atom passes the saddle point of the potential) and possible differences between initial state and

transitions state for the other vibrations are expected to be significantly smaller than the error bars), this value can directly be compared with the experimentally observed difference of 48 ± 12 meV between the activation energies for CH_3 and CD_3 decomposition.

For comparison, we also calculate the expected isotope effect for the activation energy for desorption. Here we have mainly to consider the vibration of the H(D)-atom and the CH_3 (CD_3) group against the surface. Since the vibrational energies for CH_3 are very low (65 meV [173]) and the masses are very similar ($M(\text{CD}_3)/M(\text{CH}_3)=1.2$), the contribution of the vibration of the methyl group against the surface is expected to be very small (<3 meV). The situation is different for the H(D) atoms, where the vibrational energy of H on Pt is reported to be 153 meV [173]. Assuming a ratio of 2 for the reduced masses of the vibration of atomic D and H against the surface, one obtains a difference in the zero point energies of 22 meV, contributing to the kinetic isotope effect of the methane desorption, which is much smaller than experimentally observed.

The good agreement between experimentally observed difference in the activation energy and the difference in the zero-point energies of the C-H and C-D vibrations is an indication that breaking a single C-H (C-D) bond in methyl to form a CH_2 (CD_2) methylene intermediate is the initial step in the decomposition of methyl; for the (very unlikely) simultaneous breaking of two C-H (C-D) bonds one would expect a significantly higher difference (90 meV) in the activation energy between CH_3 and CD_3 .

The fact that there is no indication of a methylene species in our time-dependent measurements leads us to the conclusion that this intermediate is rather short lived and unstable and very quickly dehydrogenates to form methylidyne on the surface, which has been proposed to be the thermodynamically most stable dehydrogenation product by Michaelidis and Hu [171]. They find activation barriers of 820 meV when going from CH_3 to CH_2 , but only 140 meV when going from CH_2 to CH [171]. An earlier report of methylene as intermediate [169] is most likely due to the erroneous assignment of surface methylidyne to methylene.

7.4.3 Summary

In this chapter in-situ adsorption and TPXPS experiments of deuterated methane were presented, leading to a changed spectral shape in the vibrational fine structure, already discussed in chapter 7.2.1, expected from an exchange of hydrogen to deuterium in the CH_x species. The comparison of the adsorption experiments shows a higher radiation induced conversion of the non-deuterated, compared to the deuterated methyl to methylidyne. A comparison of the relative initial sticking coefficient of the deuterated methane on the (111), (355) and the (322) surface of platinum to the values found for non-deuterated methane yielded values lower by a factor of 2. This low value, compared to literature, may result from the low adsorption temperature used in this work in comparison to literature, where no reaction of methyl to methylidyne and / or carbon takes place, which also underlay an isotope effect. This might explain the observed differences to literature data.

In the second part of this chapter we have shown that by temperature programmed XPS detailed information on the decomposition of methyl on Pt(111) and on stepped Pt(111) surfaces can be obtained by comparing the thermal evolution of deuterated and non-deuterated methyl. From the kinetic isotope effect, the difference in the activation barrier for the two isotopes is calculated to 48 ± 12 meV. This value compares very well to the difference in the zero point energies of the C-H and C-D vibration of two isotopes, which lead us to conclude that the first dehydrogenation step of methyl is the formation of methylene by breaking of an individual C-H bond. The methylene species, however, is short-lived and cannot be observed on the time scale of our experiment. It readily further dehydrogenates to methylidyne, in line with expectations from theory [171].

7.5 Summary

We presented a combined in-situ time-dependent HRXPS and molecular beam study of the adsorption and reaction behavior of methane on two stepped platinum surfaces, namely the (355) and the (322) surface, which was compared to results from the flat (111) surface of platinum. The analysis of the C 1s spectra showed two methyl species: one methyl adsorbed at the (111) terraces of the crystals and a second species which is attributed to a step-site adsorbed methyl. The assignment

was done due to the observed C 1s binding energy, which was similar for the terrace sites on Pt(322) and Pt(355) as on the Pt(111) crystal. For the step sites the C 1s signal of CH₃ was shifted to higher binding energies, for the (322) crystal by 300 meV and for the (355) crystal by 350 meV. From the quantitative analysis of the XP spectra the total surface coverage as well as the terrace and step coverages were obtained, showing similar total coverages for all surfaces examined. The step coverages were found to be significantly higher on the (111) steps of the (355) crystal compared to the (100) steps of the (322) crystal. In the low coverage regime, strong diffusion of methyl from terrace sites to step sites is proposed to take place. On the (355) surface this effect is even more pronounced than on the (322) surface. From the total coverages the relative initial sticking coefficient was obtained, showing similar results for all examined surfaces.

The reaction of methyl was examined by temperature programmed XPS experiments, showing a higher reactivity towards the dehydrogenation of methyl and methylidyne for the stepped surfaces compared to the flat (111) surface. Nevertheless, on all surfaces the same reaction intermediates, namely, methyl, methylidyne and pure carbon were found. The activation energy of the dehydrogenation of CH₃ adsorbed on the stepped and the flat platinum surfaces was determined to be ~110 meV lower for the stepped surfaces. The higher reactivity of the surface was even more enhanced at the (111) steps of the (355) crystal with its activation energy lowered by ~190 meV. This higher reactivity of the step-adsorbed methyl was not found in radiation induced dehydrogenation reactions. In contrast, we found a higher reactivity of the terrace adsorbed methyl towards photon induced dehydrogenation and desorption. This was attributed to the fact, that the step methyl is more strongly coupled to the substrate. This enhanced coupling allows a more efficient decay of the core hole and therefore a higher stability of this species against radiation.

The similar initial sticking coefficient and the higher reactivity of the stepped surfaces towards thermal dehydrogenation led us to the conclusion that the direct adsorption channel is not affected by the surface morphology, but the reactivity. For realistic processes at higher temperatures, this leads to a higher overall reactivity of the stepped surfaces.

The passivation of the stepped surfaces with silver mono-rows along the steps was used to elucidate the question whether the mere morphology is responsible for

the enhanced reactivity or the morphology and the chemical surrounding of the substrate. Ee found, that the passivation of the surface leads to a lower methyl coverage. The total coverage of carbon species was lowered by the amount expected from the respective amount of silver. Nevertheless, on the (355) surface a measurable amount of methyl adsorbed at step sites was found as compared to the (322) surface where it is below the detection limit. This is explained by a higher binding energy of the methyl adsorbed at step sites of the (355) surface, which is also indicated by the aforementioned higher C 1s binding energy. The existence of methyl adsorbed at step sites also implicitly shows that the silver is removed from the step sites and has to form peninsulas or even islands. The explanation for this effect is the binding energy of the respective methyl at the steps compared to the silver adsorbed at the steps, which seems to be higher for the methyl adsorbed at (111) steps.

The reaction of methyl adsorbed on the silver precovered stepped platinum surfaces is similar to the behavior of it on the clean platinum surfaces. This shows, that the overall reaction behavior seems to be more related to the morphology than to the chemical surroundings, but a clear distinction between chemical sensitivity and morphology was not possible due to the island or peninsula formation of the silver upon adsorption of methane.

In the last part of chapter 7 we addressed the differences in the adsorption and reaction behavior of deuterated methane compared to non-deuterated methane. At low temperatures, we found an isotope effect for the sticking probability by a factor of two, which is lower as found in literature at high surface temperatures. This difference might be related to the difference in surface temperatures used in this work and in literature. The higher sample temperatures used in literature might involve differences in the reaction channel, which is not directly involved in the dissociative adsorption. In the adsorption experiments a higher stability of CD_3 compared to CH_3 towards the radiation induced reaction was found, which was explained by the higher stability of the C-D bond compared to the C-H bond, regarding the different zero point energy. The TPXPS experiments which showed the reaction of methyl to methylidyne and finally pure carbon, all showed a shift to higher reaction temperatures for the decomposition of the deuterated species, as expected from the models for the C-H(D) bond breaking already introduced in chapter 2.2.2. From the reaction temperatures, the activation energies for the respective reactions by applying the Redhead equation were extracted. These values were used to determine the reaction

pathway. The existence of the intermediate state of methylene (CH_2) was established, as predicted by theory.

8 Summary

This thesis is concerned with in-situ high resolution X-ray photoelectron spectroscopy experiments of the adsorption and thermal evolution of model systems on single crystalline transition metal surfaces. We utilized for our measurements third generation synchrotron sources, which provide highly intense X-rays with a high resolution, allowing the detailed description of the adsorbate layers. The high resolution provided the possibility to study the vibrational properties of the adsorbed molecules. In this context deuterium substituted molecules were examined to ensure the assignment of vibrational modes, which show the expected changes in their vibrational frequencies. The thermal evolution of the deuterium substituted analogues showed a kinetic isotope effect and, in the case of benzene at low temperatures, a structural isotope effect was observed. In the detailed analysis of the continuous measurements, we were able to determine the coverage and temperature dependent adsorption sites and the orientation of the adsorbed molecules relative to the substrate. The thermal evolution was investigated additionally yielding surface intermediates and reaction paths of the adsorbates. In the first part the studies of different cyclic hydrocarbons, benzene and cyclohexene, are presented. By analyzing the surface chemistry of pyrrole and furan we studied the influence of heteroatoms on the molecular adsorption of ring systems, as well as on the decomposition. The adsorption of the cyclic hydrocarbons was studied in their pure form as well as in an intended coadsorption situation with small molecules. Coadsorption systems are also observed upon reaction, i.e., dehydrogenation or decomposition, of the hydrocarbons on the surfaces. Furthermore, we studied more complex, stepped Pt(111) surfaces and their influence on the adsorption and reaction of the simple hydrocarbon methane. In the following, the main results will be described in detail.

Benzene on Ni(111):

The adsorption and thermal evolution of deuterated and non-deuterated benzene on Ni(111) was studied by in-situ high-resolution X-ray photoelectron spectroscopy. The recorded C 1s spectra show vibrational fine structure due to vibrational excitations of the C-H bonds in the ionic final state. Furthermore, different adsorption sites can be identified, since carbon atoms within the same molecule, but with different positions

relative to the substrate have different C 1s binding energies. At 200 K for both C₆H₆ and C₆D₆ a well ordered ($\sqrt{7} \times \sqrt{7}$)R19.1° superstructure is observed at saturation of the chemisorbed layer, with a nominal coverage of 0.143 ML. From a quantitative analysis of the XP spectra collected during adsorption one finds that up to a coverage of 0.10 ML benzene occupies only bridge adsorption sites. At higher coverage, a change to hcp hollow sites, accompanied by a rotation of the molecules by 30°, occurs for C₆H₆ and C₆D₆. In contrast to the results at 200 K, an isotopic effect is found for the adsorption at 125 K. While the adsorption behavior for C₆D₆ is similar as at 200 K, i.e., a change occurs at 0.10 ML from bridge to hollow site adsorption, for C₆H₆ no change in the adsorption site is observed, i.e., up to saturation of the chemisorbed layer only bridge sites are occupied. Only upon heating, a site change from bridge to hcp hollow of the adsorbed C₆H₆ is induced, starting around 180 K. A simple explanation for the observed behavior is proposed.

From the coadsorption experiments we were able to extract the adsorption sites for benzene in the ordered coadsorption phases. For the coadsorption of benzene with CO we find a hollow adsorbed benzene with its C-C axis oriented along the $[\bar{2}11]$ direction, which agrees nicely with the measurements known from literature. For the coadsorption of NO with benzene, we were able to correlate the adsorption site changes with known LEED and ARUPS measurements.

Cyclohexene on Ni(111):

We studied the adsorption and reaction of cyclohexene (C₆H₁₀) on Ni(111) at different temperatures with high resolution in-situ x-ray photoelectron spectroscopy. At 125 K, we find intact cyclohexene with two distinct C 1s signals at 283.3 and 284.2 eV, due to the non-equivalent carbon atoms in the molecule. The energetic separation is significantly increased relative to the gas phase value, due to the interaction with the substrate. Upon exposure at 210 K, complete dehydrogenation of cyclohexene to benzene (C₆H₆) and hydrogen is observed; coverage dependent changes of the benzene adsorption site occur in a similar way as for pure benzene layers, which indicates a phase separation in benzene and hydrogen islands.

The thermal evolution of the adsorbed layers was studied by temperature programmed XPS and temperature programmed desorption spectroscopy. Upon heating, the benzene + hydrogen layer formed at 210 K shows a coverage dependent reorientation of the benzene molecules during partial desorption. The

cyclohexene layer adsorbed at 125 K is only partially converted to benzene and hydrogen upon heating to 185 K or 210 K, with the remaining cyclohexene being stable up to ~300 K. We propose that upon heating these molecules are stabilized by coadsorbed benzene and hydrogen; furthermore, the mobility of benzene and hydrogen in this coadsorbed layer is reduced, so that no phase separation can occur.

Furan and Pyrrole on Ni(111):

The adsorption and reaction of the heterocycles pyrrole and furan was monitored by in-situ XPS measurements. Upon adsorption we find for each heterocycle a C 1s spectrum dominated by two peaks which are separated by 0.7 eV in the case of pyrrole and by 1.1 eV in the case of furan, which is interpreted as initial state effects related to the electronegativity of the neighboring heteroatoms, N and O respectively. The peak at higher binding energies is related to the carbon atoms which are in direct neighborhood to the heteroatoms. Both adiabatic peaks show a small contribution at 400 meV higher binding energies which is due to a vibrational excitation in the core hole state.

The reaction of the heterocycles was investigated by HR-XPS in the case of furan in the C 1s and the O 1s regions, while for pyrrole the C 1s and the N 1s regions were monitored. The data allowed to determine the reaction pathways of the two heterocycles. For furan as first step the formation of CO is observed, which is desorbing at 400 K. Different hydrocarbon fragments are created on the surface upon reaction to CO. These different hydrocarbon species are a mixture of C₁ (methylidyne) to C₃ moieties, which are further dehydrogenating on the surface to yield pure carbon at higher temperatures. The reaction of pyrrole starts at first with the N-H bond scission yielding a deprotonated form of pyrrole. The subsequent reaction yields also a mixture of different carbon species, but no methylidyne was found. A clear distinction between possible reaction intermediates at this stage of the reaction was difficult as different C_x-N and C_yH_z moieties were present on the surface, allowing no clear distinction by XPS measurements. This leads to the conclusion that CO as leaving group is favored over the nitrogen analogue CN. In the later reaction we find molecular nitrogen on the surface, which is formed from the C_xN species. From C_yH_z and C_xN fragments pure carbon is formed on the surface at high temperatures.

Methane on stepped Pt(111) surfaces:

The activated adsorption of methane was investigated on two stepped Pt(355) and Pt(322) surfaces by time-dependent in-situ high-resolution XPS combined with a supersonic molecular beam; the results were compared to corresponding results on Pt(111). Both stepped surfaces have five atom row wide (111) terraces, but different step orientation, namely (111) and (100), respectively. Independent of the kinetic energy (0.45 - 0.83 eV) of impinging methane (CH_4 or CD_4), methyl is formed on all surfaces upon adsorption at 120 K. For the stepped surfaces, two different methyl species are identified from the XP spectra, attributed to adsorption at terrace sites and at step sites. The total initial sticking coefficients (for terrace + step sites) and the total coverages are very similar for all three surfaces. At low coverages, diffusion of methyl from the terraces to the steps is significantly stronger on Pt(355) than on Pt(322), and the step saturation coverage is higher on Pt(355). The thermal evolution of methyl was also investigated by in-situ temperature-programmed XPS. Overall, an enhanced reactivity towards dehydrogenation to methylidyne is found for both terrace and step sites on the stepped surfaces, with the (111) steps of Pt(355) exhibiting the highest activity.

Adsorption experiments on silver precovered platinum surfaces showed the expected effects for the total and partial coverages, namely no adsorption of methane on the silver covered parts. Interestingly, methyl is able to partly remove silver from the steps on the (355) surface, showing the stronger affinity of methyl to the platinum steps. The reaction of methyl to methylidyne and carbon showed no significant differences, as the conversion temperatures were similar to that of the clean stepped surfaces.

From the adsorption experiments with deuterated methane we were able to extract a kinetic isotope effect leading to a drop in the relative initial sticking coefficient of the deuterated methane compared to the non-deuterated methane. The comparison of the reaction of the deuterated and the non-deuterated methyl on the different platinum surfaces showed a primary kinetic isotope effect, allowing to draw conclusions on the reaction mechanism of the decomposition of methyl on the platinum surfaces. The existence of an intermediate state, namely methylene, in the decomposition of methyl to methylidyne is experimentally proved.

9 Appendixes

The appendixes will give additional information to some chapters, to support certain points or to show special topics. These facts are not shown in the respective chapters as they are not necessary for the actual interpretation. They may, however, give a deeper insight to related analyses, allow comparisons or the description was too extensive, which would have distracted the reader from the topics discussed in the respective chapters.

9.1 Appendix to chapter 2

9.1.1 Changes in the bond length and the vibrational excitations upon core excitation

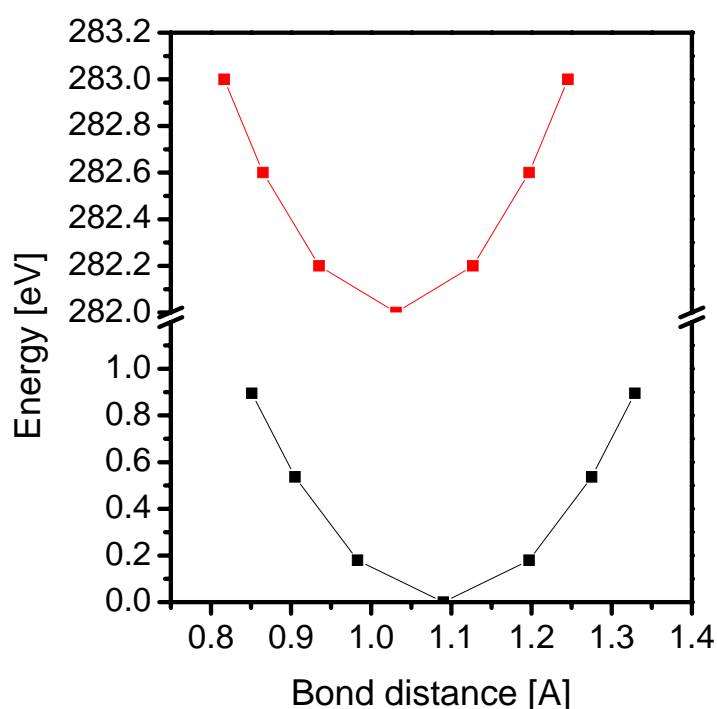


Fig. 9.1 Energy vs. bond length diagram, showing the change in the bond length and the change in the harmonic potential of the C-H bond upon excitation of the carbon 1s core level. The squares indicate the vibrational levels in the respective harmonic potential, while the squares in the origin of the parabolas correspond to the bond length.

$D_{gr} = 501 \text{ N/m}$; $D_{exc} = 696.7 \text{ N/m}$; bond length in the ground state is 1.09 \AA (CH_3).

The calculations are based on the considerations of Ref. [4]. The graph in Fig. 9.1 shows the difference in bond length and the changed potential in the C-H vibrations upon excitation of the C 1s core hole in a methyl group adsorbed on a Pt(111) surface. The potential for the C-H vibrations in the ground state and in the core hole state are calculated with the respective energies and the equations from chapter 2.1.3, while the change in bond length is taken from Ref. [4].

9.2 Appendix to chapter 4

9.2.1 Modeling of XP spectra of benzene with different functions

In this part two different descriptions of the XP spectra of benzene are discussed, allowing us to compare this data to earlier results [4, 38, 68, 151]. In Fig. 9.2 XP spectra of the saturated benzene layer are shown with corresponding fits using (a) a Doniach-Sunjic function convoluted with a Gaussian and, for comparison, (b) a Pseudo-Voigt function, which was used for the analysis in chapter 4.

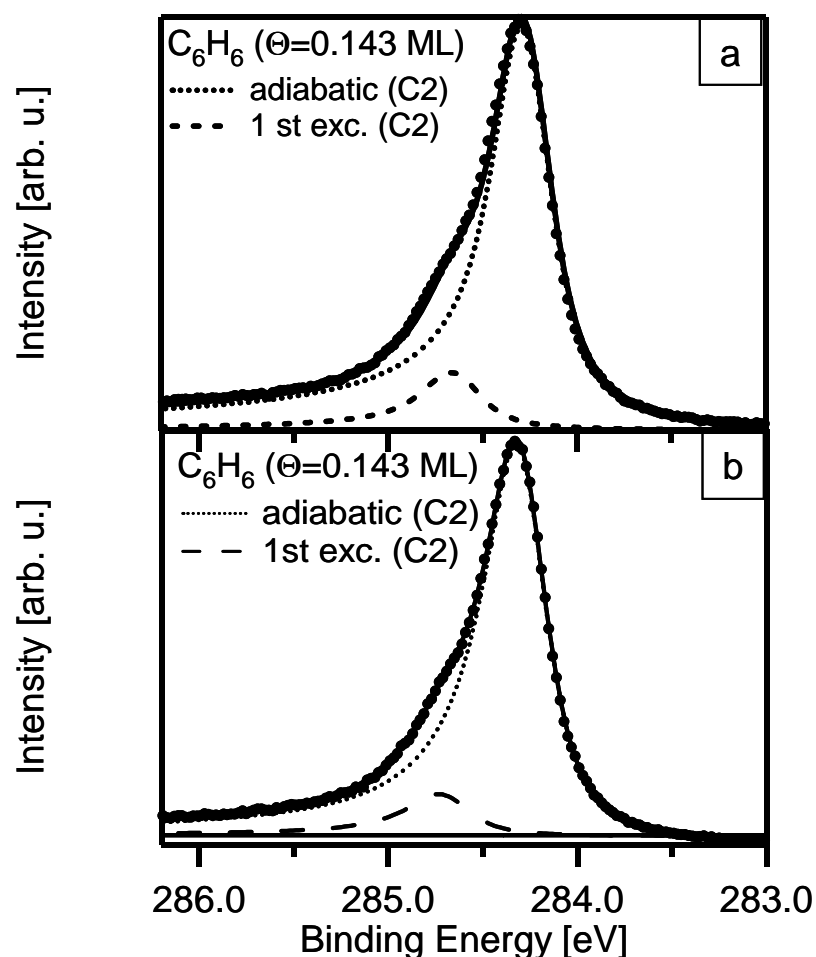


Fig. 9.2 XP spectrum of a saturated layer of C_6H_6 fitted with a) a Doniach-Sunjic function and b) a Pseudo-Voigt function. Each spectrum is fitted with two peaks that have a similar line shape, i.e., same Gaussian and Lorentzian width as well as the asymmetry factor for the Doniach-Sunjic for a); mixing factor, full width half maximum and asymmetry factor in the case of b).

In the fit with the Doniach-Sunjic function the S factor is determined to be 0.145 and the binding energy difference between the adiabatic and the first vibrationally excited state is found to be 374 meV, while for the Pseudo-Voigt function an S factor of 0.1 and a separation of the peaks of 410 meV are found. Note that the modeling of the peak is slightly worse for the Doniach-Sunjic function while the Pseudo-Voigt function shows some deviations in the regions with low intensity. We also want to point out that the use of a different function for describing the data is not changing the result of the analysis of chapter 4, but is relevant for the computation time. The use of the Doniach-Sunjic functions, thus, leads to a higher S factor as the use of the Pseudo-Voigt function. If the value of the S factor, obtained by using the Doniach-Sunjic function, are compared to values obtained for smaller hydrocarbons adsorbed on Ni(111) as, e.g., acetylene, methyl or methylidyne, the S factor is still smaller (0.145 compared to 0.17), which is related to unresolved vibrations as, e.g., C-C or ring deformation vibrations, incorporated in the adiabatic contribution.

9.2.2 Changes in desorption temperatures upon heat rate variation

The use of different heating rates in temperature programmed experiments leads to deviations in the temperature of the desorption peaks. To allow a comparison between such experiments the relation between desorption energy and desorption temperature for different heating rates the is plotted in Fig. 9.3, according to the equation of Redhead [37].

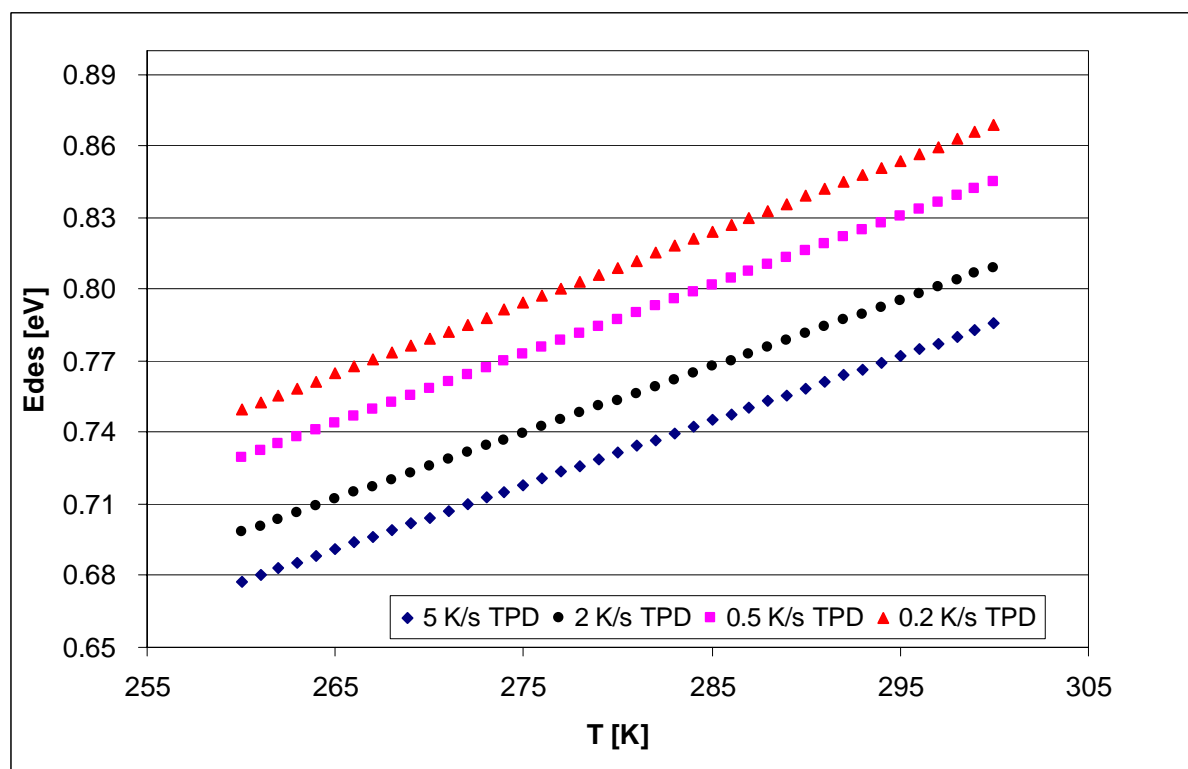


Fig. 9.3 Desorption energy vs. temperature for different heating rates β , according to [37] with $k_B=8.62 \cdot 10^{-5} \text{ eV/K}$ and $\nu=10^{13} \text{ s}^{-1}$.

The graph allows to estimate the difference in desorption temperature for different heating rates. This is typically the case for TPXPS and TPD experiments, of which the latter usually have a higher heating rate β . Examples for such comparisons can be found in chapter 4 and 5.

9.2.3 Calculation of the minority population for the adsorption of benzene at 200 K

In Table 9.1 the relative site occupation compared to the ratio of the two components C1 and C2 is shown.

Table 9.1: Calculation of the population of benzene in bridge and hollow position and their respective ratio.

Population <u>bridge(a)</u>	<u>hollow (b)</u>		<u>bridge x atoms</u>	<u>bridge y atoms</u>	<u>hollow x atoms</u>	<u>ratio</u>
1	0		4	2	0	0.500
0.95	0.05		3.8	1.9	0.3	0.463
0.9	0.1		3.6	1.8	0.6	0.429
0.85	0.15		3.4	1.7	0.9	0.395
0.8	0.2		3.2	1.6	1.2	0.364
0.75	0.25		3	1.5	1.5	0.333
0.7	0.3		2.8	1.4	1.8	0.304
0.65	0.35		2.6	1.3	2.1	0.277
0.6	0.4		2.4	1.2	2.4	0.250
0.55	0.45		2.2	1.1	2.7	0.224
0.5	0.5		2	1	3	0.200
0.45	0.55		1.8	0.9	3.3	0.176
0.4	0.6		1.6	0.8	3.6	0.154
0.35	0.65		1.4	0.7	3.9	0.132
0.3	0.7		1.2	0.6	4.2	0.111
0.25	0.75		1	0.5	4.5	0.091
0.2	0.8		0.8	0.4	4.8	0.071
0.15	0.85		0.6	0.3	5.1	0.053
0.1	0.9		0.4	0.2	5.4	0.034
0.05	0.95		0.2	0.1	5.7	0.017
0	1		0	0	6	0.000

These values, calculated according to the equation shown in chapter 4.2.1, were used to estimate the minority population of hollow adsorbed benzene molecules in the dilute benzene layer adsorbed at 200 K.

9.2.4 Low temperature adsorption of deuterated benzene

In Fig. 9.4 XP spectra of the adsorption of deuterated benzene at temperatures below 126 K are shown.

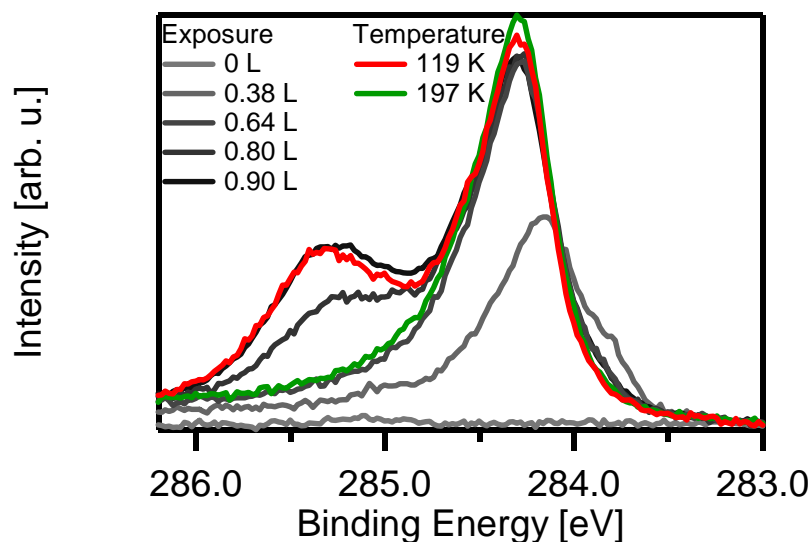


Fig. 9.4: Selected XP spectra of the adsorption of C_6D_6 at temperatures below 126 K.

The temperature of the sample was decreasing during the adsorption and was below 120 K for the last spectra (in Fig. 9.4 corresponding to 0.8 and 0.9 L). The small shoulder at a binding energy of 283.9 eV is indicative for small amounts of bridge adsorbed deuterated benzene, although multilayers are adsorbed above. This behavior is well described for non-deuterated benzene at low temperatures in chapter 4.2.2. Upon heating the layer to 119 K, corresponding to the red XP spectrum in Fig. 9.4, the contribution at 283.9 is gone, which shows the rearrangement to a layer of purely hollow adsorbed C_6D_6 . This experiment showed that below 120 K the reorientation of deuterated benzene can also be frozen as it was shown for non-deuterated benzene, showing this “frozen” layer up to 180 K.

9.3 Appendix to chapter 6

9.3.1 Fits of furan C 1s spectra obtained during a TPXPS experiment

In this chapter we show XP spectra of the thermal evolution of furan and their corresponding fits, to allow a more detailed insight into the analysis of the C 1s spectra of the TPXPS experiments. The XP spectra in Fig. 9.5 and 9.6 are chosen to show typical stages in the decomposition process, with the corresponding intermediate species, i.e., CO (black), C₃H₃ (blue) and CH (red) and C₂H₂ (red).

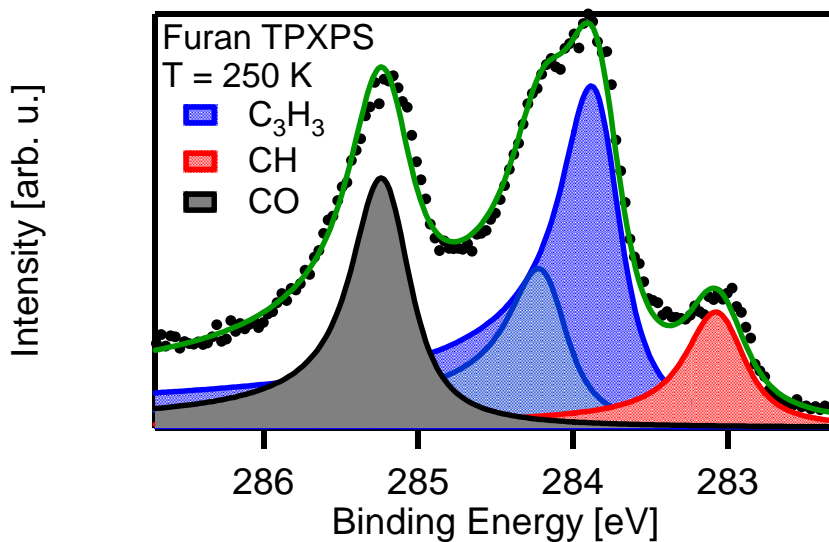


Fig. 9.5: C 1s spectrum of furan at 250 K. The photon energy was 380 eV. The contributions are modeled with Doniach-Sunjic functions.

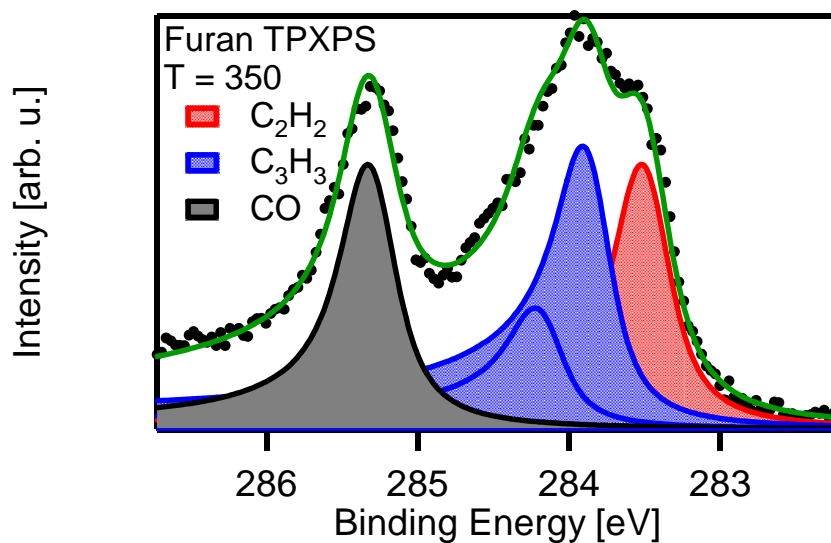


Fig. 9.6: C 1s spectrum of furan at 350 K. The photon energy was 380 eV. The contributions are modeled with Doniach-Sunjic functions.

9.3.2 Fits of pyrrole C 1s spectra obtained during a TPXPS experiment

In this chapter we show XP spectra of the thermal evolution of pyrrole and their corresponding fits, to allow a more detailed insight into the analysis of the C 1s spectra of the TPXPS experiments. The XP spectra (Fig. 9.7 – 9.9) are chosen to show typical stages in the decomposition process, with the corresponding intermediate species. In Fig. 9.7 and 9.8, C₄H₄NH and C₄H₄N are shown in black and red, respectively, while in Fig. 9.9 different C_xH_yN species are shown in different colors.

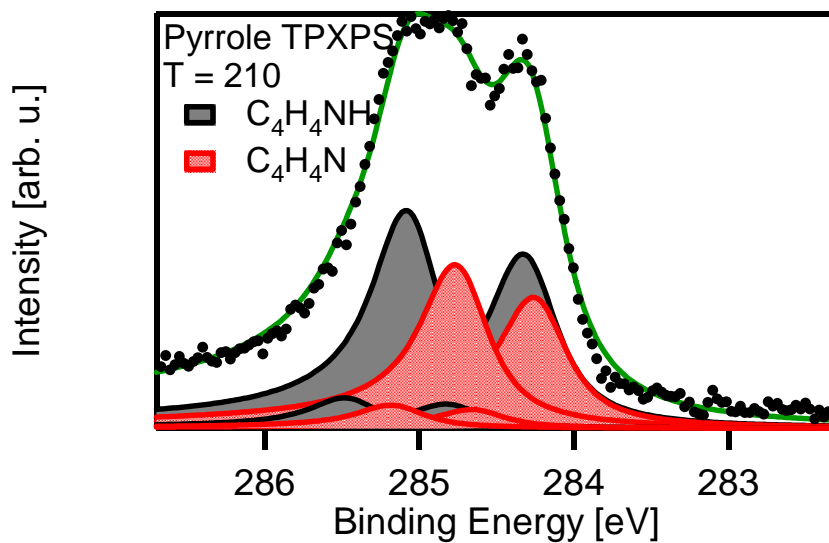


Fig. 9.7: C 1s spectrum of pyrrole at 210 K. The photon energy was 380 eV. The contributions are modeled with Doniach-Sunjic functions.

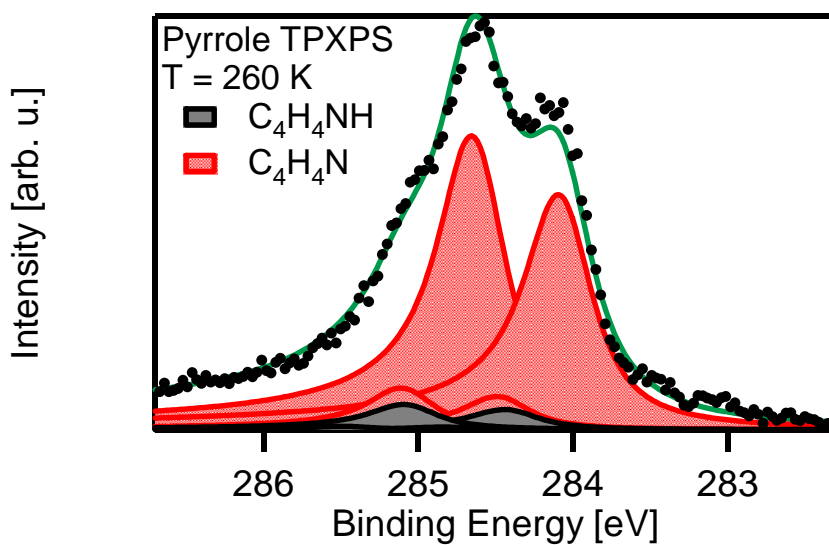


Fig. 9.8: C 1s spectrum of pyrrole at 260 K. The photon energy was 380 eV. The contributions are modeled with Doniach-Sunjic functions.

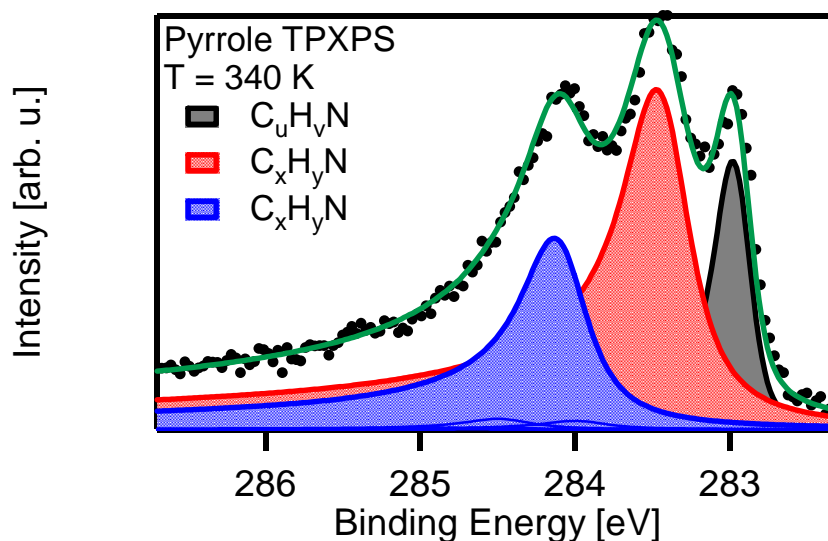


Fig. 9.9: C 1s spectrum of pyrrole at 340 K. The photon energy was 380 eV. The contributions are modeled with Doniach-Sunjic functions.

9.4 Appendix to chapter 7

9.4.1 Supporting information to chapter 7.2

In this appendix, we show in Fig. 9.10 C 1s spectra of methyl resulting from adsorption at nozzle temperatures of up to 1273 K to show, that no pyrolysis takes place already in the nozzle of the molecular beam. They are a sequel to the spectra shown in Fuhrmann et al. [151], with the spectrum at a nozzle temperature of 1073 K as overlap. The only difference occurring in the spectra is the different amount of CH formed during exposure, which is related to the different X-ray doses. This is particularly clear if comparing traces b) and c), which differ only in the applied radiation dose. The lower dose in trace c) results in a very small contribution at 283.6 eV. A quantitative analysis also showed no differences, always yielding the expected results for methyl adsorption.

Additionally, we added a table listing some C 1s binding energies of various hydrocarbons on Pt(111), to show that we are indeed able to distinguish between these species. The absence of characteristic peaks in the spectra at the cited binding energies (especially also at very low methyl coverages) rules out these hydrocarbons as pyrolysis products. Some of these binding energies are yet unpublished. A related aspect is that the sticking coefficients for most of the expected pyrolysis products would be much

higher (by a factor of 10^2 to 10^3) than for methane/methyl at low kinetic energies (as used in trace e)). This would compensate for their low amount in the impinging gas beam. Thus, this aspect further corroborates the absence of pyrolysis products under the conditions of our study.

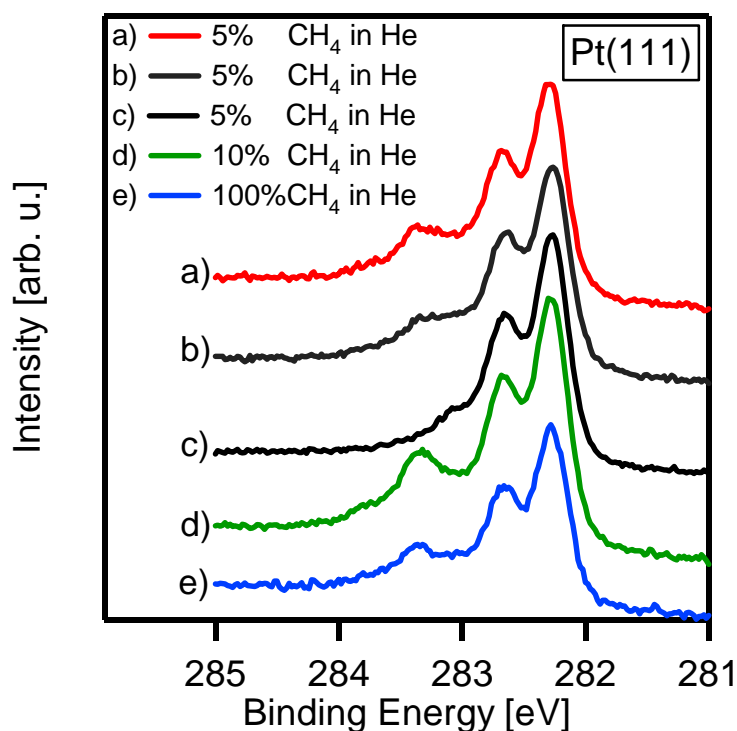


Fig. 9.10: C 1s spectra of methyl adsorbed on Pt(111) with a) $E_{kin}=0.71$ eV, $T_{Nozzle}=1073$ K, b) $E_{kin}=0.83$ eV, $T_{Nozzle}=1273$ K, c) $E_{kin}=0.83$ eV, $T_{Nozzle}=1273$ K, but measured on an area of the methyl layer not exposed to X-rays before, d) $E_{kin}=0.58$ eV, $T_{Nozzle}=1073$ K and e) $E_{kin}=0.30$ eV $T_{Nozzle}=1273$ K. All spectra were recorded with a photon energy of 380 eV at an electron emission angle of 45° .

Table 9.2: Binding energies of higher hydrocarbons on a Pt(111) surface

Hydrocarbon species	C 1s binding energy [eV]
Methylidyne (CH) [151]	283.6
Acetylene (C ₂ H ₂) [174]	284.2 *
Ethylene (C ₂ H ₄) [4]	284.3 *
Ethane (C ₂ H ₆) [174]	282.9
Propene (C ₃ H ₈) [175]	283.6
Benzene (C ₆ H ₆) [176]	285.1

* Binding energy scale of [174] shifted to lower energies to match values for ethylene from [4], due to a different calibration of the binding energy scale in the experiments.

9.4.2 Transition and characteristic temperatures together with the respective activation energies of methyl on Pt(111)

In the tables 9.3 and 9.4 the transition temperatures ($T_{50\%}$) and their respective activation energies are shown. The values clearly show the lower activation energies for the dehydrogenation of methyl and methylidyne on the stepped platinum surfaces, as well as the isotope effect, discussed in chapter 7.4.2. These values show a higher error bar as the ones used for the evaluation of the kinetic isotope effect, but are used for evaluating the actual activation energy of the primary reaction step. Note that also here a small error is included, as the maximum in the rate of the reaction is not coinciding with the $T_{50\%}$ value, but the difference is expected to be small ($< 2\text{K}$).

Table 9.3: $T_{50\%}$ temperatures for the chemical transitions and methylidyne coverages found on the surface (initial coverages of 0.11-0.17).

Surface	$T_{50\%}$ CH ₃ terrace dehydrogenation	$T_{50\%}$ CH ₃ step dehydrogenation	$T_{50\%}$ CH dehydrogenation	CH coverage at 300 K [ML]
Pt(111)	260 ± 5 K	-	500 ± 10 K	0.040 ± 0.005
Pt(322)	220 ± 5 K	220 ± 5 K	420 ± 30 K	0.050 ± 0.007
Pt(355)	215 ± 5 K	160 ± 5 K	450 ± 30 K	0.063 ± 0.007
Surface	$T_{50\%}$ CD ₃ terrace dehydrogenation	$T_{50\%}$ CD ₃ step dehydrogenation	$T_{50\%}$ CD dehydrogenation	CD coverage at 300 K [ML]
Pt(111)	275 ± 5 K	-	-	0.050 ± 0.007
Pt(322)	240 ± 5 K	245 ± 5 K	430 ± 30 K	0.051 ± 0.007
Pt(355)	225 ± 5 K	170 ± 5 K	470 ± 30 K	0.060 ± 0.007

Table 9.4: Activation energies for the chemical transitions (“-“ values are not evaluated or in the case of “CH₃“ step on Pt(111) not existing).

Surface	E _A (eV) CH ₃ terrace dehydrogenation	E _A (eV) CH ₃ step dehydrogenation	E _A (eV) CH dehydrogenation
Pt(111)	0.73	-	1.44
Pt(322)	0.62	0.62	1.19
Pt(355)	0.60	0.44	1.29
Surface	E _A (eV) CD ₃ terrace dehydrogenation	E _A (eV) CD ₃ step dehydrogenation	E _A (eV) CD dehydrogenation
Pt(111)	0.78	-	-
Pt(322)	0.67	0.69	1.23
Pt(355)	0.63	0.47	1.35

In table 9.5 we show the results of the quantitative analysis of the reaction of methyl (CH_3 and CD_3) to methylidyne (CH and CD) of various TPXPS experiments on different (111) platinum surfaces. The temperature values are the characteristic temperatures (T_s), described in chapter 7.4.2. These values were used to study the kinetic isotope effect of the reaction of methyl to methylidyne.

Table 9.5: Characteristic temperatures (T_s) and coverages for various TPXPS experiments on the three platinum surfaces. Note that all coverage values have an error of ± 0.007 ML and all temperature values of ± 2 K.

	Pt (111) T_s [K]	Pt(355) T_s [K]	Pt(322) T_s [K]	CH_3 coverage	CH coverage
CD_3	290			0.15	0.049
	291			0.14	0.051
average	290				
CH_3	275			0.17	0.040
	274			0.17	0.060
	276			0.15	0.350
	274			0.14	0.443
	276			0.13	0.043
	274			0.11	0.040
	269			0.04	0.030
average	274				
CD_3		243		0.11	0.058
step		189			
CH_3		232		0.12	0.065
step		173			
CD_3			260	0.12	0.058
CH_3			238	0.13	0.051

9.4.3 Kinetic energies of the methane

Table 9.6 shows the dependency of the kinetic energy of methane towards the uncalibrated flux of methane and helium as well as the nozzle temperature of the supersonic molecular beam. The values have been achieved by time of flight measurements in a similar experimental set up.

Table 9.6: Kinetic energies of methane in the molecular beam (taken from [38]).

CH ₄ /He-flux [sccm/sccm]	Ratio of CH ₄ /He [%]	T _{nozzle} [K]	Heating current [A]	E _{kin} [eV]
2:0	100	303	0	0.09
2:10	10	303	0	0.16
0.5:10	1.25	303	0	0.18
2:0	100	773	9.3	0.19
2:0	100	873	9.7	0.2
2:20	5	303	0	0.21
3:30	5	303	0	0.22
1:20	2.5	303	0	0.23
2:0	100	1073	10.9	0.25
2:0	100	1273	12.8	0.3
2:10	10	573	8.3	0.3
0.5:10	2.5	573	8.2	0.32
2:10	10	673	8.9	0.34
0.5:10	2.5	673	8.8	0.37
2:10	10	773	9.4	0.38
1:10	5	773	9.3	0.39
2:10	10	873	9.8	0.42
1:10	5	873	9.8	0.43
2:10	10	973	10.4	0.45
0.5:20	1.25	573	8.4	0.45
2:20	5	673	9	0.47
2:10	10	1073	11	0.49
2:20	5	773	9.5	0.54
2:10	10	1273	12.9	0.58
2:20	5	873	10.1	0.6
1:20	2.5	873	9.9	0.61
2:20	5	973	10.6	0.65
3:30	5	873	10.2	0.65
1:20	2.5	973	10.5	0.67
0.5:20	1.25	973	10.5	0.7
2:20	5	1073	11.2	0.71
1:20	2.5	1073	11.2	0.75
2:20	5	1273	12.9	0.83

Literature

- 1 K. W. Kolasinski, *Surface Science Foundations of Catalysis and Nanoscience* (Wiley, New York, Weinheim, 2002).
- 2 K. Siegbahn, C. Nordling, R. Fahlman, R. Nordberg, K. Hamrin, J. Hedman, G. Johansson, T. Bergmark, S.-E. Karlsson, I. Lindgren, and B. Lindberg, *Nova Acta Regia Soc. Sci.* **20**, Ser. IV (1967).
- 3 V. M. Oltedal, K. J. Borve, L. J. Saethre, T. D. Thomas, J. D. Bozek, and E. Kukk, *Phys. Chem. Chem. Phys.* **6**, 4254 (2004).
- 4 H.-P. Steinrück, T. Fuhrmann, C. Papp, B. Tränkenschuh, and R. Denecke, *J. Chem. Phys.* **125**, 204706 (2006).
- 5 A. Nambu, J.-M. Bussat, M. West, B. C. Sell, M. Watanabe, A. W. Kay, N. Mannella, B. A. Ludewigt, M. Press, B. Turko, G. Meddeler, G. Zizka, H. Spieler, H. van der Lippe, P. Denes, T. Ohta, Z. Hussain, and C. S. Fadley, *J. Electron Spec. Rel. Phen.* **137-140**, 691 (2004).
- 6 A. Baraldi, L. Rumiz, M. Moretuzzo, M. Barnaba, G. Comelli, S. Lizzit, G. Paolucci, R. Rosei, F. Buatier de Mongeot, and U. Valbusa, *J. Electron Spec. Rel. Phen.* **A 20**, 683 (2002).
- 7 A. Baraldi, G. Comelli, S. Lizzit, D. Cocco, G. Paolucci, and R. Rosei, *Surf. Sci. Lett.* **367**, L67 (1996).
- 8 F. Esch, A. Baraldi, G. Comelli, S. Lizzit, M. Kiskinova, P. D. Cobden, and B. E. Nieuwenhuys, *J. Chem. Phys.* **110**, 7969 (1999).
- 9 Y. Teraoka and A. Yoshigoe, *Appl. Surf. Sci.* **216**, 8 (2003).
- 10 H. Froitzheim, U. Köhler, and H. Lammering, *Phys. Rev. B* **34**, 2125 (1986).
- 11 S. Schaueremann, V. Johaneck, M. Laurin, J. Libuda, and H.-J. Freund, *Chem. Phys. Lett.* **381**, 298 (2003).
- 12 J. Libuda and H.-J. Freund, *Surf. Sci. Rep.* **57**, 157 (2005).
- 13 S. Hüfner, *Photoelectron Spectroscopy* (Springer-Verlag, Berlin Heidelberg New York, 1996).
- 14 J. Pantförder, *Photoelektronenspektroskopie im "Pressure Gap" - Aufbau einer neuen Apparatur für Messungen im Druckbereich 10⁻¹⁰ bis 1 mbar.*, PhD Thesis at Physikalische Chemie II (FAU, Erlangen, **2004**).
- 15 D. F. Ogletree, H. Bluhm, G. Lebedev, C. S. Fadley, Z. Hussain, and M. Salmeron, *Rev. Sci. Instrum.* **73**, 3872 (2002).

-
- 16 M. Henzler and W. Göpel, *Oberflächenphysik des Festkörpers* (Teubner, Stuttgart, 1994).
- 17 C. Ammon, *Elektronenspektroskopische Untersuchungen zu Herstellung und Eigenschaften ultradünner Schichten auf Kupferoberflächen*, PhD Thesis at Physikalische Chemie II (FAU, Erlangen, **2002**).
- 18 I. N. Bronstein and K. A. Semendjajew, *Taschenbuch der Mathematik* (Teubner, Stuttgart, Leipzig, 1996).
- 19 M. Borg, M. Birgersson, M. Smedh, A. Mikkelsen, D. L. Adams, R. Nyholm, C.-O. Almbladh, and J. N. Andersen, *Phys. Rev. B* **69**, 235418 (2004).
- 20 D. Briggs and M. P. Seah, *Practical Surface Analysis* (Springer-Verlag, Berlin, 1990).
- 21 H.-P. Steinrück, T. Fuhrmann, C. Papp, B. Tränkenschuh, and R. Denecke, *J. Chem. Phys.* **125**, 204706 (2006).
- 22 V. Myrseth, K. J. Borve, K. Wiesner, M. Bassler, S. Svensson, and L. J. Saethre, *Phys. Chem. Chem. Phys.* **4**, 5937 (2002).
- 23 J. N. Andersen, A. Beutler, S. L. Sorensen, R. Nyholm, B. Setlik, and D. Heskett, *Chem. Phys. Lett.* **269**, 371 (1997).
- 24 G. Wedler, *Lehrbuch der Physikalischen Chemie* (Wiley-VCH, Weinheim, 1997).
- 25 L. S. Cederbaum and W. Domcke, *J. Chem. Phys.* **64**, 603 (1976).
- 26 S. J. Osborne, S. Sundin, A. Ausmees, S. Svensson, L. J. Saethre, O. Svaeren, S. L. Sorensen, J. Vegh, J. Karvonen, S. Aksela, and A. Kikas, *J. Chem. Phys.* **106**, 1661 (1997).
- 27 R. Hesse, P. Streubel, and R. Szargan, *Surf. Interface Anal.*, in press (2007).
- 28 S. Doniach and M. Sunjic, *J. Phys. C*, 285 (1970).
- 29 M. Sunjic and D. Sokcevic, *Solid State Commun.* **18**, 373 (1976).
- 30 D. P. Woodruff and A. M. Bradshaw, *Rep. Prog. Phys.* **57**, 1029 (1994).
- 31 K. Siegbahn, U. Gelius, H. Siegbahn, and E. Olson, *Phys. Lett. A* **32**, 221 (1970).
- 32 C. S. Fadley and S. A. L. Bergstrom, *Phys. Lett. A* **35**, 375 (1971).
- 33 A. Thompson and D. Vaughan, *X-Ray Data Booklet* (°, Berkley, CA, 2001).
- 34 M. P. Seah and W. A. Dench, *Surf. Interface. Anal.* **1**, 2 (1979).
- 35 A. Baraldi, M. Barnaba, B. Brena, D. Cocco, G. Comelli, S. Lizzit, G. Paolucci, and R. Rosei, *J. Electron Spec. Rel. Phen.* **76**, 145 (1995).

-
- 36 A. M. de Jong and J. W. Niemantsverdriet, *Surf. Sci.* **233**, 355 (1990).
- 37 P. A. Redhead, *Vacuum* **12**, 203 (1962).
- 38 T. Fuhrmann, *Elektronenspektroskopische Untersuchungen zur aktivierten Adsorption und thermischen Entwicklung von einfachen Kohlenwasserstoffen auf Platin und Nickel Einkristalloberflächen*, PhD Thesis at Physikalische Chemie II (FAU, Erlangen, **2005**).
- 39 P. W. Atkins, *Physikalische Chemie* (VCH, Weinheim; Basel; Cambridge; New York, NY, 1990).
- 40 W. Braun, *Adsorption und Koadsorption kleiner Moleküle auf Übergangsmetallen und ultradünnen Übergangsmetallschichten*, PhD Thesis at Physikalische Chemie II (FAU, Erlangen, **2003**).
- 41 M. Yata and R. J. Madix, *Surf. Sci.* **328**, 171 (1995).
- 42 M. Wang and W. Bian, *Chem. Phys. Lett.* **391**, 354 (2004).
- 43 F. A. Carey and R. J. Sundberg, *Organische Chemie* (VCH, Weinheim, 1995).
- 44 U. Maitra and J. Chandrasekhar, *Resonance* **2**, 18 (1997).
- 45 C. Davisson and L. H. Germer, *Phys. Rev.* **30**, 705 LP (1927).
- 46 G. Ertl and J. Küppers, *Low Energy Electrons and Surface Chemistry* (VCH, Weinheim, 1985).
- 47 C. Papp, T. Fuhrmann, B. Tränkenschuh, R. Denecke, and H.-P. Steinrück, *Phys. Rev. B* **73**, 235426 (2006).
- 48 M. Kinne, *Kinetische Untersuchungen von Oberflächenreaktionen mittels hochaufgelöster Röntgen-Photoelektronenspektroskopie - Oxidation von CO auf Pt(111) und zugehörige Elementarschritte*, PhD Thesis at Physikalische Chemie II (FAU, Erlangen, **2004**).
- 49 B. Tränkenschuh, C. Papp, R. Streber, T. Fuhrmann, R. Denecke, and H.-P. Steinrück, *Surf. Sci.*, in press. (2007).
- 50 G. Scoles, *Atomic and molecular beam methods* (Oxford University Press, New York, 1988).
- 51 D. A. King and M. G. Wells, *Prog. Roy. Soc. A* **339**, 245 (1974).
- 52 J. C. Bertolini, G. Dalmai-Imelik, and J. Rousseau, *Surf. Sci.* **67**, 478 (1977).
- 53 R. Denecke, P. Vaterlein, M. Bassler, N. Wassdahl, S. Butorin, A. Nilsson, J.-E. Rubensson, J. Nordgren, N. Martensson, and R. Nyholm, *J. Electron Spec. Rel. Phen.* **101-103**, 971 (1999).

-
- 54 R. Neubauer, *In situ*-Untersuchungen zur Reaktivität ungesättigter, aromatischer und funktionalisierter Kohlenwasserstoffe auf einkristallinen Übergangsmetalloberflächen, PhD Thesis at Physikalische Chemie II (FAU, Erlangen, **2006**).
- 55 K. P. C. Vollhardt, *Organische Chemie* (VCH, Weinheim, 1988).
- 56 W. Braun, G. Held, H.-P. Steinrück, C. Stellwag, and D. Menzel, *Surf. Sci.* **475**, 18 (2001).
- 57 O. Dippel, F. Cemic, and E. Hasselbrink, *Surf. Sci.* **357-358**, 190 (1996).
- 58 O. Schaff, V. Fernandez, P. Hofmann, K.-M. Schindler, A. Theobald, V. Fritzsche, A. M. Bradshaw, R. Davis, and D. P. Woodruff, *Surf. Sci.* **348**, 89 (1996).
- 59 S. J. Stranick, M. M. Kamna, and P. S. Weiss, *Surf. Sci.* **338**, 41 (1995).
- 60 J. Yoshinobu, H. Tanaka, T. Kawai, and M. Kawai, *Phys. Rev. B* **53**, 7492 (1996).
- 61 G. A. Somorjai, *Introduction to Surface Chemistry and Catalysis* (Wiley, New York, 1994).
- 62 H.-P. Steinrück, W. Huber, T. Pache, and D. Menzel, *Surf. Sci.* **218**, 293 (1989).
- 63 G. Held, M. P. Bessent, S. Titmuss, and D. A. King, *J. Chem. Phys.* **105**, 11305 (1996).
- 64 W. Braun, C. Papp, G. Held, and H.-P. Steinrück, (to be published).
- 65 W. Huber, H.-P. Steinrück, T. Pache, and D. Menzel, *Surf. Sci.* **217**, 103 (1989).
- 66 F. Mittendorfer and J. Hafner, *Surf. Sci.* **472**, 133 (2001).
- 67 S. Yamagishi, S. J. Jenkins, and D. A. King, *J. Chem. Phys.* **114**, 5765 (2001).
- 68 T. Fuhrmann, M. Kinne, B. Tränkenschuh, C. Papp, J. F. Zhu, R. Denecke, and H.-P. Steinrück, *New. J. Phys.* **7**, 107 (2005).
- 69 M. Wiklund, A. Jaworowski, F. Strisland, A. Beutler, A. Sandell, R. Nyholm, S. L. Sorensen, and J. N. Andersen, *Surf. Sci.* **418**, 210 (1998).
- 70 H.-P. Steinrück, T. Fuhrmann, C. Papp, B. Tränkenschuh, and R. Denecke, *J. Phys. Chem.* **125**, 204706 (2006).
- 71 M. Kinne, T. Fuhrmann, C. M. Whelan, J. F. Zhu, J. Pantförder, M. Probst, G. Held, R. Denecke, and H.-P. Steinrück, *J. Chem. Phys.* **117**, 10852 (2002).

-
- 72 F. Bondino, G. Comelli, F. Esch, A. Locatelli, A. Baraldi, S. Lizzit, G. Paolucci, and R. Rosei, *Surf. Sci.* **459**, L467 (2000).
- 73 H. Ihm, H. M. Ajo, J. M. Gottfried, P. Bera, and C. T. Campbell, *J. Phys. Chem. B* **108**, 14627 (2004).
- 74 G. Witte, H. Range, J. P. Toennies, and C. Wöll, *Phys. Rev. Lett.* **71**, 1063 (1993).
- 75 P. S. Bagus, K. Hermann, and C. Wöll, *J. Chem. Phys.* **123** (2005).
- 76 W. Huber, *Elektronenspektroskopische Untersuchung von zyklischen Kohlenwasserstoffen auf Nickeloberflächen mit Synchrotronstrahlung*, PhD Thesis at Festkörperphysik und Technische Physik (Technische Universität, München, **1991**).
- 77 G. Held, J. Schuler, W. Sklarek, and H. P. Steinrück, *Surf. Sci.* **398**, 154 (1998).
- 78 S. Lehwald, H. Ibach, and J. E. Demuth, *Surf. Sci.* **78**, 577 (1978).
- 79 G. Held, J. Schuler, W. Sklarek, and H.-P. Steinrück, *Surf. Sci.* **398**, 154 (1998).
- 80 W. Huber, P. Zebisch, T. Bornemann, and H.-P. Steinrück, *Surf. Sci.* **258**, 16 (1991).
- 81 P. Zebisch, W. Huber, and H.-P. Steinrück, *Surf. Sci.* **258**, 1 (1991).
- 82 S. Bao, R. Lindsay, M. Polcik, A. Theobald, T. Gießel, O. Schaff, P. Baumgartel, R. Terborg, A. M. Bradshaw, N. A. Booth, and D. P. Woodruff, *Surf. Sci.* **478**, 35 (2001).
- 83 W. Huber, P. Zebisch, T. Bornemann, and H.-P. Steinrück, *Surf. Sci.* **239**, 353 (1990).
- 84 S. Tjandra and F. Zaera, *J. Catal.* **164**, 82 (1996).
- 85 D. Syomin and B. E. Koel, *Surf. Sci.* **498**, 61 (2002).
- 86 D. E. Hunka, T. Picciotto, D. M. Jaramillo, and D. P. Land, *Surf. Sci.* **421**, L166 (1999).
- 87 H. H. Hwu, J. Eng, J., and J. Chen, *J. Am. Chem. Soc.* **124**, 702 (2002).
- 88 D. H. Parker, C. L. Pettiette-Hall, Y. Li, R. T. McIver, and J. C. Hemminger, *J. Phys. Chem.* **96**, 1888 (1992).
- 89 N. A. Khan, M. B. Zellner, L. E. Murillo, and J. G. G. Chen, *Catal. Lett.* **95**, 1 (2004).
- 90 G. Held, *J. Phys.: Condens. Matter* **15**, R1501 (2003).

-
- 91 G. Held and H.-P. Steinrück, in *Physics of Covered Solid Surfaces*, edited by H. P. Bonzel (Springer, Berlin, 2005), Vol. III/42, p. 300.
- 92 C. Morin, D. Simon, and P. Sautet, *Surf. Sci.* **600**, 1339 (2006).
- 93 M. E. Bussel, F. C. Henn, and C. T. Campbell, *J. Phys. Chem.* **96**, 5978 (1992).
- 94 F. C. Henn, A. L. Diaz, M. E. Bussel, M. B. Hugenschmidt, M. E. Domagala, and C. T. Campbell, *J. Phys. Chem.* **96**, 5965 (1992).
- 95 C. L. A. Lamont, M. Borbach, R. Martin, P. Gardner, T. S. Jones, H. Conrad, and A. M. Bradshaw, *Surf. Sci.* **374**, 215 (1997).
- 96 F. Mittendorfer and J. Hafner, *J. Phys. Chem. B* **106**, 13299 (2002).
- 97 N. A. Khan, M. B. Zellner, and J. G. Chen, *Surf. Sci.* **556**, 87 (2004).
- 98 H.-P. Steinrück, W. Huber, T. Pache, and D. Menzel, *Surf. Sci.* **218**, 293 (1989).
- 99 A. Winkler and K. D. Rendulic, *Surf. Sci.* **118**, 19 (1982).
- 100 P. A. Redhead, *Vacuum* **12**, 203 (1962).
- 101 H. Beyer, W. Walter, and W. Francke, *Lehrbuch der Organischen Chemie* (Hirzel, Stuttgart, 2004).
- 102 E. Furimsky, *Appl. Cat.* **6**, 159 (1983).
- 103 M. H. Qiao, F. Q. Yan, W. S. Sim, J. F. Deng, and G. Q. Xu, *Surf. Sci.* **460**, 67 (2000).
- 104 J. Stöhr, J. L. Gland, E. B. Kollin, R. J. Koestner, A. L. Johnson, E. L. Muetterties, and F. Sette, *Phys. Rev. Lett.* **53**, 2161 (1984).
- 105 D. R. Huntley, D. R. Mullins, and M. P. Wingeier, *J. Phys. Chem.* **100**, 19620 (1996).
- 106 T. E. Caldwell and D. P. Land, *Polyhedron* **16**, 3197 (1997).
- 107 K. V. R. Chary, K. S. R. Rao, G. Muralidhar, and P. K. Rao, *Carbon* **29**, 478 (1991).
- 108 K. L. Tan, B. T. G. Tan, E. T. Kang, K. G. Neoh, and Y. K. Ong, *Phys. Rev. B* **42**, 7563 LP (1990).
- 109 B. A. Sexton, *Surf. Sci.* **163**, 99 (1985).
- 110 F.-M. Pan, P. C. Stair, and T. H. Fleisch, *Surf. Sci.* **177**, 1 (1986).
- 111 G. Tourillon, S. Raaen, T. A. Skotheim, M. Sagurton, R. Garrett, and G. P. Williams, *Surf. Sci.* **184**, L345 (1987).
- 112 G. R. Schoofs and J. B. Benzinger, *Surf. Sci.* **192**, 373 (1987).

-
- 113 F. P. Netzer, E. Bertel, and A. Goldmann, *Surf. Sci.* **199**, 87 (1988).
- 114 W. e. A. Abdallah and A. E. Nelson, *Surf. Sci.* **585**, 113 (2005).
- 115 K.-j. Kim, J. Han, T.-H. Kang, K. Ihm, C. Jeon, S. Moon, C.-C. Hwang, H.-N. Hwang, and B. Kim, *J. Electron Spec. Rel. Phen.* **144-147**, 429 (2005).
- 116 C. J. Baddeley, C. Hardacre, R. M. Ormerod, and R. M. Lambert, *Surf. Sci.* **369**, 1 (1996).
- 117 T. E. Caldwell, I. M. Abdelrehim, and D. P. Land, *J. Am. Chem. Soc.* **118**, 907 (1996).
- 118 T. E. Caldwell and D. P. Land, *J. Phys. Chem. B* **103**, 7869 (1999).
- 119 A. Loui and S. Chiang, *Appl. Surf. Sci.* **237**, 555 (2004).
- 120 R. M. Ormerod, C. J. Baddeley, C. Hardacre, and R. M. Lambert, *Surf. Sci.* **360**, 1 (1996).
- 121 A. Mulligan, S. M. Johnston, G. Miller, V. Dhanak, and M. Kadodwala, *Surf. Sci.* **541**, 3 (2003).
- 122 F. Q. Yan, M. H. Qiao, X. M. Wei, Q. P. Liu, J. F. Deng, and G. Q. Xu, *J. Chem. Phys.* **111**, 8068 (1999).
- 123 S. Letarte, A. Adnot, and D. Roy, *Surf. Sci.* **448**, 212 (2000).
- 124 E. E. Rennie, U. Hergenhan, O. Kugeler, A. Rudel, S. Marburger, and A. M. Bradshaw, *J. Chem. Phys.* **117**, 6524 (2002).
- 125 M. Mauerer, P. Zebisch, M. Weinelt, and H.-P. Steinrück, *J. Chem. Phys.* **99**, 3343 (1993).
- 126 A. A. Bakke, H.-W. Chen, and W. L. Jolly, *J. Electron Spec. Rel. Phen.* **20**, 333 (1980).
- 127 J. M. Gottfried, K. Flechtner, A. Kretschmann, T. Lukascyk, and H.-P. Steinrück, *J. Am. Chem. Soc.* **128**, 5644 (2006).
- 128 K. Hoffmann, *Anorganische Chemie* (Friedr. Vieweg & Sohn, Braunschweig, 1965).
- 129 A. Giertz, M. Bassler, O. Bjorneholm, H. Wang, R. Feifel, C. Miron, L. Karlsson, S. Svensson, K. J. Borve, and L. J. Saethre, *J. Chem. Phys.* **117**, 7587 (2002).
- 130 C. Papp, *Untersuchung der Adsorption zyklischer Kohlenwasserstoffe auf Ni(111) mit höchstauflöser Röntgen-Photoelektronenspektroskopie*, Diploma Thesis at Physikalische Chemie II (FAU, Erlangen, **2002**).

-
- 131 J. F. Zhu, M. Kinne, T. Fuhrmann, R. Denecke, and H.-P. Steinrück, *Surf. Sci.* **529**, 384 (2003).
- 132 E. Laksono, A. Galtayries, C. Argile, and P. Marcus, *Surf. Sci.* **530**, 37 (1996).
- 133 M. A. Van Hove and G. A. Somorjai, *Surf. Sci.* **92**, 489 (1980).
- 134 G. F. Froment, *J. Mol. Catal. A* **163**, 147 (2000).
- 135 T. V. Choudhary, C. Sivadinarayana, C. C. Chusuei, A. Klinghoffer, and D. W. Goodman, *J. Catal.* **199**, 9 (2001).
- 136 M. G. Poirier and C. Sapundzhiev, *Int. J. Hydrogen Energy* **22**, 429 (1997).
- 137 E. K. Lee, S. Y. Lee, G. Y. Han, B. K. Lee, T.-J. Lee, J. H. Jun, and K. J. Yoon, *Carbon* **42**, 2641 (2004).
- 138 D. J. AlberasSloan and J. M. White, *Surf. Sci.* **365**, 212 (1996).
- 139 R. J. Madix, A. Carlsson, and C. L. Kao, *Abstr. Pap. Am. Chem. Soc.* **219**, U507 (2000).
- 140 Y. Matsumoto, Y. A. Gruzdkov, K. Watanabe, and K. Sawabe, *J. Chem. Phys.* **105**, 4775 (1996).
- 141 A. F. Carlsson and R. J. Madix, *Surf. Sci.* **458**, 91 (2000).
- 142 J. A. Stinnett and R. J. Madix, *Abstr. Pap. Am. Chem. Soc.* **213**, 57 (1997).
- 143 R. Larciprete, A. Goldoni, A. Groso, S. Lizzit, and G. Paolucci, *Surf. Sci.* **482**, 134 (2001).
- 144 A. C. Luntz and D. S. Bethune, *J. Chem. Phys.* **90**, 1274 (1989).
- 145 A. C. Luntz and H. F. Winters, *J. Chem. Phys.* **101**, 10980 (1994).
- 146 D. T. P. Watson, J. van Dijk, J. J. W. Harris, and D. A. King, *Surf. Sci.* **506**, 243 (2002).
- 147 K. M. DeWitt, L. Valadez, H. L. Abbott, K. W. Kolasinski, and I. Harrison, *J. Phys. Chem. B* **110**, 6705 (2006).
- 148 T. Hiraoka, S. Yagyu, T. Kondo, T. Ikeuchi, and S. Yamamoto, *Jpn. J. Appl. Phys.* **39**, 612 (2000).
- 149 T. Kondo, T. Sasaki, and S. Yamamoto, *J. Chem. Phys.* **116**, 7673 (2002).
- 150 T. Kondo, T. Sasaki, and S. Yamamoto, *J. Chem. Phys.* **118**, 760 (2003).
- 151 T. Fuhrmann, M. Kinne, C. M. Whelan, J. F. Zhu, R. Denecke, and H.-P. Steinrück, *Chem. Phys. Lett.* **390**, 208 (2004).
- 152 T. X. Carroll, N. Berrah, J. Bozek, J. Hahne, E. Kukk, L. J. Saethre, and T. D. Thomas, *Phys. Rev. A* **59**, 3386 (1999).

-
- 153 J. John T. Yates, in *41st National Symposium of the American Vacuum Society* (AVS, Denver, Colorado (USA), 1995), Vol. 13, p. 1359.
- 154 W. A. Brown, R. Kose, and D. A. King, *Surf. Sci.* **440**, 271 (1999).
- 155 M. Rocca, L. Savio, and L. Vattuone, *Surf. Sci.* **502-503**, 331 (2002).
- 156 J. T. Yates Jr., in *41st National Symposium of the American Vacuum Society* (AVS, Denver, Colorado (USA), 1995), Vol. 13, p. 1359.
- 157 A. T. Gee, B. E. Hayden, C. Mormiche, A. W. Kleyn, and B. Riedmuller, *J. Chem. Phys.* **118**, 3334 (2003).
- 158 D. J. Oakes, H. E. Newell, F. J. M. Rutten, M. R. S. McCoustra, and M. A. Chesters, *J. Vac. Sci. Technol. A* **14**, 1439 (1996).
- 159 S. Paavilainen and J. A. Nieminen, *Phys. Rev. B* **66**, 155409 (2002).
- 160 P. Feulner, T. Niedermayer, K. Eberle, S. R., D. Menzel, A. Baumer, E. Schmich, A. Shaporenko, Y. Tai, and M. Zharnikov, *Phys. Rev. Lett.* **93**, 178302 (2004).
- 161 T. Härtel, U. Strüber, and J. Kueppers, *Thin Sol. Films* **229**, 163 (1993).
- 162 P. Gambardella, *Growth, electronic structure and magnetism of supported metal nanowires*, PhD Thesis at Physique (École polytechnique fédérale de Lausanne, Lausanne, **2000**).
- 163 U. Strüber, A. Kastner, and J. Küppers, *Thin Solid Films* **250**, 101 (1994).
- 164 P. W. Davies, M. A. Quinlan, and G. A. Somorjai, *Surf. Sci.* **121**, 290 (1982).
- 165 R. Streber, *In-situ-XPS-Untersuchungen des Einflusses von Silber auf die CO-Adsorption auf gestuften Platinoberflächen*, Diploma Thesis at Physikalische Chemie II (FAU, Erlangen, **2006**).
- 166 H. Mortensen, L. Diekhöner, A. Baurichter, and A. C. Luntz, *J. Chem. Phys.* **116**, 5781 (2002).
- 167 S. Kneitz, *Adsorptions- und Streumessungen von CO an ultradünnen Metallschichtsystemen mittels eines Überschall-Molekularstrahls*, PhD Thesis at Experimentelle Physik II (JMU, Würzburg, **1999**).
- 168 C. Papp, B. Tränkenschuh, R. Streber, T. Fuhrmann, R. Denecke, and H.-P. Steinrück, *J. Phys. Chem. C* **111**, 2177 (2007).
- 169 F. Zaera and H. Hoffmann, *J. Phys. Chem.* **95**, 6297 (1991).
- 170 F. Zaera, *Surf. Sci.* **262**, 335 (1992).
- 171 A. Michaelidis and P. Hu, *J. Am. Chem. Soc.* **122**, 9866 (2000).
- 172 R. J. Madix and S. G. Telford, *Surf. Sci.* **328**, L576 (1995).

-
- 173 A. M. Baro, H. Ibach, and H. D. Bruchmann, *Surf. Sci.* **88**, 384 (1979).
- 174 N. Freyer, G. Pirug, and H. P. Bonzel, *Surf. Sci.* **125**, 327 (1983).
- 175 A. F. Lee, K. Wilson, A. Goldoni, R. Larciprete, and S. Lizzit, *Surf. Sci.* **513**, 140 (2002).
- 176 C. Papp, B. Tränkenschuh, T. Fuhrmann, R. Denecke, and H.-P. Steinrück, to be published.

Danksagung

Ich möchte mich an dieser Stelle bei allen bedanken, die für das Gelingen dieser Arbeit einen wertvollen Beitrag geleistet haben.

- Herrn Steinrück für seine große Geduld und die vielen, langen Diskussionen. Vielen Dank auch für ihr Vertrauen und die angenehme Atmosphäre, die sie in ihrer Arbeitsgruppe schaffen.
- Herrn Denecke für die Betreuung meiner Arbeit, sowie die stetige und begeisterte Unterstützung dieser. Vielen Dank auch für die vielen und auch oft lustigen Messzeiten.
- Herrn Libuda für die Übernahme der Zweitkorrektur und die schnelle Abhandlung dieser, obwohl es ein langes Schriftstück war.
- Herrn Froitzheim für die Diskussionen über Gott, die Welt und die Wissenschaft.
- Thomas und Barbara, die über lange Zeit an meiner Seite waren, als Mitstreiter in Berlin und auch im Büro. Sie haben sogar meinen weiten Humor nachts um 5 (zumeist) noch verstanden.
- Auch der jungen BESSY-Strahlzeitcrew soll hier gedankt werden, die Messzeiten zu einem besonderen Erlebnis gemacht haben, nicht wahr Regine, Till und Michael.
- Ein besonderer Dank auch an H.-P. Bäuml, der immer Zeit hatte oder sich genommen hat und somit viele große und kleine Probleme löste.
- Herrn Wölfel und seinen Mitarbeitern, die mir immer wieder schnell bei meinen Problemen geholfen haben.
- Den Mitarbeitern des Arbeitskreises, die ein angenehmes und freundliches Arbeitsklima geschaffen haben.
- Abschließend möchte ich mich noch bei meinen Eltern bedanken, die dies schließlich und endlich erst möglich gemacht haben, auch durch ihre stete Unterstützung und ihre immer offenen Ohren.